MICROSTRUCTURE-PROPERTY DEVELOPMENT IN FRICTION STIR WELDS OF ALUMINIUM-BASED ALLOYS

By

MOATAZ M. ATTALLAH

A thesis submitted to
University of Birmingham
for the degree of
DOCTOR OF PHILOSPHY

Metallurgy and Materials
School of Engineering
University of Birmingham
September 2007

ACKNOWLEDGEMENTS

I start this by thanking Allah Almighty for giving me strength and patience. I would like to express my love and gratitude to my parents for their prayers, understanding and never-ending support during the most difficult period in my life so far.

Great appreciation goes to my supervisors, Dr. Martin Strangwood and Dr. Claire Davis, for their valuable pieces of advice, expert guidance, patience, encouragement and support they have given me throughout the PhD.

I would like to acknowledge the support of Universities-UK and the Department of Metallurgy and Materials at the University of Birmingham for offering me a Ph.D. scholarship in this distinguished research institute.

The support of the Welding Institute (TWI) for this research, especially Dr. Philip Threadgill, is highly appreciated. Special thanks go to Dr. Andreas Afseth from Novelis Technology for the provision of materials, as well as to Dr. Geoff Scamans from Innoval.

The assistance of the electron microscopy centre staff, the workshop, and the technicians and staff of Metallurgy and Materials is appreciated.

I would like to thank former and present members of the PTMM group, especially Ahmad Sulaiman, Catherine Caton, Chris Wang, and Heiko Widmann, and my colleagues in the department, Yehia El-Shazly and Cao Yurong who were such a pleasant company in the very difficult times. I would like to thank Yudie Yuan for helping me with the TEM work and for all the wisdom she tried to teach me (but she couldn't!).

Finally, I would like to dedicate this work to Rania, because without her, it would have been impossible to see a light at the end of the PhD tunnel.

ABSTRACT

Friction Stir Welding (FSW) is known to result in a complex microstructural development, with features that remain unexplained, such as: the formation of the onion rings structure. Moreover, various microstructural factors have been suggested to control the strength in Al-Mg AA5xxx welds. The influence of the basemetal microstructural parameters (e.g. grains, intermetallic particles, stored energy) on the microstructure-property development has not been previously investigated, and is the subject of the present work.

To rationalise the microstructural and local strength (hardness) development, especially within the heat affected zone (HAZ), a simple and rapid 3-D heat transfer model was established to predict the thermal fields associated with FSW. This numerical model utilises the alternating direction implicit method to simulate the transient thermal cycle based on the process parameters, thermo-physical and thermo-mechanical properties of the material. The model was fitted for the friction coefficient and contact conductance between the sheet and the backing plate using experimental torque and force data, as well as *in-situ* thermocouple measurements for AA2xxx and AA5xxx welds. The model predictions were consistent with the microstructural and microhardness development in the welds. Gleeble thermal simulations showed that the heating rate during welding affects the recrystallisation start temperature, which could delay or speed up recrystallisation.

In the thermo-mechanically affected zone (TMAZ), the onion rings structure was studied in several AA5xxx and AA2xxx welds. This follows a thorough microstructural investigation of the basemetals sheets prepared by direct chill and continuous casting, to establish the influence of the microstructural heterogeneity in the basemetal on the onion rings formation and the microstructural development. Stereological studies of the intermetallic particle distributions in the basemetal and the welds revealed that there is a direct relation between the banding of constituent particles (Al(Fe,Mn)Si or Al_6(Fe,Mn) in AA5xxx) or equilibrium phases (Al_2CuMg or Al_2Cu in AA2xxx) along the rolling direction, and the formation of the onion rings. A clear onion rings structure was defined by three microstructural features, which are: 1) the existence of fine and coarse grain bands, 2) grain boundary precipitates coinciding with the fine grain bands, and 3) coarse particle segregation in the coarse grain bands. Upon etching, these microstructural heterogeneities form the unique onion rings etching profile. The formation of the onion rings was rather independent of the process parameters and alloy type, as long as the intermetallic particles are banded regardless of their types. However, alloys with high area fraction of intermetallic particles (~> 0.02) were found to produce more pronounced microstructural heterogeneities, which resulted in a stronger etching intensity.

The microstructural heterogeneities within the AA5xxx welds, especially the interaction between the dislocations and the fine Al_6(Fe,Mn) dispersoids, indicated that establishing a structure-property model requires the incorporation of the various strengthening factors. Stereological studies of the grain size and intermetallic particle distributions in the TMAZ indicated that the hardness is a combination of various microstructural factors, with grain-boundary strengthening as the main factor, with additional contributions by Orowan strengthening by the Al_6(Fe,Mn) particles in specific locations, as well as a minor contribution by solid solution strengthening which resulted from the dissolution of Mg_2Si during welding. The high dislocation stored energy in the TMAZ, as measured by differential scanning calorimetry, was associated with the geometrically-necessary dislocations which resulted from the interaction with the intermetallic particles and grains, but do not contribute to the hardness.

TABLE OF CONTENTS

Chapter 1: General Introduction **1**
1.1. General Introduction 1
1.2. Project Aim, Objectives & Approach 4
1.3. References 6

Chapter 2: Metallurgy of Aluminium Alloys **2**
2.1. Aluminium-Magnesium (AA5xxx) Alloys 7
2.1.1. The Al-Mg System 7
2.1.2. Intermetallic Particles in AA5xxx 8
2.1.2.a. Constituent Particles in 5xxx series Alloys 9
2.1.2.b. Dispersoids in 5xxx series Alloys 11
2.1.2.c. Phase Transformations in 5xxx series Alloys 12
2.2. Aluminium-Copper Alloys (AA2xxx) Alloys 14
2.2.1. The Al-Cu System 14
2.2.2. Intermetallic Particles in AA2xxx 15
2.2.2.a. Age Hardening Precipitates in the Al-Cu System 16
2.2.2.b. Age Hardening Precipitates and Equilibrium phases in the Al-Cu-Mg System . 17
2.3. Influence of the Manufacturing Route of Al-based Alloys on the Microstructure and Properties 19
2.3.2. Microstructural Differences between DC and CC sheets 20
2.3.2.a. Micro-Segregation 20
2.3.2.b. Macro-Segregation 23
2.3.2.c. Differences in Grain and Intermetallic Particle Structures 24
2.4. Strengthening Mechanisms in Al-based Alloys 27
2.4.1. Grain boundary strengthening 27
2.4.2. Solid solution strengthening 28
2.4.3. Particle strengthening 30
2.4.4. Work hardening (dislocation-dislocation interactions) 33
2.4.4.a. Ashby's Model 33
2.4.4.b. Hansen et al. Model 35
2.4.5. Strength Models for Al-Alloys 36
2.4.5.a. Starink and Wang Model 37
2.4.5.b. Deschamps and Bréchet Model 38
2.5. Microstructural Development during Thermal and Thermomechanical Processes 40
2.5.1. The Deformed Microstructure 40
2.5.1.a. The Dislocation Stored Energy 40
2.5.1.b. Influence of Intermetallic Particles on the Stored Energy (Two Phase Alloys) . 42
2.5.2. Recovery 43
2.5.2.a. Influence of solute atoms on recovery after deformation 44
2.5.2.b. Influence of particles on recovery 45
2.5.3. Recrystallisation 46
2.5.4. Hot Deformation 48
2.5.4.a. Dynamic Recovery (DRX) 48
2.5.4.b. Dynamic Recrystallisation (DRX) 49
2.5.4.c. Factors Controlling DRV and DRX 51
2.5.5. Anisothermal Recrystallisation 51
2.6. Summary of Literature: Key Findings and Areas of Investigation 54
2.7. References 56

Chapter 3: Friction Stir Welding: Process Modelling and Microstructure 64
3.1. Classification of Weld Zones ... 65
3.1.1. Threadgill's Classification ... 65
3.1.2. Arbegast's Classification ... 66
3.2. Influence of Process Parameters on the Temperature Distribution ... 68
3.3. Modelling of the Thermal Input ... 73
3.3.1. Analytical Models ... 73
3.3.2. Numerical Thermal/Thermomechanical Models ... 76
3.3.2.a. Friction-Induced FE & FD Models ... 76
3.3.2.b. Deformation-Induced FE & CFD Models ... 77
3.4. Material Flow during FSW ... 80
3.4.1. Markers Insert Technique (MIT) Studies of Material Flow ... 80
3.4.2. Similar and Dissimilar welds ... 83
3.5. Microstructural Development due to FSW ... 87
3.5.1. Grain Structure ... 87
3.5.1.a. Recrystallisation Mechanisms ... 88
3.5.1.b. Influence of Process Parameters on Grain Size ... 91
3.5.2. Constituent Particles ... 92
3.5.3. Onion Rings Structure ... 94
3.6. Hardness Development ... 98
3.6.1. Heat Treatable Al-Alloys welds ... 98
3.6.2. Work-Hardenable Al-Alloys welds ... 102
3.7. Summary of Literature: Key Findings and Areas of Investigation ... 106
3.8. References ... 108

Chapter 4: Materials & Experimental Methods 116
4.1. Materials ... 116
4.2. Friction Stir Welding ... 118
4.3. Microstructural Investigations ... 120
4.3.1. Optical and Scanning Electron Microscopy ... 120
4.3.2. Transmission Electron Microscopy (TEM) ... 121
4.3.3. Electron Backscattered Diffraction (EBSD) ... 123
4.3.4. Stereological Methods ... 123
4.4. Differential Scanning Calorimetry ... 125
4.4.1. The device ... 125
4.4.2. Specimen and method ... 125
4.5. Mechanical Testing ... 129
4.5.1. Hardness ... 129
4.5.2. Tensile Testing ... 129
4.6. Furnace Work & Heat Treatment ... 131
4.7. Gleeble Thermo-Mechanical Simulator (GTMS) ... 132
4.8. References ... 134

Chapter 5: Basemetal Characterisation: Influence of the Processing Route 135
5.1. AA5251 ... 135
5.1.1. H34 Condition: Grain Structure and Deformed Substructure ... 135
5.1.2. O Condition: Annealed Grain Structure ... 139
5.1.3. Constituent Particles and Dispersoids ... 140

5.1.4. Effect of Heat Treatments on Hardness & Microstructure 144
5.1.4.a. Basemetal Hardness 144
5.1.4.b. Studying the microstructure-hardness development using the Gleeble & DSC 146
5.2. AA5083 149
5.2.1. Grain Structure and Deformed Substructure 149
5.2.2. Constituent Particles and Dispersoids 150
5.2.3. Effect of Heat Treatments on Hardness & Microstructure 152
5.3. AA5754-O 155
5.3.1. Grain Structure 155
5.3.2. Constituent Particles and Dispersoids 158
5.4. AA2024-T351 161
5.4.1. Grain Structure 161
5.4.2. Particle Structure 161
5.4.3. Hardness 163
5.4.4. Dissolution and Precipitation Processes in 2024-T351 163
5.5. Summary of the Basemetals Characteristics 165
5.5. Summary of the Basemetals Characteristics 165
5.6. References 166

Chapter 6: Thermal Modelling: A Tool to Rationalise the HAZ Development 169
6.1. Mathematical Modelling of Heat Flow 169
6.1.1. Constitutive Equations 169
6.1.2. Numerical Heat Flow Modelling 170
6.1.3. Heat Input Generation and Distribution 172
6.1.3.a. Heat Generation 172
6.1.3.b. Spatial Distribution of the Heat Sources 174
6.1.4. Boundary Conditions 175
6.1.5. Material Properties 175
6.1.5.a. Thermomechanical Properties 175
6.1.5.b. Thermophysical Properties 177
6.2. Fitting & Validation of the Thermal Model 179
6.2.1. Fitting: W1:2024-T351 179
6.2.1.a. Analysis of Experimental Data 179
6.2.1.b. Fitting of the Thermal Measurements 181
6.2.2. Validation: W2:2024-T351 184
6.2.3. 5754-O weld: SPECIAL COOLING OF THIN PLATES 186
6.2.3.a. Analysis of Experimental Data 186
6.2.3.b. Fitting the Thermocouple Measurements 187
6.2.3. Model Assessment 189
6.2.3.a. Numerical FD Models 189
6.2.3.b. FE and CFD Models 191
6.2.3.c. Contact Condition 192
6.3. Thermal Fields and HAZ Development 193
6.3.1. 5251-H34-weld 193
6.3.1.a. Analysis of Experimental Results 193
6.3.1.b. Predicted Thermal Fields 194
6.3.1.b. HAZ Microstructure and Microhardness 195
6.3.1.c. Simulating the HAZ Microstructural Development using Gleeble TMS 197
6.3.2. 5083-H116-weld 200
6.3.2.a. Predicted Thermal Fields 200

6.3.2.b. Microhardness Contours and HAZ microstructure 201
6.3.3. 2024-T351 203
6.3.3.a. Predicted Thermal Fields 203
6.3.3.b. Microhardness Development 204
6.4. Conclusions 207
6.5. References 208

Chapter 7: Influence of the Basemetal on the Microstructural Development 211
7.1. AA5251 (H34 and O) 211
7.1.1. Weld Macrostructure 211
7.1.2. Weld Microstructure 212
7.1.2.a. Microstructural Development (Qualitative) 213
7.1.2.b. Quantitative Metallography 216
7.1.2.c. Dislocation Structure and Precipitates 219
7.2. AA5754 (DC and CC) 222
7.2.1. Weld Macrostructure 222
7.2.1.a. DC1 (WD || RD) 222
7.2.1.b. CC1 (WD || RD) 222
7.2.1.c. CC2 (WD ⊥ RD) 223
7.2.2. Weld Microstructure 224
7.2.2.a. Microstructural Development (Qualitative) 224
7.2.2.b. Quantitative Metallography 229
7.2.2.c. Dislocation Structure and Precipitates 231
7.3. AA5083 233
7.3.1. Weld Macrostructure 233
7.3.2. Weld Microstructure 233
7.3.2.a. Microstructural Development (Qualitative) 233
7.3.2.b. Quantitative Metallography 235
7.3.2.c. Dislocation Structure and Precipitates 236
7.4. AA2024-T351 237
7.4.1. Weld Macrostructure 237
7.4.2. Weld Microstructure 237
7.4.2.a. Microstructural Development (Qualitative) 238
7.4.2.b. Quantitative Metallography 241
7.5. Analysis of Results and Discussion 243
7.5.1. Defining the Onion Rings Structure: Morphology and Parameters 243
7.5.2. Influence of the Basemetal Microstructure on the “Onion Rings” Formation 244
7.5.3. Influence of the Process Parameters on the “Onion Rings” Formation 248
7.5.4. Controlling the Formation of the ORZ and the Weld Microstructure 249
7.5.5. Microstructural Differences between 2xxx and 5xxx series alloys 251
7.6. Conclusions of Chapter 7 253
7.7. References 254

Chapter 8: Structure-Property Relations in AA5xxx Friction Stir Welds 256
8.1. AA5251 Welds 256
8.1.1. Hardness Distribution 257
8.1.2. Hall-Petch 259
8.1.3. Grain substructure 261
8.1.3.a. 5251-H34 basemetal 262
8.1.3.b. 5251-O basemetal 265

8.1.3.c. 5251 Weld 267
8.1.4. Stored Energy 268
8.1.4.a. DSC Measurements and Stored Energy Distribution in the Weld 268
8.1.4.b. Dislocation Density Strengthening Contribution 271
8.1.5. Other Strengthening Contributions 273
8.1.5.a. Solid Solution Strengthening 273
8.1.5.b. Orowan Strengthening 274
8.2. AA5754 Welds 276
8.2.1. Hardness Distribution 276
8.2.2. Grain Size Strengthening 277
8.2.3. Dislocation Stored Energy 278
8.2.3.a. DSC Measurements and Stored Energy in the Weld 278
8.2.3.b. Quantifying ρ_G due to the Non-Deformable Particles 280
8.3. AA5083 weld 281
8.3.1. Hardness Distribution 281
8.3.2. Grain Size Strengthening 282
8.3.3. Orowan Strengthening 283
8.3.4. Dislocation Stored Energy 284
8.4. Discussion 286
8.4.1. Summary of the Findings 286
8.4.2. Interpretation for the Microstructure-Property Relations 288
8.5. Conclusions 290
8.6. References 291

Chapter 9: Conclusions & Future Work **294**
9.1. Summary and Conclusions 294
9.1.1. Thermal Modelling and HAZ Development in FSW 294
9.1.2. Microstructural Development 295
9.1.2.a. Onion Rings Formation 295
9.1.2.b. Qualitative & Quantitative Microstructural Development 296
9.1.3. Structure-Property Relations in AA5xxx welds 297
9.2. Future Work 299

TABLE OF FIGURES

Fig. 2.1. The binary Al-Mg equilibrium diagram 8
Fig. 2.2. Morphologies of the Al_6Mn dispersoids in recrystallised Al-1.3 wt % Mn 12
Fig. 2.3. The Al-rich corner in the Al-Cu system 14
Fig. 2.4. Isothermal section in the Al-Cu-Mg phase diagram at 200 ˚C 18
Fig. 2.5. The age-hardening data of 2024 following solution treatment, quenching and holding in salt bath 18
Fig. 2.6. Schematic diagrams for (a) direct-chill casting 19
Fig. 2.7. Mg and Cu micro-segregation in 2124 showing (a) dendritic cells surrounded by Cu and Mg enriched boundaries, and (b) electron microprobe analysis trace across the boundaries along the dashed line in (a) 20
Fig. 2.8. Influence of the cooling rate and composition on dendrite arm spacing in Al-Cu alloys 22
Fig. 2.9. (a) Through-thickness Cu distribution in 2124 DC ingot 24
Fig. 2.10. Secondary electron SEM micrograph showing the difference in constituent particles morphology in (a) DC, (b) CC AA 5052. The bright particles are the Fe-rich phase, and the dark particles are the Mg_2Si particles 25
Fig. 2.11. Polarised light and optical micrographs of the grain and particle structures near mid-thickness in 1 mm thick sheets of annealed (a,b) CC, (c,d) DC AA 5182 26
Fig. 2.12. Comparison of the hardness development in DC and CC 5052 HB sheets of the same thickness after isochronous annealing as a function of temperature 26
Fig. 2.13. The solid solution strengthening contribution of (a) magnesium in Al-Mg alloys.. 30
Fig. 2.14. The influence of particle strength on dislocation-particle interactions showing (a) the shearing of a deformable particle by moving dislocations 31
Fig. 2.15. Dislocation-particle interactions showing the influence of particle size on strength for non-deformable particles (A) and low strength (C) and high strength (B) deformable particles 32
Fig. 2.16. Types of dislocations within a grain according to Ashby's model 33
Fig. 2.18. Calculated strengthening contribution from (a) high-angle boundaries, and (b) low angle boundary in Al-0.13%Mg alloy deformed by ECAE 36
Fig. 2.19. Predicted increase in the total dislocation density as a function of strain in single phase and particle-containing alloys. 43
Fig. 2.20. Annealing phenomena, showing the transformation from (a) a deformed microstructure, to (b) a recovered microstructure, followed by (c) initiation of recrystallisation, to (d) a fully recrystallised dislocation-free grain structure 43
Fig. 2.21. Schematic diagram for the sequence of recovery in a plastically deformed material 44
Fig. 2.22. The influence of Mg content and the extent of work hardening on recovery as a function of time at room temperature 45
Fig. 2.23. A deformed region surrounding a coarse intermetallic particle in a rolled polycrystal 47
Fig. 2.24. The influence of particle distribution and strain on PSN 48
Fig. 2.25. Stress-strain curve for a material being deformed showing the microstructural development associated with DRV, where 49
Fig. 2.26. Microstructural development during GDRX showing (b) boundary impingement of (a) oppositely serrated grain boundaries 50
Fig. 2.27. (a) The influence of solute content on the flow stress development during deformation [118] and (b) the influence of the particle size and Zener-Hollomon parameter on DRX mechanisms 51

Fig. 2.28. The influence of heating rate on (a) grain size, and (b) recrystallisation temperature 52
Fig. 3.1. Schematic diagram for FSW process and tool designs 64
Fig. 3.2. Typical microstructural zones in Al-based alloys 66
Fig. 3.3. Macrograph of AA2195 weld showing the onion rings structure and the TMAZ 66
Fig. 3.4. Arbegast's classification 67
Fig. 3.5. Temperature distribution close to the WN in 7075-T651 weld 69
Fig. 3.6. The spatial temperature distribution in 6061-T6 welds 69
Fig. 3.7. The influence of the tool rotation speed on the maximum temperature in 6063-T5 . 70
Fig. 3.8. Temperature measurements at mid-thickness for welds carried out with and without a pin in tool 71
Fig. 3.9. Determination of the contact conductance under the tool 77
Fig. 3.10. The MIT study by Seidel and Reynolds 81
Fig. 3.11. The influence of advance per revolution on stirring (AS to the left) 81
Fig. 3.12. Metallographic sections at the sheet mid-thickness of the 7050-T7541 weld 82
Fig. 3.13. FSW tool pin geometries investigated by Zettler *et al.* 83
Fig. 3.14. Dissimilar 2024-6061 weld showing macrographs 84
Fig. 3.15. Section through 6061-T6 weld with the tool removed showing material movement and deposition from the leading to the trailing edges of the tool 85
Fig. 3.16. The observation of the striations along the weld centreline in 2024-T3 weld 86
Fig. 3.17. Microstructural development due to FSW in AA1100 89
Fig. 3.18. Misorientation angle distribution in Al-Cu-Li alloy 89
Fig. 3.19. The microstructural development after post-weld annealing in 7018-T79 weld 90
Fig. 3.20. Influence of the peak temperature on grain size in AA6063 welds 92
Fig. 3.21. Influence of FSW on the intermetallic particles distribution in cast Al-alloy 93
Fig. 3.22. Micrographs of AA8009 weld 94
Fig. 3.23. Segregation of the intermetallic particles in bands on the weld crown of AA2024-T351 weld 95
Fig. 3.24. Influence of the process parameters on the onion rings morphology in 2024-T3 ... 96
Fig. 3.25. Hardness traces at mid-thickness across the weld face of AA6063-T5 welds welded at different rotation speeds, and a feed rate of 360 mm/min 99
Fig. 3.26. TEM micrographs of various weld regions in 6063-T5 weld 99
Fig. 3.27. Centreline microhardness trace at for 6061-T6 weld 100
Fig. 3.28. Distribution of the hardening precipitates in 7075-T651 weld 101
Fig. 3.29. Centreline hardness traces for 5083-O and H321 welds 103
Fig. 3.30. TEM micrographs for the microstructure in the WN 104
Fig. 4.1. Schematic diagram for FSW showing the metallurgical structure directions 119
Fig. 4.2. Photograph of the experimental setup at TWI 119
Fig. 4.3. Influence of the orientation (metallurgical direction) on the grain morphology in wrought structures 120
Fig. 4.4. Measurement of dislocation density using the TEM 122
Fig. 4.5. Point counting method 124
Fig. 4.6. Schematic diagram for the heat-flux DSC 127
Fig. 4.7. Section through the 5251 weld (slightly etched in 10% H_3PO_4 solution) showing where DSC specimens were taken from (dashed black boxes) and selected notation (U 'upper' half of sheet and D 'down' or bottom half of sheet). 127
Fig. 4.8. Example DSC trace using the 2nd run approach 128
Fig. 4.9. DSC specimen traces using the empty pans baseline and using the double-run baseline 128
Fig. 4.10. Tensile specimen dimensions 130

Fig. 4.11. The use of GTMS 132
Fig. 5.1. Grain structure in 5251-H34 136
Fig. 5.2. Through-thickness variation in the ST-RD grain characteristics in 5251-H34 137
Fig. 5.3. Grain substructure in 5251-H34 138
Fig. 5.4. Subgrain structure in 5251-H34 138
Fig. 5.5. (a) Grain structure in 5251-O, (b) histogram for the grain characteristics (ST-LT) 139
Fig. 5.6. Dislocation substructure in 5251-O 140
Fig. 5.7. (a) Micrograph for the constituent particle structure in 5251-O showing the observed types and (b) their corresponding EDS spectra, and the elemental maps for (c) Al(Fe,Mn)Si and (d) Mg_xSi 141
Fig. 5.8. Size distribution plot for the α -Al(Fe,Mn)Si and Mg_xSi particles in 5251-H34 covering the particles $D_{Eq} > 0.5\,\mu m$ 142
Fig. 5.9. Distribution of the α -constituent particles in 5251-H34: (a) banding of particle stringers along the RD, (b) histogram of the inter-particle band spacing in H34 and O basemetal 143
Fig. 5.10. 5251-O condition (a) Al_6(Fe,Mn) rod-like dispersoids observed with the specimen tilted to a 2-beam invisibility condition, g.b. = 0 with b = $[011]$ and g = $(02\bar{2})$, (b) precipitation of the Al_6(Fe,Mn) precipitates on the remnant dislocation structure, (c) corresponding EDS spectrum 144
Fig. 5.11. Through-thickness hardness variation in 5251 (a) H34-condition and (b) O-condition 145
Fig. 5.12. Hardness development (ST-RD) for the 5251-H34 basemetal specimens 146
Fig. 5.13. Micrographs of the Gleeble thermally cycled 5251-H34 basemetal at 20 ˚C/min 147
Fig. 5.14. Grain size and hardness development for the H34-basemetal specimens thermally cycled at 20 ˚C/min to peak temperature then quenched 148
Fig. 5.15. The variation in Mg_xSi due to thermal cycling 148
Fig. 5.16. Grain structure (ST-RD) in 5083-H116 149
Fig. 5.17. Deformed substructure in 5083-H116 150
Fig. 5.18. Particle structure in 5083-H116 151
Fig. 5.19. Size distributions plot for the Fe-rich and Mg_xSi particles in 5083-H116 ($> 0.5\,\mu m$) 152
Fig. 5.20. Al_6(Fe,Mn) dispersoids observed in 5083-H116 152
Fig. 5.21. Hardness (ST-LT) development due to isochronous (1hr.) heat treatments for the 5083-H116 basemetal specimens 153
Fig. 5.22. Micrograph for the 5083-basemetal annealed for 1 hr 154
Fig. 5.23. Montage of the grain structure throughout the sheet thickness of the CC 5754-O 155
Fig. 5.24. (a) Through-thickness variation of grain characteristics in the CC 5754-O (Error bars for D_{Eq}), (b) histogram for the average grain characteristics (ST-LT) 156
Fig. 5.25. Montage of the through-thickness grain structure in the DC 5754-O sheet 157
Fig. 5.26. (a) Through-thickness variation of grain characteristics in the DC 5754-O sheet (Error bars for D_{Eq}), (b) histogram for the grain characteristics (ST-LT) 157
Fig. 5.27. Size distribution of the Fe-rich constituent particles in DC and CC 5754-O sheets 159
Fig. 5.28. Distribution of the Fe-rich constituent particles in (a) 5754-DC, (b) 5754-CC 159
Fig. 5.29. (a) Two traces for the through-thickness variation in inter-particle band spacing in CC 5754-O (ST-RD), and (b) the area fraction of the Fe-rich particles in CC and DC 5754-O sheets 160

Fig. 5.30. (a) rhomboidal $Al_6(Fe,Mn)$ dispersoids observed in the CC 5754-O specimen tilted to a 2-beam invisibility condition, g.b. = 0 with b = $[001]$ and g = $(\bar{2}20)$, (b) in the DC 5754-O condition 160
Fig. 5.31. Grain structure in 2024-T351 showing (a) ST-RD plane, (b) ST-LT plane 161
Fig. 5.32. Particle structure in AA2024-T351 with example corresponding EDS spectra 162
Fig. 5.33. (a) particle structure observed under the optical microscope (the S phase is grey in colour, while the θ phase is orange/pink in colour), (b) Banding of the Cu-rich particles in 2024-T351 (ST-RD) 162
Fig. 5.34. Histogram for the D_{Eq} of Cu-containing particles in 2024-T351 163
Fig. 5.35. DSC trace for the 2024-T351 164
Fig. 6.1. Solution technique in the ADI method 171
Fig. 6.2. FSW heat input contributions due to the shoulder (Q_S), pin lateral side (Q_p), and pin base (Q_{pb}) 172
Fig. 6.3. An example for the fitted temperature-dependent tensile strength (ASM data) 176
Fig. 6.4. Variation of the thermal conductivity with temperature 178
Fig. 6.5. Torque and normal force measurements for the 2024-T3 weld (W1) 180
Fig. 6.6. (a) The thermocouple positions in the weld benchmark experiments [25], and the W1 simulated thermal cycles for both contact conditions and the thermocouple measurements (b) TC7: 4 mm from the weld centreline at the root face, and (b) TC3: 15 mm from the weld centreline on the sheet surface (ΔT: peak temperature over/undershoot). The initial undershoot in the simulated cycle results from the initial heating dwell in the measured cycle. 183
Fig. 6.7. Comparison between the simulated and measured temperature 185
Fig. 6.8. Torque and normal force measurements for the 5754-O weld 186
Fig. 6.9. The influence of the contact condition on the simulated thermal cycle compared to the thermocouple measurements 188
Fig. 6.10. Correlation between the model and (a) measured thermal cycles and (b) the maximum surface temperatures measured by the thermocouples in four identical weld runs 189
Fig. 6.11. Torque and normal force measurements for (a) 5251-H34 weld, and (b) 5251-O. 193
Fig. 6.12. (a) The thermomechanical and (b) thermophysical properties used in the model . 194
Fig. 6.13. Temperature distribution in the 5251-H34 weld 195
Fig. 6.14. The 5251-H34 weld HAZ microstructure and microhardness distribution 196
Fig. 6.15. (a,b) The influence of the heating rate on recovery/recrystallisation due to Gleeble simulation (T_C: thermocouple temperature), (c) schematic for the heating rate model . 198
Fig. 6.16. The influence of the heating rates during Gleeble simulations on the hardness at different peak temperatures 198
Fig. 6.17. Typical HAZ thermal cycles from the model to a peak temperatures 325 ˚C (a,b) and 385 ˚C (c,d), compared to simulated cycle (T_C) using Gleeble on a H34-basemetal specimen, and the corresponding microstructure 199
Fig. 6.18. Temperature distribution in the 5083-H116 weld according to the thermal model 200
Fig. 6.19. The 5083-H116 weld HAZ microstructure and microhardness distribution 202
Fig. 6.20. SRX-HAZ thermal cycle from the 5083-H116 model to a peak temperatures 360 ˚C 203
Fig. 6.21. Temperature distribution in the 2024-T351 welds according to the thermal model 203
Fig. 6.22. Hardness variation due to isothermal holds in salt bath 205

Fig. 6.23. The hardness distribution in the 2024-T351 hot and cold welds at mid-thickness (following 2 years aging), with the temperature predictions from the thermal model (WN ± 5mm, TMAZ ± 9mm) 206
Fig. 7.1. Macrograph of 5251H34-weld etched in 10 % H_3PO_4 solution 212
Fig. 7.2. Micrographs for the 5251-H34 weld..... 214
Fig. 7.3. Al_6(Fe,Mn) precipitates along the grain boundary in the WN of 5251-H34 weld .. 214
Fig. 7.4. Optical micrographs from various weld regions in the 5251-O weld..... 215
Fig. 7.5. Grain size distribution with the TMAZ/WN of 5251-O weld 216
Fig. 7.6. Grain size distribution with the TMAZ/WN of 5251-H34 weld 217
Fig. 7.7. Multi-beam TEM micrographs from different locations of the 5251-H34 weld..... 221
Fig. 7.8. Macrographs for the DC1 weld etched in Keller's reagent 223
Fig. 7.9. Macrographs for the CC1 weld etched in Keller's reagent..... 223
Fig. 7.10. Macrographs for the CC2 weld etched in Keller's reagent..... 223
Fig. 7.11. Micrographs for the 5754-O DC1 weld..... 225
Fig. 7.12. Micrographs for the 5754-O CC1 weld 226
Fig. 7.13. Micrographs for the 5754-O CC2 weld 228
Fig. 7.14. Dynamic recrystallisation in the WN of the CC1 5754-O welds..... 228
Fig. 7.15. Grain size trace at the mid-thickness of the DC1 and CC1 welds 229
Fig. 7.16. Size distribution of the Fe-rich constituent particles in the DC1 and CC1 WN..... 230
Fig. 7.17. Grain boundary structure in the 5754-O CC1 ORZ weld 232
Fig. 7.18. Macrographs for the 5083-H116 weld etched in 10% H3PO4 solution 233
Fig. 7.19. Microstructure in 5083-H116 weld..... 234
Fig. 7.20. The grain structure characteristics in the 5083-H116 weld 235
Fig. 7.21. TEM micrographs from different locations of the 5083-H116 weld..... 236
Fig. 7.22. Macrograph of 2024-T351 weld etched in Weck's reagent..... 237
Fig. 7.24. ORZ microstructure in 2024-T351 weld..... 240
Fig. 7.25. Microstructure along the longitudinal section for the 2024-T351 weld 241
Fig. 7.26. Grain structure in 2024-T341 weld..... 241
Fig. 7.27. Particle structure in 2024-T351 242
Fig. 7.28. Constituent particle structures in the investigated alloys (ST-RD plane)..... 246
Fig. 7.29. Suggested qualitative relationship for the influence of the banded particle fraction and the APR on the ORZ intensity in 5xxx-series alloys..... 250
Fig. 8.1. Macrograph for the 5251-H34 weld 257
Fig. 8.2. Hardness traces for (a) the H34-weld and (b) the O-weld..... 258
Fig. 8.3. Hall-Petch plot showing the contribution of the grain size to hardness 260
Fig. 8.4. Low resolution EBSD maps for 5251-H34 (RD-ST) plane..... 262
Fig. 8.5. EBSD map for the 5251 H34-BM 263
Fig. 8.6. Engineering stress-curves for the H34-BM 265
Fig. 8.7. EBSD map for the 5251 O-BM 266
Fig. 8.8. Engineering stress-strain curves for the O-BM 266
Fig. 8.9. EBSD map for the 5251 H34-WND 267
Fig. 8.10. DSC traces for the H34-base metal, compared to selected locations from the H34-weld 268
Fig. 8.11. DSC traces for specific locations in the O-weld..... 270
Fig. 8.12. The spatial distribution in energy release within the H34 and O-welds 270
Fig. 8.13. TEM micrographs from the weld showing precipitation of the Al_6(Fe,Mn) particles 275
Fig. 8.14. Hardness traces for the 5754-O (a) CC weld and (b) DC weld 276
Fig. 8.15. Hall-Petch plot showing the contribution of the grain size to hardness in the 5754-welds and basemetal..... 277

Fig. 8.16. DSC traces for specific locations in the 5754-O CC and DC welds..... 279
Fig. 8.17. Microhardness contour for the 5083-H116 weld..... 281
Fig. 8.18. Hardness traces for 5083-H116 282
Fig. 8.19. Hall-Petch plot showing the contribution of the grain size to hardness in the 5083-welds and basemetal..... 283
Fig. 8.20. TEM micrographs for different locations in the 5083-H116 weld 284
Fig. 8.21. DSC traces for different locations in the 5083-H116 weld..... 285

LIST OF TABLES

Table 2.1. Chemical compositions (wt %) of selected commercial 5xxx series alloys 8
Table 2.2. Potential intermetallic phases in AA5xxx alloys 10
Table 2.3. Intermetallic phases present in AA5xxx alloys..... 10
Table 2.4. Chemical composition (wt %) of commercial 2xxx series alloys..... 14
Table 2.5. Potential intermetallic phases in AA2xxx alloys 16
Table 2.6. Literature values for σ_O and k_y in some Al-Mg alloys..... 28
Table 2.7. Solid solubility and the strengthening contribution of some alloying elements 29
Table 2.8. Typical stored energy values for different materials measured by DSC..... 41
Table 3.1. Summary of the thermocouple measurement studies in welds of Al-based alloys. 68
Table 3.2. Analytical models for heat generation during FSW..... 74
Table 3.3. Grain size in the WN of welds of Al-based alloys..... 88
Table 4.1. Chemical composition of the alloys used in this study (weight percent)..... 116
Table 4.2. The welding parameters for the characterised welds 119
Table 4.3. Reactions that can be detected using the DSC and the energy type..... 127
Table 4.4. Weld regions and reactions 128
Table 4.5. Heat treatments carried out for the basemetal..... 131
Table 4.6. Conditions of the specimens thermally cycled in the GTMS 133
Table 5.1. Characteristics of the intermetallic particles in the H34 and O conditions..... 141
Table 5.2. Hardness in the different metallurgical directions 145
Table 5.3. Characteristics of the intermetallic particles in the 5754-O CC and DC sheets ... 158
Table 6.1. The welding parameters for the welds used for fitting and validation of the model 179
Table 6.2. Thermophysical properties and equation (6.14) constants for 2024-T351 181
Table. 6.3. Comparing the various models with the proposed model..... 191
Table 7.1. Characteristics of the Fe-rich intermetallic particles in the 5754-O welds..... 230
Table 7.2. Intermetallic particles in the investigated alloys and their properties..... 245
Table 7.3. Summary of the intermetallic particle characteristics associated with the ORZ and their influences within the range of process parameters studied..... 247
Table 7.4. Summary of the process-related factors associated with the ORZ and their influences within the range of process parameters studied..... 249
Table 7.5. Summary of the microstructural differences between 2xxx and 5xxx welds 251

NOMENCLATURE*

Item	*Description*
α	Dimensionless Constant, Thermal Diffusivity (m^2/s)
A_S	Shoulder contact area (m^2)
AAxxx	Aluminium Association alloy designation
ADI	Alternating Direction Implicit (Method)
AS	Advancing Side
b	Burgers vector
c	Solute Atom Concentration
CC	Continuous Casting
C_P	Specific heat capacity (J/kg.˚C)
DC	Direct-Chill
D_{Eq}, d	Grain size (equivalent diameter)
DAS	Dendritic Arm Spacing
DRV	Dynamic Recovery
DRX, DRXed	Dynamic Recrystallisation; Dynamically Recrystallised
DSC	Differential Scanning Calorimetry
EBSD	Electron Backscattered Diffraction
ECAE, ECAP	Equal Channel Angular Extrusion/Pressing
EDS	Energy Dispersive X-Ray Spectroscopy
ε	Strain
$\dot{\varepsilon}$	Strain Rate
f	Feed (traverse) speed (mm/min)
F_N	Normal (Z-axis) force (N)
F_V	Particles Volume Fraction
FSW	Friction Stir Welding; Weld
G	Shear Modulus
GP	Guinier-Preston
GTMS	Gleeble Thermomechanical Simulator
H_P	Pin height (m)
HAGB	High Angle Grain Boundary
h	Convection heat transfer coefficient ($W/m^2.$˚C)
HAZ	Heat Affected Zone
H_V	Vicker's Hardness Number
k	Thermal conductivity (W/m.˚C)
k_y	Hall-Petch Slope/Constant (MPa $\mu m^{1/2}$)
λ	Inter-particle spacing,
λ_S	Free Slip Distance.
L	Boundary Spacing
LAB	Low-Angle Boundary
M	Taylor factor
μ	Friction coefficient
MM	Marker Material
MIT	Markers Insert Technique
OM	Optical Microscope
ORZ	Onion Rings Zone

Item	*Description*
P	Normal pressure (MPa)
PLM	Polarised Light Microscope
PSN	Particle Stimulated Nucleation
Q	Heat generation (W)
q	Heat flux (W/m^2)
q_v	Volumetric heat source (W/m^3)
ρ , ρ_G , ρ_S	Total, Geometrically Necessary, Statistically Stored Dislocation Density
r	Equivalent Particle Radius
R_S, R_P	Tool Shoulder and pin radii (m)
RS	Retreating Side
σ_O , σ_P , σ_{SS}	Frictional, Particle, and Solid Solution Stress Components
σ_{YS}	Yield Strength (MPa)
SEM	Scanning Electron Microscope
SSS	Solid Solution Strengthening
τ	Shear Stress (MPa)
t	Temperature (˚C)
T	Absolute temperature (K)
TEM	Transmission Electron Microscope
TMAZ	Thermo-mechanically Affected Zone
ω	Rotation speed (rad/s)
WN	Weld Nugget
x, y, z	Space coordinates (m)
Z	Zener-Hollomon Parameter

* For symbols and abbreviations used more than three times

Chapter 1
INTRODUCTION

"Unquestionably, my friends. This valuable metal (aluminium) possesses the whiteness of silver, the indestructibility of gold, the tenacity of iron, the fusibility of copper, the lightness of glass. It is easily wrought, is very widely distributed, forming the base of most of the rocks, is three times lighter than iron, and seems to have been created for the express purpose of furnishing us with the material for our projectile."

Jules Verne, "From Earth to the Moon", 1865

1.1. General Introduction

Despite aluminium's advantages, in terms of density and formability, that were foreseen 140 years ago by the futurist novelist Jules Verne, aluminium-based alloys have not radically replaced the dominance of steels in the automotive industry. Yet, with the growing environmental concerns being placed on the automotive manufacturers to produce more fuel-efficient vehicles, it is expected that the current trend of Al-alloys replacing steels in automotive structures will continue to grow.

It has been argued that the main reason for this slow, but steady, increasing trend is that the replacement process has been carried out on a part-by-part basis, and not due to a fundamental change in the conceptual design methodologies for the automotive structures [1]. Moreover, the complexity of the technical and economic parameters considered during materials replacement processes also contributes to the slow progress towards what is known as Aluminium Intensive Vehicles (AIV) [2]. Yet, as a result of cooperation between major Al-alloys and automotive manufacturers within the last 10 years, changes in the automotive design philosophy have resulted in the introduction of more AIV cars, not only with cast components within the power train and the chassis, but also within the body-in-white (BIW) structure as shown in Fig. 1.1.

Thus, from an average of only 39 kg of aluminium in the passenger car in 1976, to 110 kg in 1996, aluminium usage is expected to grow to around 250-340 kg by 2015 [2]. The growth in

the usage of sheets in the body panels is considered to be the most considerable as they can significantly reduce the vehicle weight. Still, for this growth to be sustained, the automotive industry demands the introduction of new economic and efficient joining techniques, as well as new Al-alloys sheets of improved weldability, formability, mechanical, and corrosion-resistance properties. With the large differences between steel and aluminium in strength, physical and chemical properties, the introduction of alternative joining and forming techniques becomes crucial and necessary [3].

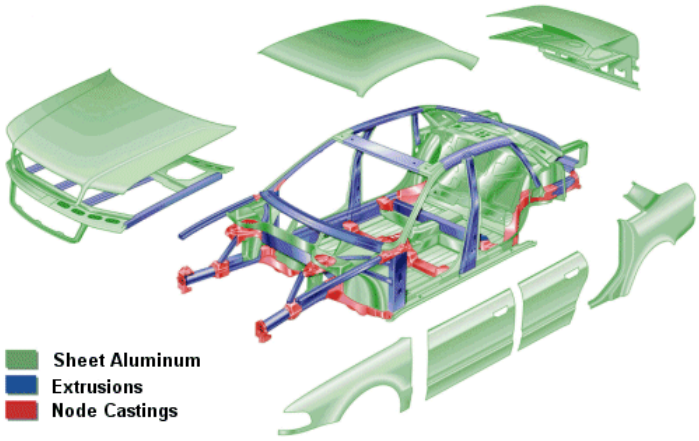

Fig. 1.1. Al-alloys usage in the body-in-white and frame for the Alcoa Audi A8 2002 [4]

Non-heat treatable work hardenable Al-Mg (5xxx) alloys together with the heat treatable Al-Mg-Si (6xxx) alloys are the classes that are currently being used by most automotive manufacturers. Currently, the 6xxx series alloys (e.g. 6016 and 6111 alloys) are the most widely used class in automotive body panels. However, this class is relatively expensive compared to the 5xxx series, but its alloys are preferred due to their formability and the strength improvement after the paint-baking process [2]. According to year 2000 statistics [1], it was believed that for Al-alloys to replace steel at the same manufacturing cost, the price of aluminium has to decrease to £1.3/kg (US$ 2.2/kg). This price cannot be achieved for the 6xxx series due to the cost of the necessary heat treatment processes, but it is achievable for the 5xxx series alloys produced by continuous casting (CC), and not direct chill casting (DC) as shown in Fig. 1.2 [1]. Despite the continuous change in prices since the previous study was conducted, the usage of 5xxx CC sheets still provides the most economical alternative for an increasing usage of Al-based alloys in the automotive industry. The 5xxx series alloys are

characterised by good formability, weldability, corrosion resistance, and mechanical properties.

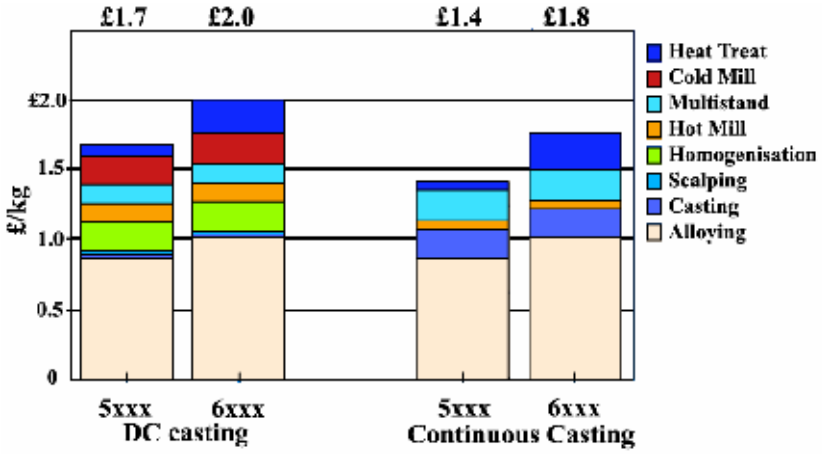

Fig. 1.2. Comparison between the prices of Al-alloys produced by DC and CC (Original data according to year 2000 statistics by [1] in US$, only for relative comparison)

Joining technologies are the other major requirement that could assist in the introduction of more Al-based alloys into the automotive industry. Traditionally, joining in automotive structures has been carried out by mechanical fastening (riveting) or, to a lesser extent, by fusion welding (electric arc). Mechanical fastening has several advantages including: the ease of automation, versatility, high speed, low capital cost and energy, with good joint quality possible. However, the process can be relatively difficult when applied to internal joints. In addition, rivets seem to be a prime target for crevice corrosion, despite the use of protective coatings [5]. On the other hand, fusion welding of Al-alloys can be quite problematic when compared to fusion joining of steels. For example, fusion welding of Al-alloys requires high heat input due to their good thermal conductivity, as well as an inert shielding gas (as in metal inert gas or MIG welding) due to the high affinity of aluminium for oxygen. Regardless of the alloy type (e.g. heat treatable or non-heat treatable), or the starting temper (aged, work hardened, annealed), the chosen welding technique should have a relatively localised thermal field since temperatures as low as 150-250 ˚C can result in a heat-affected zone (HAZ) which can weaken the joint. Temperatures close to 550 ˚C and higher can cause various defects, such as: mechanical distortion, porosity, solidification cracks, and liquation cracking [6]. Even if all these precautions are considered, the joint surface has to be meticulously cleaned

mechanically or chemically to remove any hydrocarbon compounds (e.g. lubricants) since they can lead to the formation of porosity. Recently, alternative fusion and solid-state joining techniques have been suggested and investigated, such as: resistance spot welding (RSW), laser beam welding (LBW), and diffusion bonding (DB). Yet, these techniques are still associated with technical concerns (e.g. electrode wear in RSW, LBW efficiency with highly reflective surfaces, and the surface preparation in DB), as well as their economic limitations due to the high capital investment [3].

In 1991, Wayne Thomas invented and pioneered a new family of solid-state joining techniques, which uses a combination of friction and plastic deformation by a rotating shouldered pin to weld aluminium sheets. A British patent was filed in 1991 under the name of *Friction Stir Butt Welding*, which became later known as *Friction Stir Welding* (FSW) [7, 8]. Over a short period, FSW proved itself to be of major potential for the production of high quality welds in different materials. The capital investment in FSW can be significantly reduced by adapting milling machines to perform the process. Currently, the technique has already been applied successfully to cryogenic tanks, marine structures, train panels, air frames, and even automotive BIW [9]. Due to its rapid success, commercialisation of FSW has started long before establishing a fundamental understanding of the process. Research on FSW is expected to encourage further spread of this technique in the transportation industry, notably by studying the influence of the process on material properties. This influence can only be established by linking the micron-scale material features to the macro-properties, which is the subject of the current project.

1.2. Project Aim, Objectives & Approach

The aim of this project is to establish a fundamental understanding of microstructural and property development during FSW, with a special focus on 5xxx series Al-alloys. The specific objectives (Fig. 1.3) to achieve are:

- Development and experimental verification of a simple fast numerical model for predicting the thermal profile, and hence its influence on the microstructural development, mainly in the HAZ of the welds.
- Establishing the link between basemetal microstructural characteristics, for example intermetallic particles, and the weld microstructural features, particularly the formation of the ‘onion rings’ structure.

- Determination of the main microstructural factors that control the local mechanical properties in the different regions of 5xxx welds.

The microstructural investigations in this project were performed using optical, scanning electron microscopy (SEM), and transmission electron microscopy (TEM). Mechanical testing using hardness and tensile testing was used to characterise the strength development. Thermal simulations for the HAZ microstructural development was carried out using the Gleeble™ thermomechanical simulator, and modelled using MATLAB™ 7.1.

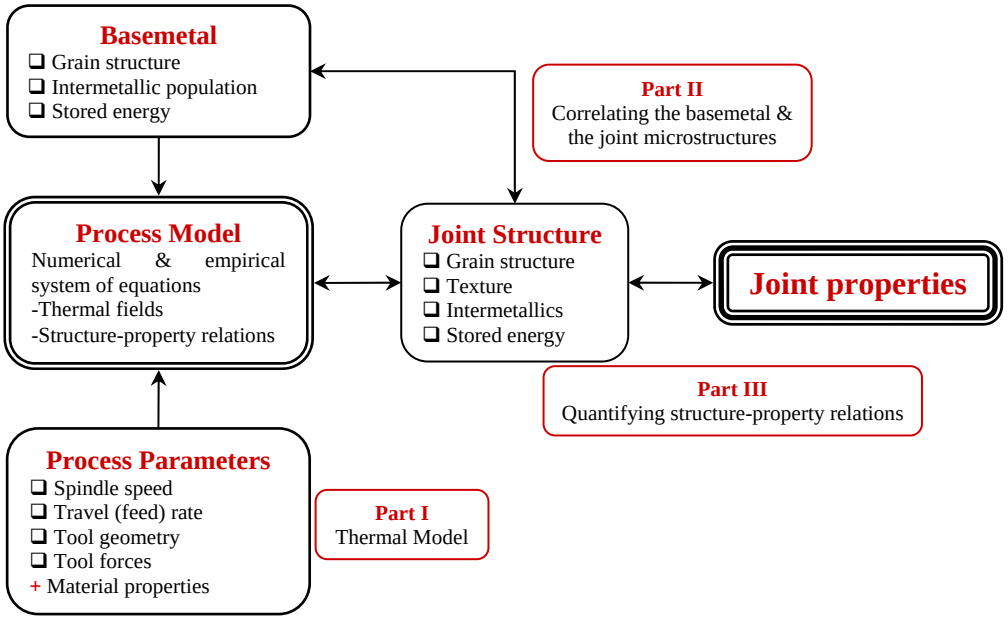

Fig. 1.3. Components required for understanding the microstructure-property development due to FSW in 5xxx series Al-based alloys

This dissertation is divided into 9 chapters. The literature review is presented in chapters 2 and 3. In chapter 2, the metallurgy of Al-based alloys is presented, focusing on the intermetallic phases present in the 5xxx and 2xxx series alloys, the influence of the processing routes (CC and DC) on the microstructure of Al-based alloys, structure-property relations, and microstructural development during thermal and thermomechanical processes. The present state of knowledge on FSW is reviewed in chapter 3, summarising the influence of the process parameters on the temperature distribution in the weld, the microstructural and property development, as well as the various numerical and analytical models that describe the heat generation and temperature distribution. Detailed description of the experimental

techniques utilised in this project is presented in chapter 4. The results and discussion is presented in chapters 5 to 8. Detailed characterisation of the investigated base alloys is presented in chapter 5, focusing on identifying the processing route, based on the microstructure and intermetallic particle structures. Chapter 6 deals with the development, fitting, and validation of the thermal model used to predict the HAZ development. Chapter 7 discusses the microstructural development in the various welds, focusing on the 'onion rings' phenomenon, and the possible influence of the processing route of the base alloy on the weld microstructure. Chapter 8 studies the structure-property relations in 5xxx-series welds, to be followed by chapter 9, which summarises the conclusions of this work and outlines possible future work. The appendix contains the peer-reviewed papers that were published to date as a result of this project.

1.3. References

[1] A. Kelkar, R. Roth, and J. Clark, "Automobile Bodies: Can Aluminum Be an Economical Alternative to Steel?" *Journal of Materials (JOM)*, vol. 53, pp. 28-32, 2001.

[2] W. S. Miller, L. Zhuang, J. Bottema, A. J. Witterbrood, P. De Smet, A. Haszler, and A. Vieregge, "Recent Developmen in Aluminium Alloys for the Automotive Industry," *Materials Science and Engineering A*, vol. 280, pp. 37-49, 2000.

[3] T. A. Barnes and I. R. Pashby, "Joining techniques for aluminium spaceframes used in automobiles: Part I -- solid and liquid phase welding," *Journal of Materials Processing Technology*, vol. 99, pp. 62-71, 2000.

[4] "http://ussautomotive.com/auto/steelvsal/alintensive.htm," United States Steel Corporation, 2005.

[5] T. A. Barnes and I. R. Pashby, "Joining techniques for aluminium spaceframes used in automobiles: Part II -- adhesive bonding and mechanical fasteners," *Journal of Materials Processing Technology*, vol. 99, pp. 72-79, 2000.

[6] G. Mathers, *The Welding of Aluminium and its Alloys*. England: CRC Press, 2002.

[7] W. M. Thomas and E. D. Nicholas, "Friction stir welding for the transportation industries," *Materials & Design*, vol. 18, pp. 269-273, 1997.

[8] W. M. Thomas, E. D. Nicholas, J. C. Needham, M. G. Nurch, P. Temple-Smith, and C. Dawes, "Patents on Friction Stir Butt Welding," International: PCT/GB92/02203; British: 9125978.8; USA: 5460317., 1991-1995.

[9] R. S. Mishra and Z. Y. Ma, "Friction stir welding and processing," *Materials Science and Engineering: R: Reports*, vol. 50, pp. 1-78, 2005.

Chapter 2
METALLURGY OF ALUMINIUM ALLOYS

2.1. Aluminium-Magnesium (AA5xxx) Alloys

The 5xxx series Al-Mg alloys possess a combination of good formability, weldability, corrosion resistance, and high strength especially in the work-hardened tempers, offering them a substantial potential for increasing usage in the transportation industry. Typical chemical compositions of commercial 5xxx series alloys are given in Table 2.1.

Iron and silicon are usually present in low amounts (~0.5 wt % each) as impurities. Minor additions (<2 wt % total and <1 wt % each) of titanium, chromium, manganese, copper, and zinc are frequent additives to the 5xxx series alloys to improve the strength and corrosion properties. Titanium is added to act as a grain refiner, while zinc is added to high magnesium Al-Mg alloys to enhance its stress corrosion cracking (SCC) resistance through the formation of a stable ternary Al-Mg-Zn phase [1].

2.1.1. The Al-Mg System

Magnesium is the principal alloying element in the 5xxx series wrought aluminium alloys. The maximum solubility of magnesium in aluminium is about 2 wt % at room temperature, and 17.4 wt % at 723 K as shown in Fig. 2.1 [2]. Even though concentrations of up to 12-13 wt % Mg can be found in cast Al-Mg alloys, wrought alloys containing beyond 5.5 wt % Mg are rarely used in the strain-hardened condition due to their high susceptibility for intergranular cracking and SCC. This is attributed to the precipitation of the highly anodic β

phase, usually given as Al_3Mg_2 or Al_8Mg_5. Below 3 wt % Mg, there is hardly any of the β phase, but it starts to precipitate along the grain boundaries in alloys with Mg content above 3.5 wt,%, making them unsuitable for operating temperatures above 65 ˚C [2-4].

Table 2.1. Chemical compositions (wt %) of selected commercial 5xxx series alloys (balance Al) [2-4]

Alloy	Mg	Si	Mn	Fe	Cr	Ti	Cu	Zn	Other
5005	0.5-1.1	0.30	0.20	0.70	0.1	-	0.20	0.25	0.15
5052	2.2-2.8	0.25	0.1	0.40	0.15-0.35	-	0.10	0.10	0.15
5251	1.7-2.4	0.40	0.1-0.5	0.50	0.15	0.15	0.15	0.15	0.15
5083	4.0-4.9	0.40	0.4-1.0	0.40	0.05-0.25	0.15	0.10	0.25	0.15
5086	3.5-4.5	0.4	0.2-0.7	0.5	0.05-0.25	0.15	-	0.25	0.15
5154	3.1-3.9	0.25	0.10	0.40	0.15-0.35	0.20	0.10	0.20	0.15
5182	4.0-5.0	0.20	0.2-0.5	0.35	0.10	0.10	0.15	0.25	0.15
5754	2.6-3.6	0.4	0.5	0.4	0.30	0.15	0.10	0.20	

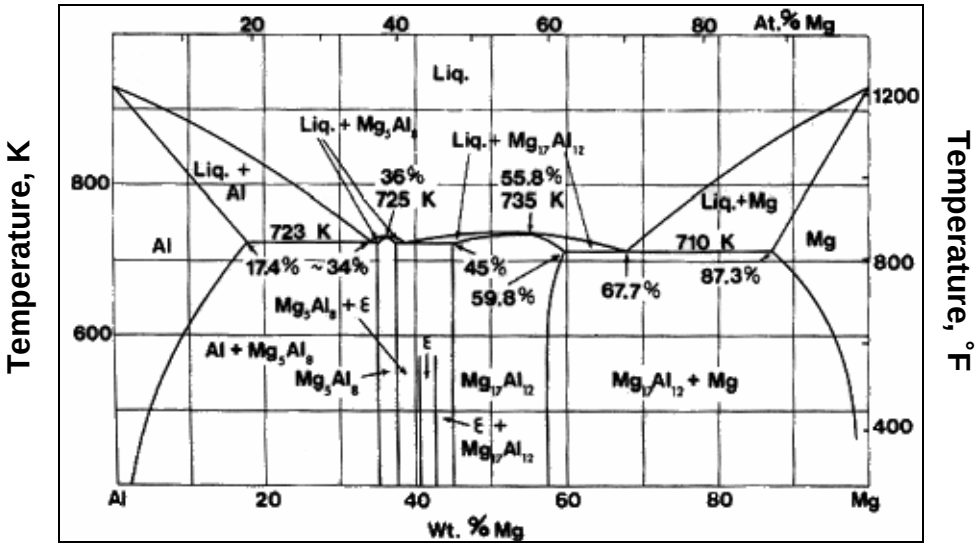

Fig. 2.1. The binary Al-Mg equilibrium diagram [2]

2.1.2. Intermetallic Particles in AA5xxx

The 5xxx series alloys can contain a range of different intermetallic particles, which can be classified into the following types [5, 6]:

1. Constituent particles (*primary precipitates*): insoluble impurity-rich which form during solidification, with size range 1-10 μm in wrought (rolled) sheets (e.g.

Al(Fe,Mn)Si, Mg_2Si, and Al_3Mg_2). The Fe/Mn-rich particles cannot be redissolved during homogenisation due to their high melting point (>700 ˚C). Yet, they can transform from one type to another, such as the transformation of Al_6(Fe,Mn) to Al(Fe,Mn)Si. Coarse Fe/Mn-rich particles (>1-2 μm in diameter) create strain incompatibility and deformation zones surrounding them in the matrix during cold deformation. During recrystallisation, new grains can nucleate at the deformed zones surrounding the particles (particle stimulated nucleation or PSN).

2. Divorced eutectic phases: soluble particles which form during solidification as divorced eutectics, such as Al_3Mg_2 and Mg_2Si. During homogenisation (~500-600 ˚C), some types can be dissolved (e.g. Al_3Mg_2), while other types (e.g. Mg_2Si) are partially dissolved, usually remaining out of solution in wrought alloys.
3. Dispersoids (*secondary precipitates*): fine precipitates which form during post-casting thermal operations (e.g. homogenisation or recrystallisation) by precipitating from the matrix. They appear in various shapes (plate-like, rod-like, rectangular, or spherical), with size range <0.5 μm (e.g. Al_6(Fe,Mn)). Their small size helps in controlling the grain size during recrystallisation through Zener drag without PSN.

2.1.2.a. Constituent Particles in 5xxx series Alloys

Literature on the constituent particles in Al-Mg-X systems (e.g. as in 5xxx and 3xxx alloys) has been extensively reviewed by Mondolfo [2], and earlier by Pearson [7]. Several investigators have studied, using electron microscopy, spectroscopy and diffraction, the particle transformations during homogenisation in 3xxx series [8-10] and 5xxx series [11-13], and have determined the phase diagrams of various quaternary systems such as: Al-Fe-Mn-Si, Al-Mg-Fe-Si, and Al-Mg-Mn-Si [14-18]. These studies have shown that the presence of a specific type of particle depends on the relative amounts of Fe or Fe+Mn to Si in the alloy. Mondolfo [2] summarised the possible intermetallic phases in these alloys as shown in Table 2.2. In the 5xxx series alloys, Mg combines with Si to form globular Mg_2Si particles. The stoichiometry of the Fe-bearing particles is very dependent on the Si and Mn amounts. Iron usually combines with both Si and Al to form Al_8Fe_2Si or $Al_{12}Fe_3Si$ in low-Mg alloys, or Al_3Fe in the absence of Cr and Mg. In the presence of Cr and Mn, other particles may be present, such as: $Al_{15}(Fe,Mn)_3Si_2$, Al_6(Fe,Mn), Al_7(Fe,Cr), or $Al_{13}(Fe,Cr)_4Si_4$ [2, 4]. Table 2.3 lists the common intermetallic particles occurring in the 5xxx series alloys and their crystal structure.

The intermetallic phases vary in their physical and mechanical properties [2]. The density of the Fe/Mn-rich particles (ρ =3000-3600 kg/m^3) is higher than that of the Al-matrix (ρ =2700 kg/m^3), whereas Mg_2Si and Al_3Mg_2 are less dense (~1880 and 2230 kg/m^3) respectively. In addition, the hardness of the Fe/Mn-rich particles ($Al_{15}(Fe,Mn)_3Si_2$ and $Al_6(Fe,Mn)$) is appreciably higher (~900-950 H_V and 700-750 H_V respectively) than most Al-alloys, compared to ~ 420 H_V for Mg_2Si and ~200-340 H_V for Al_3Mg_2 [2, 19, 20].

Table 2.2. Potential intermetallic phases in AA5xxx alloys (After [2])

Mg	Mg<2% in solid soln.	Mg>2% Al_8Mg_5	Si>0.05% Mg_2Si	Cu>0.2% Al_6CuMg_4			
Si	Fe<0.3% Mg_2Si Si<0.3% Mg>2%	Fe>0.3, Mg<2% Al_8Fe_2Si		Fe>0.3%, Mg<2%, Mn or Cr>0.1 % $Al_{15}(Fe,Mn)_3Si_2$ or $Al_{13}(Cr,Fe)_4Si_4$			
Fe	Al_3Fe	Al_8Fe_2Si	Si>0.3% Mg<2% Mn>0.1% $Al_{15}(Fe,Mn)_3Si_2$	Si<0.3% Mg>2% Mn>Fe $Al_6(Fe,Mn)$	Si>0.3% Mg<2% Cr>0.1% $Al_7(Cr,Fe)_4Si_4$	Si<0.3% Mg>2% Cr>0.1% $Al_7(Cr,Fe)$	Si<2% Fe>0.3% Cu<1% Al_7Cu_2Fe
Mn	Si<Mg $Al_6(Fe,Mn)$	Si>2 Mg $Al_{15}(Fe,Mn)_3Si_2$					
Cr	Si<Mg $Al_7(Cr,Fe)$	Si>2 Mg $Al_{15}(Cr,Fe)_4Si_4$					
Cu	Fe<Cu Al_6CuMg_4	Fe>Cu Mg<2% Al_7Cu_2Fe					
Zn	Zn<2% in solid soln.	Zn>2% Al_2Mg_3Zn					

Table 2.3. Intermetallic phases present in AA5xxx alloys* [2, 4, 7, 8, 15-18]

Phase	**Other designation**	**Lattice/Structure**	**Lattice Parameters, Å**			**c/a, α or β**
			a	**b**	**c**	
Mg_2Si	β	fcc/*Fm3m*	6.351	…	…	…
Al_6Mn	…	Ortho/*Cmcm*	6.498	7.552	8.870	…
Al_3Mg_2	β	fcc/*Fd3m*	28.16	…	…	…
Al_8Fe_2Si	α-FeSi	Hex/*P6$_3$/mmc*	12.3	…	26.3	…
$Al_{15}(Fe,Mn)_3Si_2$	α'-FeSi	bcc/*IM3*	12.548	…	…	…
$Al_{12}(Fe,Mn)_3Si_3$						
$Al_{12}Mn$	…	Cubic	~7.47	…	…	..
Al_4Mn	…	Hex	28.41	…	12.38	0.436
$Al_{15}Mn_3Si_2$	α-MnSi	Cubic	12.652	…	…	…
$Al_{10}Mn_3Si$	β MnSi	Hex/*P6$_3$/mmc*	7.513	…	7.745	1.031
Al_5FeSi	β FeSi	Mono	6.12	6.12	41.48	91˚
Al_4FeSi_2	δ-FeSi	Tet	6.16	…	9.49	1.54
$AlCr_2Mg_3$	E	fcc/*Fd3m*	14.55			
Al_6CuMg_4	T	bcc	14.31	…	…	…
$Al_{13}Cr_4Si_4$	α	fcc/*F43m*	10.971	…	…	…
$Al_3(Fe,Mn)$	…	Mono	8.08	…	12.48	107.75˚

***** The stoichiometry of some phases may vary as Cr, Mn and Fe tend to substitute for each other.

2.1.2.b. Dispersoids in 5xxx series Alloys

Both chromium and manganese are added beyond impurity levels to improve the strength (at the expense of poorer ductility), control the grain size and increase the recrystallisation temperature, through the formation of the silicon-free orthorhombic Al_6Mn fine dispersoids, which may also contain Cr and Fe [4]. The precipitation of this type of particle has been observed during homogenisation (~510-570 ˚C) in AA5182 (Al-Mg-Mn) [21]; during relatively low temperature annealing (~350 ˚C) in binary Al-1.3 wt % Mn alloy [22], and in a Sc/Zr-modified AA5754 after annealing at 400 ˚C [23]. The presence of the particles raised significant interest because of its possible influence on grain size control. Finely dispersed particles are known to hinder grain boundary motion during recrystallisation [24].

The orientation relationship between the Mn-containing dispersoids and the Al-matrix was previously studied by Ratchev *et al.* [21] in AA5182 homogenised between 510 ˚C and 570 ˚C, and by Yang *et al.* [22] in Al-1.3 wt % Mn annealed at 350 ˚C. Both studies reported similar particle morphologies; rounded or rhomboidal (0.1-0.4 μm in size, with low aspect ratio), and plate-like (>1.2 μm in length, with high aspect ratio) as shown in Fig. 2.2). However, different orientation relationships between the matrix and particles were reported. Ratchev *et al.* found that a semi-coherent orientation relationship existed for the plate-like dispersoids (denoted p) with the matrix (m) of type $[100]_m \parallel [\bar{2}10]_p$ and $(0\bar{1}1)_m \parallel (001)_p$ with a habit plane of $\{135\}_m$, whereas the rhomboidal particles (R) are incoherent. Based on this, the R-dispersoids were predicted to have a more significant role in retarding recrystallisation by pinning the grain boundaries. Yang *et al.* showed that all the plate-like and most of the rhomboidal dispersoids showed two orientation relationships which can be written as: $(110)_m \parallel (111)_p$, $[001]_m \parallel [\bar{2}11]_p$ and less frequently $(110)_m \parallel (111)_p$, $[1\bar{1}2]_m \parallel [1\bar{2}1]_p$, whereas no orientation relationship was found for the rounded particles. It is probable that the differences in the Mn and Mg solute atom amounts types in both alloys could have produced the observed differences in the orientation relationships.

The influences of the homogenisation temperature and cooling rate by water quenching (WQ) versus furnace cooling (FC) on the morphology of the particles (size and shape) were also investigated by Ratchev *et al.* [21]. It was shown that increasing the homogenisation temperature from 510 ˚C to 570 ˚C increased the volume fraction of P-dispersoids and

decreased that of the R-dispersoids. Nonetheless, the size of the R-dispersoids was unaffected by the variation in temperature, compared to the size of the P-dispersoids, which increased with the increase in temperature. Compared to FC, WQ created a more heterogeneous particle distribution; particles of both types were concentrated in the inter-dendritic region, with a smaller volume fraction than FC. It was suggested that the fine R-dispersoids dissolve at high temperatures, while the coarser ones continue to grow.

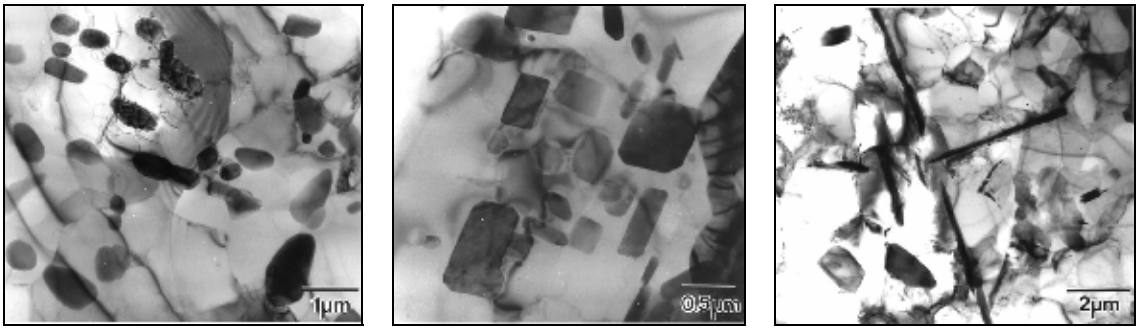

(a) Rounded (b) Rhomboidal (c) Plate-like

Fig. 2.2. Morphologies of the Al_6Mn dispersoids in recrystallised Al-1.3 wt % Mn [22]

2.1.2.c. Phase Transformations in 5xxx series Alloys

It is known that the cubic α-Al(Fe,Mn)Si phase forms during homogenisation from the Al_6(Fe,Mn) phase in what is known as the 6-to-α transformation. Several reports discussed the stability of the Al_6(Fe,Mn) phase during homogenisation of 3xxx and 5xxx series alloys, reporting different thermal treatments (~500-600 ˚C) leading to the occurrence of the 6-to-α transformation. This transformation is enhanced by the presence of Si [8-13, 20, 25, 26] (> 0.3 wt % Si [2], Table 2.2), causing the following eutectoid decomposition to take place [8]:

$$3\ Al_6(Fe,Mn) + Si \rightarrow \alpha\text{-}Al_{12}(Fe,Mn)_3Si + 6\ Al \qquad (2.1)$$

Li and Arnberg [9] found that this transformation starts at 400 ˚C in direct-chill (DC) cast AA3003 dynamically heated at a rate of 50 ˚C/hr, with the fraction of the α-particles increasing with the increase in temperature and homogenisation time. Hutchinson *et al.* [25] also reported that increasing the homogenisation temperature from 560 ˚C to 600 ˚C in AA3004 was also found to promote the dominance of the α-phase, decreasing the particle

density and doubling the size. They attributed this to the dissolution of $Al_6(Fe,Mn)$, followed by re-precipitation on the α -particles, instead of Ostwald ripening of the fine α -particles.

It is known that the α -phase improves the galling resistance during the drawing and ironing operation in can-body manufacturing due to its higher hardness compared to $Al_6(Fe,Mn)$ [8, 20]. However, controlling the size of the α -phase is also important as coarse α -particles (> 2 μm) form deformation zones during rolling. Upon annealing, these zones act as nucleation sites for recrystallisation, resulting in the development of undesirable texture components, which ultimately produces earing on the drawn cans [20, 25].

2.2. Aluminium-Copper Alloys (AA2xxx) Alloys

The 2xxx series represents the main class used in the aerospace transportation industry due to the high strength levels attained by precipitation strengthening. However, the corrosion resistance and weldability are the poorest among all Al-alloys [2-4]. Typical chemical compositions of commercial 2xxx series alloys are given in Table 2.4.

Table 2.4. Chemical composition (wt %) of commercial 2xxx series alloys (balance Al) [2-4]

Alloy	Cu	Si	Fe	Mn	Mg	Zn	Cr	Ti	Other*
2011	5.0-5.6	0.40	0.70	-	-	0.30	-	-	0.2-0.6
2014	3.9-5.0	0.5-1.2	0.70	0.4-1.2	0.2-0.8	0.25	0.1	0.15	-
2017	3.5-4.5	0.2-0.8	0.70	0.4-1.0	0.4-0.8	0.25	0.1	0.15	-
2024	3.8-4.9	0.50	0.50	0.3-0.9	1.2-1.8	0.25	0.1	0.15	-
2036	2.2	0.50	0.50	0.1-0.4	0.3-0.6	0.25	0.1	0.15	-
2218	3.5-4.5	0.90	1.0	0.20	1.2-1.8	0.25	0.1	-	-
2224	3.8-4.4	0.12	0.15	0.3-0.9	1.2-1.8	0.25	0.1	0.15	-
2090	2.4-3.0	1.10	0.12	0.05	0.25	0.1	0.05	0.15	0.08-0.15

* Other elements (<0.5 wt % each): Pb, Sn, Zr, and Ni

2.2.1. The Al-Cu System

Copper is the principal alloying element in the 2xxx series alloys. Copper has a maximum solubility of ~0.1 wt % at room temperature, and 5.7 wt % at 548 ˚C as shown in Fig. 2.3.

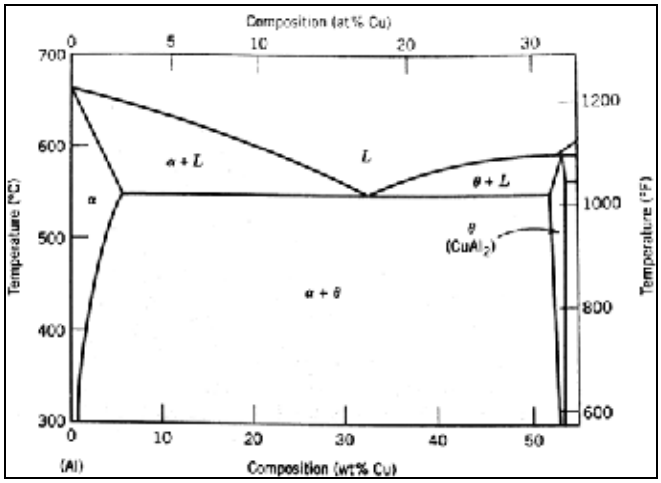

Fig. 2.3. The Al-rich corner in the Al-Cu system [27]

In the Al-rich end of the Al-Cu system, a eutectic reaction takes place at a composition of 33.2 wt % Cu and 548 ˚C. The resulting eutectic contains both α-aluminium and the θ-Al_2Cu intermetallic phase. The Cu-content in the θ-phase is within a range of 52.5 to 53.7 wt % at the eutectic temperature, with the range narrowing as the temperature drops [2, 4]. In commercial alloys, the Cu-concentration can reach up to 10-14 wt % in cast alloys, but for wrought alloys, the concentration is limited to 4-6 wt % (around the maximum solubility of Cu in α-aluminium).

2.2.2. Intermetallic Particles in AA2xxx

Due to the many alloying elements and impurities in the 2xxx series, the intermetallic particle structure can be considered as the most complex among all Al-alloys. Additions of magnesium are often used to improve the strength [4]. The addition of lithium to Al-Cu(Mg) alloys has also been found to significantly enhance the strength and weldability to levels higher than any other Al-alloy class, yet increasing the price [3]. Other elements may exist as impurities (e.g. silicon and iron), or as additives to improve the strength, such as: manganese, titanium, zinc, and chromium.

Mondolfo [2] reviewed the intermetallic particles in the 2xxx series alloys, as shown in Table 2.5 which lists the commonly observed phases. Generally, the alloying elements in the 2xxx series alloys form two types of intermetallic particles in the aluminium matrix:

1. Age hardening metastable and stable (soluble) precipitates: fine spherical or plate-like coherent precipitates (few nanometres thick) that form only during room or low-temperature aging after solution heat treatment and quenching. They are the main strengthening mechanism due to their small size. On further aging, these phases coarsen until they transform to incoherent equilibrium phases (reaching 1-10 μm size) which contain Cu and/or Mg, such as: θ-Al_2Cu or S-Al_2CuMg phases. They differ from primary precipitates in that they can be fully re-dissolved at around ~515-550 ˚C. During recrystallisation, the concurrent dissolution/precipitation of these phases can influence the resulting grain structure depending on the starting material condition (e.g. solution-treated or aged) and the type of the precipitates.
2. Constituent (*primary* insoluble) particles: which contain Si, Fe, or Mn, in addition to Cu or Mg, such as $Al_{12}(Fe,Mn)_3Si$, Al_7Cu_2Fe, or $Al_5Cu_2Mg_8Si_6$ (1-10 μm size).

Table 2.5. Potential intermetallic phases in AA2xxx alloys (After [2])

Cu	Cu<2% in solid soln.	Cu>2% Al_2Cu	Fe>>Si Al_7Cu_2Fe or $Al_6(Cu,Fe)$	Mg>1/2Si Al_2CuMg or Al_6CuMg_4	Mn>>Fe $Al_{20}Cu_2Mn_3$ or $Al_6(Cu,Fe,Mn)$	Mg<Si $Al_5Cu_2Mg_8Si_6$ $Al_{15}(Cu,Fe,Mn)_3Si_2$
Fe	Si>2Mg Al_8Fe_2Si or Al_5FeSi	Fe>>Si Al_7Cu_2Fe or Al_6 (Cu,Fe) or Al_3FeSi		Mn>0. 1% $Al_6(Cu,Fe,Mn)$ or $Al_{15}(Cu,Fe,Mn)_3Si_2$		
Si	Si>Fe Al_5FeSi	Si<Fe, Mg>Si Mg_2Si	Mg ≈ Si $Al_5Cu_2Mg_8Si_6$	Mn>0. 1% $Al_{15}(Cu,Fe,Mn)_3Si_2$	Si>>Mg+Fe Si	
Mg	Mg<0.2% in solid soln.	Si>0.6Mg<1Mg Mg_2Si	Si ≈ Mg $Al_5Cu_2Mg_8Si_6$	Si<<0.6Mg Al_2CuMg	Cu<Mg Al_6CuMg_4	
Mn	Mn<0.2% in solid soln.	Fe>Si $Al_6(Fe,Mn)$	Fe<Si $Al_{15}(Cu,Fe,Mn)_3Si_2$	Fe,Si<<Mn $Al_{20}Cu_2Mn_3$		
Zn	Zn<2% in solid soln.	Zn>2% $Al_3Cu_5Zn_2$				

2.2.2.a. Age Hardening Precipitates in the Al-Cu System

The 2xxx series alloys differ from the 5xxx in that they attain their strength through precipitation-hardening. Because of the nature of the Al-Cu system (Fig. 2.3), if an alloy of composition less than 5 wt % Cu is heated to the α region (~515-550 ˚C) to force all the copper to go into solution then quenched, a supersaturated solution will form. Since supersaturation is unstable, a driving force exists to precipitate the excess copper to reach a metastable or equilibrium state [2-4, 6, 27].

This precipitation sequence in the Al-Cu system is as follows:

SSS α ➔ GP1 zones➔ GP2 zones θ'' ➔ θ' ➔ θ

where SSS is the supersaturated solid solution. On aging the alloy at room temperature, GP1 (Guinier-Preston) zones form, which are coherent disk-shaped regions of few atoms thick (0.4-0.6 nm), parallel to $\{001\}_\alpha$ and 8-10 nm in diameter. If the alloy is heated to around 100 ˚C or higher, GP2 zones (θ'') replace GP1 zones. These are also coherent plate-like precipitates parallel to $\{001\}_\alpha$, which are 1-4 nm thick and 10-100 nm in diameter. On further heating, θ' forms, which are semi-coherent plate-like precipitates also parallel to $\{001\}_\alpha$, and 10-150 nm thick. If heating continues, the incoherent micron-sized equilibrium phase θ

(Al_2Cu) forms. The material attains its strength through the interaction of the precipitates to dislocations (cutting or Orowan bowing).

2.2.2.b. Age Hardening Precipitates and Equilibrium phases in the Al-Cu-Mg System

A special class of the 2xxx series is the Mg and Mn-containing 2xxx alloys, commercially known as Duralumin. Their composition range is 4-4.5 wt % Cu, 0.5-1.5 wt % Mg, and 0.5-1.0 wt % Mn [2]. Magnesium is known to accelerate and intensify the natural aging response in Al-Cu alloys. Depending on the relative amounts of Cu, Mg and Si, the equilibrium phase may differ. The S-phase (Al_2CuMg) forms when the Cu:Mg ratio is larger than 2 and Mg:Si ratio is larger than 1.7. When the Mg:Si ratio is ~1.7, both Mg_2Si and Al_2Cu are present (Table 2.5).

Although researchers disagree on the crystal structure and orientation of the hardening phases, there is general agreement that the type of the hardening phase depends on the relative amounts of Mg to Cu. In alloys with a Cu:Mg ratio larger than 8:1, the Al_2Cu is the main hardening phase. When the ratio is between 8:1 to 4:1, both Al_2Cu and Al_2CuMg exist, and then Al_2CuMg becomes the hardening phase for ratios between 4:1 to 1.5:1. The precipitation sequence in Al-Cu-Mg alloys has been extensively reviewed and investigated using calorimetry, transmission electron microscopy and atom probe [2, 28-33]. The confusion about the precipitation for an alloy like 2024 can be shown in Fig. 2.4, where the phase diagram shows that, for the composition ranges of this alloy, it appears to exist in a 3-phase region ($\alpha + \theta + S$). Yet, it is generally agreed that for this alloys, the S-phase is the more dominant. Generally, the precipitation sequence in the Al-Mg-Cu alloys, where Al_2CuMg is the hardening phase, is given as:

SSS α ➔ GPB zones➔ S'' ➔ S'➔ S (Al_2CuMg)

The GPB zones form as clusters of Mg and Cu atoms, ~1-2 nm in diameter. The clusters continue to grow by heating to a cylindrical shaped S'', developing to S' which can exceed 10 nm in thickness. On further heating, the precipitates continue to grow until the equilibrium-S forms, which is micron-sized [2].

The development in the precipitate type and size during heating is associated with a change in hardness. Following solution treatment and quenching, the Al-Cu-Mg alloys experience an increase in hardness by natural aging at room temperature (T3). Artificial aging can also be used to increase the hardness, but it requires a careful selection of the aging time and temperature, Fig. 2.5. In 2024, the hardness of the a solution-treated condition increases upon aging at from ~95 H_V to ~140 H_V due to the formation of the GPB zones, which dissolve on further heating, resulting in a drop in hardness to ~110-130 H_V. However, on further heating the hardness increases again due to the precipitation of the S'/S'' phases, which increase the hardness to ~150 H_V (peak aging, T6) [34].

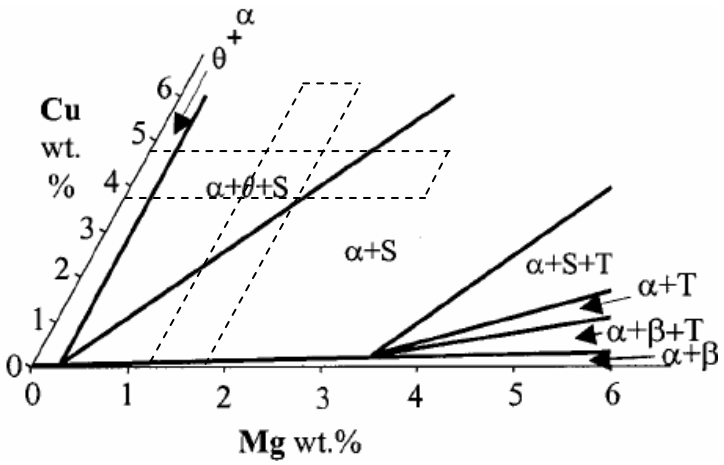

Fig. 2.4. Isothermal section in the Al-Cu-Mg phase diagram at 200 ˚C, where: α=Al-matrix, S= Al_2CuMg, θ= Al_2Cu, T =Al_6CuMg_4, β=$Al_{12}Mg_{17}$. The dashed lines show the composition range for 2024 [31]

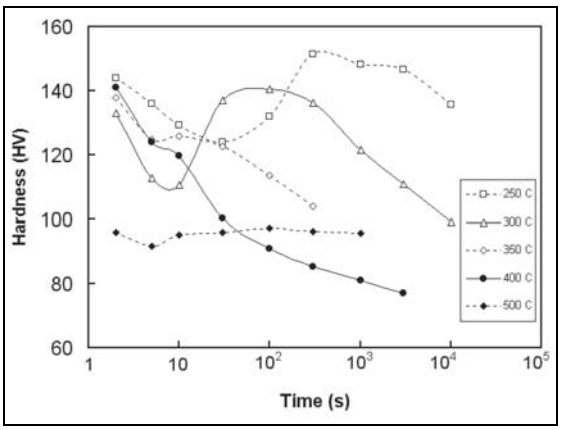

Fig. 2.5. The age-hardening data of 2024 following solution treatment, quenching and holding in salt bath [34]

2.3. Influence of the Manufacturing Route of Al-based Alloys on the Microstructure and Properties

2.3.1. Manufacturing routes for Al-based alloys

Currently, sheets of Al-based alloys are produced either by DC-casting or twin-roll continuous casting (CC) as shown in Fig. 2.6. DC casting is the main process that has traditionally been used, until the introduction of CC about a decade ago [3, 6].

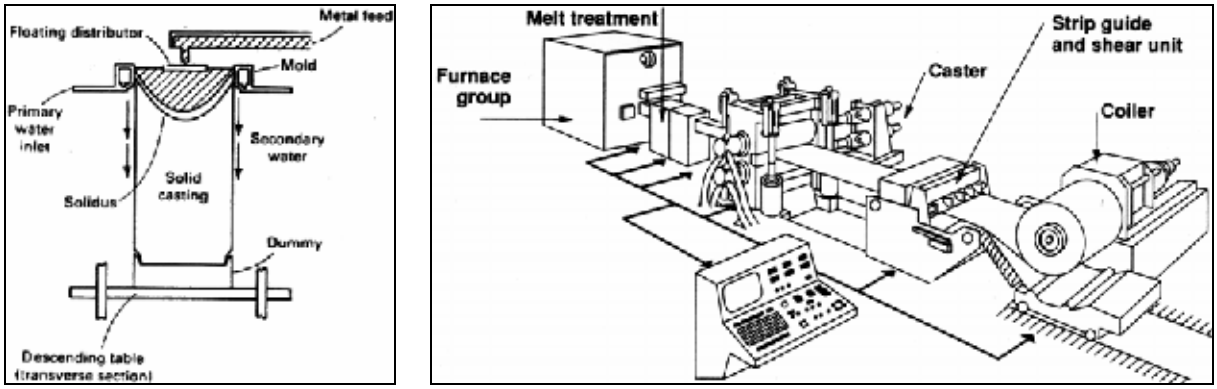

(a) (b)

Fig. 2.6. Schematic diagrams for (a) direct-chill casting [3], and (b) twin roll casting [35]

In DC-casting, the material is cast in the form of billets or ingots, with typical sizes of 1.2 m in diameter for billets, and 1.5×0.5 m for ingots that are rolled afterwards, reaching 5 to 30 mm thick by 2 m wide for plate and strip products. During DC (Fig. 2.6-a), molten metal is fed through a mould, where it gets sprayed by water from outside, and further cooled as the solidified ingot is pulled downwards. This involves a slow cooling rate of about 1 to 5 $K.s^{-1}$ which results in the creation of a coarse dendritic structure with macro-segregation, as well as surface defects [3, 6]. After casting, the cast is usually scalped to remove any surface defects. Then, it is subjected to a series of thermal treatments (homogenisation at ~600 ˚C) and thermomechanical treatments (hot rolling) to optimise the microstructure and attain the desired shape. These post-casting operations are avoided or minimised by using CC instead of DC. In twin-roll CC (Fig. 2.6-b), molten metal is pushed through the gap between two water-cooled rolls. The casting process produces slabs around 25 mm in thickness, which are directly hot rolled afterward, and coiled or sheared depending on the thickness required. The process is capable of producing sheets 0.5-8 mm thick [35-37]. With cooling rates of about

100 to 1000 $K.s^{-1}$, a fine microstructure results, with smaller inter-dendritic spacings compared to the DC-cast materials.

2.3.2. Microstructural Differences between DC and CC sheets

The main difference between the DC and CC processes is in the cooling rates (V_c), with DC materials experiencing a much slower cooling rate (1-5 $K.s^{-1}$) compared to CC materials (100-1000 $K.s^{-1}$). This influences the average dendritic arm spacing (DAS), the extent of micro and macro-segregation, grain size, and size of constituent particles [3, 35, 38-40].

2.3.2.a. Micro-Segregation

Micro-segregation results from non-equilibrium cooling during solidification. Lack of sufficient time for the alloying elements to diffuse in the solidifying matrix can result in a cored dendritic microstructure, with a concentration gradient across the dendrites as shown in Fig. 2.7. In Al-based alloys, micro-segregation takes place due to the limited solute solubility of the alloying elements in aluminium. The rejection of solutes from solidifying dendrites leads to the formation of solute-enriched regions that ultimately form intermetallic particles (divorced/non-equilibrium eutectic) at the end of solidification in eutectic alloys [6, 41]. The DAS is directly linked to the extent of micro-segregation, as both are directly related to the cooling rate at which solidification takes place.

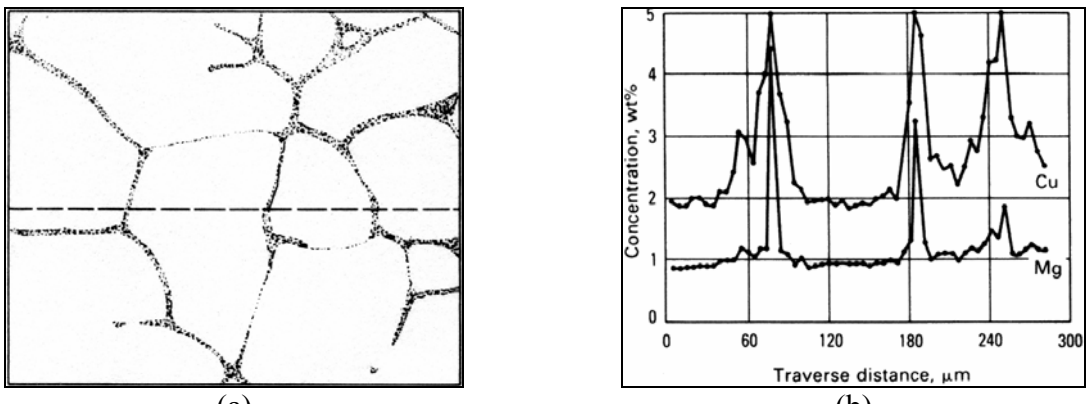

(a) (b)

Fig. 2.7. Mg and Cu micro-segregation in 2124 showing (a) dendritic cells surrounded by Cu and Mg enriched boundaries, and (b) electron microprobe analysis trace across the boundaries along the dashed line in (a) [3]

The relation between the DAS and cooling rate for Al-alloys is given in the form of:

$$DAS = AV_c^{-n} \tag{2.2}$$

where A and n are material-specific constants. A listing of the equation constants for various Al-based alloys is available elsewhere [38].

Despite the lack of studies comparing the DAS for CC and DC-cast alloys of the same composition, it is agreed that faster cooling rates would result in fine DAS and a uniform distribution of fine constituent particles, compared to coarser DAS and coarse intermetallic particles [3]. However, in CC sheets, the sharp through-thickness thermal gradients result in a non-uniform DAS, increasing from ~5 μm at the surface to ~8 μm at the centre in CC Al-0.5Fe-0.2Si alloy, due to the fast cooling rates on the surface [35].

The influence of the cooling rate on DAS and micro-segregation, as given by equation (2.2), was validated for a wide range of cooling rates in experimental casting experiments. Davis [3] reported that equation (2.2) can be fitted over a wide range of Cu-composition up to the eutectic composition only, for cooling rates from 1.67×10^{-3} to 16.7 $K.s^{-1}$. The increase in both the solute content and the cooling rate was found to decrease the DAS (Fig. 2.8). Eskin *et al.* [38] also fitted equation (2.2) for six binary Al-Cu alloys with different copper compositions (0.98 to 1.86 wt %), cast in the range of cooling rates from 0.1 to 20 $K.s^{-1}$. They showed that the coefficient A was strongly dependent on the Cu concentration. The cooling rate was also correlated to the amount of non-equilibrium eutectic and micro-segregation. However, the trend was rather complicated. The non-equilibrium eutectic was initially found to increase with the increase in the cooling rate for the rates < 1 $K.s^{-1}$, followed by a gradual decrease within the range from 1 to 10 $K.s^{-1}$. Such a trend was attributed to the limited extent of Cu diffusion at high cooling rates.

Liu and Kang [42] fitted equation (2.2) for two Al-Mg alloys (7 and 11 wt %), covering a range of cooling rates from 0.5 to 10000 $K.s^{-1}$. An increase in micro-segregation (qualitatively, based on the eutectic fraction) was observed with the increase in the cooling rate or Mg-content. However, the Mg-concentration in the eutectic phase decreased with the increase in cooling rate. In a different study, Glenn *et al.* [43] studied the extent of micro-segregation in grain-refined and non-refined AA5182 ingots, as well as the influence of the cooling rates, by investigating the through ingot depth variation of micro-segregation. They

found that the micro-segregation range (difference between maximum and minimum Mg concentration) increases with the decrease in cooling rate in grain refined ingots, reaching to ~5 wt % Mg, whereas it is independent of the cooling rate in non-grain refined ingots at ~2.5-3 wt % Mg. They concluded that the difficulty in correlating the experimental observations with the theoretical micro-segregation models, and the disagreement regarding the influence of specific parameters, result from the differences between the alloying elements in their diffusion characteristics. For instance, during post-solidification homogenisation, considerable diffusion can occur for Mg atoms at temperatures as low as 350 ˚C, which is not the case for Cu atoms.

It is important to highlight that equation (2.2) is a simplified formulation for micro-segregation. It is known that segregation is influenced by the flow characteristics of a variable composition fluid [44], which accordingly explain the difficulty in correlating the simple representation with the experimental investigations.

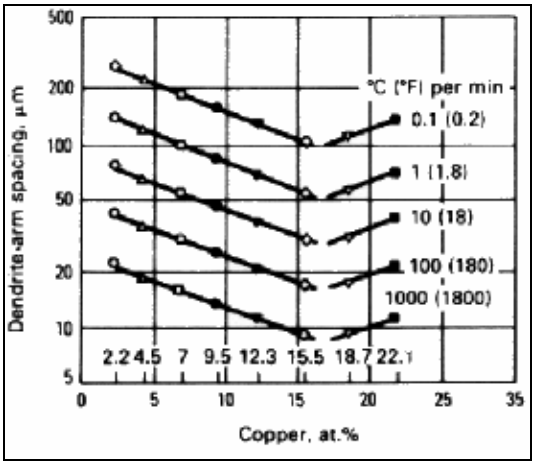

Fig. 2.8. Influence of the cooling rate and composition on dendrite arm spacing in Al-Cu alloys [3]

To reduce the microstructural heterogeneity resulting from micro-segregation, Al-alloys are typically homogenised. Homogenisation enhances the strength, ductility, and the heat treatment response of heat treatable Al-alloys by forcing the hardening solutes into solution [41]. At the same time, in 3xxx and 5xxx series alloys, homogenisation is beneficial in

transforming and precipitating the Mn-containing precipitates from solid solution to control the grain structure and formability as discussed in section 2.1.2.c.

2.3.2.b. Macro-Segregation

Macro-segregation is normally observed in DC ingots with thickness larger than 405 mm [41, 44, 45]. Macro-segregation is defined as a through-thickness heterogeneous re-distribution of the alloying elements in the casting, compared to the alloy's nominal composition. Differences in the cooling rate from the surface to the centre create compositional variations in the solidifying liquid, which becomes solute-rich or solute-depleted by the selective freezing of specific alloying elements. As a result, density differences occur between the solid and liquid phases. Solidification shrinkage and convection currents can also induce flow fields for the solute-rich liquid in the direction of heat flow.

In DC cast ingots, solute enrichment near the surface takes place due to solidification shrinkage, associated with the high cooling rates, which pushes the solutes to the ingot surface causing positive segregation, as well as the exudation of the solute-rich inter-dendritic liquid towards the surface. Consequently, the neighbouring region becomes solute-depleted. With a decrease in cooling rates, the solidifying liquid becomes rich in lower-melting constituents, building up positive segregation again. However, at the ingot centre, a considerable fall in solute composition takes place [44, 46]. Common levels for DC macro-segregation are within ±5% of the nominal composition, except for the surface where the variation could further increase, Fig. 2.9-a [3, 47]. Yu and Granger [48] explained that the centreline negative segregation results from the settling of solute-depleted free-floating dendrites which formed at the top of the sump (melt), Fig. 2.9-b, then swept downwards by convection.

In CC, the rapid cooling rates and the roll pressure force the solute-rich liquid towards the central region causing centreline segregation, which consequently result in the formation of the intermetallic particles [35].

It is known that macro-segregation is not significantly affected by homogenisation. However, macro-segregation can be minimised in the casting by decreasing the ingot thickness, and control the casting procedure by decreasing the casting and increasing the amount of superheat to maintain the homogeneity of the molten metal for a considerable time [3].

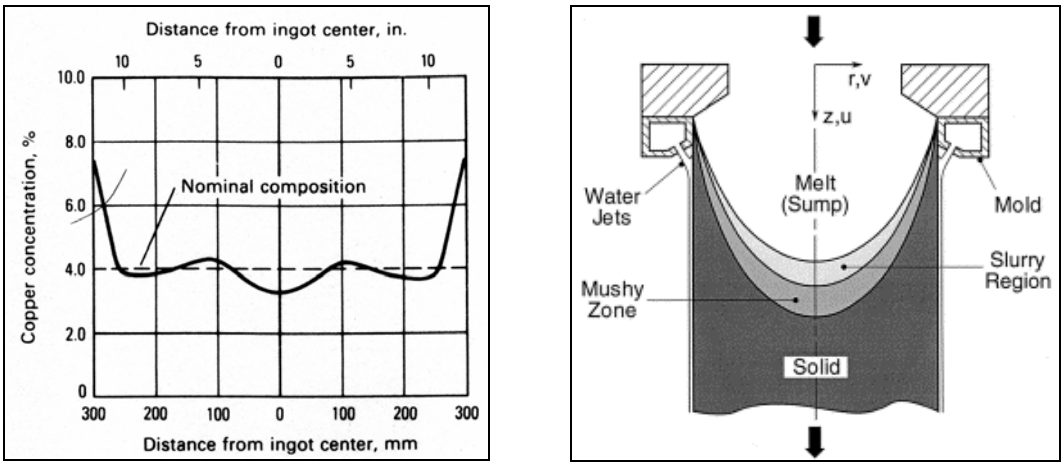

(a) (b)

Fig. 2.9. (a) Through-thickness Cu distribution in 2124 DC ingot [3], (b) melt flow [44]

2.3.2.c. Differences in Grain and Intermetallic Particle Structures

The grain size is a function of the DAS, and thus can be related to the cooling rate in a similar manner to the DAS. However, the grain size is also dependent on other parameters, such as the usage of grain refiners, impurity level and intermetallic particles [38, 45]. Several studies have compared the microstructures of DC and CC alloys of the same composition (e.g. 5052 [39, 40], 5754 [49] and 5182 [37, 39, 49, 50]). Despite having the same chemical compositions, DC and CC sheets showed significant differences in particle and grain structures as shown in Fig. 2.10 and 2.11.

Compared to DC sheets, Fe-containing constituent particles were relatively finer ($< 1\ \mu m$) in the CC sheets (five times finer than in DC as reported in the review by Li [35]), higher in number density, and occurring in bands of segregated coarse particles in the central region of the sheet [39, 49]. Baldacci *et al.* [51] found that the Fe-containing particles tend to break up more rapidly than Mg_2Si with the increasing strain during hot rolling of AA5182. This was attributed to the branched morphology of the Fe/Mn-rich particles compared to the more rounded morphology of Mg_2Si. Particle break-up was found to align the particles along the rolling direction. In DC, particles were more uniformly distributed and relatively coarser due to Ostwald ripening [20] or transformation from one type to another during homogenisation [9, 10, 20, 52]. The particles types, though, were the same ($Al_6(Fe,Mn)$ or Al(Fe,Mn)Si, depending on the Si content of the alloy, and clusters of Mg_2Si) [39, 40, 49, 50, 53].

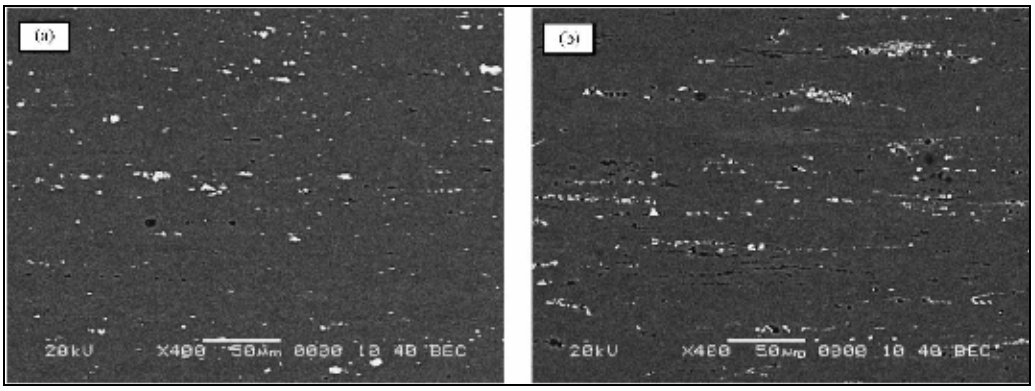

Fig. 2.10. Secondary electron SEM micrograph showing the difference in constituent particles morphology in (a) DC, (b) CC AA 5052. The bright particles are the Fe-rich phase, and the dark particles are the Mg_2Si particles [40]

In the as-cast condition, DC ingots show a three-zones structure (i.e. chill zone, columnar grains, and equiaxed zone in the centre), compared to only two zones (i.e. columnar and equiaxed, with the columnar zones growing perpendicular to the sheet surface) in CC. The DAS increases from the surface (where high cooling rates exist) towards the centre [35]. Similarly, differences in grain structure morphology were also observed in annealed CC and DC sheets of roughly the same composition [39, 53]. Grains in the as-DC cast condition are generally coarser than those in the as-CC condition. However, the grain structure of the CC condition is very heterogeneous, varying through the thickness from a fine grain structure near the surface, to a coarser structure within the bulk, ending with a fine band in the centre, Fig. 2.11.

The differences in the particle structure between CC and DC sheets is a direct result of the particle distributions in both conditions as observed by Slamova *et al.* [39], where the fine grains band in the CC-sheets centre coincides with centreline segregation which contain high density of intermetallic particles, Fig. 2.11-(a,b). During annealing, coarse constituent particles act as nucleation sites for recrystallisation due to the deformation zones surrounding them, leading to PSN [49]. Fine-sized particles and dense distributions result in a fine grain structure by pinning the grains. In the DC sheets, the lower density of intermetallic particles results in a coarser grain size, Fig. 2.11-(c,d).

In addition, due to the high cooling rate during CC, some elements remain in solution (e.g. Mn). Further annealing or hot rolling may induce concurrent precipitation of Mn-rich

precipitates (e.g. Al_6Mn), which have been found to significantly impede recrystallisation [50], or refine the grain structure [49, 54]. These influences result in the difference in the mechanical properties of DC and CC sheets. The fine grain structure, along with retention of solutes in solution, result in relatively higher strength in CC sheets (Fig. 2.12). Yet, with annealing and precipitation of the elements in solution, the hardness of both conditions becomes similar [55].

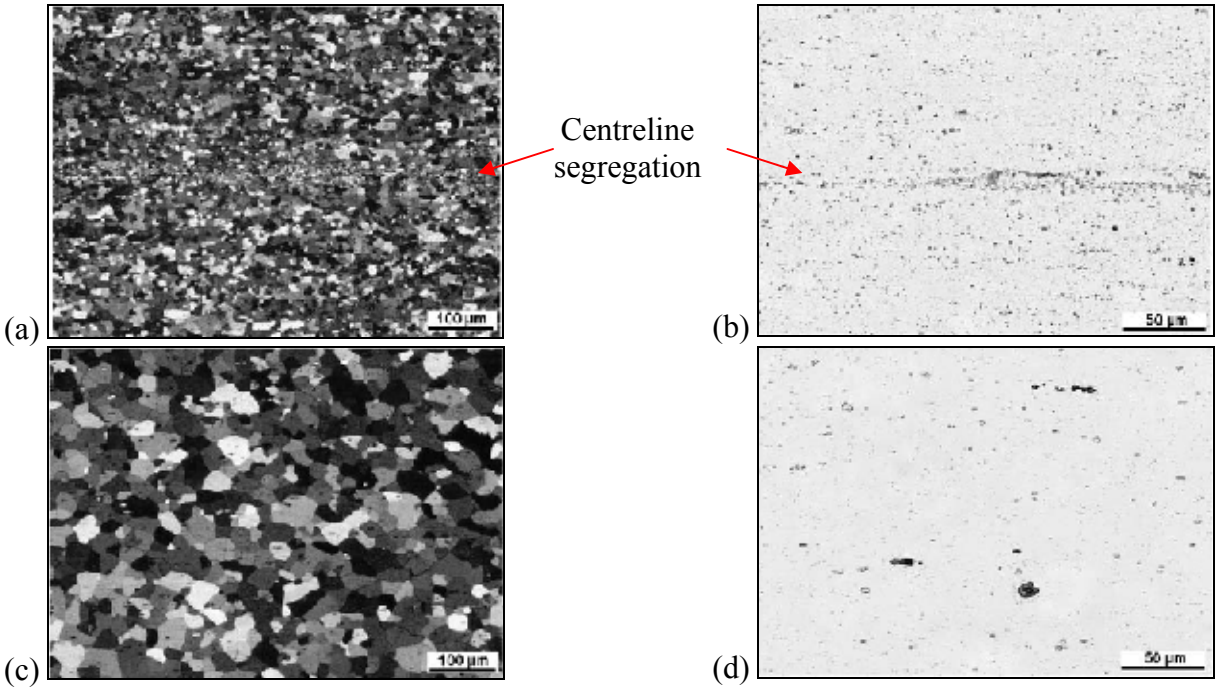

Fig. 2.11. Polarised light and optical micrographs of the grain and particle structures near mid-thickness in 1 mm thick sheets of annealed (a,b) CC, (c,d) DC AA 5182 [39]

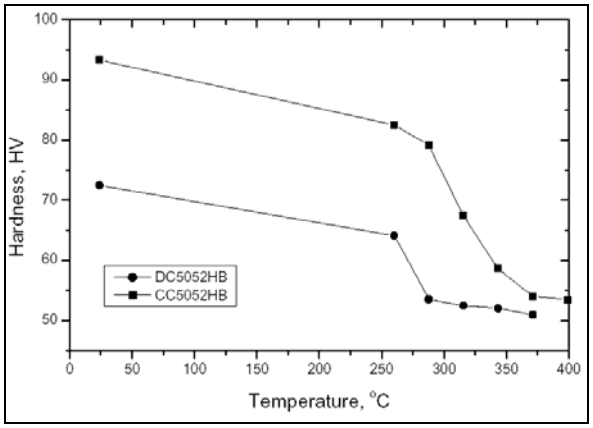

Fig. 2.12. Comparison of the hardness development in DC and CC 5052 HB sheets of the same thickness after isochronous annealing as a function of temperature [40]

2.4. Strengthening Mechanisms in Al-based Alloys

Plastic deformation in polycrystalline materials takes place through the motion of dislocations. The existence of any barriers within the crystalline structure that hinder the motion and glide of the dislocations strengthens the material [56]. In Al-based alloys, either age-hardenable or strain-hardenable, strength is the sum of several microstructural factors (mechanisms) that hinder the dislocation motion. These strengthening parameters are: a) grain-boundary strengthening, b) solid-solution strengthening, c) particle strengthening (Orowan looping), and d) dislocation-dislocation strengthening-interaction [6, 27, 41, 56-59].

2.4.1. Grain boundary strengthening

The relationship between the grain size (d) and the yield strength (σ_{YS}) in a polycrystalline material is represented by the Hall-Petch equation, which is given as:

$$\sigma_{YS} = \sigma_O + k_y d^{-1/2} \tag{2.3}$$

where σ_O is the frictional stress contribution, and k_y is the Hall-Petch slope, which is a measure of the resistance to slipping across the grain boundary [56, 60]. The frictional stress component may be divided into two parts [56]; σ_{ST}, which is a structure-dependent temperature independent component that is related to long-range dislocation interactions (100-1000 Å) with solutes (σ_{SS}), precipitates (σ_P), and dislocations; and σ_T, which is a temperature dependent contribution that is related to the inherent short-range (<10 Å) resistance of the lattice to dislocation movement, also known as Peierls stress.

$$\sigma_{YS} = \sigma_{ST} + \sigma_T + k_y d^{-1/2} \tag{2.4}$$

In face centred cubic (FCC) and close-packed hexagonal (CPH) materials, the latter contribution is very low, compared to in body-centred cubic (BCC) materials. Due to the difficulty in separately quantifying the Peierls component, it is usually included within the frictional stress [56, 61].

The Hall-Petch relation for Al-Mg alloys has been investigated in several reports and established for strained and annealed alloys [61-71]. Typical σ_O and k_y values are shown in Table 2.6. Lloyd and co-workers [61-64] studied the Hall-Petch relation for various binary

and commercial Al-Mg alloys using conventional rolling and annealing to generate variations in grain size. They noted that the Mg-content, or other alloying elements (e.g. Mn), can significantly influence σ_O and k_y. Furukawa and co-workers [65-68] also studied the grain size influence on strength for sub-micron grain structures produced utilising equal channel angular pressing/extrusion (ECAP/ECAE) or torsion, followed by static annealing. They indicated that the relation can be applied even for deformed structures with grain sizes as fine as ~90 nm. However, a decrease in the k_y value was observed for grain sizes < 150 nm [65]. This decrease was attributed to the influence of extrinsic dislocations, which move freely through the non-equilibrium boundaries of the ultra-fine grains. Generally, the Hall-Petch relation can be used to relate the strength and grain size in the annealed condition. However, the possible interactions from solid solution strengthening and the deformed microstructure need to be separately considered to maintain the consistency of the relation.

Table 2.6. Literature values for σ_O and k_y in some Al-Mg alloys

Alloy	Treatment	σ_O (MPa)	k_y (MPa.m$^{1/2}$)	Reference
AA5052	Rolling/Annealing	37	0.215	[61]
AA5754		42.7	0.275	
Al-5Mg-0.2Mn (wt %)		82	0.2154	
Al-5 Mg		85	0.15	
AA5182	Ditto	57.6	0.30	[62]
Pure Al-99.99%	ECAP	11.1	0.115	[67]
Al-1Mg (wt %)		22.3	0.131	
Al-3Mg (wt %)		60.7	0.148	

2.4.2. Solid solution strengthening

In some Al-based alloys (e.g. Al-Mg and Al-Mn-Mg, and Al-Si alloys), strength is attained through solid solution strengthening combined with work-hardening. Solute atoms included in the lattice of a specific element, either by substituting an atom or by occupying an interstitial site, cause the solvent lattice to experience distortion fields surrounding the solute atom. Experimental observations and theoretical models show that the strengthening contribution due to solid solution σ_{SS} is proportional to the solute composition (c) such that [59]:

$$\sigma_{SS} \propto \sum_i \sqrt{c_i} \tag{2.5}$$

In some reports [61, 63, 72, 73], the relationship between the strengthening contribution of a specific alloying element and the solute content was represented as a linear relation. Alloying elements in solution with aluminium have different strengthening contributions, which is dependent on the solubility limits (Table 2.7).

Table 2.7. Solid solubility and the strengthening contribution of some alloying elements

Element	**Max. Solubility in binary Al-X alloys (wt %)** [4]	**Temperature (˚C)**	**Strength Increment MPa/wt %** [61, 63, 72]	**Range (wt%)**
Cr	0.77	660	--	--
Cu	5.65	550	~70	0-0.05
Fe	0.052	655	~200	0-0.025
Li	4.0	600	--	--
Mg	14.9	450	~16-19	2-8
Mn	1.82	660	~85	0-0.1
Ni	0.05	640	--	--
Si	1.65	580	20	0-0.2
Ti	1.0	665	~45	0-0.18
Zn	82.8	380	--	--
Zr	0.28	660	--	--

Of the elements which are normally present in Al-based alloys, iron and nickel have the least solid solubility in aluminium, compared to zinc and magnesium which have solubilities > 10 wt %. Other elements, such as copper, lithium, magnesium and silicon, have solubilities > 1 wt %, but less than 10 wt %. Hence, magnesium is the principal alloying element that it used to strengthen aluminium by solid solution strengthening due to its large solubility limit, while zinc, copper and lithium strengthen aluminium by precipitation hardening.

In the 5xxx series alloys, magnesium atoms pin dislocations, which can be seen during tensile testing at yielding where the stress-strain curve shows serrated jumps known as the Portevin-Le Chatelier (PLC) effect. This is a result of dislocation-solute interactions, where solute atoms pin the dislocations causing a load drop when dislocations manage to escape from the solute atoms [56].

As shown in Fig. 2.13-a, Mg additions enhance the strength of aluminium at the expense of the ductility. For every 1% Mg addition, the yield strength of the annealed condition increases by ~16-19 MPa in the range from 2 to 8 wt %. Mahon and Marshall [74] studied the influence of various alloying elements on the strength in binary Al-alloy foils as shown in Fig. 2.13-b.

Their findings show that the existence of other elements in solution (e.g. iron and manganese) can also provide a significant strengthening contribution, provided that it can be kept in solution. However, iron, which is the most effective element, has a solid solubility ~ 0.01 wt % in foil alloys.

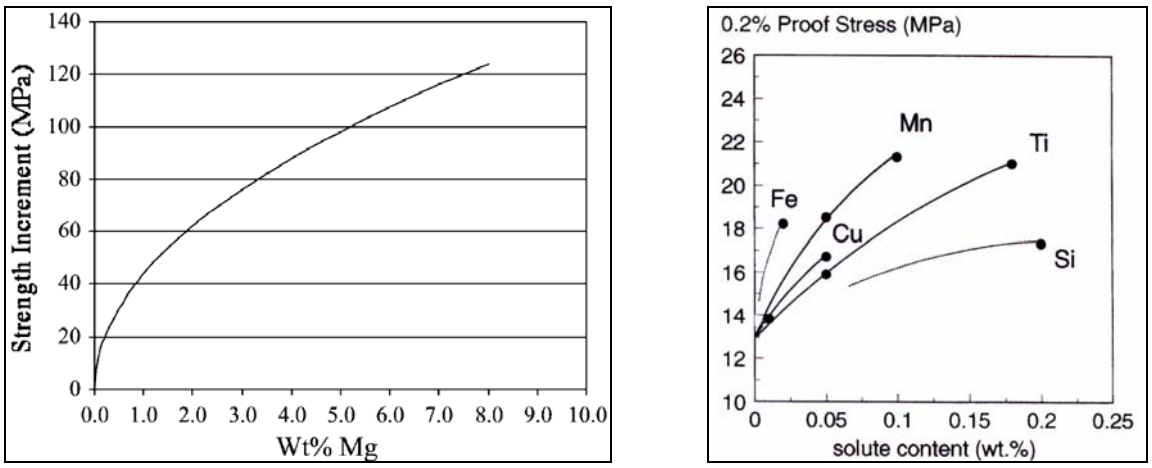

Fig. 2.13. The solid solution strengthening contribution of (a) magnesium in Al-Mg alloys [72], and (b) its influence on the yield stress in binary Al-X alloys [74]

2.4.3. Particle strengthening

The existence of fine precipitates or particles within the matrix provides another contribution to strength, through hindering dislocation movement (i.e. dislocation-particle interactions). However, this depends on the particle strength, type (crystallographic orientation relationship), size and number density. When a moving dislocation meets a particle, there are two possible scenarios (Fig. 2.14) [6, 24, 56, 58]:

a. If the particle is weak (deformable), it will be energetically favourable for the dislocation to shear (cut through) the particle (Fig. 2.14-a).
b. If the particle is strong (non-deformable), the dislocation will bow between the particles, leaving dislocation rings around the particles (Fig. 2.14-b).

In age-hardenable alloys (e.g. 2xxx), the precipitates (e.g. GP-zones and the metastable phases) are generally of the first type, which are cut during deformation by the dislocation depending on their sizes and distribution. When these particles have a coherent or semi-

coherent orientation relationship with the matrix, the host lattice is distorted around them, producing a misfit strain ε which hinders the dislocation movement. The particle strengthening σ_P of these precipitates is given as [56]:

$$\sigma_P \propto G\,\varepsilon^{3/2}\left(rF_V\right)^{1/2} \tag{2.6}$$

where G is the matrix shear modulus, r is the particle radius, and F_V is the volume fraction of the precipitates.

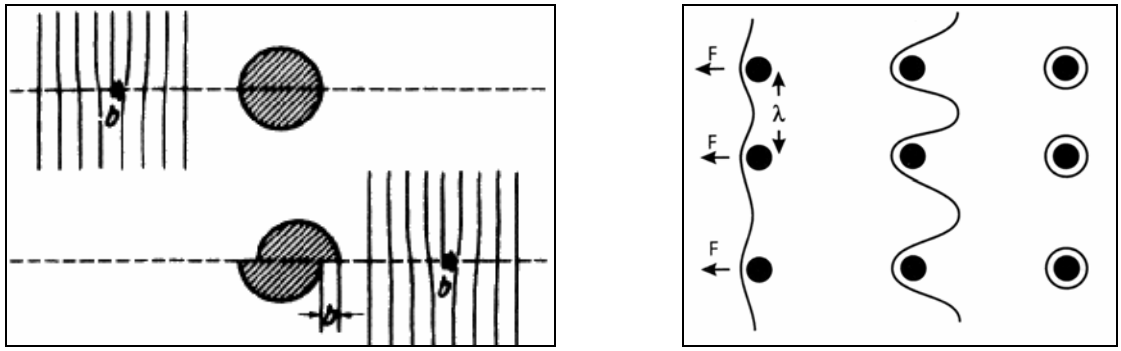

(a) (b)

Fig. 2.14. The influence of particle strength on dislocation-particle interactions showing (a) the shearing of a deformable particle by moving dislocations [6], and (b) the formation of dislocation loops around non-deformable particles [24]

Another possible mechanism for deformable particles happens when a particle with an ordered structure (e.g. Al_2Cu (θ') or $Al_3(Zr,Sc)$) is sheared (Fig. 2.14-a), thus creating a new interphase boundary and anti-phase domain-boundary (APB), which increases the energy in the lattice by creating larger particle-matrix area. However, this effect is very small for coherent precipitates (e.g. GP-zones) due to their small size and the small misfit they create. If the particle is non-deformable, incoherent, and causes a large misfit, dislocations tend to bow around it, leaving behind dislocation rings. This mechanism of dislocation interaction is called Orowan looping (Fig. 2.14-b). The shear stress τ required to loop a dislocation around a particle is given by [6, 24, 56, 58]:

$$\tau = Gb/\lambda \tag{2.7}$$

where λ is the average inter-particle spacing. For a random distribution of particles having a volume fraction of F_V, the inter-particle spacing for particles of equivalent circle radius r is given as:

$$\lambda = \left(2\pi/3F_V\right)^{1/2} r \tag{2.8}$$

In work-hardenable alloys (e.g. 3xxx and 5xxx), particle strengthening is not considered a major strengthening contribution due to the differences in particle characteristics between age-hardenable and work-hardenable alloys. Most particles in work-hardenable alloys (constituent particles or dispersoids) come from the impurity elements (Fe, Mn, or Si), and they are predominantly insoluble [2]. After homogenisation, they normally coarsen and decrease in number density [10], which increases their inter-particle spacing. Nonetheless, in Al-Fe-Si foil alloys (1xxx and 8xxx), it has been reported that the fine non-deformable dispersoids (0.1-0.3 μm) provided a considerable particle (Orowan) strengthening contribution, in the absence of solid solution strengthening [74].

In Sc/Zr modified 5xxx alloys [23, 72, 75], the formation of the $L1_2$ $Al_3Sc_{1-x}Zr_x$ coherent ordered particles was found to provide a combined Orowan/APB strengthening contributions, with the former mechanism operating for particles under 20-25 nm, and the latter for sizes larger than this range [72]. Such a transition in the particle strengthening effect has been observed before [58]. As shown in Fig. 2.15, there is a specific size (P) where maximum strength can be obtained by combining particle strengthening of non-deformable (curve A), and deformable particles (curve C) through adjusting the particle size. An increase in the area fraction of the particles will raise both curves, while an increase in the particle strength will raise curve C to curve B, thus decreasing the optimum particle size to P'.

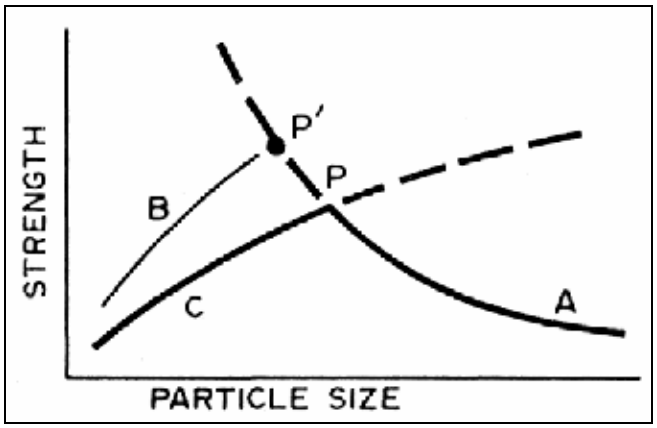

Fig. 2.15. Dislocation-particle interactions showing the influence of particle size on strength for non-deformable particles (A) and low strength (C) and high strength (B) deformable particles [6]

2.4.4. Work hardening (dislocation-dislocation interactions)

Another strengthening mechanism results from the dislocation-dislocation interactions, which is the main mechanism for strain (work) hardening during cold working. There are two models which are used to explain the work hardening contribution in Al-based alloys, which are: Ashby's model and Hansen *et al.* model.

2.4.4.a. Ashby's Model

Ashby [76] studied the dislocation interactions with themselves and other crystalline obstacles (e.g. boundaries, particles, and solute atoms) and their influences on the dislocation mobility. He suggested that the dislocations accumulating during deformation within the structure can be classified into two types: 'geometrically necessary dislocations' ρ_G which exist to accommodate the constraints imposed by grain boundaries and non-deformable particles, and 'statistically stored dislocations' ρ_S, which occur within the grains independent of any constraints imposed by the grain boundaries, Fig. 2.16. Thus, work hardening effects are associated with ρ_S.

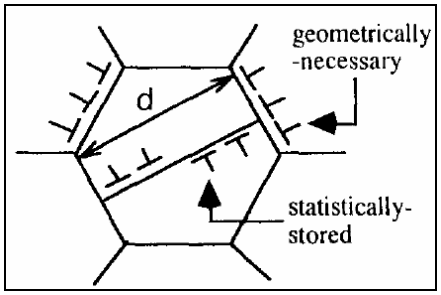

Fig. 2.16. Types of dislocations within a grain according to Ashby's model [77]

Based on this, the relation between σ_{YS} and the dislocation density can be given as:

$$\sigma_{YS} = \sigma_O + \alpha M G b \sqrt{\rho_T} \tag{2.9}$$

where *M* is Taylor's factor, α is a constant, and ρ_T is the total dislocation density, which is given as:

$$\rho_T = \rho_G + \rho_S \tag{2.9-a}$$

Ashby suggested that both dislocation types can be represented in terms of structural factors (e.g. grain size and particles) and shear strain γ, such that:

$$\rho_G = 4\gamma/bd \tag{2.10-a}$$

and

$$\rho_S = 4\gamma/b\lambda_S \tag{2.10-b}$$

where λ_S is the free slip distance, and b is the Burger's vector.

For non-deformable particles of volume fraction F_V and of average radius *r*, ρ_G can be given as:

$$\rho_G = 3F_V\gamma/rb \tag{2.10-c}$$

It has been reported that equation (2.9) could not be strictly applied for aluminium alloys [78, 79]. One uncertain factor about the work-hardening contribution of ρ_S is the free slip distance λ_S, and its dependence on the strain. Fujita and Tabata attempted to establish relations that link the grain size and deformation sub-structure to flow stress in high purity aluminium, to avoid any influences from particle or solute atom strengthening [78]. Their findings showed that the Hall-Petch relation always correlated well with the yield stress. In deformed materials, the Hall-Petch slope was found to increase an increase in strain, however it showed two ranges of linear functions with the transition happening at about 80 μm. They attributed this influence to the variation in the mean free path (slip distance) of mobile dislocations [78].

Thompson *et al.* [79] also noted the λ_S decreased with strain in pure aluminium (with a λ_S range of 2 to 8 μm) regardless of grain size, suggesting that Ashby's relations can be applied only at low strains (ε<0.2). Recent work by Lloyd and Court [61] on structure-property relations in Al-Mg alloys has shown that the strain dependence of λ_S is influenced by the Mg-solute content within a strain range of ε<0.15, whereby, at low Mg solute content (2.55-3 wt% Mg) λ_S is dependent on the strain because of the dominance of dislocation-dislocation interactions during straining, compared to dislocation-solute interactions. Yet, for high solute content (5 wt% Mg), the influence of the Mg-solutes on hindering dynamic recovery increases, thus making λ_S independent of strain, with an estimate of ~ 0.2 nm for λ_S.

2.4.4.b. Hansen et al. Model

Due to the shortcomings observed in Ashby's model when explaining the strength in deformed materials and the mean free path, Hansen and co-workers developed a structure-property model for deformed materials, with more measurable and consistent microstructural features [80-85]. During deformation, the dislocations rearrange themselves within the high-angle grains into *cells* with dense dislocation walls (DDW) and *subgrains* which are crystallites that have small misorientations with respect to each other (low-angle subgrain boundaries). Depending on the amount of strain, the substructure can show a lamellar-like structure, with layers of cells and subgrains within the grains as shown in Fig. 2.17. Hansen suggested that since the deformed substructure is composed of boundaries (grain or subgrain boundaries) they all contribute to the resulting strength and flow stress of the material. Yet, his approach depends on utilising electron backscattered diffraction (EBSD) to define the structural parameters.

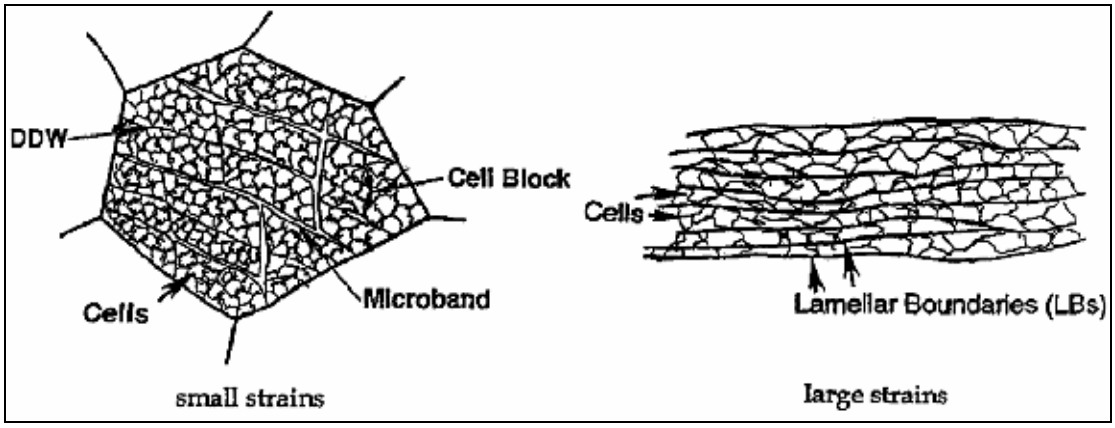

Fig. 2.17. The development of the deformed microstructure at (a) small to medium strain (ε =0.06-0.8), (b) large strains (ε >1) [85]

By looking into the EBSD maps obtained for a deformed microstructure, it is possible to distinguish: the grains, separated by high angle grain boundaries (HAGB) with misorientation angles $\theta \geq 15^{\circ}$, and the subgrains, separated by low angle ($15^{\circ}>\theta>1^{\circ}$) boundaries (LAB). Two important factors are calculated from the EBSD maps using a stereological approach: d which is the average HAGB spacing, and $\overline{L}_{XY\,LAB}$ which is the average subgrain boundary

spacing. Accordingly, a modified Hall-Petch structure-property equation can be represented as:

$$\sigma_{YS} = \sigma_O + kd^{-1/2} + M\alpha Gb\sqrt{\frac{3\bar{\theta}_{LAB}}{\bar{L}_{XY\,LAB}b}} \tag{2.11}$$

where $\bar{\theta}_{LAB}$ is the average misorientation angle for LABs only. It was found in several studies that the strengthening contribution of the LABs is the dominant factor in controlling the strength in deformed materials. Bowen *et al.* [80] used Hansen's model in studying the structure-property development in Al-0.13% Mg alloy deformed by ECAE to a von Mises strain of 10. It was found that the LAB spacing strength contribution can account for 2/3rd of the flow stress, while the Hall-Petch contribution (from HAGB spacing and frictional stress) accounts only for 1/3rd of the material flow stress in deformed structures, Fig. 2.18.

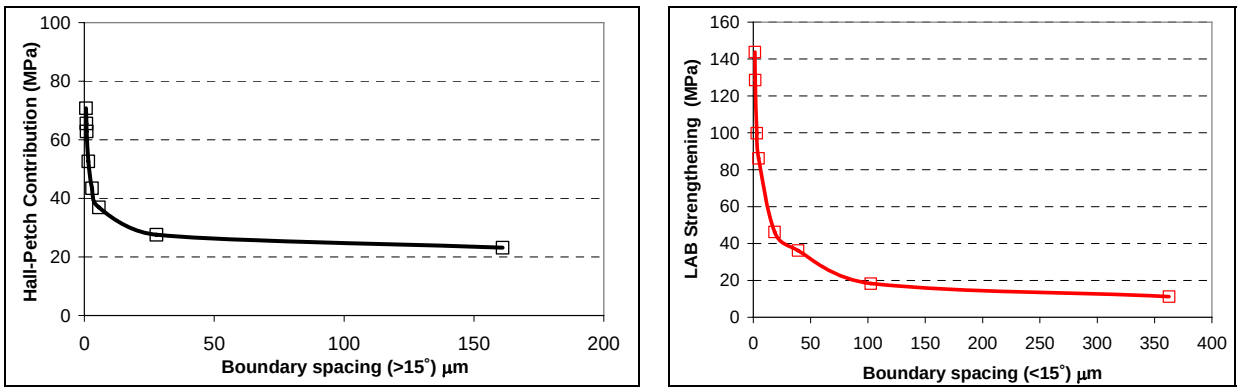

(a) (b)

Fig. 2.18. Calculated strengthening contribution from (a) high-angle boundaries, and (b) low angle boundary in Al-0.13%Mg alloy deformed by ECAE (data after [80])

2.4.5. Strength Models for Al-Alloys

The previous sections discussed the individual strengthening mechanisms that affect the resultant material strength. Most of the structure-property models for Al-alloys considered that the overall strength equals the sum of the individual factors based on the assumption that these parameters are additive (i.e. superposition can be applied). For example, a structure property relationship can be given by [61]:

$$\sigma_{YS} = \sigma_T + \sigma_{SS} + \sigma_P + \alpha MGb\sqrt{\rho_T} \tag{2.12}$$

The main concern in any model is the experimental tools used to quantify the microstructural features (e.g. grains, particles, solutes, and dislocations). In this section, two models will be discussed: Starink and Wang model [73, 86], which can be used for strain or age hardenable materials, and Deschamps and Bréchet model [87, 88], which mainly focuses on age-hardenable alloys.

2.4.5.a. Starink and Wang Model

Starink and Wang [73, 86] established a structure-property model, in which they simplified the superposition of the strengthening contributions. Similar to Hansen's model, it also depends on using EBSD (along with TEM) to characterise the microstructural parameters. In this model, the yield strength is given as:

$$\sigma_Y = \sigma_{GB} + M.\tau_{tot} \tag{2.13}$$

where σ_{GB} is the grain boundary strengthening, M is Taylor's (orientation) factor and τ_{tot} is the critical resolved shear stress (CRSS) which is given as:

$$\tau_{tot} = \tau_o + \tau_{SS} + \left(\tau_D^2 + \tau_{ppt}^2\right)^{1/2} \tag{2.13-a}$$

where τ_O is intrinsic strengthening, τ_{SS} is the solid solution strengthening, τ_D is the dislocation strengthening, and τ_{ppt} is the precipitation strengthening contributions. The grain boundary strengthening contribution is given as:

$$\sigma_{GB} = k\, d^{-1/2} \tag{2.14}$$

where the constant k is given as:

$$k = M.\left(G\, b\, \tau^* / 2\pi\right)^{1/2} \tag{2.14-a}$$

and τ^* is the CRSS for annealed crystals which is taken as $\tau^* = \tau_0 + \tau_{ss}$.

The solid solution strengthening is given as:

$$\tau_{SS} = \sum k_j . c_j^n \tag{2.15}$$

The strain-hardening (dislocation strengthening) is given as:

$$\tau_D = \alpha G b \sqrt{\rho} \tag{2.16}$$

In the absence of precipitation, the formula becomes:

$$\sigma_{YS} = \sigma_{GB} + M.\left(\tau_o + \tau_{ss} + \alpha G b\sqrt{\rho}\right) \quad (2.17)$$

EBSD was used to determine Taylor's factor and the dislocation density using the Bishop-Hill calculation method built-in to the EBSD software. TEM was used to determine the dislocation density by stereological analysis of the TEM images. The model was able to predict the strength with accuracies of up to 96% in strain hardened Al-Mg-Cu-Mn alloy. However, it seemed that resolving the dislocation density using the TEM was limited to low strains (0.1-0.4). In addition, the dislocation density estimates by EBSD seemed to be slightly lower than those obtained by the TEM [73]. To apply this model for age-hardenable alloys, TEM was used to determine the size of the precipitates in order to account for τ_{ppt}. Depending on the alloy temper, the precipitates size and type, the particle strengthening mechanism is determined (shearing or by-passing). However, in their work, Starink and Wang considered work-hardened [73] or over-aged cases [86].

2.4.5.b. Deschamps and Bréchet Model

In their model, Deschamps and Bréchet utilised small angle X-ray scattering (SAXS), differential scanning calorimetry (DSC), and TEM to relate the state of the precipitates (e.g. type, size and volume fraction) to the strength [87, 88]. SAXS can be used to estimate the volume fraction and size of the precipitates in a reference specimen of a given condition (e.g. naturally aged with GPB zones). This can be later related to the energy released by dissolving the GPB zones in the DSC. Thus, in a condition containing different types of precipitates (e.g. GPB and S/S' phases), the volume fraction of a specific phase can be determined by comparing its energy release to that in the reference specimen [89].

In the case of shearing (e.g. GPB-zones), $\sigma_{P/S}$ can be given as:

$$\sigma_{P/S} = 0.7M\alpha^{3/2}G\sqrt{r \times F_V / b} \quad (2.18)$$

In the case of by-passing (e.g. S(S') phase in Al-Cu-Mg alloys), $\sigma_{P/B}$ is given as:

$$\sigma_{P/B} = K'G\frac{b}{r}\sqrt{F_V} \quad (2.19)$$

where both *K'* and α are fitted parameters.

The resultant σ_P is computed using a Pythagorean relation such that [87]:

$$\sigma_P = \sqrt{\sigma_{P/S}^2 + \sigma_{P/B}^2} \tag{2.20}$$

Accordingly, the complete structure-property relation can be written as:

$$\sigma_{YS} = \sigma_o + \sigma_{GB} + \sigma_{SS} + \sigma_P \tag{2.21}$$

Deschamps *et al.* [89] showed that this strengthening model can be reliably used to model the complex strength development in 2024-T351 friction stir welds. The model, however, relies on the use of SAXS to determine the precipitate development.

2.5. Microstructural Development during Thermal and Thermomechanical Processes

Microstructural development, associated with the thermal and thermomechanical processes, has received a great deal of attention in metallurgical research during the past century due to its practical importance to the industry (e.g. metalworking processes). During these processes, the material undergoes various microstructural changes that control its properties. Thus, modelling and characterising these phenomena have provided tools for metallurgists to understand, control and 'design' the material structure.

2.5.1. The Deformed Microstructure

2.5.1.a. The Dislocation Stored Energy

When the material is plastically deformed, an amount of the work done is expended as heat, yet a small amount (known as the *stored energy*) is retained inside the material, depending on the processing parameters (i.e. temperature and deformation rate). This energy is due to the generation of crystalline defects such as point defects and dislocations. Based on the dislocation theory, the dislocation density ρ is related to the dislocation stored energy (E) such that [57]:

$$E = \rho \frac{Gb^2 f(\nu)}{4\pi} \ln\left(\frac{R}{R_0}\right) \tag{2.22-a}$$

where R_0 is the inner radius of the dislocation core (taken between b and 5b), R is the outer radius (taken as the inter-dislocation core spacing, $\rho^{-1/2}$), and $f(\nu)$ is a function of Poisson's ratio ($f(\nu)= (1-\nu/2)/(1-\nu)$, considering both screw and edge dislocations.

In the literature [24], this expression is commonly replaced by an approximate expression in the form of:

$$E = \alpha \rho G b^2 \tag{2.22-b}$$

where α is the dislocation interaction parameter, which is of the order of 0.5.

In a plastically deformed material, dislocation density levels are within a range of 10^{15} to 10^{17} dislocations/m^2, which decreases with recovery and recrystallisation to reach ~10^{11} in an annealed material [24, 56]. As discussed in section 2.4, such a variation in the dislocation

density is expected to influence the material strength. Thus, it is necessary to establish techniques to quantify the dislocation density in order to link it with the material strength. Several techniques can be used to quantify the dislocation density in deformed structures, such as DSC, EBSD and TEM [24, 73, 90, 91].

The utilisation of DSC provides an indirect approach to measure the dislocation density by measuring the stored energy released on annealing the specimen in the calorimeter, without concerns about possible artefacts associated with TEM specimen preparation [91]. There are several reports in the literature discussing the utilisation of DSC to measure the dislocation stored energy of deformed pure copper [77, 92, 93], nickel [94, 95], pure iron [96], and aluminium-based alloys [97-103]. The stored energy release in moderately deformed Al-alloys ($\varepsilon = 0.5 - 3$) is only ~0.2-0.5 J/g [102], compared to a release of 30-35 J/g for the precipitation of S'+$\theta''+\theta'$ phases in AA2024 [28]. Thus, it is always a concern that the dislocation stored energy could be overshadowed by other phase transformations during DSC measurements. Typical values for dislocation stored energy measured by DSC are given in Table 2.8.

Table 2.8. Typical stored energy values for different materials measured by DSC

Alloy	Treatment	Peak range	Explanation	Energy release	Source
Pure Al	Torsion (-196 ˚C, strain=6.75)	-40-0 ˚C	Recrystallisation	69.6 J/mol	[24]
Pure Cu	Rolled ($\varepsilon = 0.32$-3.35)	250-450 ˚C	Recrystallisation	10-45 J/mol	[77]
Pure Cu	Rolled ($\varepsilon = 0.5$-1.2)	275-550 ˚C	Recrystallisation	5-30 J/mol	[92]
Cu/Cu-Al	Shock-deformed ($\varepsilon = 0.25$)	275 ˚C	Recrystallisation	7-30 J/mol	[93]
Ni	ECAP, torsion	250-410 ˚C	Recrystallisation	33-345 J/mol	[95]
Pure Ni	Rolled ($\varepsilon = 0.2$-2.5)	400-630 ˚C	Recrystallisation	5-45 J/mol	[94]
Pure Fe	Rolled ($\varepsilon = 0.8$)	400 ˚C	Recrystallisation	15.1 J/mol	[96]
AA1145 DC AA1145 CC	Rolled (85% reduction)	304-419 ˚C 302-432 ˚C	Recrystallisation	11.3 J/mol 22.6 J/mol	[97]
AA1145 AA8011	Rolled ($\varepsilon = 0.22$-1.39)	319-418 ˚C 286-388 ˚C	Recrystallisation	2.3-9.6 J/mol 1.1-13.5 J/mol	[98]
1xxx	Compressed (60% reduction)	400-460 ˚C	Recrystallisation	0.41-0.46 J/g*	[100]
AA5052	ECAP ($\varepsilon = 4$-8)	300-400 ˚C	Recrystallisation	--	[101]
Al-2.5Mg	Rolled ($\varepsilon = 0.1$-3)	120 ˚C 300-450 ˚C	Mg-clusters Recrystallisation	-- 0-0.39 J/g	[102]
Al-7.6Mg	Cryogenic ball milling	100-230 ˚C 370 ˚C	Recovery Recrystallisation	450 J/mol 410 J/mol	[103]
AA1xxx	H19 (extra hard temper)	300-350 ˚C 398 ˚C	Recovery Recrystallisation	-- --	[99]

*J/g = (J/mol)/molar mass in grams

Since the total dislocation stored energy is the sum of the contributions from both ρ_G and ρ_S (defined in section 2.4.4), the relationship between the stored energy (E), strain and grain size can be given as:

$$E = \alpha G b^2 \left(\rho_S + \rho_G\right) \tag{2.23-a}$$

$$E = E_S + K\left(\frac{1}{d}\right) \tag{2.23-b}$$

where E_S is the stored energy due to ρ_S, and K is a strain-dependent constant.

The relationship between the strain, grain size and the stored energy has been studied in a number of reports in nickel and copper [77, 94, 104]. As predicted by equation (2.23), it was found that the finer the grain size is, the higher the total energy at a given strain is, and the lower the recrystallisation temperature is. This is because the energy stored is also the driving force for recrystallisation. Liu and Baker [94, 104] found that the relation between the stored energy and strain in deformed pure copper can be divided into three stages: stage I (ε<0.4-0.9) where the stored energy rapidly increases with the increase in strain; stage II (ε<2-2.5) where the increase becomes slow; and stage III where the stored energy becomes independent of strain. ρ_S was found to increase with the increase in strain, while ρ_G was found to saturate and becomes strain independent in moderate and high strains (>10%).

2.5.1.b. Influence of Intermetallic Particles on the Stored Energy (Two Phase Alloys)

As discussed in section 2.4.4, incoherent non-deformable particles contribute to the dislocation density due to their crystalline incompatibility with the matrix. Few reports have studied the relationship between the presence of intermetallic particles and deformation stored energy [24, 105]. As shown in Fig. 2.19, the existence of particles is expected to increase the dislocation density, depending on the average size and volume fraction of particles. Still, this increase does not lead to a change in the trend between dislocation density and strain observed for non-particle containing alloys. However, these data are only available for low strain deformation ($\varepsilon = 0.1$-3.5).

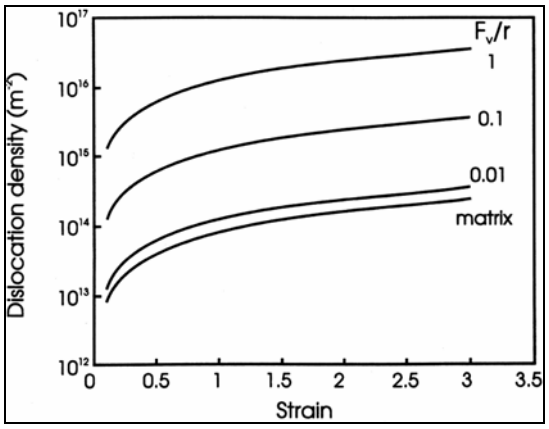

Fig. 2.19. Predicted increase in the total dislocation density as a function of strain in single phase and particle-containing alloys. Estimates are based on a matrix grain size of 100 μm. (F_V is particle volume fraction and r is particle radius) [24]

2.5.2. Recovery

Thermal exposure of deformed materials leads to the modification of the dislocation structure, either by dislocation re-arrangement (*recovery*) or annihilation and creation of a dislocation-free grain microstructure (*recrystallisation*), in order to reach a lower energy configuration [24, 41, 57, 59]. These diffusion-controlled, time and temperature dependent developments are termed *annealing phenomena*, as shown in Fig. 2.20.

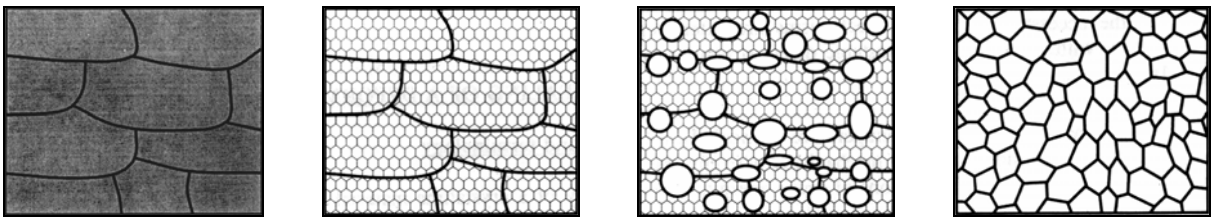

Fig. 2.20. Annealing phenomena, showing the transformation from (a) a deformed microstructure, to (b) a recovered microstructure, followed by (c) initiation of recrystallisation, to (d) a fully recrystallised dislocation-free grain structure [24]

Recovery and recrystallisation are two competing processes in which the dislocations produced during plastic deformation attain a lower energy configuration by annihilating or re-arranging themselves. Depending on the amount of stored energy, temperature, and material

type, deformed materials undergo *recovery* by re-arranging the tangled dislocations into a cellular structure, which later grows into *subgrains* as shown in Fig. 2.21. When recovery happens during deformation, it is called *dynamic recovery* (DRV). Several parameters control the rate and extent of recovery. Recovery depends on the mobility of the dislocations, which depends on the stacking fault energy of the material. In aluminium, rapid dislocation climb and cross slip enhances recovery after deformation due to the high stacking fault energy. Solute atoms and particles also affect recovery due to their interaction with dislocations either during or after deformation.

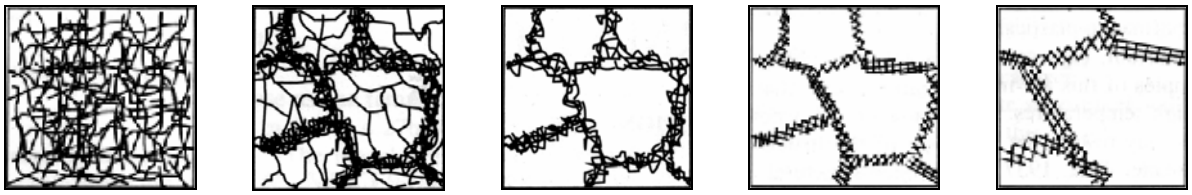

Fig. 2.21. Schematic diagram for the sequence of recovery in a plastically deformed material: (a) tangled dislocations, (b) formations of cells, (c) annihilation of the dislocations inside the cells, (d) subgrain formation, (e) subgrain growth [24]

2.5.2.a. Influence of solute atoms on recovery after deformation

Solute atoms are known to influence recovery and dislocation mobility by pinning the dislocations thus preventing DRV from taking place during deformation. This results in an increase in stored energy, which ultimately enhances *static* recovery after deformation [24]. Among all Al-based alloys, Al-Mg alloys are known to recover most rapidly following deformation [106], and even faster than pure Al [24].

It was reported that the extent of recovery at a given temperature, as measured by electrical resistivity changes, in Al-Mg alloys of different Mg-content (0-1.68 at. %) deformed to the same strain, was found to increase with the increase in the Mg-content [107]. Janecek *et al.* also studied the influence of Mg solute content on post-deformation recovery at room temperature in four CC Al-Mg alloys between 2.2 and 4.18 wt % Mg using TEM. They found that the higher the Mg-content, the greater the dislocation pinning effect, which tended to delay DRV during deformation. In the low Mg alloy (2.2 wt %), a recovered microstructure

showing subgrains was found, with the morphology gradually switching to cells with tangled dislocations with increasing Mg content [108]. Nes [106] cited a two decades long experiment performed in the 1930s-1940s on the influence of deformation and Mg- on recovery rates. Recovery was calculated using the fraction residual strain hardening ($R = \sigma(t) - \sigma_O / \sigma_d - \sigma_O$), where $\sigma(t)$ and σ_d are the instantaneous and as-deformed stress). It showed that the rate of post-deformation recovery at room temperature increases with an increase in Mg content, and a decrease in the amount of cold deformation, Fig. 2.22. A major outcome of this classical experiment is that Al-Mg alloys are typically given a so-called 'stabilising' treatment (H3x temper) by briefly annealing between 120-175 ˚C after deformation to prevent recovery from occurring during operation [4, 106].

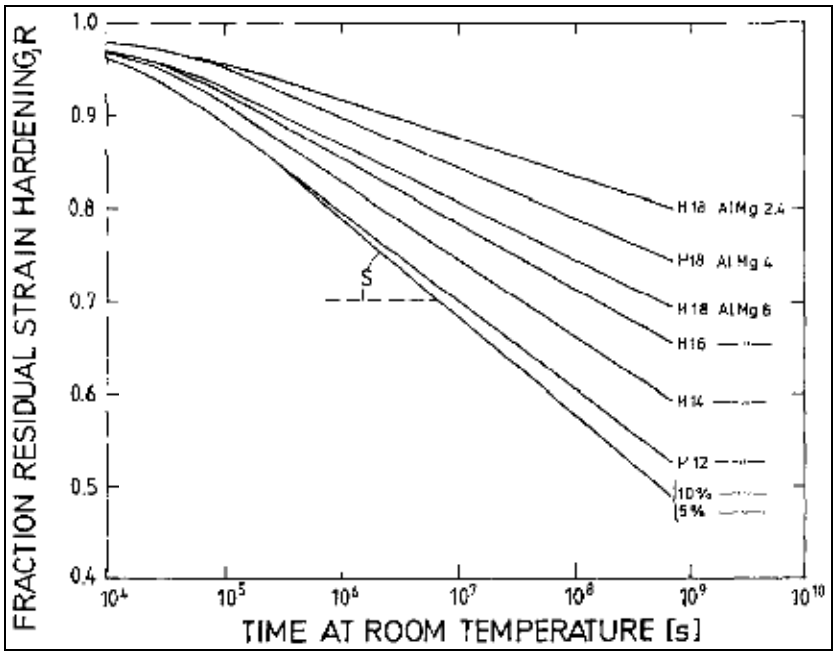

Fig. 2.22. The influence of Mg content and the extent of work hardening on recovery as a function of time at room temperature (H12, H14, H16, and H18: quarter, half, three-quarters and full hard temper designation respectively) [106]

2.5.2.b. Influence of particles on recovery

The influence of particles on recovery has been studied in particulate-reinforced [109], and intermetallic particle-containing (constituent particles or dispersoids) Al-based alloys [110-112]. Ferry and Munroe [109] investigated recovery in Al_2O_3 particulate-reinforced AA2014

metal matrix composite (MMC) compared to a monolithic AA2014 after cold rolling. They showed that the MMC experienced *enhanced recovery* at room temperature following deformation. On annealing at higher temperatures, the rate of recovery in the MMC was rapid compared to the alloy. The existence of particles increased the driving force for recovery by refining the dislocation substructure, especially in the regions surrounding Al_2O_3 particle clusters.

In a different study, Verdier *et al.* [110-112] used the TEM to study the development of dislocation structures during deformation and recovery in two Al-2.5%Mg alloys; one was prepared from a high purity alloy, and the other from commercial purity alloy thus containing Fe-rich dispersoids and particles (150-300 nm in size). The development and the morphology of the dislocation structure were found to be dependent on the purity of the alloy and the presence of dispersoids, yet without influencing the strength development during recovery. At low-strains (ε=0.1), the presence of fine dispersoids in the less-pure alloy delayed the formation of the cellular structures, whereas in the dispersoid-free alloy the dislocations arranged themselves in a channel-like dislocation structure, yet without showing a typical cellular structure [110, 111]. After recovery, the channel-like structure in the dispersoid-free alloy developed into elongated sharp-walled cells. For larger strains (ε=3), both alloys showed a similar wavy dislocation structure, with elongated subgrains. The researchers combined this study with the usage of DSC [102], which led them to determine that the proportionality between dislocation stored energy and strength was only valid at low strains (ε<0.5). They attributed this to the observed formation of a subgrain structure at ε>0.5 [111, 112], which agrees with Hansen's strength model [80-85].

2.5.3. Recrystallisation

Similar to recovery, recrystallisation can occur during deformation, where it is termed *dynamic recrystallisation* (DRX), as opposed to *static* recrystallisation (SRX) which takes place depending on prior storage of energy. Recrystallisation mechanisms can also be classified into *continuous* mechanisms, which happen homogeneously throughout the structure, and *discontinuous* mechanisms, which happen heterogeneously. In Al-based alloys, recrystallisation is strongly influenced by the presence of constituent particles and dispersoids. Due to the crystalline misfit caused by their presence, coarse intermetallic particles (1-10 μm) are surrounded by deformed regions of high stored energy, which provide

a greater driving force for recrystallisation locally (Fig. 2.23). Fine particles (<1 μm) can exert a pinning pressure on the recrystallising grains, controlling their final size [24].

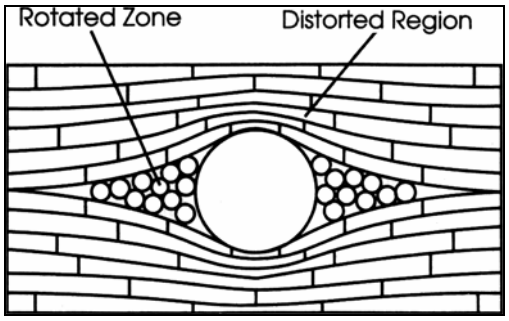

Fig. 2.23. A deformed region surrounding a coarse intermetallic particle in a rolled polycrystal [24]

One recrystallisation mechanism is known as particle stimulated nucleation (PSN); where recrystallisation initiates in a discontinuous manner at locations of high stored energy (e.g. in the vicinity of coarse particles, hence the name). In PSN, sub-boundary migration proceeds to consume the deformation zones surrounding the particle. The condition for PSN to occur is given as:

$$d_g \geq \frac{4\gamma_{GB}}{P_D - P_Z} \tag{2.24}$$

where d_g is the critical particle diameter for PSN, γ_{GB} is the grain-boundary energy between the nucleus and the deformed zone, P_D and P_Z are the deformation stored energy (driving force) for recrystallisation and the retarding force due to particle pinning respectively [24, 113]. Equation 2.24 refers to the competition between two particle influenced mechanisms which happen during recrystallisation, which are PSN and particle pinning of a grain boundary (Zener drag), which retards recrystallisation. The Zener pinning pressure is given as:

$$P_Z = \frac{3 F_V \gamma_{GB}}{d} \tag{2.25}$$

Thus, PSN occurrence necessitates specific microstructural characteristics with respect to the particle distribution and stored energy (i.e. prior deformation) as shown in Fig. 2.24. This is a simplified representation, but it indicates that the transition between PSN and retardation of recrystallisation is bound by the particle characteristics and the extent of strain. It has been found that the boundary between PSN and retardation of recrystallisation corresponds to F_v/d

of 0.1 μm^{-1}, and d should be greater than ~0.8-1 μm. Thus, for a given F_v, an increase in d encourages PSN (i.e. for $F_v/d > 0.1$, recrystallisation is retarded). Yet, for the same F_v/d, an increase in the deformation strain (ε) would incite DRV, which can also retard PSN. This explains the region to the left of the line AB, where the F_v will be insufficient to accelerate PSN. For Al-based alloys, where DRV occurs, line AB will move to the right. However, for materials where DRV does not occur (e.g. copper), line AB will move to the left.

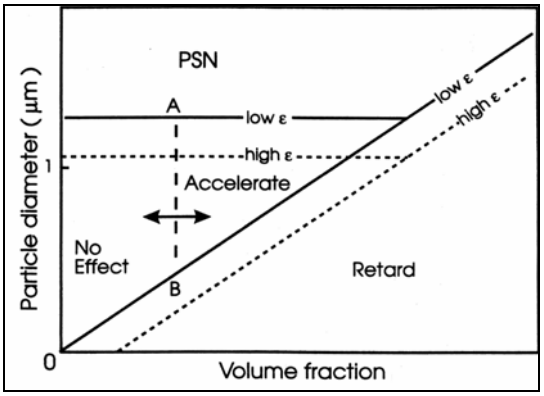

Fig. 2.24. The influence of particle distribution and strain on PSN [24]
(line AB will move to the left for materials with low stacking-fault)

2.5.4. Hot Deformation

DRV and DRX are unique features of hot deformation. Hot deformation processes are usually defined using the Zener-Hollomon parameter (Z), which is a factor of the deformation strain rate ($\dot{\varepsilon}$) and temperature (T) such that:

$$Z = \dot{\varepsilon} \exp(Q/RT) \tag{2.25}$$

2.5.4.a. Dynamic Recovery (DRX)

In high stacking fault materials (e.g. Al-based alloys), rapid dislocation movement encourages DRV, leading to softening. DRV is similar to *static* recovery, whereby dislocations move by climb and cross-slip to re-arrange themselves in a lower-energy configuration, developing a subgrain-structure. The factors that control static recovery (e.g. solute atoms and particles) act in a similar manner for DRV. As shown in Fig. 2.25, a characteristic stress-strain curve for a material undergoing deformation shows an initial stage to a strain ε_m of ~0.5-1 where the

subgrain structure develops, after which the subgrain and dislocation structure almost reaches steady-state, which can be seen in the form of a constant flow stress.

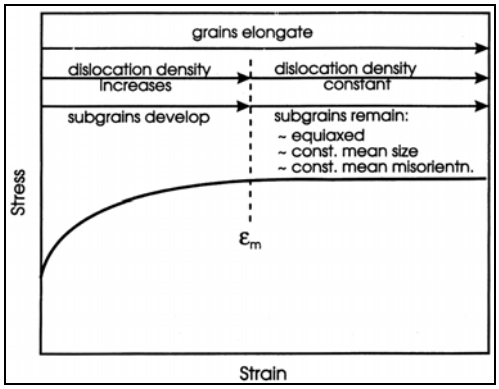

Fig. 2.25. Stress-strain curve for a material being deformed showing the microstructural development associated with DRV, where ε_m is the limit for steady-state [24]

The Z-parameter is considered as an indication of the flow stress during deformation, and thus it was believed to be related to the subgrain size (D_R) using the empirical relation [114]:

$$Z\, D_R^m = \text{constant} \tag{2.25-a}$$

where m is between 0.4 and 1. Derby [114] investigated the validity of the previous relation for a number of metals and minerals, based on which he suggested that D_R is related to the process flow stress (σ) using:

$$\frac{\sigma}{G}\left(\frac{D_R}{b}\right)^{2/3} = K \tag{2.25-b}$$

where K is a constant between 1 and 10.

Sellars [115] also showed that the steady-state flow stress during hot deformation and the recrystallised grain size in different metals show a similar proportionality given by:

$$\sigma \propto D_R^{-n} \tag{2.25-c}$$

where n is a constant between ½ and 1.

2.5.4.b. Dynamic Recrystallisation (DRX)

Depending on the hot deformation parameters, DRX may follow DRV provided that the dislocation level reaches a critical value. DRX involves the recrystallisation of new grains at the old grain boundaries. The process can also happen in a *continuous* or *discontinuous*

manner. In high-stacking fault materials (e.g. Al-alloys), DRX is a *continuous* process which may happen by three different mechanisms: geometric dynamic recrystallisation (GDRX), progressive lattice rotation, and PSN [24, 116].

The first mechanism, GDRX, follows extensive DRV, where grains extensively elongate during deformation, showing serrated boundaries. As deformation continues, the serrated boundaries become closer. Interpenetration and impingement of oppositely serrated boundaries, or bulging of matching serrations (the shaded region in Fig. 2.26-b), takes place, Fig. 2.26. This results in an equiaxed fine grain structure, depending on the amount of flow stress [24, 117]. The second mechanism, progressive lattice rotation, is a strain-induced recrystallisation mechanism, where the subgrains existing near the grain boundaries rotate forming a misorientation gradient from the grain centre to the boundary. This gradient further develops with deformation to high angle grain boundaries. The third mechanism, PSN, occurs in particle-containing alloys (e.g. AA5xxx), where nucleation of recrystallised grains during deformation was also found to initiate near to coarse particles, similar to PSN in SRX.

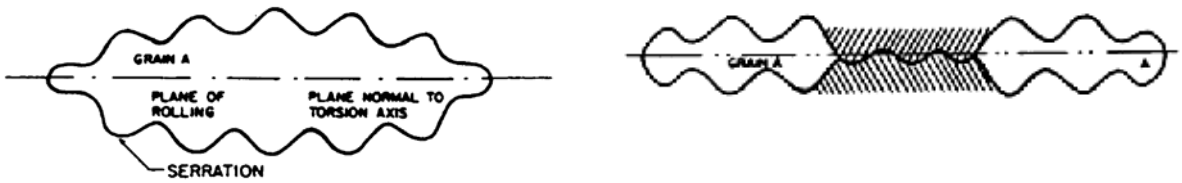

Fig. 2.26. Microstructural development during GDRX showing (b) boundary impingement of (a) oppositely serrated grain boundaries [116]

In materials with low-stacking fault energy, DRX prefers the *discontinuous* (heterogeneous) manner since the process depends on the extent of recovery processes that may take place, which controls the critical subgrain size. Microstructural features that represent the initiation sites for *discontinuous* DRX include, in addition to subgrains, solutes, coarse intermetallic particles, and HAGBs [116].

2.5.4.c. Factors Controlling DRV and DRX

Similar to static recovery and SRX, DRV and DRX are influenced by the solutes and intermetallic particles due to their effect on energy storage during deformation, in addition to the deformation parameters. As shown in Fig. 2.27-a, the increase in the Mg-solute content increased the flow stresses as a function of Z, which will ultimately affect the stored energy, the process kinetics, and the resulting microstructure grain size [118]. This area has not been completely covered as most of the work in the literature deals with pure and low alloying content alloys. Similarly, the particle size and the Zener-Hollomon parameter influence the DRX mechanism, or even recrystallisation after hot deformation, as shown in Fig. 2.27-b. At low temperature and/or high strain rates (i.e. $Z > 10^{12}$), dislocations accumulating at the coarse particles (>1 μm) during deformation can form nucleation sites for recrystallisation. The particle size controls the transition from retardation/pinning to PSN [24, 116, 117, 119, 120]

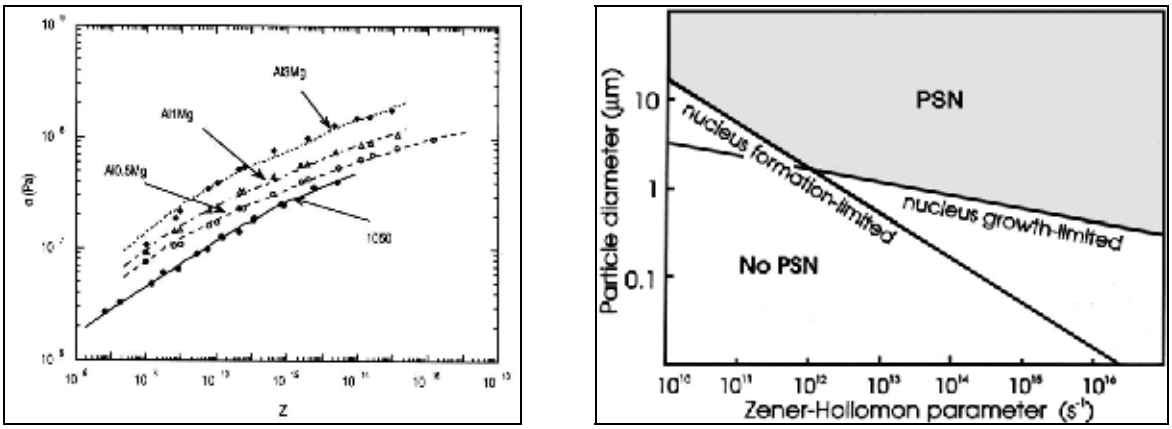

(a) (b)

Fig. 2.27. (a) The influence of solute content on the flow stress development during deformation [118] and (b) the influence of the particle size and Zener-Hollomon parameter on DRX mechanisms [24]

2.5.5. Anisothermal Recrystallisation

In processes with transient thermal cycles (e.g. welding), heating rates can go beyond 100 ˚C/s. Several reports have shown that the interaction between recovery and recrystallisation phenomena appears to be different in anisothermal recrystallisation operations [121-126]. Despite a lack of sufficient studies on Al-alloys [121-123], several reports on anisothermal recrystallisation of steels showed that the recrystallisation temperature and grain size depend

on the heating rate [124, 125]. Ferry and Jones [121] investigated the influence of heating rate on the grain size and recrystallisation behaviour in single phase and particle-containing cold rolled Al-alloys using electrical resistance heating. They found that in particle-containing Al-alloys, the increase in the heating rate (between 100 to 1000 ˚C/s) results in a decrease in the recrystallised grain size, as well as a decrease in the temperature required for complete recrystallisation compared to batch annealing as shown in Fig. 2.28. In a different work, Go *et al.* [122] found that the temperature required to obtain 95% softening ($T_{0.95}$) in cold-rolled 5754 increased with the increase in the heating rate, until a critical heating rate (10 ˚C/s in this case), where any further increase in the heating rate did not affect $T_{0.95}$.

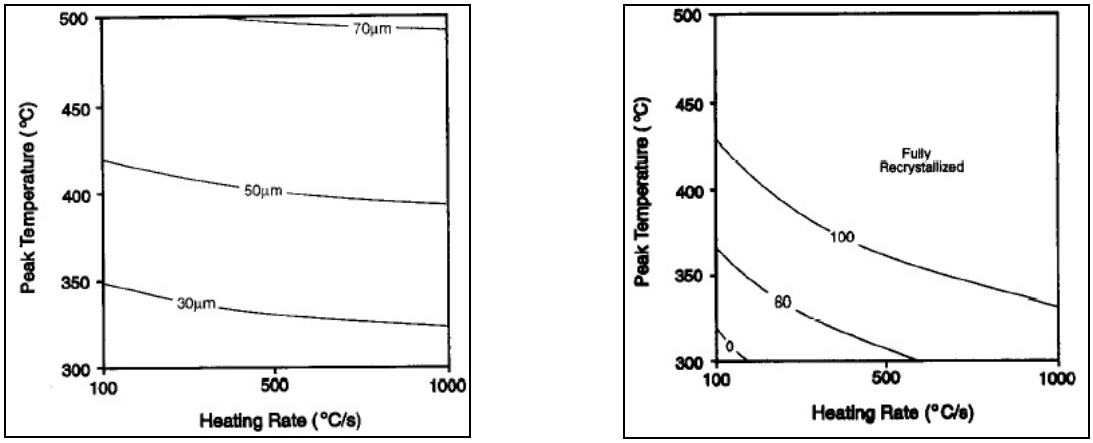

(a) (b)

Fig. 2.28. The influence of heating rate on (a) grain size, and (b) recrystallisation temperature in particle-containing Al-0.8%Si alloy [121]

Atkinson also observed this phenomenon in pure iron and steel, and termed it ultra-rapid annealing (URA) due to the decrease in the recrystallisation temperature associated with higher heating rates [124, 125]. However, Muljono *et al.* carried out a similar study on steels where they found the same heating rate effects on the grain size, but not on the recrystallisation temperature, which led them to describe URA as an experimental artefact [126].

Several attempts were carried out to model the strength development associated with anisothermal recovery and recrystallisation processes. Miller *et al.* [123] suggested a temperature-compensated equivalent time parameter τ which is given as:

$$\tau = t \exp(-Q/RT) \tag{2.26}$$

where *t* is time for full recovery at a constant temperature T. By adding the time parameters of anisothermal operations, it was possible to model the strength development. Go *et al.* [122] also used a similar "effective time" concept to model anisothermal annealing in Al-Mg alloys. Nonetheless, both techniques are empirical methods that require performing several heat treatments at different temperatures and rates to estimate the strength development only during anisothermal operations, without relating it to the microstructural development.

2.6. Summary of Literature: Key Findings and Areas of Investigation

As summarised in this chapter, the structure-property relations and the microstructural development during thermal and thermomechanical processes are among the most studied topics in the physical metallurgy of Al-based alloys. The following points summarise the current state of knowledge, highlighting the areas of further investigation.

- Al-based alloys have a very complex intermetallic particle structure. The particle types formed in a specific alloy is highly dependent on the composition and the thermal treatments experienced following casting. Slight compositional variations or specific heat treatments can be used to favour the formation of a specific particle type (sections 2.1 and 2.2).
- The spatial distribution of the particle structure depends on the casting route (DC versus CC), which also leads to significant microstructural differences in the grain structure and consequently the mechanical properties. These differences result from the difference in cooling rate during casting (section 2.3).
- The strength of Al-based alloys is a resultant of various strengthening contributions: grain-boundary strengthening, solid solution strengthening, particle strengthening, and work-hardening (dislocation strengthening).
- Theoretical understanding and quantitative relationships for the different strengthening mechanisms, except for work hardening, have been established (section 2.4). Ashby's model for work-hardening has been shown to be limited in its application (at high strains and in its consideration of the effects of recovery). However, the model is widely used to estimate dislocation densities. Other models (e.g. Hansen *et al.*) have been recently introduced to quantify dislocation strengthening (section 2.4.4).
- The presence of intermetallic particles has a significant influence on the microstructural development during deformation, thermal and thermomechanical processing. The particles influence the amount of deformation stored energy, which consequently affect recovery and recrystallisation. Several recrystallisation mechanisms are currently well understood (section 2.5). However, the occurrence of recrystallisation due to transient thermal exposures is not completely understood, with the current models failing to accurately synchronously predict the microstructure and strength development (section 2.5).

The work presented in this dissertation studies the microstructure-property development in a solid-state welding process, which is also described as a severe plastic (thermomechanical) deformation process. The following areas have been identified as requiring further study:

- The influence of the processing route condition on the microstructure and strength before and after thermomechanical deformation. In particular commercial alloys need to be assessed as most of the structure-property modelling and microstructural development work has been performed on pure alloys.
- The structure-property development at high strain deformation and the quantification of the microstructural strengthening factors using experimental techniques.
- The influence of the transient thermal exposure on the microstructure and property development.

2.7. References

[1] M. C. Carroll, P. I. Gouma, M. J. Mills, G. S. Daehn, and B. R. Dunbar, "Effects of Zn Additions on the Grain Boundary Precipitation and Corrosion of Al-5083," *Scripta Mater.*, vol. 42, pp. 335-340, 2000.

[2] L. F. Mondolfo, *Aluminum Alloys: Structure and Properties*. London: Butterworth, 1976.

[3] J. R. Davis, *Aluminum and Aluminum Alloys*. Ohio: American Society for Metals (ASM), 1993.

[4] J. E. Hatch, *Aluminum: Properties and Physical Metallurgy*. Ohio: American Society for Metals (ASM), 1984.

[5] E. Anselmino, A. Miroux, and S. van der Zwaag, "Dispersoid quantification and size distribution in hot and cold processed AA3103," *Materials Characterization*, vol. 52, pp. 289-300, 2004.

[6] I. J. Polmear, *Light Alloys: Metallurgy of the Light Metals*. Bristol: St. Edmundsbury Press Ltd., 1995.

[7] W. B. Pearson, *Handbook of Lattice Spacings and Structures of Metals and Alloys*, vol. 2. Oxford: Pergamon Press, 1967.

[8] D. T. L. Alexander and A. L. Greer, "Solid-State Intermetallic Phase Transformations in 3xxx Aluminium Alloys," *Acta Materialia*, vol. 50, pp. 2571-2583, 2002.

[9] Y. J. Li and L. Arnberg, "Evolution of Eutectic Intermetallic Particles in DC-cast AA3003 Alloy during Heating and Homogenization," *Materials Science and Engineering A*, vol. 347, pp. 130-135, 2003.

[10] Y. J. Li and L. Arnberg, "Quantitative Study on the Precipitation Behavior of Dispersoids in DC-cast AA3003 Alloy during Heating and Homogenization," *Acta Materialia*, vol. 51, pp. 3415-3428, 2003.

[11] Y. J. Li and L. Arnberg, "A Eutectoid Phase Transformation for the Primary Intermetallic Particle from Al_m(Fe,Mn) to Al_3(Fe,Mn) in AA5182 Alloy," *Acta Materialia*, vol. 52, pp. 2945-2952, 2004.

[12] Y. J. Li and L. Arnberg, "Solidification Structures and Phase Selection of Iron-Bearing Eutectic Particles in a DC-cast AA5182 Alloy," *Acta Materialia*, vol. 52, pp. 2673-2681, 2004.

[13] F. H. Samuel, A. M. Samuel, H. W. Doty, and S. Valtierra, "Influence of Composition, Sr Modification, and Annealing Treatment on the Structure and Properties of Cast Al-4Pct Mg Alloys," *Metallurgical and Materials Transactions A*, vol. 34A, pp. 115-129, 2003.

[14] E. Balitchev, T. Jantzen, I. Hurtado, and D. Neuschutz, "Thermodynamic Assessment of the Quaternary System Al-Fe-Mn-Si in the Al-Rich Corner," *Computer Coupling of Phase Diagrams and Thermochemistry*, vol. 27, pp. 275-278, 2003.

[15] J. G. Barlock and L. F. Mondolfo, "Structure of Some Aluminium-Iron-Magnesium-Manganese-Silicon Alloys," *Zeitschrift für Metallkunde*, vol. 66, pp. 605-611, 1975.

[16] G. Davignon, A. Serneels, B. Verlinden, and L. Delaey, "An Isothermal Section at 550 °C in the Al-Rich Corner of the Al-Fe-Mn-Si System," *Metallurgical and Materials Transactions A*, vol. 27A, pp. 3357-3361, 1996.

[17] A. L. Dons, "Simulation of Solidification - A Short Cut to a Better Phase Diagram for Al-Mg-Fe-Si Alloys," *Zeitschrift für Metallkunde*, vol. 82, pp. 684-688, 1991.

[18] A. L. Dons, "Superstructures in α-Al(Mn,Fe,Cr)Si," *Zeitschrift für Metallkunde*, vol. 76, pp. 151-153, 1985.

[19] V. Milekhine, M. I. Onsoien, J. K. Solberg, and T. Skaland, "Mechanical properties of FeSi (ε), $FeSi_2$ (ζα) and Mg_2Si," *Intermetallics*, vol. 10, pp. 743-750, 2002.

[20] R. G. Kamat, "AA3104 can-body stock ingot: characterization and homogenization," *JOM*, vol. 48, pp. 34-38, 1996.

[21] P. Ratchev, B. Verlinden, and P. Van Houtte, "Effect of Preheat Temperature on the Orientation Relationship of $(Mn,Fe)Al_6$ Precipitates in an AA5182 Aluminium-Magnesium Alloy," *Acta Materialia*, vol. 43, pp. 621-629, 1995.

[22] P. Yang, O. Engler, and H.-J. Klaar, "Orientation Relationship between Al_6Mn Precipitates and the Al Matrix during Continuous Recrystallization in Al-1.3%Mn," *Journal of Applied Crystallography*, vol. 32, pp. 1105-1118, 1999.

[23] C. B. Fuller, A. R. Krause, D. C. Dunand, and D. N. Seidman, "Microstructure and Mechanical Properties of a 5754 Aluminum Alloy Modified by Sc and Zr Additions," *Materials Science and Engineering A*, vol. 338, pp. 8-16, 2002.

[24] F. J. Humphreys and M. Hatherly, *Recrystallization and Related Annealing Phenomena*. Great Britain: Pergamon, 1995.

[25] W. B. Hutchinson, A. Oscarsson, and A. Karlsson, "Control of microstructure and earing behaviour in aluminium alloy AA 3004 hot bands," *Materials Science and Technology*, vol. 5, pp. 1118-1127, 1989.

[26] M. Warmuzek and A. Gazda, "An Analysis of Cooling Rate Influence on the Sequence of Intermetallic Phases Precipitation in Some Commercial Aluminium Alloys," *Journal of Analytical Atomic Spectrometry*, vol. 14, pp. 535-537, 1999.

[27] W. F. Smith, *Principles of Materials Science and Engineering*, 3rd ed. New York: McGraw-Hill, 1996.

[28] C. Badini, F. Marino, and E. Verne, "Calorimetric study on precipitation path in 2024 alloy and its SiC composite," *Materials Science & Engineering A: Structural Materials: Properties, Microstructure and Processing*, vol. A191, pp. 185-191, 1995.

[29] J. Majimel, G. Molenat, F. Danoix, O. Thuillier, D. Blavette, G. Lapasset, and M. J. Casanove, "High-resolution transmission electron microscopy and tomographic atom probe studies of the hardening precipitation in an Al-Cu-Mg alloy," *Philosophical Magazine*, vol. 84, pp. 3263-3280, 2004.

[30] G. W. Smith, W. J. Baxter, and R. K. Mishra, "Precipitation in 339 and 2124 aluminum: a caveat for calorimetry," *Journal of Materials Science*, vol. 35, pp. 3871-3880, 2000.

[31] S. C. Wang and M. J. Starink, "Precipitates and intermetallic phases in precipitation hardening Al-Cu-Mg-(Li) based alloys," *International Materials Reviews*, vol. 50, pp. 193-215, 2005.

[32] S. C. Wang, M. J. Starink, and N. Gao, "Precipitation hardening in Al-Cu-Mg alloys revisited," *Scripta Materialia*, vol. 54, pp. 287-291, 2006.

[33] A. M. Zahra, C. Y. Zahra, and M. Dumont, "Effects of Ag or Si on precipitation in the alloy Al-2.5 mass% Cu-1.5 mass% Mg," *Philosophical Magazine*, vol. 85, pp. 3735-3754, 2005.

[34] H. R. Shercliff, M. J. Russell, A. Taylor, and T. L. Dickerson, "Microstructural modelling in friction stir welding of 2000 series aluminium alloys," *Mecanique & Industries*, vol. 6, pp. 25-35, 2005.

[35] B. Q. Li, "Producing thin strips by twin-roll casting - part I: process aspects and quality issues," *JOM*, vol. 47, pp. 29-33, 1995.
[36] R. E. J. Sanders, "Technology Innovation in Aluminum Products," *JOM*, vol. 53, pp. 21-25, 2001.
[37] X. F. Yu, Y. M. Zhao, X. Y. Wen, and T. Zhai, "A study of mechanical isotropy of continuous cast and direct chill cast AA5182 Al alloys," *Materials Science and Engineering A*, vol. 394, pp. 376-384, 2005.
[38] D. Eskin, Q. Du, D. Ruvalcaba, and L. Katgerman, "Experimental study of structure formation in binary Al-Cu alloys at different cooling rates," *Materials Science and Engineering A*, vol. 405, pp. 1-10, 2005.
[39] M. Slamova, M. Karlik, F. Robaut, P. Slama, and M. Veron, "Differences in microstructure and texture of Al-Mg sheets produced by twin-roll continuous casting and by direct-chill casting," *Materials Characterization*, vol. 49, pp. 231-240, 2002.
[40] Y. M. Zhao, W. Wen, and J. G. Morris, "The differences in particle structures and recrystallization behaviors between DC and CC AA5052 aluminum alloys," *Materials Science and Engineering A*, vol. 373, pp. 167-174, 2004.
[41] R. E. Reed-Hill and R. Abbaschian, *Physical Metallurgy Principles*, 3rd ed. Boston: PWS-Kent Publishing Company, 1992.
[42] Y. L. Liu and S. B. Kang, "Solidification and segregation of Al-Mg alloys and influence of alloy composition on cooling rate," *Materials Science and Technology*, vol. 13, pp. 331-336, 1997.
[43] A. M. Glenn, S. P. Russo, J. D. Gorman, and P. J. K. Paterson, "The effect of grain refining on the microsegregation of aluminium-magnesium alloy 5182," *Micron*, vol. 32, pp. 841-850, 2001.
[44] C. J. Vreeman, M. J. M. Krane, and F. P. Incropera, "Effect of free-floating dendrites and convection on macrosegregation in direct chill cast aluminum alloys. Part I: Model development," *International Journal of Heat and Mass Transfer*, vol. 43, pp. 677-686, 2000.
[45] S. Kalpakjian, *Manufacturing Processes for Engineering Materials*, 3rd ed. California: Addison Wesley Longman, Inc., 1997.
[46] A. V. Reddy and C. Beckermann, "Modeling of Macrosegregation Due to Thermosolutal Convection and Contraction-Driven Flow in Direct Chill Continuous Casting of an Al-Cu Round Ingot," *Metallurgical and Materials Transactions B: Process Metallurgy and Materials Processing Science*, vol. 28, pp. 479-489, 1997.
[47] Q. Du, D. G. Eskin, and L. Katgerman, "Modeling Macrosegregation during Direct-Chill Casting of Multicomponent Aluminum Alloys," *Metallurgical and Materials Transactions A (Physical Metallurgy and Materials Science)*, vol. 38A, pp. 180-189, 2007.
[48] H. Yu and D. A. Granger, "Macrosegregation in aluminum alloy ingot cast by the semicontinuous direct chill (DC) method," presented at Aluminum Alloys: Their Physical and Mechanical Properties, EMAS, UK, 1986.
[49] X.-M. Cheng and J. G. Morris, "Texture, microstructure and formability of SC and DC cast Al-Mg alloys," *Materials Science and Engineering A*, vol. 323, pp. 32-41, 2002.
[50] W. C. Liu, T. Zhai, and J. G. Morris, "Comparison of recrystallization and recrystallization textures in cold-rolled DC and CC AA 5182 aluminum alloys," *Materials Science and Engineering A*, vol. 358, pp. 84-93, 2003.
[51] A. Baldacci, A. Bigot, H. Klocker, and J. H. Driver, "Constituent particle break-up during hot rolling of AA 5182," presented at Hot Deformation of Aluminum Alloys III, San Diego, CA, USA, 2003.

[52] A. L. Dons, "The Alstruc homogenization model for industrial aluminum alloys," *Journal of Light Metals*, vol. 1, pp. 133-149, 2001.

[53] J. Liu and J. G. Morris, "Recrystallization microstructures and textures in AA 5052 continuous cast and direct chill cast aluminum alloy," *Materials Science and Engineering A*, vol. 385, pp. 342-351, 2004.

[54] J. G. Morris and W. C. Liu, "Al alloys: The influence of concurrent precipitation on recrystallization behavior, kinetics, and texture," *JOM*, vol. 57, pp. 44-47, 2005.

[55] Y. H. Zhao, X. Z. Liao, Z. Jin, R. Z. Valiev, and Y. T. Zhu, "Microstructures and mechanical properties of ultrafine grained 7075 Al alloy processed by ECAP and their evolutions during annealing," *Acta Materialia*, vol. 52, pp. 4589-4599, 2004.

[56] R. W. Hertzberg, *Deformation and Fracture Mechanics of Engineering Materials*, 4 ed. USA: John Wiley & Sons Inc., 1996.

[57] R. W. K. Honeycombe, *The Plastic Deformation of Metals*, 2nd ed. London: Eward Arnold, 1984.

[58] A. Kelly and R. B. Nicholson, "Strengthening Methods in Crystals." Amsterdam: Elsevier Publishing Company Ltd., 1971.

[59] D. Peckner, "The Stengthening of Metals." New York: Reinhold Publishing Corporation, 1964.

[60] J. D. Embury, "Strengthening by Dislocation Substructures," in *Strengthening Methods in Crystals*, A. Kelly and R. B. Nicholson, Eds. Amsterdam: Elsevier Publishing Company Ltd., 1971.

[61] D. J. Lloyd and S. A. Court, "Influence of grain size on tensile properties of Al-Mg alloys," *Materials Science and Technology*, vol. 19, pp. 1349-1354, 2003.

[62] G. B. Burger, A. K. Gupta, P. W. Jeffrey, and D. J. Lloyd, "Microstructural control of aluminum sheet used in automotive applications," *Materials Characterization*, vol. 35, pp. 23-39, 1995.

[63] S. A. Court, K. M. Gatenby, and D. J. Lloyd, "Factors affecting the strength Al-3 and formability of alloys based on wt.% Mg," *Materials Science & Engineering A: Structural Materials: Properties, Microstructure and Processing*, vol. A319-321, pp. 443-447, 2001.

[64] H. Jin and D. J. Lloyd, "Effect of a duplex grain size on the tensile ductility of an ultra-fine grained Al-Mg alloy, AA5754, produced by asymmetric rolling and annealing," *Scripta Materialia*, vol. 50, pp. 1319-1323, 2004.

[65] M. Furukawa, Z. Horita, M. Nemoto, R. Z. Valiev, and T. G. Langdon, "Microhardness measurements and the Hall-Petch relationship in an Al-Mg alloy with submicrometer grain size," *Acta Materialia*, vol. 44, pp. 4619-4629, 1996.

[66] M. Furukawa, Y. Iwahashi, Z. Horita, M. Nemoto, N. K. Tsenev, R. Z. Valiev, and T. G. Langdon, "Structural evolution and the Hall-Petch relationship in an Al-Mg-Li-Zr alloy with ultra-fine grain size," *Acta Materialia*, vol. 45, pp. 4751-4757, 1997.

[67] H. Hasegawa, S. Komura, A. Utsunomiya, Z. Horita, M. Furukawa, M. Nemoto, and T. G. Langdon, "Thermal stability of ultrafine-grained aluminum in the presence of Mg and Zr additions," *Materials Science & Engineering A: Structural Materials: Properties, Microstructure and Processing*, vol. A265, pp. 188-196, 1999.

[68] J. Wang, Y. Iwahashi, Z. Horita, M. Furukawa, M. Nemoto, R. Z. Valiev, and T. G. Langdon, "Investigation of microstructural stability in an Al-Mg alloy with submicrometer grain size," *Acta Materialia*, vol. 44, pp. 2973-2982, 1996.

[69] A. Gholinia, F. J. Humphreys, and P. B. Prangnell, "Production of ultra-fine grain microstructures in Al-Mg alloys by coventional rolling," *Acta Materialia*, vol. 50, pp. 4461-4476, 2002.

[70] J. S. Hayes, R. Keyte, and P. B. Prangnell, "Effect of grain size on tensile behaviour of a submicron grained Al-3 wt-%Mg alloy produced by severe deformation," *Materials Science and Technology*, vol. 16, pp. 1259-1263, 2000.

[71] M. A. Munoz-Morris, C. Garcia Oca, and D. G. Morris, "Mechanical behaviour of dilute Al-Mg alloy processed by equal channel angular pressing," *Scripta Materialia*, vol. 48, pp. 213-218, 2003.

[72] K. L. Kendig and D. B. Miracle, "Strengthening mechanisms of an Al-Mg-Sc-Zr alloy," *Acta Materialia*, vol. 50, pp. 4165-4175, 2002.

[73] S. C. Wang, Z. Zhu, and M. J. Starink, "Estimation of dislocation densities in cold rolled Al-Mg-Cu-Mn alloys by combination of yield strength data, EBSD and strength models," *Journal of Microscopy*, vol. 217, pp. 174-178, 2005.

[74] G. J. Mahon and G. J. Marshall, "Microstructure-property relationships in O-temper foil alloys," *JOM*, vol. 48, pp. 39-42, 1996.

[75] Y. A. Filatov, V. I. Yelagin, and V. V. Zakharov, "New Al-Mg-Sc alloys," *Materials Science and Engineering A*, vol. 280, pp. 97-101, 2000.

[76] M. F. Ashby, "The Deformation of Plastically Non-Homogeneous Alloys," in *Strengthening Methods in Crystals*, A. Kelly and R. B. Nicholson, Eds. Amsterdam: Elsevier Publishing Company Ltd., 1971.

[77] D. Mandal and I. Baker, "Measurement of the energy of grain boundary geometrically-necessary dislocations in copper," *Scripta Metallurgica et Materialia*, vol. 33, pp. 831-836, 1995.

[78] H. Fujita and T. Tabata, "Effect of Grain Size and Deformation Sub-Structur eon Mechanical Properties of Polycrystalline Aluminum," *Acta Metallurgica*, vol. 21, pp. 355-365, 1973.

[79] A. W. Thompson, M. I. Baskes, and W. F. Flanagan, "The dependence of polycrystal work hardening on grain size," *Acta Metallurgica*, vol. 21, pp. 1017-1028, 1973.

[80] J. R. Bowen, P. B. Prangnell, D. J. Jensen, and N. Hansen, "Microstructural parameters and flow stress in Al-0.13% Mg deformed by ECAE processing," *Materials Science and Engineering A*, vol. 387-389, pp. 235-239, 2004.

[81] N. Hansen, "Effect of Grain Size and Strain on the Tensile Flow Stress of Aluminium at Room Temperature," *Acta Metallurgica*, vol. 25, pp. 863-869, 1977.

[82] N. Hansen, "Hall-petch relation and boundary strengthening," *Scripta Materialia*, vol. 51, pp. 801-806, 2004.

[83] N. Hansen, "Boundary strengthening in undeformed and deformed polycrystals," *Materials Science and Engineering A*, vol. 409, pp. 39-45, 2005.

[84] N. Hansen, X. Huang, R. Ueji, and N. Tsuji, "Structure and strength after large strain deformation," *Materials Science and Engineering A*, vol. 387-389, pp. 191-194, 2004.

[85] D. A. Hughes and N. Hansen, "High angle boundaries formed by grain subdivision mechanisms," *Acta Materialia*, vol. 45, pp. 3871-3886, 1997.

[86] M. J. Starink and S. C. Wang, "A model for the yield strength of overaged Al-Zn-Mg-Cu alloys," *Acta Materialia*, vol. 51, pp. 5131-5150, 2003.

[87] A. Deschamps and Y. Brechet, "Influence of predeformation and agEing of an Al-Zn-Mg alloy--II. Modeling of precipitation kinetics and yield stress," *Acta Materialia*, vol. 47, pp. 293-305, 1998.

[88] A. Deschamps, F. Livet, and Y. Brechet, "Influence of predeformation on ageing in an Al-Zn-Mg alloy--I. Microstructure evolution and mechanical properties," *Acta Materialia*, vol. 47, pp. 281-292, 1998.

[89] C. Genevois, A. Deschamps, A. Denquin, and B. Doisneau-cottignies, "Quantitative investigation of precipitation and mechanical behaviour for AA2024 friction stir welds," *Acta Materialia*, vol. 53, pp. 2447-2458, 2005.

[90] F. J. Humphreys, "Grain and subgrain characterisation by electron backscatter diffraction," *Journal of Materials Science*, vol. 36, pp. 3833-3854, 2001.

[91] M. J. Starink, "Analysis of aluminium based alloys by calorimetry: Quantitative analysis of reactions and reaction kinetics," *International Materials Reviews*, vol. 49, pp. 191-226, 2004.

[92] D. Mandal and I. Baker, "Determination of the stored energy and recrystallization temperature as a function of depth after rolling of polycrystalline copper," *Scripta Metallurgica et Materialia*, vol. 33, pp. 645-650, 1995.

[93] A. Rohatgi and K. S. Vecchio, "The variation of dislocation density as a function of the stacking fault energy in shock-deformed FCC materials," *Materials Science and Engineering A*, vol. 328, pp. 256-266, 2002.

[94] I. Baker, L. Liu, and D. Mandal, "The effect of grain size on the stored energy of cold work as a function of strain for polycrystalline nickel," *Scripta Metallurgica et Materialia*, vol. 32, pp. 167-171, 1995.

[95] A. P. Zhilyaev, G. V. Nurislamova, S. Surinach, M. D. Baro, and T. G. Langdon, "Calorimetric measurements of grain growth in ultrafine-grained nickel," *Materials Physics and Mechanics*, vol. 5, pp. 23-30, 2002.

[96] F. Scholz, J. H. Driver, and E. Woldt, "The stored energy of cold rolled ultra high purity iron," *Scripta Materialia*, vol. 40, pp. 949-954, 1999.

[97] C. Garcia-Cordovilla and E. Louis, "Differential Scanning Calorimetry Study of Recovery and Recrystallization in a Commercial Al-Fe-Si Alloy (AA1145)," *Scripta Metallurgica*, vol. 18, pp. 549-553, 1984.

[98] C. Garcia-Cordovilla and E. Louis, "A differential scanning calorimetry study of recrystallization and its interaction with precipitation in Al-Fe-Si commercial alloys (AA1145 and AA8011)," *Journal of Materials Science*, vol. 21, pp. 971-979, 1986.

[99] W. H. Hildebrandt, "Differential Scanning Calorimetry Evaluations of Recrystallization Behavior in Aluminum Sheet," *Metallurgical Transactions A (Physical Metallurgy and Materials Science)*, vol. 10A, pp. 1045-1048, 1979.

[100] J. Lendvai, G. Honyek, A. Juhasz, and I. Kovacs, "Differential Scanning Calorimetry Study of the Release of Stored Energy in an Al-Fe Alloy," *Scripta Metallurgica*, vol. 19, pp. 943-946, 1985.

[101] T. L. Tsai, P. L. Sun, P. W. Kao, and C. P. Chang, "Microstructure and tensile properties of a commercial 5052 aluminum alloy processed by equal channel angular extrusion," *Materials Science and Engineering A*, vol. 342, pp. 144-151, 2003.

[102] M. Verdier, I. Groma, L. Flandin, J. Lendvai, Y. Brechet, and P. Guyot, "Dislocation densities and stored energy after cold rolling of Al-Mg alloys: Investigations by resistivity and differential scanning calorimetry," *Scripta Materialia*, vol. 37, pp. 449-454, 1997.

[103] F. Zhou, X. Z. Liao, Y. T. Zhu, S. Dallek, and E. J. Lavernia, "Microstructural evolution during recovery and recrystallization of a nanocrystalline Al-Mg alloy prepared by cryogenic ball milling," *Acta Materialia*, vol. 51, pp. 2777-2791, 2003.

[104] L. Liu and I. Baker, "Dependence of recrystallization temperature and stored energy on rolling strain in polycrystalline copper," *Scripta Metallurgica et Materialia*, vol. 28, pp. 197-200, 1993.

[105] D. Mandal and I. Baker, "On the effect of fine second-phase particles on primary recrystallization as a function of strain," *Acta Materialia*, vol. 45, pp. 453-461, 1997.

[106] E. Nes, "Recovery revisited," *Acta Metallurgica et Materialia*, vol. 43, pp. 2189-2207, 1995.
[107] C. Panseri, F. Gatto, and T. Federighi, "Interaction between solute magnesium atoms and vacancies in aluminium," *Acta Metallurgica*, vol. 6, pp. 198-204, 1958.
[108] M. Janecek, M. Slamova, and M. Hajek, "Structural transformations in continuously cast Al-Mg alloys," *Journal of Alloys and Compounds*, vol. 378, pp. 316-321, 2004.
[109] M. Ferry and P. R. Munroe, "Enhanced recovery in a particulate-reinforced aluminium composite," *Materials Science and Engineering A*, vol. 358, pp. 142-151, 2003.
[110] M. Verdier, F. Bley, M. Janecek, F. Livet, J. P. Simon, and Y. Brechet, "Characterization of dislocation structures and internai stresses in Al-Mg alloys during recovery by synchrotron radiation," *Materials Science and Engineering A*, vol. 234-236, pp. 258, 1997.
[111] M. Verdier, Y. Brechet, and P. Guyot, "Recovery of AlMg alloys: flow stress and strain-hardening properties," *Acta Materialia*, vol. 47, pp. 127-134, 1999.
[112] M. Verdier, M. Janecek, Y. Brechet, and P. Guyot, "Microstructural evolution during recovery in Al-2.5%Mg alloys," *Materials Science and Engineering A*, vol. 248, pp. 187-197, 1998.
[113] K. Marthinsen, O. Daaland, T. Furu, and E. Nes, "The spatial distribution of nucleation sites and its effect on recrystallization kinetics in commercial aluminum alloys," *Metallurgical and Materials Transactions A: Physical Metallurgy and Materials Science*, vol. 34, pp. 2705-2715, 2003.
[114] B. Derby, "The dependence of grain size on stress during dynamic recrystallisation," *Acta Metallurgica et Materialia*, vol. 39, pp. 955-962, 1991.
[115] C. M. Sellars and Q. Zhu, "Microstructural modelling of aluminium alloys during thermomechanical processing," *Materials Science and Engineering A*, vol. 280, pp. 1-7, 2000.
[116] R. D. Doherty, D. A. Hughes, F. J. Humphreys, J. J. Jonas, D. J. Jensen, M. E. Kassner, W. E. King, T. R. McNelley, H. J. McQueen, and A. D. Rollett, "Current issues in recrystallization: a review," *Materials Science and Engineering A*, vol. 238, pp. 219-274, 1997.
[117] H. Jazaeri and F. J. Humphreys, "The transition from discontinuous to continuous recrystallization in some aluminium alloys: II - annealing behaviour," *Acta Materialia*, vol. 52, pp. 3251-3262, 2004.
[118] E. Nes, K. Marthinsen, and B. Ronning, "Modelling the evolution in microstructure and properties during processing of aluminium alloys," *Journal of Materials Processing Technology*, vol. 117, pp. 333-340, 2001.
[119] H. Jazaeri and F. J. Humphreys, "The transition from discontinuous to continuous recrystallization in some aluminium alloys: I - the deformed state," *Acta Materialia*, vol. 52, pp. 3239-3250, 2004.
[120] H. J. McQueen, "Elevated-temperature deformation at forming rates of $10^{-2}$to 10^{2} s^{-1}," *Metallurgical and Materials Transactions A: Physical Metallurgy and Materials Science*, vol. 33, pp. 345-362, 2002.
[121] M. Ferry and D. Jones, "High-rate annealing of single-phase and particle-containing aluminium alloys," *Scripta Materialia*, vol. 38, pp. 177-183, 1997.
[122] J. Go, W. J. Poole, M. Militzer, and M. A. Wells, "Modelling recovery and recrystallisation during annealing of AA 5754 aluminium alloy," *Materials Science and Technology*, vol. 19, pp. 1361-1368, 2003.
[123] W. S. Miller, A. Burger, D. Sampath, and M. R. van der Winden, "Temperature compensated time concept as a tool for the modelling of aluminium alloys," *Materials Science Forum*, vol. 331, pp. 757-762, 2000.

[124] M. Atkinson, "Bifurcation of thermal restoration processes in deformed iron and steel," *Materials Science and Engineering A*, vol. 262, pp. 33-38, 1999.
[125] M. Atkinson, "On the credibility of ultra rapid annealing," *Materials Science and Engineering A*, vol. 354, pp. 40-47, 2003.
[126] D. Muljono, M. Ferry, and D. P. Dunne, "Influence of heating rate on anisothermal recrystallization in low and ultra-low carbon steels," *Materials Science and Engineering A*, vol. 303, pp. 90-99, 2001.

Chapter 3

FRICTION STIR WELDING PROCESS MODELLING & MICROSTRUCTURE

Friction Stir Welding (FSW) is a new solid-state welding technique that was invented at the Welding Institute (TWI) in 1991 [1]. Joining takes place by means of a non-consumable rotating shouldered tool with a threaded or fluted-pin to provide a combination of frictional heating by the tool shoulder, and stirring of the plasticised material by the pin along the joint line, Fig. 3.1.

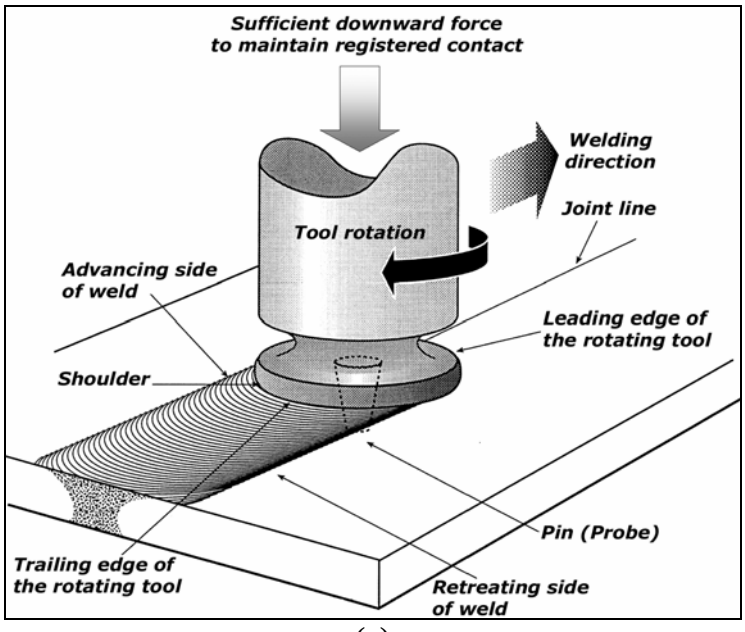

(a)

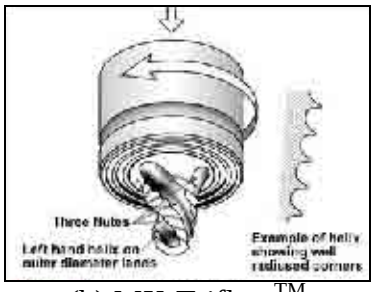

(b) MX-Triflute™

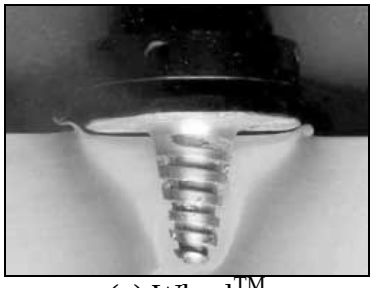

(c) Whorl™

Fig. 3.1. Schematic diagram for FSW process and tool designs [2, 3]

The process has demonstrated immense success with joining difficult-to-weld Al-based alloys due to the localised thermal field provided by the tool which minimises the loss in mechanical properties, compared to fusion welding processes [3]. The solid-state joining technique also provides a better joint quality due to the lack of liquation, cracking, or porosity. FSW has also been successfully applied to stainless steels and other non-ferrous alloys (e.g. Ti, Mg, Cu, Ni, composites, thermoplastics, and dissimilar metals), but has not yet been commercialised at the same level as Al-based alloys. Possible weld positions include: butt, lap, edge, contour and T-welds [2].

3.1. Classification of Weld Zones

welds exhibit a unique morphology of the weld zones that differs from the zones in fusion welds due to the absence of a fusion zone. There are two classifications for the weld zones. The first (Threadgill's classification, [4]) is based on the microstructural zones, while the second (Arbegast's classification, [5]) is based on the processing history of the weld zones during FSW. Both nomenclatures were developed for Al-based alloys; however they are generally applicable to other alloys as well.

3.1.1. Threadgill's Classification

Threadgill [4] has classified welds into four microstructural zones, which are: a weld nugget (WN), a thermomechanically affected zone (TMAZ), a heat affected zone (HAZ), beyond which the unaffected basemetal (BM exists) as shown in Fig. 3.2. The WN refers to the region previously occupied by the tool pin. In the literature, this region is sometimes referred to as the stirred zone (STZ) [6]. The extent of the TMAZ is the trapezoidal region whose bases are the shoulder diameter and the pin diameter, including regions C and D in Fig. 3.2. The stirring action experienced within the TMAZ/WN during FSW leads to the formation of dynamically recrystallised grains in D and plastically deformed or partially recrystallised grains in C. Beyond the TMAZ, a typically narrow HAZ exists, where only a diminishing thermal-field is experienced until reaching the unaffected BM.

Because of the rotation direction of the tool, the weld morphology appears asymmetric between the advancing side (AS) to the retreating side (RS). Towards the AS, where the traverse speed and the tangential velocity component of the rotating tool are in the same

direction, the TMAZ/HAZ boundary appears sharper compared to the RS where the boundary is more diffuse. Other features include an extended flow arm from the WN towards the AS, and concentric circles within the WN, generally at the bottom (lower half) of the sheet, referred to as onion rings as shown in Fig. 3.3.

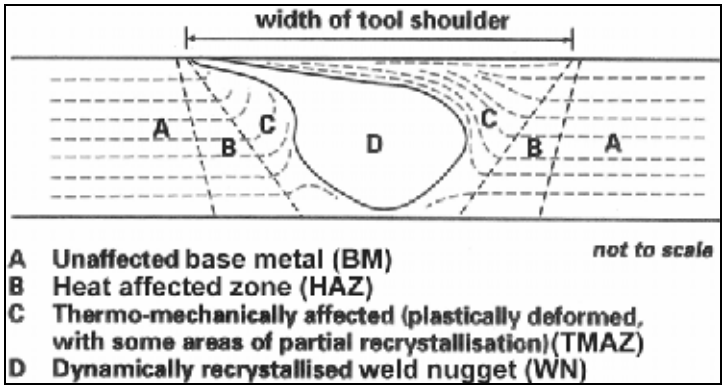

Fig. 3.2. Typical microstructural zones in Al-based alloys (advancing side to the left) [4]

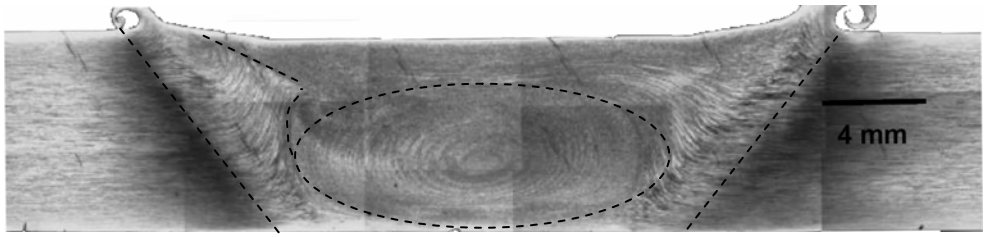

Fig. 3.3. Macrograph of AA2195 weld showing the onion rings structure and the TMAZ [7]

3.1.2. Arbegast's Classification

As shown in Fig. 3.4, Arbegast classified the weld along the feed direction into five zones: a) preheat, b) initial deformation, c) extrusion, d) forging, and e) cool down zones. This classification is based on the suggestion that FSW is an extrusion process, as also suggested in several reports [7, 8].

In the preheat zone, the temperature increases due to the moving thermal field surrounding the tool, which is stronger at the top due to shoulder friction. Close to the tool, an initial deformation zone forms because of the stress (P_{max}) which is caused by the moving tool and the high temperature. The softened material is forced to flow around the tool in the extrusion

zone where it gets extruded between the pin threads, with a small amount trapped below the tool in the vortex swirl zone. Behind the tool, the stirred material from the front is deposited in the forging zone, and cool down zone. The widths of the zones depend on the process parameters and thermal and thermomechanical properties of the material being welded [5]. This classification clarifies the influence of the moving thermal field in softening the material in front of the tool prior to stirring, as well as the cooling of the region behind the tool. However, since the characterisation of the weld microstructural zones is mostly performed on the weld face, Threadgill's classification will be used in this report, with references to Arbegast's notation when discussing the microstructural development ahead to the moving tool.

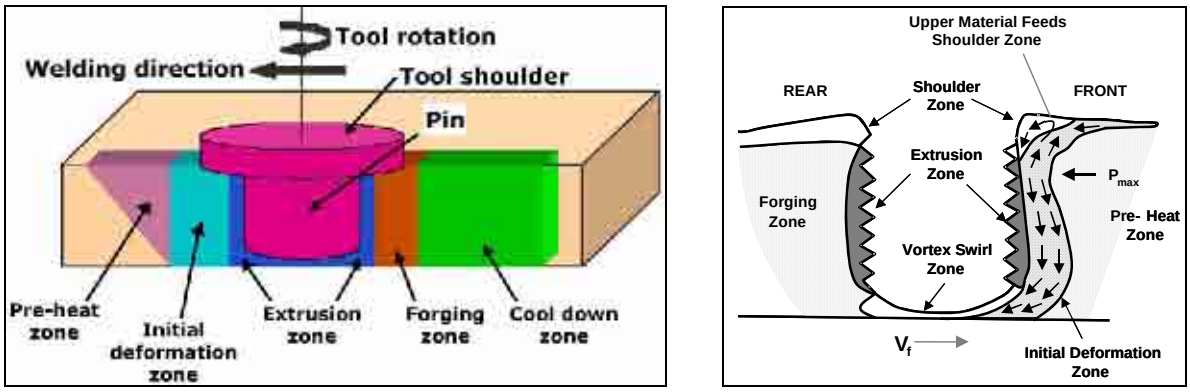

Fig. 3.4. Arbegast's classification of (a) the processing zones during FSW, and (b) the deformation zone surrounding a tool moving with speed V_f, against a pressure of P_{max} [5]

3.2. Influence of Process Parameters on the Temperature Distribution

The process is primarily controlled by two machine-related parameters: the tool rotation speed (N, rpm) and the feed rate (*f*, mm/min). The normal Z-axis force (F_N, N) is another controlling parameter, yet this depends on whether the process is carried out using a *force-controlled* (self-adjustable constant force) or *position-controlled* machine. Another parameter is the tool tilt angle. The tool/spindle is usually tilted by 1-4.5˚ degrees to the feed direction to force the plasticised material to flow from the front to the back and be deposited uniformly behind the tool. Other secondary parameters include: 'environmental' parameters, such as: *in-situ* and post-weld cooling and heating of the workpiece/anvil, and 'practice' parameters, such as: the plunge depth, pin length, plasticising dwell time (after the initial plunging), and plunging position (from the sheet edge) [2, 9]. Several studies have examined the influence of the welding parameters on the spatial temperature distribution and the maximum temperature (T_{max}) using embedded thermocouples [9-13] as summarised in Table 3.1.

Table 3.1. Summary of the thermocouple measurement studies in welds of Al-based alloys

Material	Plate thickness (mm)	Rotation speed (rpm)	Feed rate (mm/min)	Sp. Dist.*	Para. St.**	T_{max} (˚C)	Reference
6061-T6	6.4	300-1200	120	√	√	425-475	Tang *et al.* [13]
7075-T651	6.35	-	-	√	-	475	Mahoney *et al.* [10]
1100-H24 6063-T5	4	500-3600 800-3600	132 360	-	√	400-525 385-533	Sato *et al.* [11, 12]
7075-T7351	9.53	300, 500	102, 203	-	√	460-515	Record *et al.* [9]

* Sp.Dist.: Spatial temperature distribution study, ** Para.St. Parametric study

Concerning the spatial temperature distribution in the weld, Mahoney *et al.* [10] indicated that the temperature within the weld reached a maximum of 475 ˚C below the shoulder, decreasing downwards and away from the WN in 7075-T651 weld, Fig. 3.5. Investigating the influence of the rotation speed on the spatial distribution, Tang *et al.* [13] reported a T_{max} range of 425 to 475 ˚C as the rotation speed is increased from 300 to 1000 rpm in 6061-T6 weld welded using a tool of 20 mm and 6.5 mm shoulder and pin diameters respectively. The temperature was found to drop from T_{max} to ~340-375 ˚C within less than 10 mm of the centreline, Fig. 3.6-a. No significant temperature differences were found between the AS and RS, or across the sheet thickness and the WN, Fig. 3.6-a. Possible inaccuracies in this experiment could

result from the measurements retrieved from the thermocouples placed near the weld centreline as they were slightly displaced by the tool, but not damaged.

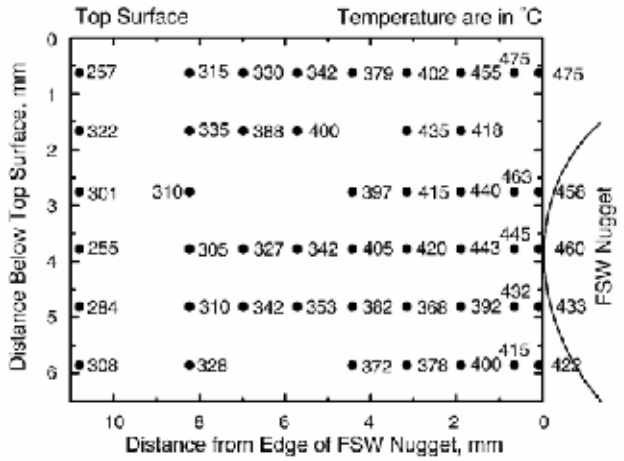

Fig. 3.5. Temperature distribution close to the WN in 7075-T651 weld. Each temperature point refers to the maximum temperature recorded by an embedded thermocouple (tool geometry was not reported). [10]

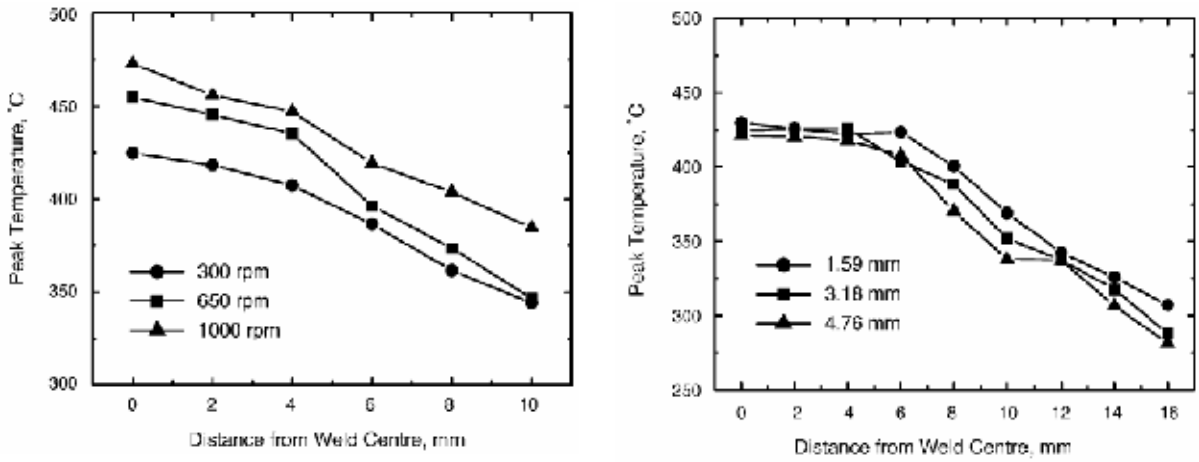

(a) (b)

Fig. 3.6. The spatial temperature distribution in 6061-T6 welds showing (a) the influence of the tool rotation speed on the temperature measured at mid-thickness, and (b) the temperature distribution as a function of depth for the weld carried out at 400 rpm. [13]

Sato *et al.* [11, 12] also investigated the influence of the rotation speed on $\underline{T_{max}}$ in 1100-H24 and 6063-T5 welds, using a thermocouple embedded at the bottom of the WN, covering a larger rotation speed range (500-3600 rpm). Despite the differences between the alloys, the

range of temperatures measured is roughly similar, with T_{max} increasing from 400 to 525 ˚C for 6063, and from 385 to of 533 ˚C in 1100 for the change in rotation speed, Fig. 3.7. However, the temperature in 6063 seems to sharply increase between 1600 and 1800 rpm, and then the increase becomes less steep [11], compared to a uniform gradual increase in 1100 [12]. Since the heat input is controlled by the adiabatic deformation, an increase in temperature would result in a decrease in the flow stress, with a significant decrease upon reaching the solidus-temperature (incipient melting) [14]. The solidus-temperature is known to depend on the alloy type, but it is normally lower in age-hardenable alloys. It is also known that, in age-hardenable alloys, the thermal conductivity experiences an increase following the dissolution of the precipitates, which could result in more heat flow to the weld [15]. These reasons could explain the minor differences between the temperatures observed in the age-hardenable 6063 and work-hardenable 1100, although experimental inaccuracies (e.g. thermocouple re-positioning or touching the tool) should not be eliminated.

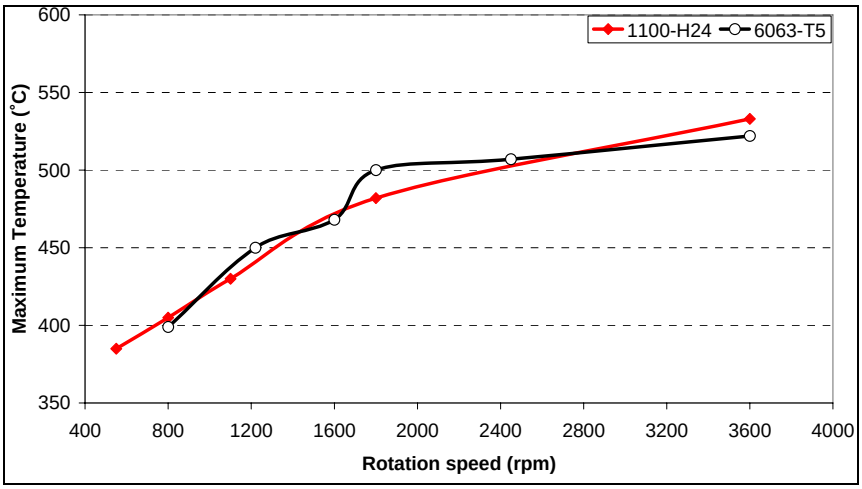

Fig. 3.7. The influence of the tool rotation speed on the maximum temperature in 6063-T5 (feed rate = 360 mm/min) and 1100-H24 (feed rate = 132 mm/min) welds (data after [11, 12])

With regard to other welding parameters, Record *et al.* [9] used statistical analysis to study the relative significance of various environmental and practice parameters on T_{max} using thermocouples embedded in the tool. Statistical analysis of the responses showed that (in order of significance) the rotation speed, feed rate, and plunge depth are the most important variables in controlling the tool temperature within the range of parameters investigated. The result of this study contradict the earlier investigation by Tang *et al.* [13], which also

investigated the influence of the plunge depth and the pin heat input using a pin-less tool, suggesting that the pin has an insignificant heat input since the absence of the pin led to an trivial decrease in the WN temperature (~15 ˚C), Fig. 3.8. A similar suggestion was given by Russell and Shercliff [16], putting an estimate for the pin heat input at 2 % of the total heat input. However, it was later understood that the fraction of the heat input given by the pin depends on the relative diameters of the pin and shoulder, and pin length [17], where early studies used relatively large shoulders and small pins. Recently, with the increase in plate thickness and the reduction of shoulder diameters, it was found that the pin heat input can contribute up to 20 % of the heat input depending on the process parameters [17, 18], as will be discussed in section 3.3.

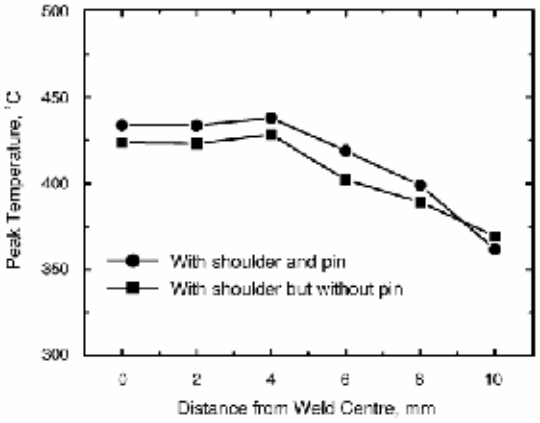

Fig. 3.8. Temperature measurements at mid-thickness for welds carried out with and without a pin in tool [13]

Arbegast [5] suggested an empirical formula that relates the maximum weld temperature (T, ˚C) to the alloy melting temperature (T_m, ˚C), rotation speed (ω, rpm) and feed rate (v, inch/min), based on the temperature measurements for various types of Al-based alloys. Using a given tool, depth of penetration, and sheet thickness, the maximum temperature can be related to a pseudo heat-index parameter given by (ω^2/v) using:

$$\frac{T}{T_m} = K\left(\frac{\omega^2}{v \times 10^4}\right)^{\alpha} \tag{3.1}$$

where K is a constant between 0.65 and 0.75 and the exponent α is between 0.04 and 0.06 for 6.4 mm thick sheets. Based on the temperature measurements for 2195, 2024, AFC458, 6061, 5083, and 7075 alloys, T_{max} was found to fall between $0.6T_m$ and $0.9T_m$ (˚C). However, the process parameters range, within which this model was fitted, was not indicated. It is now evident though that the heat generation and T_{max} saturate beyond ~3000 rpm in most Al-alloys

[11, 12], which was attributed to the softening of the material close to the solidus temperature [19], or the occurrence of slip at the tool-weld metal interface [20]. In fact, the influence of the change in rotation speeds on T_{max} becomes more noticeable at low speeds [21].

Generally, temperature measurements during FSW of Al-based alloys have shown that the process is a solid-state welding process, with a T_{max} between 400 and 550 ˚C. T_{max} is observed under the shoulder, where the maximum heat flux exists. The temperature increases with an increase in the rotation speed, a decrease in the feed rate, or precisely the pseudo-heat index, and an increase in the plunge depth. Based on the thermocouple measurements, it can be concluded that the temperatures generated do not appear to be strongly influenced by the alloy type in most cases, except when the incipient melting temperature is exceeded, which is in any case undesirable for weld integrity. The difficulty in obtaining reliable thermocouple measurements within the weld emphasises the need for computer models that can predict the temperatures in the weld.

3.3. Modelling of the Thermal Input

3.3.1. Analytical Models

Analytical models for heat generation during FSW (Table 3.2) can be classified into three types: friction-induced [14, 17, 22, 23], deformation-induced [16-18, 24-26], and models which consider both heat generation types [18, 27]. The first type suggests that the heat generation during FSW happens due to frictional heating below the tool and around the pin. The second type links the heat generation to the adiabatic plastic deformation between the plasticised material and the tool. The mixed-models suggest that both mechanisms are active, and that transition between can occur depending on the process parameters as will be discussed in the following sections.

Russell and Shercliff [16] used the classical Rosenthal (point source) analytical equation [28] to calculate the thermal fields, assuming that plastic deformation during FSW takes place at a constant τ of 5% of the yield strength at room temperature. Such an approximation gave reasonable thermal predictions only beyond the shoulder periphery (i.e. HAZ). Frigaard *et al.* [14] were the first to suggest a friction-induced model, similar to heat generation in radial friction welding, with constant heat flux under the shoulder, and ignoring the heat input due to the pin (Eq. 3.2 in Table 3.2). Chao *et al.* [29] later improved the heat flux distribution by formulating a radial distribution for the heat flux intensity (Eq. 3.3 in Table 3.2). Later, Colegrove *et al.* [17, 22] presented an analytical term for the pin heat generation, which showed that the pin heat generation contribution could reach up to 20% of the total heat generation (Eq. 3.4 in Table 3.2). A limitation for such models is the estimation of the friction coefficient μ. Limited data are available on the variation of the friction coefficient with temperature and pressure. Thus, in most studies the friction coefficient was constant during welding (between 0.3 and 0.5, either assumed or fitted [23]); becoming zero once incipient melting is reached [14, 23].

The analytical equations in deformation-induced heat generation models do not differ significantly from friction-induced models, where the friction term (μP) is replaced by the deformation flow stress (τ) [16-18, 24-26].

Table 3.2. Analytical models for heat generation during FSW

Model	Heat Input	#
Frigaard *et al.* [14]	Friction induced, under the shoulder → $Q_S = \frac{2\pi}{3}\mu P \omega R_S^3 ;\ P = \frac{F_N}{\pi R_S^2}$	(3.2)
Chao & Qi [29, 30]	Radial heat flux→ $q(r) = \frac{3Q_S\, r}{2\pi\left(R_S^3 - R_P^3\right)}$, such that $R_S \le r \le R_P$	(3.3)
Colegrove *et al.* [17, 22]	Shoulder → $Q_S = \frac{2\pi}{3}\mu P \omega\left(R_S^3 - R_P^3\right);\ P = \frac{F_N}{\pi R_S^2}$ Pin → $Q_P = 2\pi R_P h\bar{Y}\frac{V_m}{\sqrt{3}} + \frac{2\pi\mu\bar{Y}R_P h V_{RP}}{\sqrt{3\left(1+\mu^2\right)}} + \frac{4F_P\mu V_m\cos\theta}{\pi}$ V_m, V_{RP}, and θ are empirical functions given as: $\theta = 90^\circ - \lambda - \arctan(\mu)$, $V_m = \frac{\sin\lambda}{\sin\left(180^\circ - \theta - \lambda\right)}R_P\omega$ $V_{RP} = \frac{\sin\theta}{\sin\left(180^\circ - \theta - \lambda\right)}R_P\omega$, where λ is the thread helix angle.	(3.4)
Schmidt & Hattel [18]	$Q_{Welding} = \delta Q_{total,\,sticking} + (1-\delta)Q_{total,\,sliding}$ δ is a dimensionless state-variable indicating the contact condition.	(3.5)
Reynolds *et al.* [24]	The welding torque at the tool interface can be given as: $T_{Welding} = T_{shoulder} + T_{pin\ bottom} + T_{pin\ lateral}$ $T_{shoulder} = \int_{R_P}^{R_S}(\tau r)(2\pi r)dr$, $T_{pin\,bottom} = \int_0^{R_P}(\tau r)(2\pi r)dr$, $T_{pin\,lateral} = (\tau R_P)(2\pi R_p H_p)$ $Q_{Welding} = \frac{2\pi}{3}\tau\left[\left(R_S^3 - R_P^3\right) + R_P^3 + 3R_P^2 H_P\right]\omega$ $= \frac{2\pi}{3}\tau\left[R_S^3 + 3R_P^2 H_P\right]\omega$ Welding power: $Q_{Welding} = T_{Welding}.\omega$	(3.6)

List of Symbols

Symbol	Definition	Symbol	Definition
R_S, R_P	Shoulder and pin radii (m)	Q	Heat generation (W)
H_P	Pin height (m)	Q	Heat flux (W/m^2)
A_S	Shoulder contact area (m^2)	q_v	Volumetric heat source (W/m^3)
F_N, F_P	Normal and traverse forces (N)	T	Torque (N.m)
h	Sheet thickness (m	$\bar{Y}$	Yield stress (Pa)
ω	Rotation speed (rad/S)	μ	Friction coefficient
P	Normal pressure (Pa)	τ	Shear stress (Pa)

Recently, Schmidt and Hattel [18] introduced a model which considers both friction-induced and deformation-induced heat generation, or the slip and stick conditions (Eq. 3.5 in Table 3.2). In the slip (sliding) condition, the pressure applied by the tool is less than the deformation stress at a given temperature, thus friction between the tool and the material causes heat generation. If the matrix sticks to the tool, heat is generated through the internal friction between the material layers. This formulation agrees with the torque-based formulation suggested by Reynolds *et al.* [24] which enables inverse modelling of the heat generation by calculating the friction/deformation condition based on the measured welding torque and power (Eq. 3.6 in Table 3.2).

3.3.2. Numerical Thermal/Thermomechanical Models

Numerical modelling of FSW has been performed using finite-difference (FD) methods [14, 23, 26], based on analytical heat generation equations [17, 18] or finite-element (FE) [17, 22, 25, 29-34], or material flow modelling using analytical [35, 36] or computational fluid dynamics (CFD) models [19, 21, 37, 38]. The various models were used to provide information on the thermal fields [14, 16, 22, 23, 25, 26, 29, 30, 35], residual stresses [29, 31], material flow and the deformation strains [17, 22, 32-35], due to FSW. These models can be also classified based on the heat generation mechanisms; friction or deformation-induced.

3.3.2.a. Friction-Induced FE & FD Models

Among the earliest models was the thermal model by Frigaard *et al.*[14]. A 3-D FD Eulerian code was developed, based on Fourier's 2nd law, to estimate the hardness development in age-hardening Al-alloys by modelling the thermal fields and transient cycles. Their model adopted a friction-induced heat generation approach of a shouldered-tool, without considering the plastic deformation by the pin (Eq. 3.2 in Table 3.2). However, the total heat input was distributed as square fluxes across the thickness, contained within the shoulder and pin diameters at the sheet surface and below respectively. A constant friction coefficient of 0.4 was used that becomes zero once the weld temperature reaches the incipient melting temperature of the alloy. Reasonable temperature predictions (±20-30 ˚C from experimental measurements) were obtained, although a large overshoot was observed during the cooling section of the thermal cycle. Several FD or FE models were later developed based on the friction-induced approach [22, 23, 31, 39]. Some of them, though, improved this approach by considering the pin heat generation by adiabatic plastic deformation [22].

The friction-induced approach has some shortcomings. First, the constant friction coefficient value is an arbitrary empirical value, which does not have any physical significance. It also ignores the local variations around the tool, and the influence of other factors (e.g. contact conductance or the variation of μ with temperature). Although literature values for the friction coefficient for steel on aluminium were used [14], the influence of the contact-condition (stick or slip), or of temperature on μ was ignored.

3.3.2.b. Deformation-Induced FE & CFD Models

It was suggested in some early models that the heat is generated during FSW due to the adiabatic deformation of the plasticised material, yet using a constant value of deformation shear stress (τ) to calculate the heat generation. Chao and co-workers [29, 30] also assumed τ, but with different values (60, 80 and 100% of the yield stress at a given temperature within the TMAZ, HAZ, and BM respectively), to model the residual stress development. Reasonable temperature predictions (± 20-30 ˚C) were obtained only following rigorous fitting. However, both approaches lacked physical proof for their assumptions.

Following the introduction of the deformation-induced heat sources by Reynolds *et al.* [24] and Schmidt *et al.* [18], various FE thermal (uncoupled) models were developed. Simar *et al.* [25] used this approach to model the FSW thermal cycle in 6005-T6. Since this approach is not based on fitting the heat generation source (i.e. μ or τ), another parameter required fitting, which was the contact conductance between the workpiece and the backing plate. Based on their findings, it was shown that a perfect contact exists under the tool region, decreasing in the rest of the workpiece with the distance from the tool region. A similar result was also obtained by Kovacevic *et al.* [31], who used the stress field generated by the moving tool to estimate the contact conductance around the tool, Fig. 3.9.

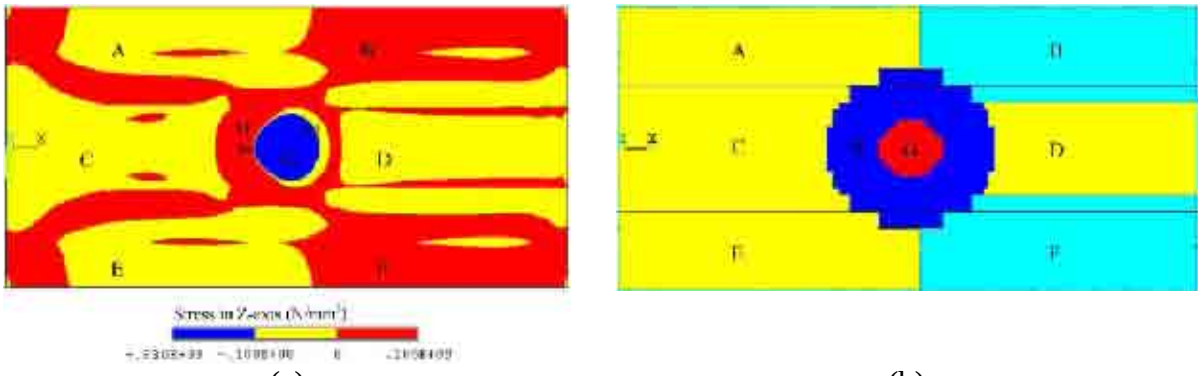

(a) (b)

Fig. 3.9. Determination of the contact conductance under the tool using (a) the stress distribution at the bottom of the tool to (b) estimate the contours of contact conductance. Tool motion is to the left, with the conductance level G>H>(A, C, D, E)>(B, F) [31]

With the complex deformation taking place during FSW, it is impossible to couple both the thermal and flow fields in a single model using a Lagrangian (deformable mesh), or an

Eulerian (non-deformable mesh) FE formulation due to the severe mesh distortion. The former approach could be useful to model residual stress problems, while the latter approach can be used for thermal or fluid flow models. Thus, to produce fully coupled FSW models, it is necessary to use a complex FE formulation known as the Arbitrary-Lagrangian-Eulerian (ALE) formulation, where the motion of the coordinate system is possible through re-meshing (nodal displacement) according to the user's need.

Xu and Deng [33, 40] used the ALE formulation to study the material flow during FSW using ABAQUS. This model was capable of studying the velocity, stress, and strain distributions surrounding the tool assuming frictional-contact and slipping interface scenarios, predicting the markers flow and the formation of the onion rings structure, which was linked to variations in strain surrounding the moving tool. However, the model was not fully coupled as the temperatures were based on thermocouple measurements. Schmidt and Hattel also used the ALE formulation to developed the first fully coupled thermomechanical model on ABAQUS/Explicit with the Johnson-Cook elastic-plastic material law [32]. A constant contact conductance was used everywhere under the sheet. Despite the wealth of information that this model can provide (e.g. material velocity, plastic strains, and temperatures across the weld), a major shortcoming for it was the long processing time for reaching the steady-state (14 days on a 3 GHz Pentium PC to reach only 10 seconds of model time). Their experimental validation concluded that the sticking condition is mostly dominant at the tool matrix interface for the welding parameters they investigated (400 rpm and 120 mm/min) [36]. However, recent work by Colegrove and Shercliff [21, 37] raised doubts regarding the use of Johnson-Cook model in FSW thermomechanical modelling since it ignores the possible effects from precipitate dissolution/precipitation, strain-rate sensitivity, deformation near the solidus temperature, as well as the validity of the thermomechanical database itself (typically based on ASM data).

An alternative thermomechanical modelling approach was to use CFD to model the flow fields (strain and strain rates), as well as the temperature development. Among the earliest work, Bendzsak *et al.* developed a CFD model for the heat transfer and material flow in FSW, with the deformed material modelled as a non-Newtonian fluid, and heat generation occurring by viscous flow [41]. Some simplifications, related to the heat generation and temperature fields, were made to compensate for the limited computational capabilities at that time. Colegrove *et al.* [22] also probed material flow using the thermal predictions produced by an

FE model to investigate the velocity and pressure distribution around the tool. Generally, those early flow models and others (e.g. Askari *et al.* [34]) were uncoupled or sequentially-coupled, and limited by the computational power and software at that time.

Later, several models were introduced using FLUENT CFD package, which uses an Eulerian fluid flow scheme. Initially, FLUENT was used by Seidel and Reynolds [19] to establish a 2-D fluid flow model, representing the process as a flow moving towards a rotating cylinder with a stick condition and modelling the material as a viscous non-Newtonian fluid using a modified Sellars-Tegart effective deviatoric flow stress formulation. This approach, also used later by Colegrove and co-workers [21, 37, 38], addresses the concern related to strain-rate as this formulation was found to hold in pure Aluminium to strain rates ~1000 s^{-1}. Moreover, to consider the deformation of the softened material close to solidus temperature, the material viscosity was forcibly reduced 50 K from the solidus temperature. Reynolds and Seidel model was used to predict the FSW flow fields and the X-force (longitudinal), and the results were compared to their experimental material flow work, which will be discussed in the following section. Colegrove and co-workers CFD models were first used to optimise the FSW tool design based on the flow fields due to different geometries, which resulted in the development of the Trivex^{TM} tool [37, 42], was recently used to successfully predict the thermal and flow fields due to FSW in various heat-treatable Al-alloys [37, 38].

Other models were also developed to specifically study the material flow fields during FSW [22, 34, 35]. However, the main concerns (e.g. processing time, temperature-dependent material property data, fitting parameters, verification of results) still exist. A more recent trend is the introduction of simple FSW thermal numerical modelling packages or modules for commercial use (e.g. TS4D [43] and Comsol-Multiphysics [44]). These models are less computationally-intensive compared to FE and CFD models. This trend is expected to continue as long as these simple models are capable of producing reliable predictions, with the least processing time, assumptions, and fitting parameters.

3.4. Material Flow during FSW

Several studies have looked into material flow during FSW. The aim of these studies was to visualise the complex flow fields of the plastically deformed material around the tool, or for tool design optimisation. This was observed either using embedded marker materials [7, 8, 36, 42, 45, 46], or in similar and dissimilar welds [8, 46-49].

3.4.1. Markers Insert Technique (MIT) Studies of Material Flow

The MIT approach involves the utilisation of a material of a different density or etching response. Different researchers used spherical steel shots [8], rectangular inserts [7], Al-matrix composites [45], titanium powder [46], or copper foils [36, 42] aligned along or normal to the welding direction, then using a combination of metallography, radiography, or X-ray computer micro-tomography to study the flow path of the marker material (MM).

In one of the first trials, Colligan [8] used steel shots (∅ 0.38 mm) embedded in a groove in 6.4 mm thick 6061-T6 and 7075-T6 sheets along the welding direction at different heights across the thickness and lateral distances from the tool axis. Radiographic imaging of the welds revealed that the steel shots moved in two patterns: chaotic scattering, which was observed in tracers located at the top close to the shoulder, or continuously aligned above their initial height by stirring behind the tool elsewhere. Currently, Colligan's results are viewed with suspicion due to the significant difference between steel and aluminium in density and strength, in addition to the size of the shots which was comparable to the thread spacing, which could disturb the representation of the flow-fields during stirring [2, 36]. To avoid these concerns, Seidel and Reynolds [7] used instead AA5456 markers (1.8 mm thick × 2.7 mm high) embedded in AA2195 8.1 mm thick sheet to visualise the flow fields, Fig. 3.10-a. Following welding, thin slices (0.25 mm thick) were cut from the weld top surface downwards, etched with Keller's reagent to show a 2D flow pattern, and then images were re-constructed in 3D to show the full flow pattern. It was found that material flow around the tool is asymmetric, where the RS MM was stirred behind the tool, and the AS MM was pushed in front of the tool, with the majority of the MM deposited behind the tool, Fig. 3.10-b. Stirring occurred only at the top of the weld, where the RS MM was moved to mix with the AS MM, whereas a distinctive interface between the AS and RS MM was found from the mid-thickness of the sheet downwards, Fig. 3.10-c. Through the sheet thickness, the intensity

of mixing was found to be qualitatively larger closer to the tool shoulder. The AS MM near the tool was transported downward, while the RS MM is pushed upwards. Material flow and mixing were found to intensify with an increase in the tool diameter and a decrease in the advance per revolution (APR), giving sufficient time for stirring, Fig. 3.11.

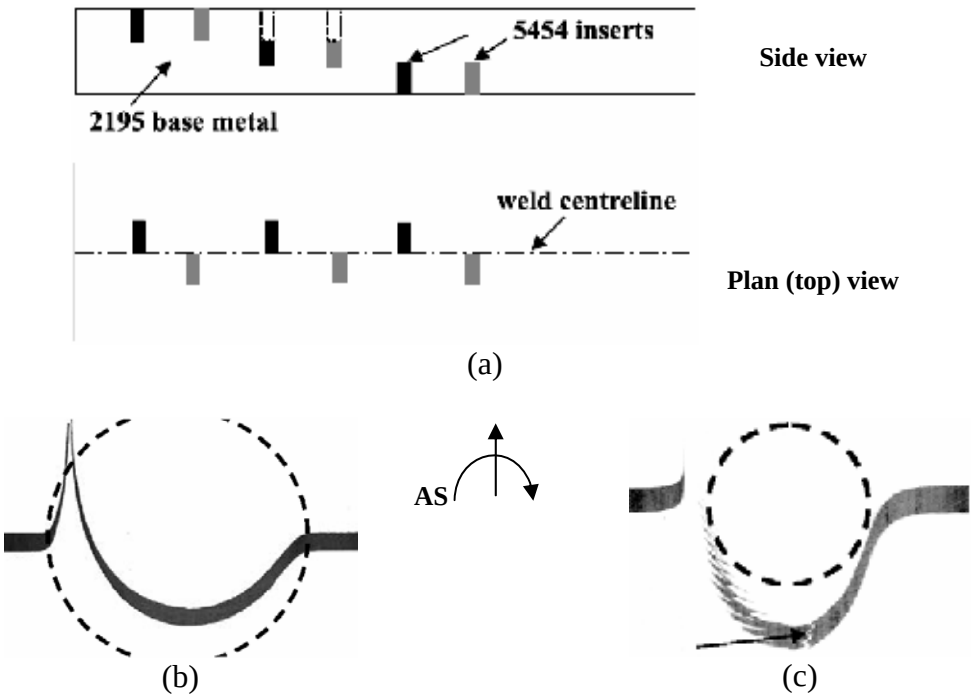

Fig. 3.10. The MIT study by Seidel and Reynolds (a) the location of the embedded markers, (b) the plan view flow pattern at 0.25 mm from the weld top (dashed circle refers to the shoulder), and (c) at mid-thickness (dashed circle refers to the pin, arrow refers to the boundary between AS and RS MM) [7]

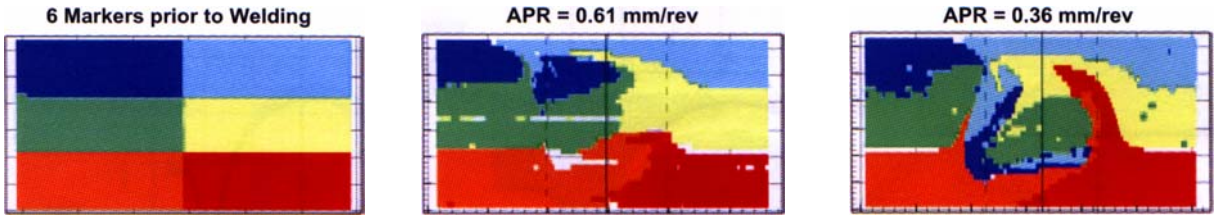

Fig. 3.11. The influence of advance per revolution on stirring (AS to the left) [7]

In recent studies, the use of particles [45] or powders [46] as MMs was introduced as alternative tracers that do not alter the flow. London and co-workers [45] studied material flow in 6.35 mm thick 7050-T7451 weld welded at 350 rpm and 102 mm/min. Markers of Al-

30 vol.% SiC and Al-20 vol.% W composites of a rectangular cross section (0.79×0.51 mm) were positioned parallel to the feed direction at the AS, RS or weld centreline at the sheet mid-thickness. Both markers contained particles of sizes which are traceable using metallography and X-ray imaging (2-15 μm-sized SiC particles with a density of ~3200 kg/m^3, and 20-25 μm-sized W particles, with a density of 192500 kg/m^3). It was found that for the MM located at the weld centreline, the MM was sheared and deposited behind the tool in a streaky pattern, Fig. 3.12-a. The MM was lifted from mid-thickness by ~2.1 mm, which is probably due to the action of the tilted threaded tool, then sheared, and then plunged down again by the thread action. Not all the MM was deposited behind the tool as some MM was carried along with the thread. It was also found that the AS MM was dispersed over a wider region behind the tool, Fig. 3.12-b.

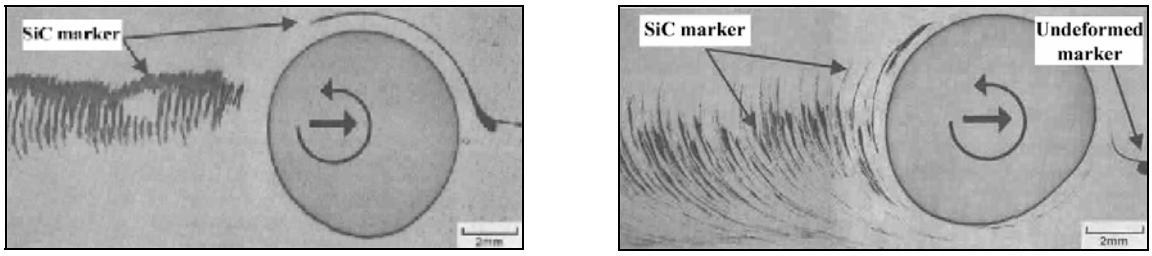

(a) (b)

Fig. 3.12. Metallographic sections at the sheet mid-thickness of the 7050-T7541 weld, showing (a) the streaky fashion forming at the wake of the tool for MM placed at the weld centreline, and (b) the wide dispersion of the AS MM behind the tool [45]

The MIT was also used, alongside computer modelling, to optimise the tool design and to study the flow conditions. Colegrove *et al.* [42] used MIT to investigate the flow fields surrounding current and hypothetical tool designs, combined with CFD modelling to optimise new tool designs based on their mixing properties on thin copper foils placed along the weld centreline. It was suggested that profiled unthreaded tools could also be used for FSW, with an advantage of better tool fatigue strength over threaded tools due to the lack of threads. Zettler *et al.* also used MIT to compare the flow fields in 2024 and 6056 welds for conical unthreaded, threaded, and threaded profiled (with three flats) tools using Ti powder (30-90 μm in size) as MM, Fig. 3.13. It was shown that the existence of threads or profiles is crucial for weld integrity and a lack of voids. Schmidt *et al*. [36] also used MIT to estimate the flow velocity at the vicinity of the tool based on analytical equations for the material flow. They

used a combination of metallography, X-ray and computer tomography to study the flow of 0.1 mm thick copper foils placed at the weld centreline parallel to the feed direction in a 2024-T3 3 mm thick weld, welded at 400 rpm and 120 mm/min. Based on the flow velocity estimates, it was indicated that the sticking condition was dominant during FSW for this welding condition, which they predicted in their earlier modelling work [18, 32].

(a) conical unthreaded (b) threaded (c) threaded with three flats

Fig. 3.13. FSW tool pin geometries investigated by Zettler *et al.* [46]

Despite the wealth of information provided by the MIT studies, there is a concern that the use of MMs of different density and flow characteristics (e.g. steel and copper), or large inserts (e.g. balls, foils, or rectangular inserts), could alter the flow fields surrounding the tool, thus providing a flawed description of the material flow [2, 36, 45]. It can be concluded from the previous studies that the selection of an appropriate MM is crucial for the credibility of MIT experiments. An ideal MM should be a material that can be distinguished following welding, and it should not alter the flow fields because of its size or flow characteristics. Thus, as suggested by London *et al.* [45], this ideal MM should be a radioactive marker of the same welded alloy. In a simpler approach, studying the flow fields in similar and dissimilar welds was also found to provide useful results on material flow.

3.4.2. Similar and Dissimilar welds

Similar and dissimilar welds were also used to investigate the material flow during FSW in various studies. Studies were carried out on dissimilar Al-based alloys using the difference in etching response to observe the flow fields [47-50], or dissimilar metals (e.g. aluminium and magnesium [51-53], copper [54], or stainless steel [55]).

Murr and co-workers [47-49] were the first to investigate flow phenomena using dissimilar Al-based alloys. Dissimilar welds for 2024 and 6061 welded at 400, 800 and 1200 rpm, and 60 mm/min were investigated to study FSW mixing and flow patterns [47]. FSW produced complex vortex and swirl flow fields of a chaotic nature, as well as an 'onion rings' structure, Fig. 3.14-a. It was suggested that the vertical spacing between the linear dark (6061) and bright (2024) bands on the sectional view along the welding direction is equal to the pin screw thread spacing (1.27 mm), Fig. 3.14-b. The linear bands on the sectional view were found to be closely-spaced alternating striations (~0.1 mm thick), Fig. 3.14-(c-e). Thus, the weld face morphology was a section through the complex flow fields forming at the wake of the tool. More recent studies, by the same group, for a wider range of 2xxx, 5xxx, 6xxx, and 7xxx dissimilar welds, showed that the relative location of the soft/strong alloy (i.e. AS or RS) determines the intensity of the vortex and swirl patterns in the onion rings, whereby a more distinct structure was observed when a soft material is placed at the AS [48]. The existence of the striations was explained to be due to the wiping/filling action of the tool, where material is wiped and sheared or peeled from the front AS by the tool threads, rotated, and then deposited at the wake of the tool. With the combined linear and rotary motions, material from the RS is dragged and fills in between the AS material layers [49].

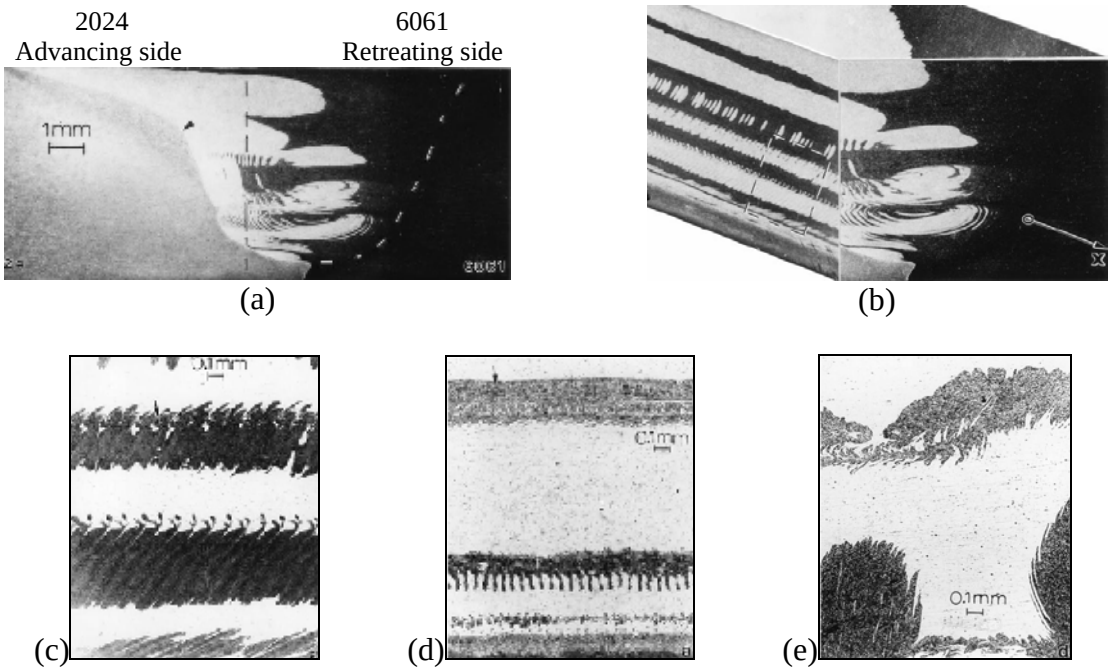

Fig. 3.14. Dissimilar 2024-6061 weld showing macrographs for (a) weld face, (b) sectional view through the weld centreline, and micrographs for the sectional view welded at 60 mm/min and (c) 400 rpm, (d) 800 rpm, (e) 1200 rpm [47]

Studies on dissimilar metals also showed similar flow phenomena. However, the difference in strength also caused unique flow features such as: lamellar shear bands in AA6061-T6/AZ91D alloys weld [53], constitutional liquation and formation of Al-Mg intermetallics in AA1050/AZ31 weld welded at a relatively high rpm [52, 54], and Al-Cu intermetallics 6061-T6/copper weld [51].

The vertical striations observed in dissimilar welds were also observed by Colligan [8] using a 'stop-action' technique in similar 6061-T6 weld. This technique investigates the material flow during FSW by suddenly stopping the welding process, followed by unscrewing the tool from the exit hole, thus leaving the material within the thread undamaged in the keyhole. As shown in Fig. 3.15, a section through a keyhole shows that the material curls in the tool thread (A), until it becomes fully developed (B). This material is carried by the thread and gets deposited behind the tool. The macrostructure shows vertically-oriented banded striations across the sheet mid-thickness. Zettler *et al.* [46] also observed the formation of striations at the weld centreline along the welding direction in similar 2024-T3, Fig. 3.16. To study the influence of the tool geometry on this phenomenon, they suggested a striation index ratio (*t/b*), which is the ratio of the spacing between the striations (*t*) to the thickness of the smaller striation (*b*). They found that the striation index was smaller for the profiled threaded tool, compared to the circular threaded tool in the welds welded at APR < 0.25 mm/rev. However, it was similar for larger APRs [46].

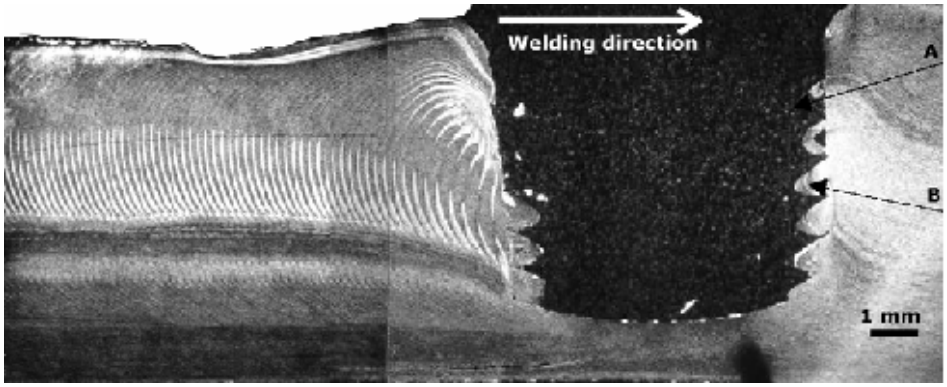

Fig. 3.15. Section through 6061-T6 weld with the tool removed showing material movement and deposition from the leading to the trailing edges of the tool [8]

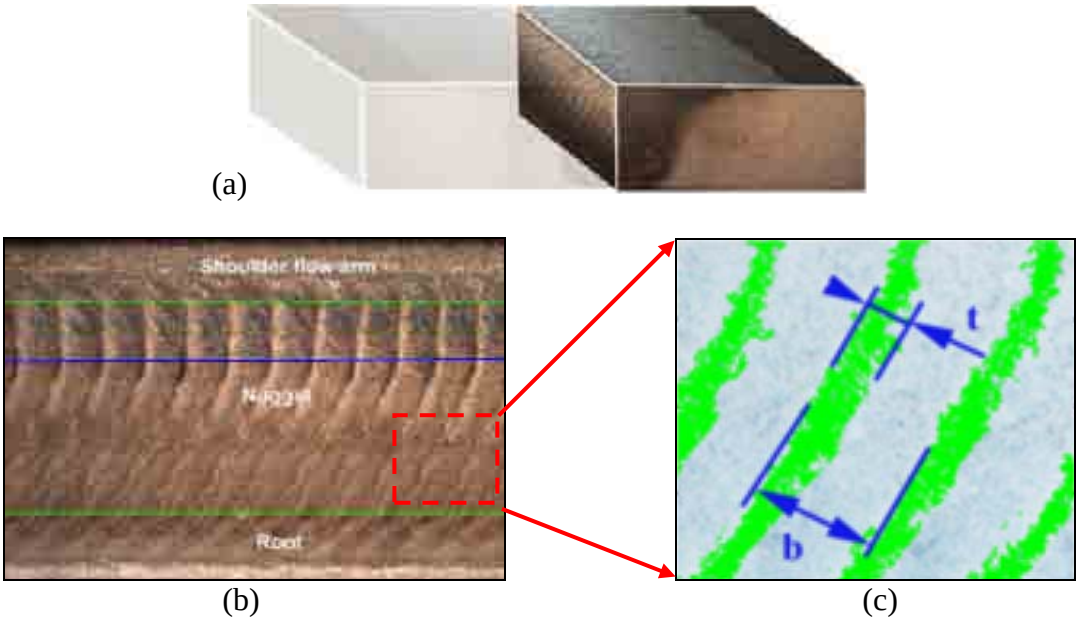

Fig. 3.16. The observation of the striations along the weld centreline in 2024-T3 weld in (a,b) and (c) the striation index [46]

The studies discussed in this section observed the flow phenomena in FSW (e.g. onion rings, vertical striations) on the macro-level only, without investigating the microstructural heterogeneities that could lead to the indicated etching trends. More detailed microstructural investigations were performed to understand the flow phenomena as will be discussed in the following section.

3.5. Microstructural Development due to FSW

Microstructural development due to FSW has been studied for various Al-based alloy classes (1xxx [56-63], 2xxx [4, 6, 64-77], 5xxx [4, 60, 61, 70, 78-83], 6xxx [11, 58, 83-87], 7xxx [4, 10, 66, 74, 88-90], 8xxx [91, 92], and cast alloys [93, 94]). FSW results in a series of microstructural alterations within the characteristic zones (WN, TMAZ, and HAZ) that influence the weld microstructure (grain structure, texture, precipitates and particles), and accordingly its mechanical properties. In the TMAZ and WN, the combined influence of plastic deformation and thermal stirring develops a dynamically recrystallised fine grain structure [6, 10, 14, 47-50, 53, 56, 58, 68, 71, 84, 95-97]. Thermal stirring also causes some types of the intermetallic particles and precipitates to undergo thermal dissolution and mechanical break-up [64, 74]. In the HAZ, thermally-stimulated developments take place, such as: recovery, recrystallisation, dissolution or precipitation.

Generally, the microstructural development due to FSW is described in terms of: a) grain structure, b) intermetallic particles, and c) the onion rings structure. It is important to mention that the microstructural development in the characteristic zones depends on the type of the material (i.e. heat-treatable or work-hardenable alloy). Due to this, the development in the particle structure, mentioned under this section, will only focus on the constituent and equilibrium particles. Further details on the development of the hardening precipitates in heat-treatable alloys will be mentioned under the structure-property development in section 3.6.1.

3.5.1. Grain Structure

Several reports have shown that dynamic recrystallisation during FSW leads to grain refinement, with grain sizes between 2 and 13 μm normally observed within the WN/TMAZ, depending on the process parameters (Table 3.3). However, grain sizes < 1 μm were also found in some welds in which special cooling was employed (e.g. using liquid nitrogen, dry ice+methanol) [90]. Reports on the grain structure development during FSW focused on three aspects; the recrystallisation mechanism in FSW, influence of the process parameters, and prediction of the grain size.

Table 3.3. Grain size in the WN of welds of Al-based alloys

Material	Plate thickness (mm)	Tool geometry	Rotation speed (rpm)	Feed rate (mm/min)	BM grain size(μm)	WN grain size (μm)	Reference
2095-T4	1.6	Standard	1000	246	3	2.2-3.6	[6]
7075-T651	6.35	Standard	--	127	--	3-10	[10]
6063-T5	4	Standard	800-3600	180	63.3	5.9-17.8	[11]
2017-T6	3	Standard	1250	60		9-10	[48]
1100-cast	6.35	Standard	400	60	28	15	[57]
1100-cast	6.0	Standard	400	60	5000×500	4	[58]
1050-O	5	Standard	1540	30	30-40	1-2	[59]
5083-O	6	--	--	--	18	4	[60]
5052-O	2	Standard	2000-4000	500-2000	17	3-16.1	[61]
2024	6.35	Standard	200-300	25.4		2-3.9	[65]
2024-T3	6	Standard	850	120	150×25	4	[69]
5251-O	6	Standard	800	150	100×35	10	[70]
2024-T351 2524-T351	6.4	Standard	215-360 120-480	77-267 51-203	-- --	3.1-5 1.2-7.2	[75]
5754-Hxx	2	Standard	--	100	--	6.4-13.5	[78]
5083-Hxx	6.35	Standard	400	25.4-50.8	--	6.5-8.5	[79]
5083-Hxx	3	Standard	--	100-200	50×5	10-13	[80]
5083-O	6-10	Standard	-	46-132	30×25	10	[83]
6061-T6	6.3	Standard	300-1000	90-150	100	10	[84]
7050-T745	6.35	Standard	400	100	--	1-5	[88]
7075-T651	6.35	Standard	350, 400	102, 152		3.8-7.5	[98]

* Standard: Cylindrical threaded tool

3.5.1.a. Recrystallisation Mechanisms

As indicated in chapter 2, dynamic recrystallisation (DRX) mechanisms can be classified into: discontinuous DRX (DDRX), geometric DRX (GDRX), DRX by progressive lattice rotation (PLR), and DRX by particle stimulated nucleation (PSN) [99, 100]. DDRX is characteristic of materials with low-stacking fault energies and, hence is not commonly seen in Al-alloys.

Murr *et al.* [58] studied the microstructure development due to FSW in cast-AA1100 alloy. FSW was found to replace the dendritic structure in the base alloy with an equiaxed recrystallised fine grain structure (size of 4 μm), with large misorientation angles (>15˚), Fig. 3.17. FSW also led to a significant decrease in dislocation density in the weld compared to the parent alloy, which shows that full DRX took place. Murr *et al.* also observed similar influences due to FSW in a heat treatable Al-alloy (6061-T6), indicating that DRX also decreased the dislocation density [84].

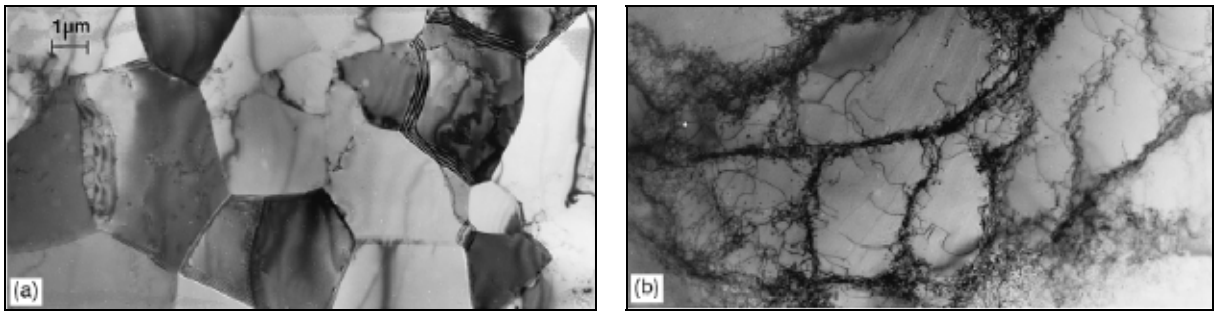

Fig. 3.17. Microstructural development due to FSW in AA1100 showing (a) WN dislocation-free DRX grains compared to (b) basemetal with cellular dislocation structure [58] (Images have same magnification)

Jata and Semiatin [71] used electron backscattered diffraction (EBSD) techniques to study the nature of the recrystallisation mechanism in a rolled Al-Li-Cu alloy weld. The DRXed fine grain structure in the WN was generally dislocation-free, although a few residual dislocation cells at the grain boundaries were observed, which suggests that DRX and/or dynamic recovery (DRV) may not have been finished. It was also observed that a fraction of low-angle boundaries (<10˚) in the base alloy were transformed in the weld to high-angle boundaries (between 15 and 35˚), producing a uniform distribution compared to the base alloy, Fig. 3.18. Such a development is characteristic of CDRX mechanisms, specifically dislocation-glide-assisted PLR. An estimate for Zener-Hollomon parameter of 2.9×10^{13} was calculated for the deformation during FSW. Su *et al.* [90] also suggested that CDRX took place in the WN of 7050-T651 weld. They suggested that CDRX is initiated by DRV via subgrain growth and absorption of dislocations into boundaries, which grow to recrystallised grains on further thermomechanical deformation.

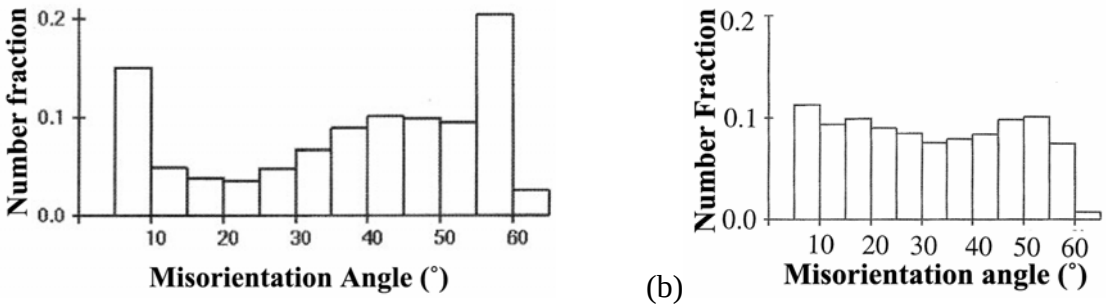

Fig. 3.18. Misorientation angle distribution in Al-Cu-Li alloy: a) base alloy, b) weld WN [71]

Frigaard *et al.* [14] attempted to determine the extent of recrystallisation in 6082-T6 and 7108-T79 welds by performing post-weld annealing. They observed two regions in the TMAZ; one that recrystallised (near the top and in the WN base), while the other (occupying the middle region of the WN across the thickness) did not recrystallise, Fig. 3.19. As a result, they concluded that the microstructure contains both dynamically recovered regions, which recrystallised upon annealing, and recrystallised regions which did not change.

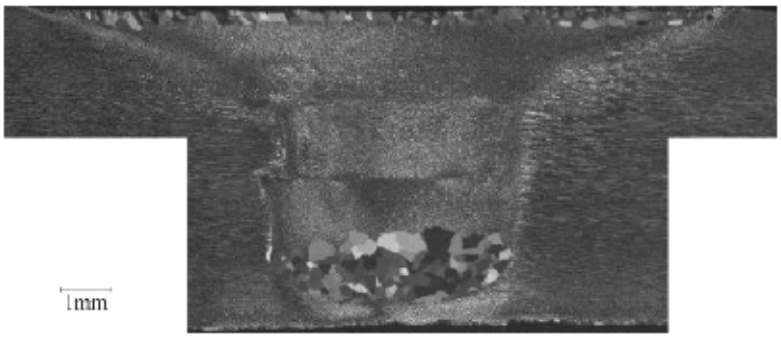

Fig. 3.19. The microstructural development after post-weld annealing in 7018-T79 weld [14]

Recently, Fonda *et al.* [68] used a 'stop-action technique' with EBSD to investigate the microstructural development in 2195 weld. By qualitatively studying the microstructure around the tool, which was stopped during FSW, it was found that the fine grain structure continuously develops due to lattice rotations resulting from the shear deformation in front of the tool. An additional influence from dynamic recovery was also suggested. More recently, Prangnell and Heason [96] performed further quantitative studies using EBSD on the same weld investigated by Fonda *et al.* [68]. They suggested that grain refinement during takes place during FSW through GDRX by grain subdivision when the material is deformed at high strains rather than by PLR. By investigating the misorientation angles in the recrystallised material as a function of the distance from the tool, they ruled out PLR as a mechanism for DRX. A strong {112}<110> also texture was found within the WN.

It is expected that the confusion regarding the recrystallisation mechanism during FSW is affected by the differences in process and material-related parameters. The influence of material parameters (e.g. parent metal condition, solute drag, intermetallic particles and precipitates) on recrystallisation is rarely considered. It is known that solutes (e.g. Zn and Mg in Al-based alloys) can restrict dislocation glide, which makes PLR a favoured mechanism

rather than GDRX. Similarly, intermetallic particles provide a pinning effect on the dislocations. Accumulation of dislocations at the particles during thermomechanical deformation can initiate another recrystallisation mechanism, which is PSN [99, 100].

3.5.1.b. Influence of Process Parameters on Grain Size

Few attempts to relate the process parameters to the grain size have been carried out [2, 11, 101]. To be able to predict the grain size using constitutive equations for DRX (e.g. Zener-Hollomon parameter), it is necessary to identify both the temperature and strain rates during FSW. The other option is to empirically study the influence of the process parameters on the grain size. It was generally found that the grain size increases with an increase in the tool rotation speed and/or a decrease in the feed rate [2, 11]. Mishra [2] attempted to generalise this observation by linking the pseudo-heat index (ω^2/v) to the grain size. However, the grain size did not show a systematic increase with the increase in the pseudo-heat index. Instead, a particular rotation and feed speeds combination, or heat input, was required for a specific alloy welded using a certain tool to create the finest grain size

Sato *et al.* [11, 102] suggested that the WN grain size in AA6063 welds develops by static grain growth (GG) of the DRXed grains during the thermal cycle, which is given as:

$$D^2 - D_0^2 = A\exp\left(-Q/RT\right)t \tag{3.7}$$

where D_0 and D are the grain sizes following DRX (initial) and GG (final) respectively, A is a constant, Q is the activation energy for GG, R is the gas constant, T is the maximum temperature during welding, and t is the time period of the cooling section in which GG occurred. D_0^2 was considered negligible, compared to D^2, since the size of DRXed grains observed using TEM was ~0.6 μm, compared to final grain size between 5 and 25 μm [11]. Accordingly, D can be related to the T for 6063 welds welded at a constant feed rate of 360 mm/min and rotation speeds between 800 and 3600 rpm, such that:

$$\ln D = -Q/2RT + \ln\left(At\right)/2 \tag{3.8}$$

The data showed a good fit between ln D and 1/T, Fig. 3.20. However, the deformation effects on grain size are not dealt with in this model, which could affect the driving force for GG.

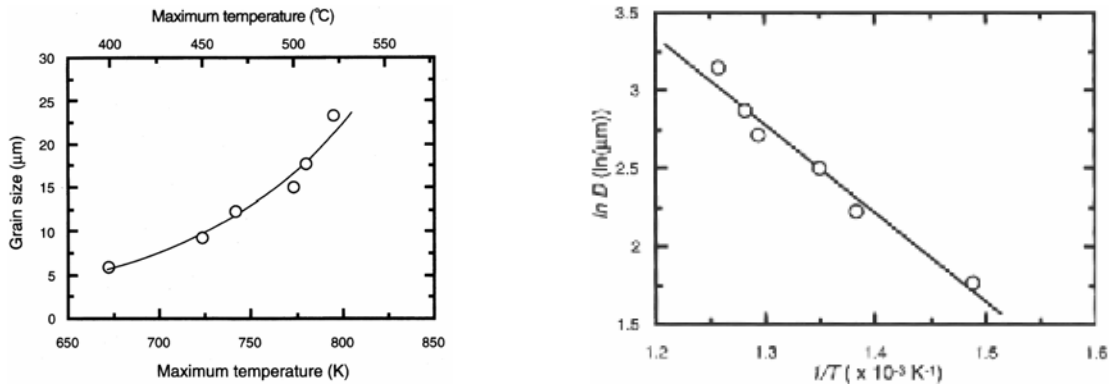

Fig. 3.20. Influence of the peak temperature on grain size in AA6063 welds [11]

Fratini and Buffa [101] suggested an alternative approach to predict the final grain size using constitutive equations for CDRX, based on the estimate by Jata and Semiatin [71] for the deformation conditions in FSW which suggested that recrystallisation occurs by CDRX (section 3.5.1.a). FE modelling using DEFORM (with adaptive re-meshing) was performed to predict the temperature, strain, and strain rate. Using this model, the steady state grain size following CDRX is given by:

$$D_{CDRX} = C\,\varepsilon^{k}\,\dot{\varepsilon}^{j}\,D_0^{h}\,\exp\left(-Q/RT\right) \tag{3.9}$$

where C, *h*, *j* and *k* are material parameters, ε is the strain, and $\dot{\varepsilon}$ is the strain rate. The model was fitted for AA6082-T6 weld using grain size measurements to fit the CDRX equation. Good predictions of the grain size within the WN centre were obtained. However, the quality of the predictions decreased as a function of depth and distance from the weld centreline, with good fit being lost at the base or outside the WN (in the TMAZ edge). The model was not designed to model the HAZ grain size development. The model was not verified by temperature measurements, which could explain the inconsistent predictions.

3.5.2. Constituent Particles

Studies on welds of wrought alloys [10, 64, 76, 77], cast alloys [2, 50, 93, 94], and rapidly-solidified alloys with a high volume fraction of constituent particles [91], showed three trends within the stirred WN. First, FSW was found to modify the particle structure by stirring, breaking-up and re-distributing faceted, needle-like or dendritic particle structures (e.g. as-cast structure, Fig. 3.21) [2, 94]. Second, an improvement in the TMAZ/WN strength

was also indicated [91, 93]. Finally, particle-rich and particle-poor bands were clearly observed [10, 50, 91], forming the banded structure known as the onion rings structure.

Mishra and co-workers [2] reported utilising FSW to modify the particle structure in cast A356 alloy. They reported that acicular Si particles were broken up, decreasing their aspect ratio from 25 to 2, homogeneously distributing them within the WN. FSW also eliminated porosity and heterogeneous distributions of particles in the cast alloy. Recently, Baeslack *et al.* [91] investigated welds in rapidly-solidified powder metallurgy AA8009. The base alloy contained a high volume fraction of submicron $Al_{13}(Fe,V)_3Si$ dispersoids. Upon FSW at 1200 rpm-258 mm/min, a banded structure was found to form within the WN as shown in Fig. 3.22. By observing the banded structure under the SEM, it was found that the preferentially etched regions contained a high number density of particles. Nonetheless, the weld was found to exhibit a uniform distribution of the dispersoids once welded at 428 rpm-114 mm/min. It was reported that the heterogeneous distribution led to failure of transverse tensile specimens at the WN/TMAZ boundary towards the AS, where segregation of $Al_{13}(Fe,V)_3Si$ particles was observed.

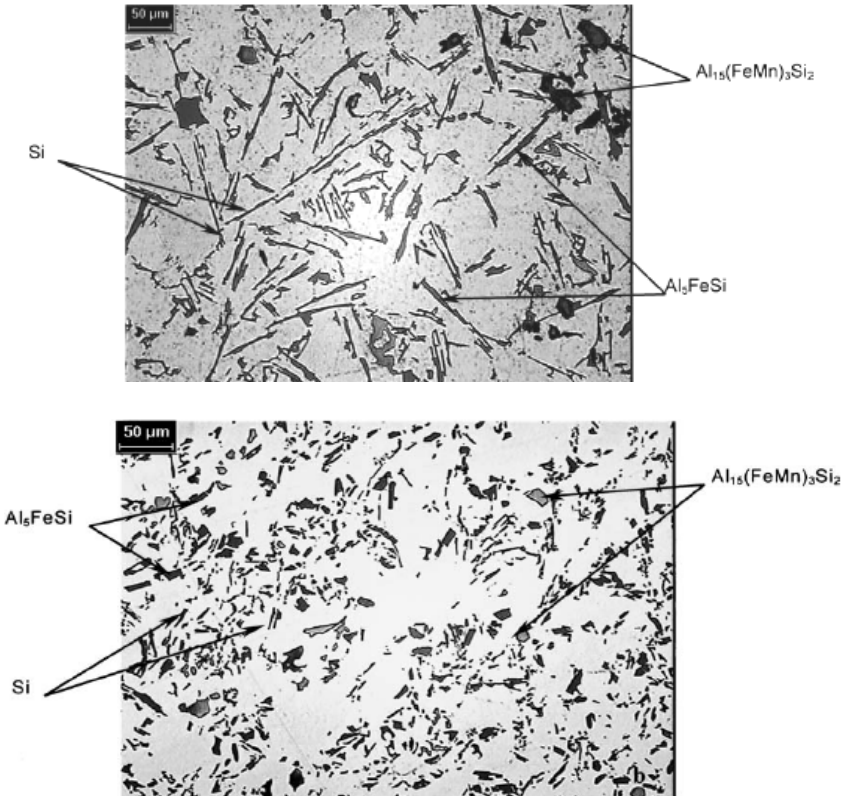

(a) As-cast A413

(b) A413 weld

Fig. 3.21. Influence of FSW on the intermetallic particles distribution in cast Al-alloy [94]

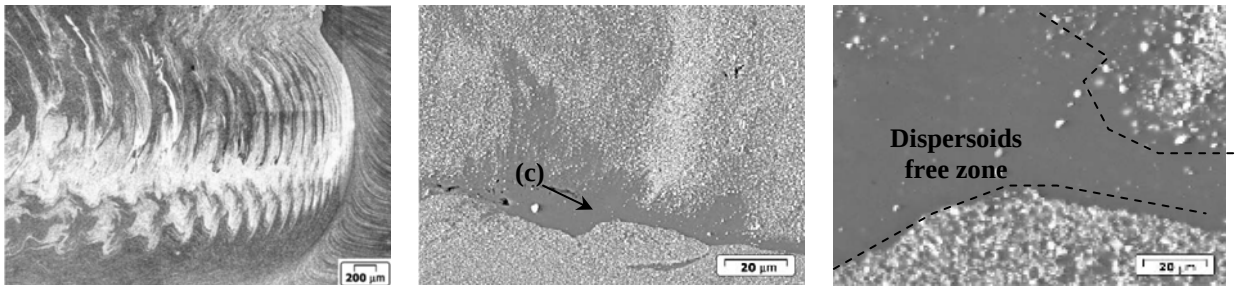

(a) (b) (c)

Fig. 3.22. Micrographs of AA8009 weld showing (a) the banded structure towards the AS and WN/TMAZ boundary, (b) segregated dispersoids surrounding a dispersoids free zone (arrowed), and as shown in (c) [91]

It was reported that the mechanical break-up of particles and the elimination of porosity in cast alloys during FSW resulted in an improvement in the mechanical properties of the weld. Lee *et al.* [93] reported a 20% improvement in the strength of FSWed A356 alloy in full weld tensile specimens, parallel to the feed direction, in comparison to the base alloy. Similarly, Rodriguez *et al.* [94] reported an increase of 15% in the hardness of the WN of A319 and A413 cast alloys. They attributed this increase to the strengthening contribution of the fragmented particles. Both studies employed relatively high rotation speeds (1000-1600 rpm) to ensure homogeneous particle break-up.

As shown in various reports, FSW disturbs the particle structure by breaking-up the intermetallic particles in the basemetal. Nonetheless, the final distribution does not always result in a homogeneous distribution, which is a key feature that associates local variations in particle distribution in the weld with the formation of the onion rings structure.

3.5.3. Onion Rings Structure

The term ‘onion rings’, first given by Threadgill [4], refers to the existence of a preferentially-etched region of concentric ellipses or randomly-oriented bands in the TMAZ/WN of welds. The ‘onion rings’ structure has been observed in various monolithic and dissimilar Al-based alloys [2, 4, 10, 64, 75-78, 80, 91, 93, 96, 97, 103, 104]. The reason for their existence has been variously attributed to grain size variations [10, 76, 77], distribution of intermetallic particles [2, 10, 64, 76, 77, 91, 93], alternating material layers in dissimilar welds [104], material flow around the tool [64, 96, 97, 103], or differences in texture between the bands

[96, 97], which ultimately resulted in the distinguishable etching response. Nonetheless, full understanding of the reasons behind its occurrence remains uncertain.

Grain size variations were first reported by Mahoney *et al*. [10], who found that the onion ring bands within the WN of 7075-T651 weld contained alternating bands of coarse grains (5-10 μm) and fine grains (3-5 μm), with the coarse grain bands having a lower volume fraction of Cr-rich dispersoids and $MgZn_2$ precipitates. Sutton and co-workers [76, 77] also observed a periodic variation in grain size, constituent particle, and hardness distributions across the bands in 2024-T351 and 2524-T351 welds. They performed microstructural studies on horizontal sections of the weld [76], as well as the weld face [77] for various welding parameters. In general, the grain size and the difference between the average grain sizes across the coarse and fine bands were found to increase with an increase in the peak temperature as expected for the range of welding parameters investigated (120 to 480 rpm and 51 to 267 mm/min). The constituent particles identified (Cu-rich and (Fe,Mn,Cu)-rich) were found to segregate in bands that were clearly distinguished from the weld crown towards the base (Fig. 3.23). On the weld face, it was found that the volume fraction and size of the particle decreased from 0.04 and 7 μm in the base alloy to a minimum of ~0.01 and 4 μm in the WN (towards the AS). As the thermal exposure only is not expected dissolve the constituent particles to that extent, the particle development was thus attributed to the mechanical break-up of the coarse particles [77].

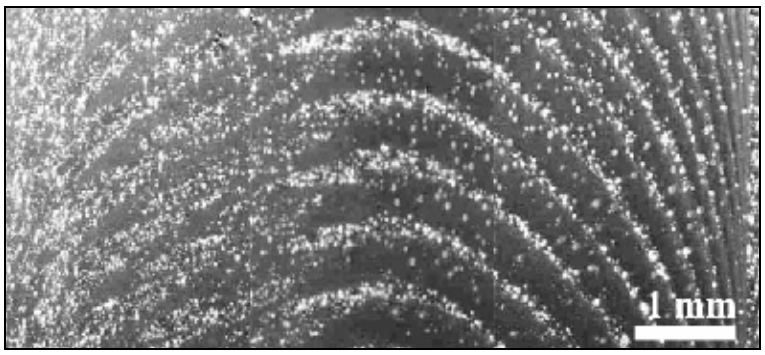

Fig. 3.23. Segregation of the intermetallic particles in bands on the weld crown of AA2024-T351 weld, welded at 200 mm/min and 360 rpm [76]

The grain size banding was also observed by Jin *et al.* within the WN of 5754 weld [78]. A 20-50 μm thick band of very fine grains (2 μm) was observed surrounded by coarser grains (8.3 μm). In contrast to the previous studies, the fine grains band was found to coincide with the existence of fragmented Al_2O_3 particles. However, there was no continuous oxide film at the boundary between the fine grains band and the surrounding regions. Neither the size of the particles, nor their role in causing the grain size banding, were indicated by the authors. It was suggested that the source of these particles comes from the base plate surface oxide layer.

Krishnan [103] presented an explanation for the existence of the onion rings. By investigating this phenomenon on the macro-scale in 6061 and 7075 welds welded between 400-1440 rpm and 120-288 mm/min, he suggested that material flow around the tool results in the extrusion of semi-cylindrical material layers behind the tool, where the spacing between the extruded layers equals the APR value. Thus, on sectioning the weld, the onion rings appear. Earlier, Biallas *et al.* [64] investigated the appearance of the rings in 2024-T3 welds welded within a range of parameters of 800 to 2400 rpm and 80 to 240 mm/min, yet at a constant APR. As shown in Fig. 3.24, there was a change in the morphology of the rings, tending to vanish with the increase in rotation speed and feed rate, which disagrees with the explanation suggested by Krishnan. They attributed the formation of the onion rings to the reflection of the stirred material layers on the walls of the groove that would hypothetically form if the tool was milling through the material. This reflection would form concentric tubes of decreasing radii at the wake of the tool. It was also indicated that the rings contain fragmented and segregated constituent particles, which are expected to be more effectively broken with the increase in rotation speed.

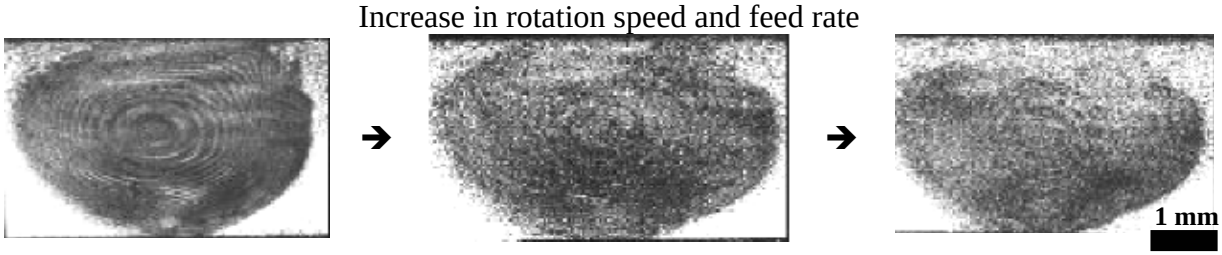

Fig. 3.24. Influence of the process parameters on the onion rings morphology in 2024-T3 [64]

More recently, a new hypothesis has been proposed that the origin of the 'onion rings' structure (i.e. the selective etching response) can be attributed to differences in orientation texture. Schneider and Nunes [97] performed texture measurements across the 'onion rings' in 2195-T8 weld welded using 200 rpm and 152 mm/min. They suggested that the material flow during FSW results from the superposition of two complex flow fields; one associated with the forward motion of the tool and the other with the rotational motion. It was reported that some parts of the weld were found to have a strong shear fibre orientation texture with the {111} poles aligned with the axis of rotation of the tool, and others a randomly oriented texture, which was attributed to the intermittent deposition of stirred material behind the tool along with the motion causing a shear discontinuity followed by sudden recrystallisation. However, Prangnell and Heason [96] reported that the difference in texture between the bands is only a difference in the shear plane/direction, with all the bands showing a generally similar {112}<110> texture. Still, they attributed the variations to the material flow around the tool and the APR since the bands (on the surface) were related to the APR.

Despite the various studies on characterising the 'onion rings' structure, a full explanation giving the causes behind its origin has not yet been presented. As reported, the rings may be associated with the complex material flow around the tool associated with the linear advance and rotation, or as represented by the APR. The rings could also be regarded as regions of microstructural heterogeneity in terms of the grain size bimodality, particles segregation, precipitation, and/or textural effects.

3.6. Hardness Development

In heat-treatable alloys, the hardness is primarily controlled by the thermally-induced dissolution and precipitation processes, which are essentially controlled by the thermal profile, whereas in work-hardenable alloys, the hardness is a balance of various influences; grain size, particles, solutes and dislocation hardening.

3.6.1. Heat Treatable Al-Alloys welds

Three characteristic microstructural features of welds are associated with the hardness development of the weld; the fine grain structure resulting from DRX, mechanical break-up of constituent particles, and dissolution/precipitation processes of hardening phases and dispersoids. The relative contribution of a specific microstructural strengthening factor depends on type of the alloy (i.e. work (strain) hardenable or precipitation (age) hardenable).

Sato and co-workers [11, 86, 87] studied the microstructural and hardness development in 6063-T4 and T5 welds as a function of the rotation speed, as well as the precipitate morphology within different regions of the weld. First, FSW was found to create a softened region (SOF) within the WN, with the hardness reaching its minimum close to the solution-treated hardness at the TMAZ/HAZ boundary as shown in Fig. 3.25. Beyond the minimum, the hardness was found to increase with the decrease in the thermal field experienced during FSW away from the tool and shoulder. The increase in rotation speed from 800 to 2450 rpm did not change the general trend, but it slightly influenced the width of the softened region and the HAZ hardness [11, 86]. It can be noticed that the softened region width increased from 10 mm to 18 mm by increasing in rotation speed from 800 to 2450 rpm, which reflects the localised nature of the heat source in FSW.

This hardness trend was related to the *in-situ* dissolution and re-precipitation processes that took place during FSW. Although the grain size within the softened region was ~20 μm, compared to ~60-80 μm within the HAZ/BM, the precipitation strengthening influence of the $\beta'' - \beta'$ precipitates was the dominant factor in controlling the weld strength rather than the grain size. TEM investigations for the four regions (Fig. 3.26) revealed that the morphology of the SOF region was similar to the morphology of the solution-treated condition, showing complete dissolution of the strengthening precipitates. On the other hand, the MIN, LOW and

BM regions were found to contain two types of precipitates; ~40 nm long needle-like precipitates with high coherency giving a major strengthening contribution, and ~200 nm long rod-like precipitates of low coherency giving accordingly a minor strengthening contribution [11]. The high volume fraction of rod-like precipitates at the minimum hardness location (MIN) was the reason for its low hardness, compared to needle-like precipitates observed in both LOW and BM. Post-weld aging was also found to significantly improve the hardness distribution [11].

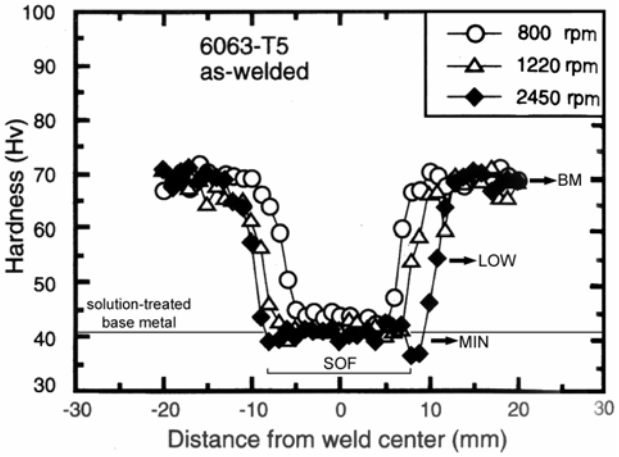

Fig. 3.25. Hardness traces at mid-thickness across the weld face of AA6063-T5 welds welded at different rotation speeds, and a feed rate of 360 mm/min [86]

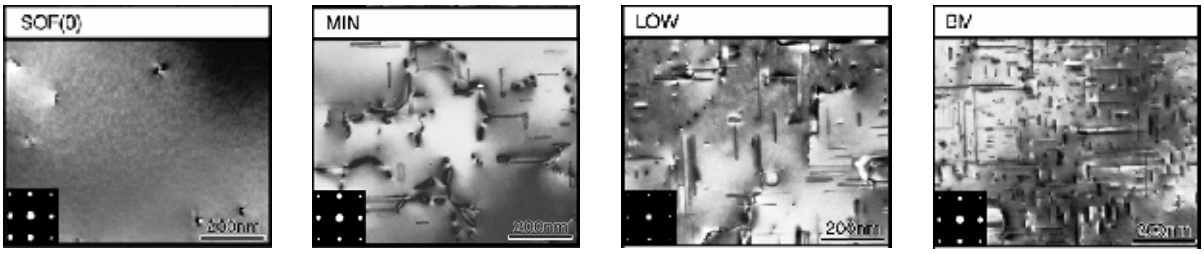

Fig. 3.26. TEM micrographs of various weld regions in 6063-T5 weld [87]

Liu *et al.* [84] also studied the hardness development in 6061-T6 weld by performing TEM investigations of various weld regions. The use of a relatively low rotation speed (400 rpm), meant that the maximum temperature experienced was ~425 ˚C. This caused the hardness trace to be more like a (W)-shaped trend (Fig. 3.27), with the hardness of the softened region at ~60-70 H_V, reaching a minimum of ~50 H_V at the HAZ/TMAZ boundary. The WN/TMAZ was found to contain a mixture of coherent, semi-coherent, and incoherent precipitates, instead of the SOF morphology observed in the previous study. Svensson *et al.* [83] also

observed a similar hardness profile. Thus, it appears that the process parameters do influence the shape of the hardness trace in 6xxx welds.

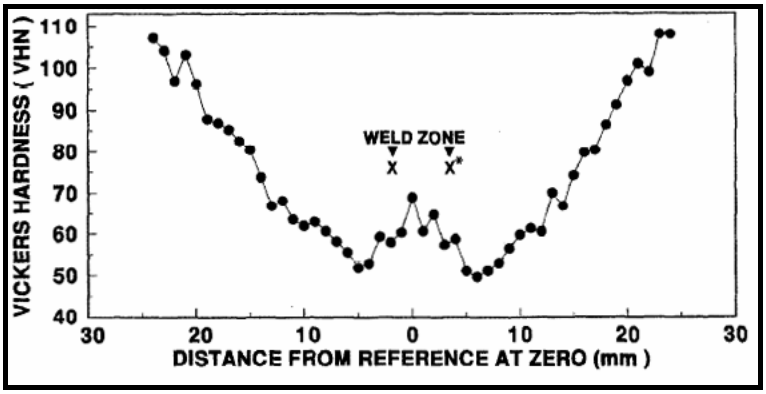

Fig. 3.27. Centreline microhardness trace at for 6061-T6 weld [84]

Ehrström *et al.* [66] studied the influence of artificial cooling on the hardness profiles in 2024-T351 and 7010-T7651, which is an important practice to minimise the thermal fields experienced by the HAZ in heat-treatable Al-alloys welds. The details of the artificial cooling approach were not mentioned, although it is believed that cooling was performed by liquid CO_2 spraying (typical for welds produced by BAE [105]). In 7010-T7651 weld, it was found that artificial cooling does not affect the hardness of the WN, whereas the HAZ width on each weld side decreased by ~3 mm when cooled. In 2024-T351 weld, the opposite happened with the hardness in the WN of the cooled weld being lower by ~10 H_V than the un-cooled weld. Artificial cooling decreased the temperature experienced during FSW, which minimised the amount of precipitates dissolved during welding. As a result, a smaller quantity of GP-zones formed following welding in the cooled weld. Benavides *et al.* [106] also reported similar trends in 2024 weld cooled with liquid nitrogen.

Recently, Genevois *et al.* [69, 70] utilised a more quantitative approach to study the structure-property development in 2024-T3 and T6 welds. They characterised the weld using differential scanning calorimetry (DSC), small-angle X-ray scattering (SAXS), and TEM to quantify the distribution of S'/S hardening precipitates and their influence on the hardness. SAXS measurements showed that there are three sub-regions within the HAZ of the T3-weld, which experienced full dissolution of the GP-zones (farthest from the TMAZ), dissolution of

GP-zones and precipitation of S' precipitates, and dissolution and precipitation of coarse S phase. Within these regions, the hardness was found to decrease, increase, followed by a significant decrease to a minimum point (at the TMAZ boundary) respectively. Within the TMAZ/WN, the high temperature, assisted by fragmentation of particles, dissolves most of the precipitates, which explains the increase in hardness in the TMAZ/WN after natural aging because of the formation of GP-zones. Such a distribution of the hardening precipitates is generally experienced in various alloys (e.g. 7075-T651 weld, Fig. 3.28 [10]), however SAXS enabled the quantification of the size, area fraction and distribution in a more convenient way compared to TEM.

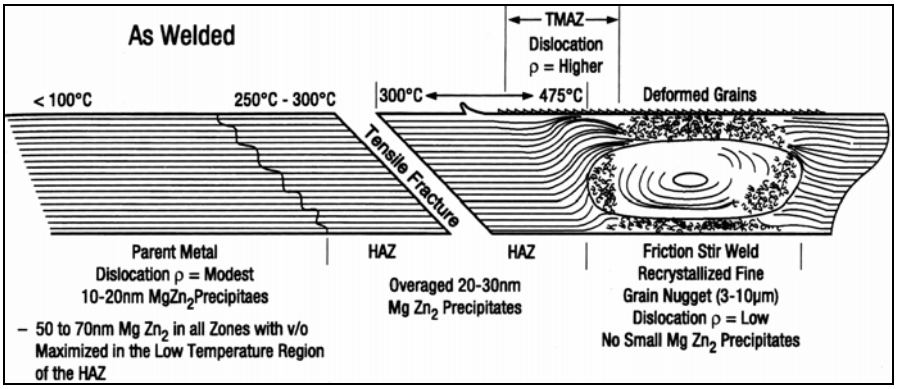

Fig. 3.28. Distribution of the hardening precipitates in 7075-T651 weld [10]

Modelling the structure-property development in heat treatable Al-alloys has been normally carried out using a mathematical model for the strength development in age-hardening Al-alloys during welding, established by Grong and Myhr [107-112]. This model describes the kinetics of the dissolution, re-precipitation and aging processes following non-isothermal cycles (e.g. welding). This is performed by dividing the thermal cycle into short isothermal steps, which are summed up to calculate an equivalent time of isothermal hold at a specific temperature. This equivalent time represents an equivalent 'kinetic strength' for the dissolution of the strengthening precipitates [107]. Calibration of the model for a specific alloy is carried out by producing master-curves showing the hardness development at different temperatures as a function of time. However, the model does not predict the microstructural development in terms of the distribution of the hardening phases.

This model was initially established for 6xxx alloys welds [109]. Then, it was successfully used by Frigaard *et al.* to model the hardness development in 6082-T6 and 7108-T79 friction stir welds. Hyoe *et al.* [113] also used the same approach in 7075-T7351, and similarly by Sullivan *et al.* [114] for 7449-T7, and Simar *et al.* in 6005A-T6 welds [115]. The approach was expanded by Shercliff and Russell [16, 116] expanded to 2xxx series (2014-T6) welds. One shortcoming that was highlighted by the work of Shercliff and Russell that this model can only be applied to T6 and T7 models, since it correlates the hardness change to the dissolution of the hardening phases, which were originally at their maximum volume fraction. Thus, it was not possible to use this model in Cu-containing alloys (e.g. 2024-T3) where thermal exposure could lead, not only to dissolution, but also to over-aging and artificial-aging [116]. To solve these concerns and to include more in-depth modelling of the microstructural development, Kamp *et al.* [117, 118] recently established an alternative model to predict the hardness development in 7xxx series friction stir welds by modelling the precipitate size and volume fraction development following thermal exposure. However, calibration of this model is more sophisticated as it requires more modelling and experimental tools (e.g. SAXS) to be fitted.

3.6.2. Work-Hardenable Al-Alloys welds

In work-hardenable Al-based alloys, two hardness trends can be observed depending on the starting condition of the material, particularly with respect to the HAZ development. In work-hardened conditions (e.g. rolled or plastically deformed), the HAZ experiences local softening associated with recovery and recrystallisation depending on the intensity of the thermal field. For the annealed (O) condition, the width of the HAZ becomes very limited and the hardness is nearly constant throughout the weld [4, 83]. Nonetheless, an increase in the hardness can still be observed within the TMAZ/WN in O-condition welds due to grain refinement by DRX [4, 81, 83, 119] (Fig. 3.29).

The same increase can also be observed in strain-hardened conditions within the WN, where the minimum hardness occurs within the HAZ. By comparing the hardness development within the TMAZ of annealed and severely plastically deformed 1100 alloy welds welded at 500 rpm and 720 mm/min, Sato *et al.* [120] showed that FSW treats both conditions similarly. This means that the influence of the stored energy in the basemetal on the structure-property

development is limited to the HAZ development, which means that the TMAZ/WN hardness development does not depend on the extent of the basemetal stored energy.

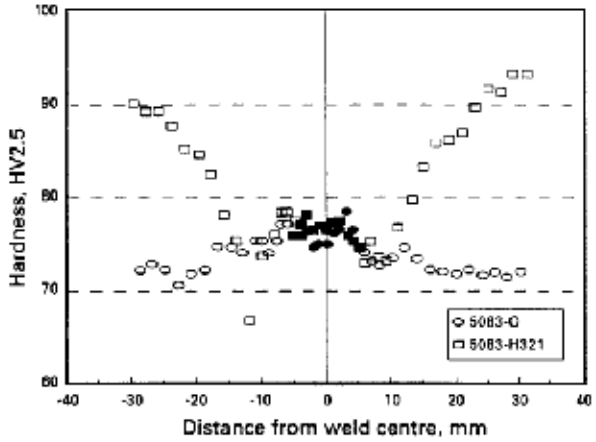

Fig. 3.29. Centreline hardness traces for 5083-O and H321 welds [4]

Studies on the microstructural and hardness development in work-hardenable Al-alloys welds were carried out by Sato and co-workers [12, 60, 61, 81, 82, 120, 121]. The weld strength has been related to the grain size using the Hall-Petch relationship [60, 61, 81, 82], and the influence of the submicron fragmented particles or dispersoids that block the dislocation movement (dislocation looping, Orowan hardening) [60, 82]. However, the dominance of a specific strengthening parameter was found to differ between various alloys. In 1080-O weld, it was possible to relate the TMAZ/WN hardness to the grain-size using the Hall-Petch relation. However, in 5083-O weld, grain-size strengthening was not sufficient to account for the TMAZ/WN hardness. One difference between the welds was that in the 5083-weld, the WN was observed to contain submicron $Al_6(Fe,Mn)$ dispersoids within the grains. These particles were surrounded by dislocations, compared to low-dislocation density precipitate-free WN in 1080-O weld as shown in Fig. 3.30.

It is evident that the preference of a specific strengthening mechanism is dependent on the basemetal. In 1080-O, 1050-O, and 5052-O welds, the hardness development within the weld could be explained by grain size strengthening using the Hall-Petch relation [60, 61, 81, 82]. However, in 5083-O, further strengthening by Orowan strengthening was necessary to account for some of the higher WN hardness than predicted by grain size. It was suggested though that an additional contribution from dislocation hardening should make up for any

remaining discrepancy, especially because it is the dominant mechanism in work-hardening alloys [83]. However, several studies have shown that a low dislocation density is observed in the WN [58, 60]. Further work is still needed to fill in the gaps related the contributions made by the different strengthening parameters in work-hardening Al-based alloys.

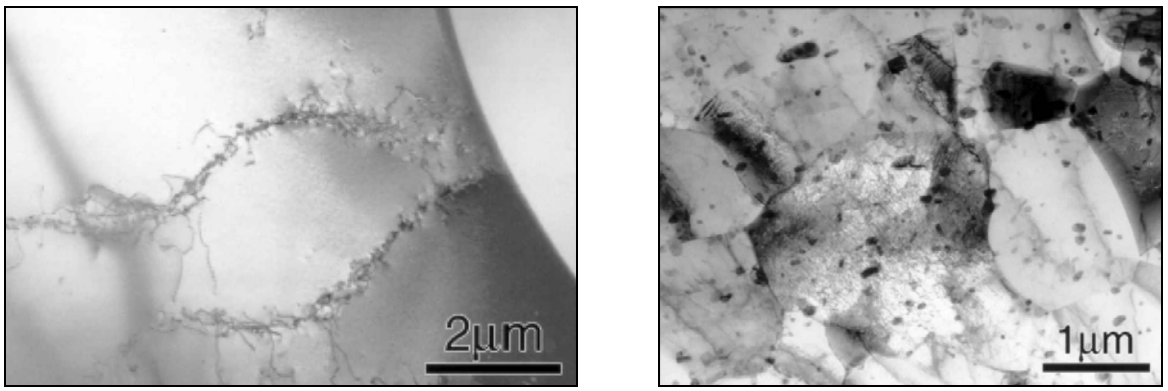

(a) 1080-O (b) 5083-O

Fig. 3.30. TEM micrographs for the microstructure in the WN [60]

Modelling the structure-property development, in the HAZ of work-hardenable Al-alloys welds, has only been recently performed by Peel *et al.* [122]. The hardness development is empirically represented by the relative softening (F_s), which is given as:

$$F_S = 1 - \left(\frac{H_{V\,HT} - H_{V\,FS}}{H_{V\,FH} - H_{V\,FS}} \right) \tag{3.10}$$

where $H_{V\,HT}$, $H_{V\,FS}$ and $H_{V\,FH}$ are the heat-treated, fully softened (O) and fully hardened conditions. Master-curves are also established, showing the softening development at different temperatures as a function of time, to determine the softening activation energy (Q). The researchers used an approach similar to the one established by Grong and Myhr [107-112] for heat-treatable alloys, by dividing the weld thermal cycle into short isothermal treatments. The short isothermal cycles (δt_i) at temperature T_i are then used to calculate an effective time (t_{eff}) using:

$$t_{eff} = \sum_i \delta t_i \exp\left(-Q/RT_i\right) \tag{3.11}$$

The effective time is then used to estimate the fraction softened using a modified version of the Johnson-Mehl-Avrami-Kolmogrov (JMAK) equation. This model, however, does not take into account the microstructural process that take place (i.e. recovery, recrystallisation and grain growth).

3.7. Summary of Literature: Key Findings and Areas of Investigation

This chapter summarises the modelling and experimental studies related to FSW. The following points summarise the current state of knowledge, highlighting the areas requiring further investigation.

- FSW of Al-based alloys is a solid-state welding process which produces a localised thermal field, with welding occurring between 400 and 550˚C. The heat input increases with an increase in the rotation speed, a decrease in the feed rate, and an increase in the plunge depth. The alloy type does not seem to strongly influence the weld temperature.
- Several analytical and numerical models have been developed to predict the FSW heat generation and thermal fields. Heat generation is believed to occur by a combination of plastic deformation and friction, although models have been developed using each scenarios, producing reliable predictions, yet with rigorous fitting.
- Material flow during FSW occurs by repeated deposition of sheared material from in front to behind the tool, with mixing occurring under the tool shoulder. MIT experiments, however, failed to agree on an explanation for the onion rings or the vertical striations observed on the sectional view.
- FSW results in a drastic microstructural development in the grain and particle structures. The constituent particles are fragmented and re-distributed during FSW. DRX occurs within the WN producing fine grains, although the exact DRX mechanism is still debated. Different levels of the dislocation density were also observed, with dislocation-free grains observed in pure alloys, compared to high densities in particle-containing alloys. Generally, quantitative microstructural studies of the FSW microstructural development are limited.
- The onion rings structure has been observed in various alloys, and was linked to grain size and particle variations. Some explanations attributed this phenomenon to the material flow or textural effects associated with FSW, although these explanations do not explain the reason for the microstructural heterogeneities associated with it.
- In heat-treatable alloys welds, the hardness was reported to be controlled by the thermally-induced dissolution and precipitation processes, whereas in work-hardenable alloys, the hardness was variably linked to the influence of grain size and particle strengthening.

The work presented in this dissertation studies the microstructure-property development in FSW, with a special attention on the influence of the basemetal microstructural parameters. Accordingly, the following areas have been identified for investigation:

- Thermal modelling of FSW, with experimental verification using thermocouple measurements and microstructural studies, while minimising the fitting effort and parameters required, to obtain reasonable predictions.
- The influence of the basemetal processing route condition on the microstructural development due to FSW; focusing on:
    - Quantifying the grain and particle structure development.
    - The development of the onion rings structure and the possible parameters controlling its formation.
    - The dislocation structure development in the WN.
- Quantifying the structure-property relations in 5xxx series welds.

3.8. References

[1] W. M. Thomas, E. D. Nicholas, J. C. Needham, M. G. Nurch, P. Temple-Smith, and C. Dawes, "Patents on Friction Stir Butt Welding," International: PCT/GB92/02203; British: 9125978.8; USA: 5460317., 1991-1995.

[2] R. S. Mishra and Z. Y. Ma, "Friction stir welding and processing," *Materials Science and Engineering: R: Reports*, vol. 50, pp. 1-78, 2005.

[3] W. M. Thomas and E. D. Nicholas, "Friction stir welding for the transportation industries," *Materials & Design*, vol. 18, pp. 269-273, 1997.

[4] P. Threadgill, "Friction Stir Welds in Aluminium Alloys: Preliminary Microstructural Assessment," *TWI Bulletin*, vol. 38, pp. 30-33, 1997.

[5] W. J. Arbegast, "Modeling friction stir joining as a metal working process," presented at Hot Deformation of Aluminum Alloys III, San Diego, CA, United States, 2003.

[6] H. G. Salem, "Friction stir weld evolution of dynamically recrystallized AA 2095 weldments," *Scripta Materialia*, vol. 49, pp. 1103-1110, 2003.

[7] T. U. Seidel and A. P. Reynolds, "Visualization of the material flow in AA2195 friction-stir welds using a marker insert technique," *Metallurgical and Materials Transactions A: Physical Metallurgy and Materials Science*, vol. 32, pp. 2879-2884, 2001.

[8] K. Colligan, "Material flow behavior during friction stir welding of aluminum," *Welding Journal (Miami, Fla)*, vol. 78, pp. 229-237, 1999.

[9] J. H. Record, J. L. Covington, T. W. Nelson, C. D. Sorensen, and B. W. Webb, "Fundamental Characterization of Friction Stir Welding," presented at 5th International Symposium on Friction Stir Welding, Metz, France, 2004.

[10] M. W. Mahoney, C. G. Rhodes, J. G. Flintoff, R. A. Spurling, and W. H. Bingel, "Properties of friction-stir-welded 7075 T651 aluminum," *Metallurgical and Materials Transactions A: Physical Metallurgy and Materials Science*, vol. 29A, pp. 1955-1964, 1998.

[11] Y. S. Sato, M. Urata, and H. Kokawa, "Parameters Controlling Microstructure and Hardness during Friction-Stir Welding of Precipitation-Hardenable Aluminum Alloy 6063," *Metallurgical and Materials Transactions A*, vol. 33, pp. 625-635, 2002.

[12] Y. S. Sato, H. Watanabe, S. H. C. Park, and H. Kokawa, "Grain Growth in Friction Stir Welded Al Alloy 1100 during Postweld Heat Treatment," presented at 5th International Symposium on Friction Stir Welding, Metz, France, 2005.

[13] W. Tang, X. Guo, J. C. McClure, L. E. Murr, and A. Nunes, "Heat input and temperature distribution in friction stir welding," *Journal of Materials Processing and Manufacturing Science*, vol. 7, pp. 163-172, 1998.

[14] Ø. Frigaard, Ø. Grong, and O. T. Midling, "A process model for friction stir welding of age hardening aluminum alloys," *Metallurgical and Materials Transactions A: Physical Metallurgy and Materials Science*, vol. 32, pp. 1189-1200, 2001.

[15] R. V. Preston, H. R. Shercliff, P. J. Withers, and S. D. Smith, "Finite element modelling of tungsten inert gas welding of aluminium alloy 2024," *Science and Technology of Welding & Joining*, vol. 8, pp. 10-18, 2003.

[16] M. J. Russell and H. R. Shercliff, "Analytical Modelling of Microstructure Development in Friction Stir Welding," presented at the First International Symposium on Friction Stir Welding, Rockwell Science Center, Thousand Oaks, CA, 1999.

[17] H. R. Shercliff and P. A. Colegrove, "Modelling of Friction Stir Welding," in *Mathematical Modelling of Weld Phenomena*, vol. 6, H. Cerjak and H. K. H. D. Bhadeshia, Eds. London: Maney Publishing, 2002, pp. 927–974.

[18] H. Schmidt, J. Hattel, and J. Wert, "An analytical model for the heat generation in friction stir welding," *Modelling and Simulation in Materials Science and Engineering*, vol. 12, pp. 143-157, 2004.

[19] T. U. Seidel and A. P. Reynolds, "A 2-D friction stir welding process model based on fluid mechanics," *Science and Technology of Welding and Joining*, vol. 8, pp. 175-183, 2003.

[20] P. A. Colegrove and H. Shercliff, "Experimental and numerical analysis of aluminium alloy 7075-T7351 friction stir welds," *Science and Technology of Welding and Joining*, vol. 8, pp. 360–368, 2003.

[21] P. A. Colegrove and H. R. Shercliff, "3-Dimensional CFD modelling of flow round a threaded friction stir welding tool profile," *Journal of Materials Processing Technology*, vol. 169, pp. 320-327, 2005.

[22] P. A. Colegrove, M. Painter, D. Graham, and T. Miller, "3-dimensional flow and thermal modelling of the friction stir welding process," presented at 2nd International Symposium on Friction Stir Welding, Gothenburg, Sweden, 2000.

[23] M. Song and R. Kovacevic, "Numerical and experimental study of the heat transfer process in friction stir welding," *Proceedings of the Institution of Mechanical Engineers, Part B: Journal of Engineering Manufacture*, vol. 217, pp. 73-85, 2003.

[24] A. P. Reynolds, Z. Khandkar, T. Long, W. Tang, and J. Khan, "Utility of relatively simple models for understanding process parameter effects on FSW," presented at Thermec 2003 Processing and Manufacturing of Advanced Materials, Jul 7-11 2003, Madrid, Spain, 2003.

[25] A. Simar, T. Pardoen, and B. d. Meester, "Influence of the friction stir welding parameters on the power input and temperature distribution in Aluminium alloys," presented at 5th International Symposium on Friction Stir Welding, Metz, France, 2004.

[26] F. Palm, U. Henneböhle, V. Erofeev, E. Karpuchin, and O. Zaitzev, "Improved Verification of FSW-Process Modelling Relating to the Origin of Material Plasticity," presented at 5th International Symposium on Friction Stir Welding, Metz, France, 2004.

[27] P. Vilaca, L. Quintino, and J. F. Dos Santos, "ISTIR - Analytical thermal model for friction stir welding," *Journal of Materials Processing Technology*, vol. 169, pp. 452-465, 2005.

[28] D. Rosenthal, "The Theory of Moving Source of Heat and its Application to Metal Transfer," *Transactions ASME*, vol. 43, pp. 849-866, 1946.

[29] Y. J. Chao and X. Qi, "Heat Transfer and Thermo-Mechanical Modeling of Friction Stir Welding Joining of AA6061-T6 Plates," presented at the First International Symposium on Friction Stir Welding, Rockwell Science Center, Thousand Oaks, CA, 1999.

[30] Y. J. Chao, X. Qi, and W. Tang, "Heat transfer in friction stir welding-experimental and numerical studies," *Transactions of the ASME. Journal of Manufacturing Science and Engineering*, vol. 125, pp. 138-145, 2003.

[31] R. Kovacevic, V. Soundararajan, and S. Zekovic, "Thermo-mechanical model with adaptive boundary conditions for friction stir welding of Al 6061," *International Journal of Machine Tools & Manufacture*, vol. 45, pp. 1577-1587, 2005.

[32] H. Schmidt and J. Hattel, "A local model for the thermomechanical conditions in friction stir welding," *Modelling and Simulation in Materials Science and Engineering*, vol. 13, pp. 77-93, 2005.

[33] S. Xu and X. Deng, "A Three-Dimensional Model for the Friction-Stir Welding Process," presented at 21st Southeastern Conference on Theoretical and Applied Mechanics (SECTAM XXI), Orlando, Florida, 2002.

[34] A. Askari, S. Silling, B. London, and M. Mahoney, "Modeling and analysis of friction stir welding processes," presented at Proceedings of Symposium on Friction Stir Welding and Processing, Nov 4-8 2001, Indianapolis, IN, United States, 2001.

[35] P. Heurtier, M. J. Jones, C. Desrayaud, J. H. Driver, F. Montheillet, and D. Allehaux, "Mechanical and thermal modelling of Friction Stir Welding," *Journal of Materials Processing Technology*, vol. 171, pp. 348-357, 2006.

[36] H. N. B. Schmidt, T. L. Dickerson, and J. H. Hattel, "Material flow in butt friction stir welds in AA2024-T3," *Acta Materialia*, vol. 54, pp. 1199-1209, 2006.

[37] P. A. Colegrove and H. R. Shercliff, "CFD modelling of friction stir welding of thick plate 7449 aluminium alloy," *Science and Technology of Welding and Joining*, vol. 11, pp. 429, 2007.

[38] P. A. Colegrove, H. R. Shercliff, and R. Zettler, "Model for predicting heat generation and temperature in friction stir welding from the material properties," *Science and Technology of Welding and Joining*, vol. 12, pp. 284, 2007.

[39] M. Song and R. Kovacevic, "Thermal modeling of friction stir welding in a moving coordinate system and its validation," *International Journal of Machine Tools and Manufacture*, vol. 43, pp. 605-615, 2003.

[40] S. Xu and X. Deng, "Two and three dimensional finite element models for the friction stir welding process," presented at 4th International Symposium on Friction Stir Welding, Park City, Utah, 2003.

[41] G. J. Bendzsak, T. H. North, and C. B. Smith, "An Experimentally Validated 3D Model for Friction Stir Welding," presented at 2nd International Symposium on Friction Stir Welding, Gothenburg, Sweden, 2000.

[42] P. A. Colegrove, H. R. Shercliff, and P. Threadgill, "Modelling and Development of Trivex™ Friction Stir Welding Tool," presented at The 4th International Symposium on Friction Stir Welding, Park City, Utah, USA, 2003.

[43] A. Mackwood, "TS4D User Guide," University of Essex, UK, 2001.

[44] P. A. Colegrove, "Modelling the Heat Generation, Temperature and Microstructure of Friction Stir Welds using Comsol Multiphysics," presented at Comsol Users Conference, Birmingham, UK, 2006.

[45] B. London, M. Mahoney, W. Bingel, M. Calabrese, R. H. Bossi, and D. Waldron, "Material flow in friction stir welding monitored with Al-SiC and Al-W composite markers," presented at Friction Stir Welding and Processing II. 2003, San Diego, CA, USA, 2003.

[46] R. Zettler, S. Lomolino, J. F. d. Santos, T. Donath, F. Beckmann, T. Lippman, and D. Lohwasser, "A Study on Material Flow in FSW of AA2024-T351 and AA6056-T4," presented at 5th International Symposium on Friction Stir Welding, Metz, France, TWI, Cambridge, 2004.

[47] Y. Li, L. E. Murr, and J. C. McClure, "Flow visualization and residual microstructures associated with the friction-stir welding of 2024 aluminum to 6061 aluminum," *Materials Science and Engineering A*, vol. 271, pp. 213-223, 1999.

[48] S. H. Kazi and L. E. Murr, "Complex flow phenomena associated with friction-stir welding of aluminum alloys," Indianapolis, IN, United States, 2001.

[49] M. Guerra, C. Schmidt, J. C. McClure, L. E. Murr, and A. C. Nunes, "Flow patterns during friction stir welding," *Materials Characterization*, vol. 49, pp. 95-101, 2002.

[50] W.-B. Lee, Y.-M. Yeon, and S.-B. Jung, "The joint properties of dissimilar formed Al alloys by friction stir welding according to the fixed location of materials," *Scripta Materialia*, vol. 49, pp. 423-428, 2003.

[51] J. H. Ouyang and R. Kovacevic, "Material flow and microstructure in the friction stir butt welds of the same and dissimilar aluminum alloys," *Journal of Materials Engineering and Performance*, vol. 11, pp. 51-63, 2002.

[52] Y. S. Sato, S. H. C. Park, M. Michiuchi, and H. Kokawa, "Constitutional liquation during dissimilar friction stir welding of Al and Mg alloys," *Scripta Materialia*, vol. 50, pp. 1233-1236, 2004.

[53] A. C. Somasekharan and L. E. Murr, "Microstructures in friction-stir welded dissimilar magnesium alloys and magnesium alloys to 6061-T6 aluminum alloy," *Materials Characterization*, vol. 52, pp. 49-64, 2004.

[54] J. Yan, X. Zhiwu, L. Zhiyuan, L. Lei, and Y. Shiqin, "Microstructure characteristics and performance of dissimilar welds between magnesium alloy and aluminum formed by friction stirring," *Scripta Materialia*, vol. 53, pp. 585-589, 2005.

[55] H. Uzun, C. Dalle Donne, A. Argagnotto, T. Ghidini, and C. Gambaro, "Friction stir welding of dissimilar Al 6013-T4 To X5CrNi18-10 stainless steel," *Materials and Design*, vol. 26, pp. 41-46, 2005.

[56] D. P. Field, T. W. Nelson, Y. Hovansky, and K. V. Jata, "Heterogeneity of Crystallographic Texture in Friction Stir Welds of Aluminum," *Metallurgical and Materials Transactions A*, vol. 32, pp. 2869-2877, 2001.

[57] O. V. Flores, C. Kennedy, L. E. Murr, D. Brown, S. Pappu, B. M. Nowak, and J. C. McClure, "Microstructural Issues in a Friction-Stir-Welded Aluminum Alloy," *Scripta Materialia*, vol. 38, pp. 703-708, 1998.

[58] L. E. Murr, G. Liu, and J. C. McClure, "Dynamic recrystallization in friction-stir welding of aluminum alloy 1100," *Journal of Materials Science Letters*, vol. 16, pp. 1801-1803, 1997.

[59] N. Saito, I. Shigematsu, T. Komaya, T. Tamaki, G. Yamauchi, and M. Nakamura, "Grain refinement of 1050 aluminum alloy by friction stir processing," *Journal of Materials Science Letters*, vol. 20, pp. 1913-1915, 2001.

[60] Y. S. Sato, S. H. C. Park, and H. Kokawa, "Microstructural factors governing hardness in friction-stir welds of solid-solution-hardened Al alloys," *Metallurgical and Materials Transactions A: Physical Metallurgy and Materials Science*, vol. 32, pp. 3033-3042, 2001.

[61] Y. S. Sato, M. Urata, H. Kokawa, and K. Ikeda, "Hall-Petch relationship in friction stir welds of equal channel angular-pressed aluminium alloys," *Materials Science and Engineering A*, vol. 354, pp. 298-305, 2003.

[62] Y. S. Sato, F. Yamashita, Y. Sugiura, S. H. C. Park, and H. Kokawa, "FIB-assisted TEM study of an oxide array in the root of a friction stir welded aluminium alloy," *Scripta Materialia*, vol. 50, pp. 365-369, 2004.

[63] H. Liu, M. Maeda, H. Fujii, and K. Nogi, "Tensile properties and fracture locations of friction-stir welded joints of 1050-H24 aluminum alloy," *Journal of Materials Science Letters*, vol. 22, pp. 41-43, 2003.

[64] G. Biallas, R. Braun, C. Dalle Donne, G. Staniek, and W. A. Kaysser, "Mechanical Properties and Corrosion Behavior of Friction Stir Welded 2024-T3," presented at 1st International Symposium on Friction Stir Welding, Thousand Oaks, CA, USA, 1999.

[65] I. Charit and R. S. Mishra, "High strain rate superplasticity in a commercial 2024 Al alloy via friction stir processing," *Materials Science and Engineering A*, vol. 359, pp. 290-296, 2003.

[66] J. C. Ehrstrom, A. Bigot, L. Cervi, and H. Gerard, "Microstructure and properties of aluminum alloys friction stir welds for aircraft application," Leganes, Madrid, Spain, 2003.

[67] R. W. Fonda and J. F. Bingert, "Microstructural evolution in the heat-affected zone of a friction stir weld," *Metallurgical and Materials Transactions A: Physical Metallurgy and Materials Science*, vol. 35 A, pp. 1487-1499, 2004.

[68] R. W. Fonda, J. F. Bingert, and K. J. Colligan, "Development of grain structure during friction stir welding," *Scripta Materialia*, vol. 51, pp. 243-248, 2004.

[69] C. Genevois, A. Deschamps, A. Denquin, and B. Doisneau-cottignies, "Quantitative investigation of precipitation and mechanical behaviour for AA2024 friction stir welds," *Acta Materialia*, vol. 53, pp. 2447-2458, 2005.

[70] C. Genevois, A. Deschamps, and P. Vacher, "Comparative study on local and global mechanical properties of 2024 T351, 2024 T6 and 5251 O friction stir welds," *Materials Science and Engineering: A*, vol. 415, pp. 162-170, 2006.

[71] K. V. Jata and S. L. Semiatin, "Continuous dynamic recrystallization during friction stir welding of high strength aluminum alloys," *Scripta Materialia*, vol. 43, pp. 743-749, 2000.

[72] H. J. Liu, H. Fujii, M. Maeda, and K. Nogi, "Tensile properties and fracture locations of friction-stir-welded joints of 2017-T351 aluminum alloy," *Journal of Materials Processing Technology*, vol. 142, pp. 692-696, 2003.

[73] W. D. Lockwood, B. Tomaz, and A. P. Reynolds, "Mechanical response of friction stir welded AA2024: Experiment and modeling," *Materials Science and Engineering A*, vol. 323, pp. 348-353, 2002.

[74] M. Strangwood, J. E. Berry, D. P. Cleugh, A. J. Leonard, and P. L. Threadgill, "Characterisation of the Thermo-mechanical Effects on Microstructural Development in Friction Stir Welded Age Hardening Aluminium-based Alloys," presented at 1st International Symposium on Friction Stir Welding, Thousand Oaks, CA, USA, 1999.

[75] M. A. Sutton, B. Yang, A. P. Reynolds, and J. Yan, "Banded microstructure in 2024-T351 and 2524-T351 aluminum friction stir welds. Part II. Mechanical characterization," *Materials Science and Engineering A*, vol. 364, pp. 66-74, 2004.

[76] M. A. Sutton, B. Yang, A. P. Reynolds, and R. Taylor, "Microstructural studies of friction stir welds in 2024-T3 aluminum," *Materials Science and Engineering A*, vol. 323, pp. 160-166, 2002.

[77] B. Yang, J. Yan, M. A. Sutton, and A. P. Reynolds, "Banded microstructure in AA2024-T351 and AA2524-T351 aluminum friction stir welds. Part I. Metallurgical studies," *Materials Science and Engineering A*, vol. 364, pp. 55-65, 2004.

[78] H. Jin, S. Saimoto, M. Ball, and P. L. Threadgill, "Characterisation of microstructure and texture in friction stir welded joints of 5754 and 5182 aluminium alloy sheets," *Materials Science and Technology*, vol. 17, pp. 1605-1614, 2001.

[79] I. Charit and R. S. Mishra, "Evaluation of microstructure and superplasticity in friction stir processed 5083 Al alloy," *Journal of Materials Research*, vol. 19, pp. 3329-3342, 2004.

[80] M. Peel, A. Steuwer, M. Preuss, and P. J. Withers, "Microstructure, mechanical properties and residual stresses as a function of welding speed in aluminium AA5083 friction stir welds," *Acta Materialia*, vol. 51, pp. 4791-4801, 2003.

[81] Y. S. Sato, Y. Sugiura, and H. Kokawa, "Hardness Distribution and Microstructure in Friction Stir Weld of Aluminum Alloy 5052," presented at 4th International Symposium on Friction Stir Welding, Park City, Utah, USA, 2003.

[82] Y. S. Sato, Y. Sugiura, Y. Shoji, S. H. C. Park, H. Kokawa, and K. Ikeda, "Post-weld formability of friction stir welded Al alloy 5052," *Materials Science and Engineering A*, vol. 369, pp. 138-143, 2004.

[83] L.-E. Svensson, L. Karlsson, H. Larsson, B. Karlsson, M. Fazzini, and J. Karlsson, "Microstructure and Mechanical Properties of Friction Stir Welded Aluminium Alloys with Special Reference to AA 5083 and AA 6082 aluminium," *Science and Technology of Welding and Joining*, vol. 5, pp. 285-296, 2000.

[84] G. Liu, L. E. Murr, C. S. Niou, J. C. McClure, and F. R. Vega, "Microstructural aspects of the friction-stir welding of 6061-T6 aluminum," *Scripta Materialia*, vol. 37, pp. 355-361, 1997.

[85] O. V. Mishin, A. Godfrey, and L. Ostensson, "Comparative microstructural characterization of a friction-stir-welded aluminum alloy using TEM and SEM-based techniques," *Metallurgical and Materials Transactions A: Physical Metallurgy and Materials Science*, vol. 37A, pp. 489-496, 2006.

[86] Y. S. Sato, H. Kokawa, M. Enomoto, and S. Jogan, "Microstructural evolution of 6063 aluminum during friction-stir welding," *Metallurgical and Materials Transactions A: Physical Metallurgy and Materials Science*, vol. 30, pp. 2429-2437, 1999.

[87] Y. S. Sato, H. Kokawa, M. Enomoto, S. Jogan, and T. Hashimoto, "Precipitation sequence in friction stir weld of 6063 aluminum during aging," *Metallurgical and Materials Transactions A: Physical Metallurgy and Materials Science*, vol. 30A, pp. 3125-3130, 1999.

[88] K. V. Jata, K. K. Sankaran, and J. J. Ruschau, "Friction Stir Welding Effects on Microstructure and Fatigue of Aluminum Alloy 7050-T7461," *Metallurgical and Materials Transactions A*, vol. 31, pp. 2181-2192, 2000.

[89] C. G. Rhodes, M. W. Mahoney, W. H. Bingel, R. A. Spurling, and C. C. Bampton, "Effect of friction stir welding on microstructure of 7075 aluminum," *Scripta Materialia*, vol. 36, pp. 69-75, 1997.

[90] J.-Q. Su, T. W. Nelson, R. Mishra, and M. Mahoney, "Microstructural investigation of friction stir welded 7050-T651 aluminium," *Acta Materialia*, vol. 51, pp. 713-729, 2003.

[91] W. Baeslack, K. Jata, and T. Lienert, "Structure, properties and fracture of friction stir welds in a high-temperature Al-8.5Fe-1.3V1.7Si alloy (AA-8009)," *Journal of Materials Science*, vol. 41, pp. 2939-2951, 2006.

[92] M. B. D. Ellis and M. Strangwood, "Welding of rapidly solidified alloy 8009 (Al-8.5Fe-1.7Si-1.3V): preliminary study," *Materials Science and Technology*, vol. 12, pp. 970-977, 1996.

[93] W. B. Lee, Y. M. Yeon, and S. B. Jung, "The improvement of mechanical properties of friction-stir-welded A356 Al alloy," *Materials Science & Engineering A: Structural Materials: Properties, Microstructure and Processing*, vol. A355, pp. 154-159, 2003.

[94] N. A. Rodriguez, E. Almanza, C. J. Alvarez, and L. E. Murr, "Study of friction stir welded A319 and A413 aluminum casting alloys," *Journal of Materials Science*, vol. 40, pp. 4307-4312, 2005.

[95] Y. Li, L. E. Murr, and J. C. McClure, "Solid-state flow visualization in the friction-stir welding of 2024 Al to 6061 Al," *Scripta Materialia*, vol. 40, pp. 1041-1046, 1999.

[96] P. B. Prangnell and C. P. Heason, "Grain structure formation during friction stir welding observed by the 'stop action technique'," *Acta Materialia*, vol. 53, pp. 3179-3192, 2005.

[97] J. A. Schneider and A. C. Nunes Jr., "Characterization of plastic flow and resulting microtextures in a friction stir weld," *Metallurgical and Materials Transactions B: Process Metallurgy and Materials Processing Science*, vol. 35, pp. 777-783, 2004.

[98] Z. Y. Ma, R. S. Mishra, and M. W. Mahoney, "Superplastic deformation behaviour of friction stir processed 7075 Al alloy," *Acta Materialia*, vol. 50, pp. 4419-4430, 2002.

[99] R. D. Doherty, D. A. Hughes, F. J. Humphreys, J. J. Jonas, D. J. Jensen, M. E. Kassner, W. E. King, T. R. McNelley, H. J. McQueen, and A. D. Rollett, "Current issues in recrystallization: a review," *Materials Science and Engineering A*, vol. 238, pp. 219-274, 1997.

[100] F. J. Humphreys and M. Hatherly, *Recrystallization and Related Annealing Phenomena*. Great Britain: Pergamon, 1995.

[101] L. Fratini and G. Buffa, "CDRX modelling in friction stir welding of aluminium alloys," *International Journal of Machine Tools & Manufacture*, vol. 45, pp. 1188-1194, 2005.

[102] Y. S. Sato, H. Kokawa, K. Ikeda, M. Enomto, S. Jogan, and T. Hashimoto, "Microtexture in the Friction Stir Weld of an Aluminum Alloy," *Metallurgical and Materials Transactions A*, vol. 32, pp. 941-948, 2001.

[103] K. N. Krishnan, "On the formation of onion rings in friction stir welds," *Materials Science and Engineering A*, vol. 327, pp. 246-251, 2002.

[104] Y. S. Sato, Y. Kurihara, and H. Kokawa, "Microstructural Characteristics of Dissimilar Butt Friction Stir Welds of AA7075 and AA2024," in *6th International Symposium on Friction Stir Welding*, vol. 2. St. Sauveur, Montreal, Canada: TWI, Cambridge, 2006, pp. 849-854.

[105] M. Jariyaboon, "PhD Thesis: Corrosion of Friction Stir Welds in High Strength Aluminium Alloys," in *Department of Metallurgy and Materials, University of Birmingham, UK*, 2005.

[106] S. Benavides, Y. Li, L. E. Murr, D. Brown, and J. C. McClure, "Low-temperature friction-stir welding of 2024 aluminum," *Scripta Materialia*, vol. 41, pp. 809-815, 1999.

[107] Ø. Grong, *Metallurgical Modelling of Welding*, 2nd ed. London: The Institute of Materials, 1997.

[108] Ø. Grong and O. R. Myhr, "Additivity and isokinetic behaviour in relation to diffusion controlled growth," *Acta Materialia*, vol. 48, pp. 445-452, 2000.

[109] O. R. Myhr and O. Grong, "Process modelling applied to 6082-T6 aluminium weldments--II. Applications of model," *Acta Metallurgica et Materialia*, vol. 39, pp. 2703-2708, 1991.

[110] O. R. Myhr and Ø. Grong, "Modelling of non-isothermal transformations in alloys containing a particle distribution," *Acta Materialia*, vol. 48, pp. 1605-1615, 2000.

[111] O. R. Myhr, O. Grong, and S. J. Andersen, "Modelling of the age hardening behaviour of Al-Mg-Si alloys," *Acta Materialia*, vol. 49, pp. 65-75, 2001.

[112] O. R. Myhr, O. Grong, H. G. Fjaer, and C. D. Marioara, "Modelling of the microstructure and strength evolution in al-mg-si alloys during multistage thermal processing," *Acta Materialia*, vol. 52, pp. 4997-5008, 2004.

[113] T. Hyoe, P. A. Colegrove, and H. R. Shercliff, "Thermal and microstructure modelling in thick plate aluminium alloy 7075 friction stir welds," San Diego, CA, USA, 2003.

[114] J. D. Robson, A. Sullivan, H. R. Shercliff, and G. McShane, "Microstructural Evolution During Friction Stir Welding of AA7449," presented at 5th International Symposium on Friction Stir Welding, Metz, France, 2004.

[115] A. Simar, Y. Bréchet, B. de Meester, A. Denquin, and T. Pardoen, "Sequential modeling of local precipitation, strength and strain hardening in friction stir welds of an aluminum alloy 6005A-T6," *Acta Materialia*, vol. 55, pp. 6133, 2007.

[116] H. R. Shercliff, M. J. Russell, A. Taylor, and T. L. Dickerson, "Microstructural modelling in friction stir welding of 2000 series aluminium alloys," *Mecanique & Industries*, vol. 6, pp. 25-35, 2005.

[117] N. Kamp, A. Sullivan, and J. D. Robson, "Modelling of friction stir welding of 7xxx aluminium alloys," *Materials Science and Engineering: A*, vol. 466, pp. 246, 2007.

[118] N. Kamp, A. Sullivan, R. Tomasi, and J. D. Robson, "Modelling of heterogeneous precipitate distribution evolution during friction stir welding process," *Acta Materialia*, vol. 54, pp. 2003, 2006.

[119] I. Shigematsu, Y. J. Kwon, K. Suzuki, T. Imai, and N. Saito, "Joining of 5083 and 6061 aluminum alloys by friction stir welding," *Journal of Materials Science Letters*, vol. 22, pp. 353-356, 2003.

[120] Y. S. Sato, Y. Kurihara, S. H. C. Park, H. Kokawa, and N. Tsuji, "Friction stir welding of ultrafine grained Al alloy 1100 produced by accumulative roll-bonding," *Scripta Materialia*, vol. 50, pp. 57-60, 2004.

[121] Y. S. Sato, H. Takauchi, S. H. C. Park, and H. Kokawa, "Characteristics of the kissing-bond in friction stir welded Al alloy 1050," *Materials Science and Engineering: A*, vol. 405, pp. 333-338, 2005.

[122] M. J. Peel, A. Steuwer, and P. J. Withers, "Dissimilar friction stir welds in AA5083-AA6082. Part II: process parameter effects on microstructure," *Metallurgical and Materials Transactions A (Physical Metallurgy and Materials Science)*, vol. 37A, pp. 2195-2206, 2006.

Chapter 4

MATERIALS & EXPERIMENTAL METHODS

4.1. Materials

Four different alloys were investigated in this study. Their chemical compositions are shown in Table 4.1.

Table 4.1. Chemical composition of the alloys used in this study (weight percent)

Alloy	Temper	Mg	Cu	Mn	Fe	Si	Ti	Cr	Zn	Al	Other‡
5251*	**H34/O**	1.94	0.10	0.35	0.50	0.32	0.03	0.11	0.06	Bal.	0.06
5083*	**H116**	4.22	0.03	0.57	0.26	0.08	0.01	0.09	0.01	Bal.	0.005
5754†	**O-DC/CC**	2.6-3.6	0.10	0.5	0.4	0.40	0.15	0.30	0.20	Bal.	
2024†	**T351**	1.5	4.35	0.60	0.50	0.50	0.15	0.10	0.25	Bal.	0.15

*: Measured, †: Nominal
‡: Other elements (<0.05 wt% each): Pb, Sn, Zr, and Ni.

AA5251 5 mm thick sheets were supplied by TWI in the H34 temper (work-hardened to half-hard, then stabilised by heating for a short time from 120 ˚C to 175 ˚C to enhance ductility, stabilise the mechanical properties, and avoid age softening) [1]. Some of the sheets were heat-treated to the fully-annealed condition (O). This alloy has a Mg-content less than 3 % wt, which should avoid the precipitation of β (Mg_5Al_8) phase [2].

AA5083 5 mm thick sheets were supplied by Novelis in the H116 condition, which is a special temper, similar to H321, for Al-Mg alloys with Mg-content more than 3% wt, but

work-hardened to stabilise mechanical properties and make the alloy suitable for marine applications.

AA5754 2.3 mm thick sheets were supplied by Novelis in two batches: one manufactured by direct-chill casting (DC), and the second manufactured by twin-roll horizontal continuous-casting (CC). Both batches were hot rolled to gauge and annealed. Although both batches belong to the same alloy type and with almost the same chemical composition, they differ in their constituent particles distribution due to the casting technique, which should consequently affect the resulting joint microstructure.

AA2024 6.3 mm thick sheets were supplied by BAE in the T351 condition (solution-treated, stress relieved by stretching to 1.5-3%, followed by natural aging). This is an Al-Cu-Mg precipitation-hardenable alloy, with totally different recrystallisation behaviour, constituent particles and dispersoids compared to the 5xxx series alloys. Thus, it was used to compare microstructural development with the strain-hardenable alloys, and also for thermal modelling purposes.

The manufacturing routes for 5251, 5083 and 2024 were not provided. However, low Mg Al-alloys (<2.5% wt Mg) such as 5251 are known to be prepared by CC, whereas high Mg Al-alloys (e.g. 5083) and 2024 are typically manufactured by DC [3].

4.2. Friction Stir Welding

A total of 8 welds were studied, either by microstructural characterisation or thermal simulations. The welds can be divided into four sets. Details of the welding parameters are provided in Table 4.2. First, a set of two 5251 welds were produced for the two tempers (H34 and O). Second, three welds for 5754 were produced for the two batches (2 welds for CC, and 1 weld for DC, all thermocoupled). Both sets were welded on the ESAB machine at TWI, Cambridge using the same welding parameters. The third set was a single 5083 weld provided by Novelis using different welding parameters. Finally, a set of two 2024 welds were produced at BAE Advanced Technology Centre (ATC). Their welding parameters were selected to maximise the difference in the pseudo heat-index $\left(\omega^2/v\right)$, thus creating a cold (low-temperature) weld and a hot (high-temperature) weld without affecting the weld integrity. The welds were characterised approximately 2 years after they were welded, which means that natural aging following welding would have achieved a stable hardness level.

All the 5251, 5083, 2024, and 5754-DC welds were carried out such that the welding direction (WD) was aligned with the rolling direction (RD) as shown in Fig. 4.1. For the 5754-CC welds, the WD was parallel to the RD in the first weld (CC1), and normal to the RD for the second weld (CC2). In each weld of the 5754-CC/DC set, K-type thermocouples were fixed in small surface indents on the AS and RS of the weld at distances of 10, 15 and 20 mm from the butting faces of the plates. All the thermocouples were taped using an aluminium foil tape to the sheet surface as shown in Fig. 4.2. The sheets were gripped to the machine bed through a vacuum system to ensure quicker cooling. The ESAB machine also measured the rotation speed, torque, and the tool forces.

Table 4.2. The welding parameters for the characterised welds

Alloy	Set	ID	Length (mm)	Rotation Speed (RPM)	Feed Rate (mm/min)	Z-Force (kN)	Tool	Tool dim. (mm)		
								D_S	D_P	H_P
5251-H34	1	H34	950	500	500	14.2	MX-Triflute	25	9	4.7
5251-O		O	950	500	500	14.5	MX-Triflute	25	9	4.7
5754-O CC	2	CC-1	340	500	500	14.9	MX-Triflute	15	6	2
		CC-2	340	500	500	14.7	MX-Triflute	15	6	2
5754-O DC		DC-1	470	500	500	16.7	MX-Triflute	15	6	2
5083-H116	3	H116	--	200	300	20	Threaded	18	6	4.7
2024-T351	4	CW[1]	375	215	154	20	Threaded	24	10	5.5
		HW[2]	375	468	75	24	Threaded	24	10	5.5

[1]: cold weld, [2]: hot weld
* The tool specifications for sets 3 & 4 were estimated based on the weld macrostructure

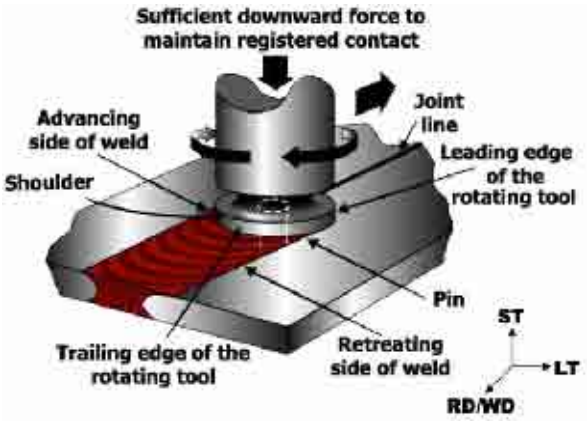

Fig. 4.1. Schematic diagram for FSW showing the metallurgical structure directions: long transverse (LT), short transverse (ST), and rolling direction (RD) with respect to the welding direction (WD) and the location of the advancing side (AS) and retreating side (RS) with respect to the direction of rotation

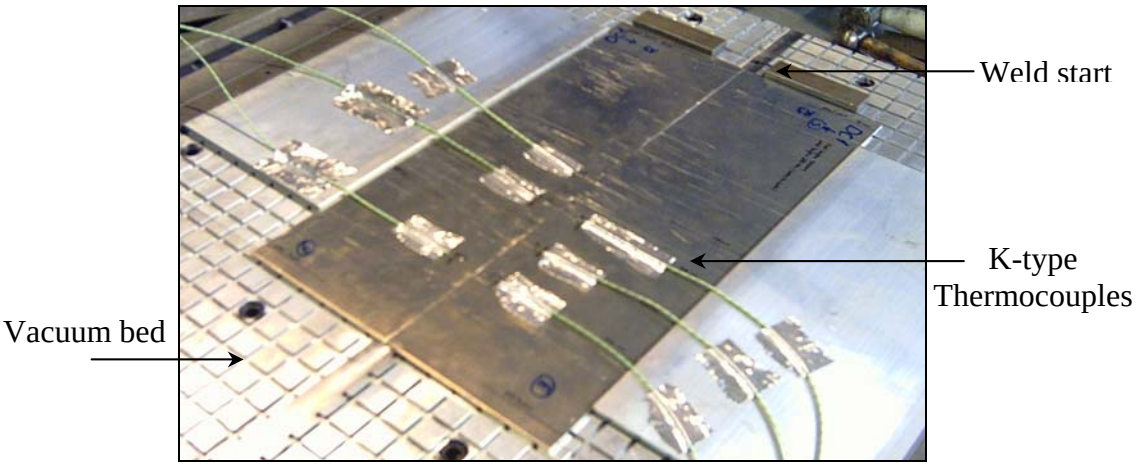

Fig. 4.2. Photograph of the experimental setup at TWI

4.3. Microstructural Investigations

4.3.1. Optical and Scanning Electron Microscopy

Metallographic investigations were carried out for the basemetal and the weldments to quantify the grain size and intermetallic population characteristics. It is known that the grain morphology is dependent on the metallurgical direction or the investigated plane, especially in wrought materials as shown in Fig. 4.3. In wrought alloys, the ST-RD plane was used to measure the size of the elongated (lath-shaped) grains since the deformed microstructure is indistinguishable on the ST-LT. In annealed materials, grain size measurements were carried out on the ST-LT plane instead to easily relate them to the recrystallised grains on the ST-LT plane of the welds (also referred to as weld face). Particle distribution and stereological analysis of banding was performed on the ST-RD plane in both conditions. Weld characterisation for the grain and particle distributions was always carried out on the ST-LT plane since the welding direction was parallel to the RD for the majority of the welds.

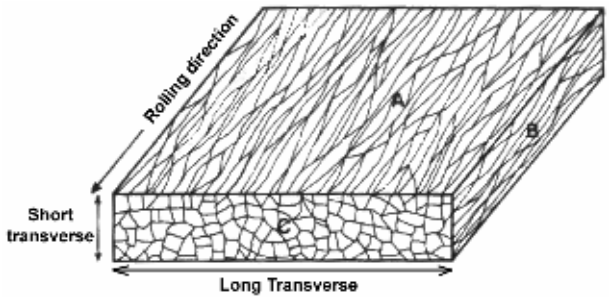

Fig. 4.3. Influence of the orientation (metallurgical direction) on the grain morphology in wrought structures [2]

Microstructural investigations were carried out using the Leica^{TM} DMRX microscope, equipped with Zeiss KS300^{TM} image analysis software which was also used to analyse SEM images showing the particle structure. Basemetal and weldment specimens were cut using a slow speed diamond cutter to minimise deformation. They were later mounted in self-curing resin, ground to 1200 grade-SiC paper, polished using 15, 6 and 3 μm diamond suspensions, to a final polishing stage using a 0.05 μm colloidal-silica suspension finish. Particle size measurements and scanning electron microscope (SEM) examinations were likewise carried out on polished (unetched) specimens. The minimum detectable particle size was taken as 0.5 μm for the optical micrographs, and 0.2 μm for SEM micrographs. Polished specimens were

also examined in a JEOL 6060 SEM equipped with an Oxford instruments Inca 300 energy dispersive X-ray spectroscopy (EDS) system for characterisation of the constituent particles, grain boundary precipitates, and matrix composition. The SEM was operated at 15 kV for spectroscopy, and 20 kV for imaging.

For microscopic investigation, electrolytic-etching (anodising) was carried out in fresh Barker's reagent (5 ml HBF_4 in 200 ml H_2O solution) with a stainless steel cathode for 2 minutes at 20 V. All specimens were viewed under polarised light on the Leica DMRX to observe individual grains. A two-stage alkaline-etchant, based on Weck's reagent, was used to reveal the grain structure of the recrystallised weld nugget. The first stage requires the immersion of a polished specimen in the first etch (2 g NaOH in 100 ml distilled water solution) for less than a minute depending on the grain size (shorter time, ~30 seconds, for fine grain structure). Then, after rinsing in distilled water and drying, the specimen is immersed in the second etch (4 g $KMnO_4$, 1 g NaOH, 100 ml distilled water solution) for ~10-15 seconds. This etchant has the advantage of etching the aluminium matrix grains, while leaving the intermetallic phases and precipitates intact. $KMnO_4$ in the second stage uniquely reveals the particles [4]. It also does not need electrical contact like Barker's reagent, and uses harmless chemicals compared to Keller's reagent for example.

For macroscopic examination, Weck's reagent was found to show the weld profile only in the presence of grain boundary precipitation, especially for the 2024 welds. Polished 5xxx specimens responded better when etched using 10% H_3PO_4 solution for 90 seconds at 65 ˚C, or using 20 g $CuCl_2$ in 100 ml H_2O solution followed by swabbing with HNO_3.

4.3.2. Transmission Electron Microscopy (TEM)

TEM was used in the current study to investigate the various phenomena associated with FSW, together with the basemetal structure and its influence on the resulting development. Specimens were made by spark-eroding 3 mm discs from 200 μm thick slices from the weld face (ST-LT plane) and the basemetal ST-RD plane. The discs were mechanically ground to about 150 μm thickness, followed by polishing in a twinjet electro-polishing system using an electrolyte of 5% perchloric acid in ethanol at -25 ˚C, and a polishing voltage of 20 V. Specimens were cleaned and stored under pure ethanol.

Bright-field imaging and diffraction TEM experiments were carried out on a 200 kV Philips CM20 TEM to study the deformed /dislocation structure using the 2-beam condition, and the precipitates and dispersoids. CBED (convergent beam electron diffraction) patterns were used to measure the foil thickness. Composition analysis of the fine precipitates was carried out in a Philips TECNAI F20 FEG-TEM with scanning TEM (STEM), equipped with an Oxford Instruments ISIS EDS system.

For imaging of dislocations, TEM micrographs were taken when the specimen was tilted to a two-beam condition to obtain images of high contrast [5]. The two-beam condition is also known as the **g.b** (g-dot-b) analysis since a specific beam direction is used such that a specific diffracted (**g**) is strong. In FCC materials, dislocations lie on the {111} planes, with **b** = a/2 <110>. If the dot product **g.b = 0**, this is known as the invisibility criterion where no dislocations can be viewed (out of contrast). For instance, using a $[011]$ beam direction, using diffracted **g** from $[02\bar{2}]$, the dot product $[02\bar{2}]\bullet[011]=0$, which causes the dislocations to be invisible. However, using a diffracted **g** of $[200]$, dislocations can be made visible. Even though some diffracted beams can give a non-zero product, the magnitude of the product affects the image whereby the larger the product the better the quality. Since dislocations are line defects, estimating their density requires the calculation of the thickness of the TEM specimen. This is done using the Kossel-Möllenstedt (K-M) fringes shown in Fig. 4.4, according to the technique outlined by Williams and Carter [6].

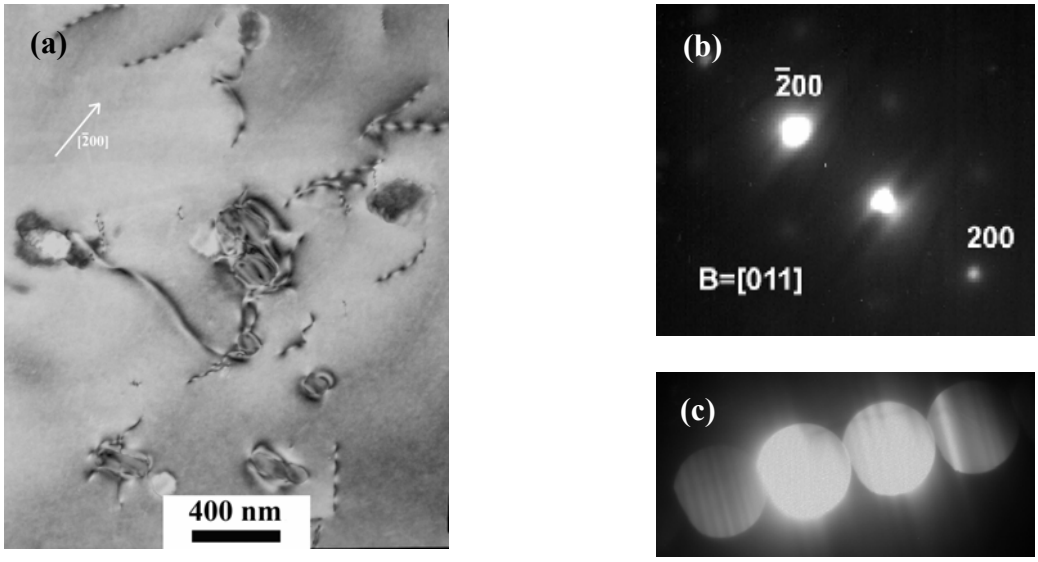

Fig. 4.4. Measurement of dislocation density using the TEM involves
(a) image taken at a 2-beam condition, (b) corresponding diffraction pattern, (c) K-M fringes

4.3.3. Electron Backscattered Diffraction (EBSD)

For accurate measurement of the grain size, especially in deformed microstructures or in the weld, as well as micro-texture determination [7], the use of EBSD has progressed over the past decade with the development of field-emission gun (FEG) SEMs and image acquisition and analysis software. Investigations were carried out on FEG-SEM JEOL 7000, equipped with an Oxford INCA crystal EBSD system.

For the basemetal specimens, sections from the ST-RD plane were investigated. For the welds, specimens were prepared from the weld face. Polishing was carried out in a similar manner to that for metallographic specimens, but using a relatively longer time on the final polishing stage (~20 minutes). This is followed by electro-polishing in 5% perchloric acid in ethanol solution at a temperature of -20 ˚C for 1 minute at 20 V and 30 mA to remove the deformed layer or any residual surface damage created during polishing.

4.3.4. Stereological Methods

Quantifying the various microstructural features (e.g. grains, particles, dislocations, and structural directionality) provides further knowledge regarding the nature of the structure. In measuring the grain and particle size, KS300^{TM} was used to define the grain or particle geometry by feret minimum/maximum (F_{min}/F_{max}) which is the smallest/largest distance that passes through the centroid, feret ratio (F_{ratio}), the particle or grain area (A), as well as the equivalent circle diameter assuming a spherical grain which is given as:

$$D_{Eq} = \sqrt{4A/\pi} \tag{4.1}$$

To measure structural features such as the inter-particle band spacing and the dislocations, a stereological line-intercept technique was used [8]. In this method, a matrix of orthogonal equidistant lines of lengths L_1 and L_2, numbers n_1 and n_2, are plotted on the image in the case of dislocations, or a set of n equidistant vertical lines of length L in the case of measuring the bands spacing as shown in Fig. 4.5. The number of intersections N_1 and N_2 with the dislocations in both axes is counted. Knowing the thickness of the TEM foil (t), the dislocation density can be estimated by:

$$\rho = \left(\frac{N_1}{n_1 L_1} + \frac{N_2}{n_2 L_2} \right) \frac{1}{t} \tag{4.2}$$

For the particle-bands spacing, the number of bands N intersecting *n* equidistant vertical lines of length L is counted. Elongated inclusions and bands of inclusions with lengths greater than half the separation between the vertical lines were represented by horizontal lines. Accordingly, the inter-particle bands spacing is given by:

$$d_{spacing} = nL/N \tag{4.3}$$

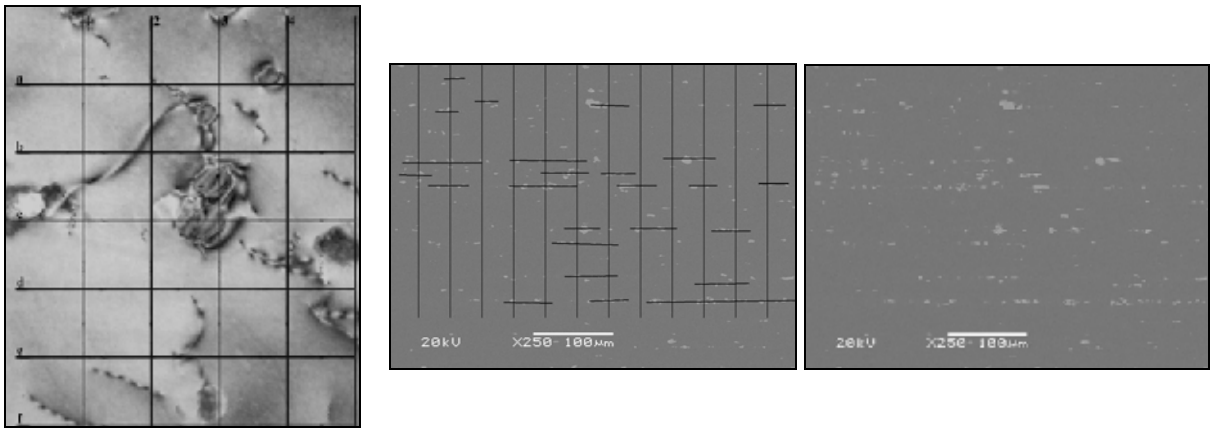

(a) (b)

Fig. 4.5. Point counting method for (a) dislocations, (b) particle bands spacing

4.4. Differential Scanning Calorimetry

4.4.1. The device

There has been recent progress in utilising Differential Scanning Calorimetry (DSC) to indirectly measure precipitation, recrystallisation and other transformations in Al-based alloys [9]. Examples of these reactions and how they are detected using the DSC are given in Table 4.3. Generally, there are two types of DSC devices: power-compensated and heat-flux. In the current study, DSC thermal analysis was performed in the heat-flux DSC 404C Pegasus® calorimeter. As shown in Fig. 4.6, such a device uses a calorimeter (furnace) where both the specimen and reference pans are located. Both pans are positioned on the heat flux plate, and temperature is recorded during isothermal or anisothermal cycles. The reference pan is usually left empty or with a specimen whose thermal properties can be used as a reference. Based on the difference in temperature between the specimen and reference thermocouples and the calibration data established, differential power gained as a function of the sample temperature can be calculated.

Calorimetry provides a means to determine the dislocation density by measuring the release of stored energy, which provides a feasible and simple technique when compared to transmission electron microscopy (TEM). The dislocation density (ρ) is related to the released stored energy per unit volume (E) through:

$$E = \rho \alpha G b^2 \tag{4.4}$$

where α is a dimensionless dislocation interaction parameter, G is the shear modulus, and b is the Burger's vector.

4.4.2. Specimen and method

Small specimens (~3.5x2.5x1.5 mm, ~35 mg) were cut from the weld transverse cross-section as shown in Fig. 4.7 using a low-speed SiC cutting disk for the characterisation of the various effects associated with FSW. Specimens were thermally cycled in fully recrystallised Al_2O_3 pans in a flowing Ar atmosphere at a heating rate of 20 ˚C/min. A block of fully annealed commercially pure Al-alloy (99.5%) or 5251-O of virtually the same mass as the specimen was used as a reference. The latter provides a reference of matching temperature-dependent thermal properties, and being similar in mass reduces the thermal imbalance of the

calorimeter. Another approach was also performed to assess the repeatability of some conditions by using commercially pure annealed Al pans for both the sample and reference, while leaving the reference pan empty, with the double run. After the first run, the calorimeter was left to cool down without removing the sample, the second run (being flat indicating no transformations taking place) was used as a baseline as shown in Fig. 4.8. Quantification of the exothermic peak characteristics (start, end, energy release) was performed using Proteus-NETZSCH software. A list of the DSC work carried out is listed in Table 4.4.

Generally, the obtained signal has to be subtracted from a baseline. The baseline was measured either by running the same heating schedule with empty pans, or by carrying out a second run for the same specimens. Both approaches calculated the same amount of energy released as shown in Fig. 4.9. Yet, the double run approach minimised the low temperature peaks which are actually due to the thermal imbalance of the calorimeter (i.e. imbalance during the initial heating phase).

There is always a concern with this approach that other phase transformations could shadow the trace, as discussed in section 2.5.1.a. In 5xxx alloys, three types of particles exist (β-Mg_5Al_8, Fe/Min-rich particles, and Mg_xSi), which could possibly undergo phase transformations. For β-Mg_5Al_8, the investigated alloys were chosen with Mg wt % less than 3.5 (5251 and 5754), or in the stabilised condition (5083), to avoid β-precipitation. Moreover, the maximum temperature in the thermal cycle (425 ˚C) was chosen to avoid the dissolution of the Mg_xSi, which is known to happen at higher temperatures [2]. For the Fe/Mn-rich particles, their dissolution is known to occur at temperatures higher than the alloys melting points. However, the Mn atoms present in solution could possibly precipitate during heating. This will not be the case for the specimens extracted from the weld, as the welding thermal exposure would have precipitated them already, or for the DC alloys as this happens during homogenisation, but maybe in CC parent alloys which were not annealed. Previous DSC work on Fe/Mn-precipitation showed that the Mn-precipitation occurs between 400 and 500 ˚C in Al-5 wt % Mn alloy [10], which could possibly interfere with the measurements. For this purpose, 5251-H34 basemetal specimens were thermally cycled at 20 ˚C/min to several temperatures in the Gleeble (as will be explained later) to measure the hardness and intermetallic particles development to compare it to the DSC trace, and to identify the recrystallisation peak. It is important to point out that there are other techniques

(e.g. electrical conductivity and thermo-electric power), which have been previously used to detect the temperatures at which precipitation of solutes starts (Mn, Fe, Si, and Cu) [11-13], and could have been useful in determining the extents of Mn precipitation or Mg_xSi dissolution. However, these techniques were not accessible during the time this work was performed.

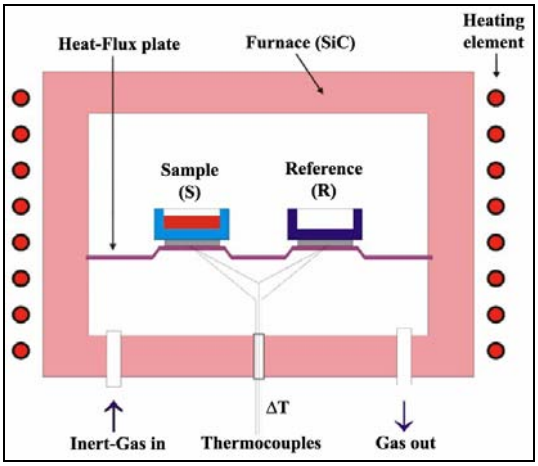

Fig. 4.6. Schematic diagram for the heat-flux DSC (similar to 404C Pegasus®) [14]

Table 4.3. Reactions that can be detected using the DSC and the energy type

Reaction	Energy type	Example
Recovery	Exothermic	Deformed structures
Recrystallisation	Exothermic	
Grain Growth	Exothermic	
Dissolution	Endothermic	GP-zones dissolution
Precipitation/Coarsening	Exothermic	In Al-Cu system θ'
Melting	Endothermic	Constituent particles

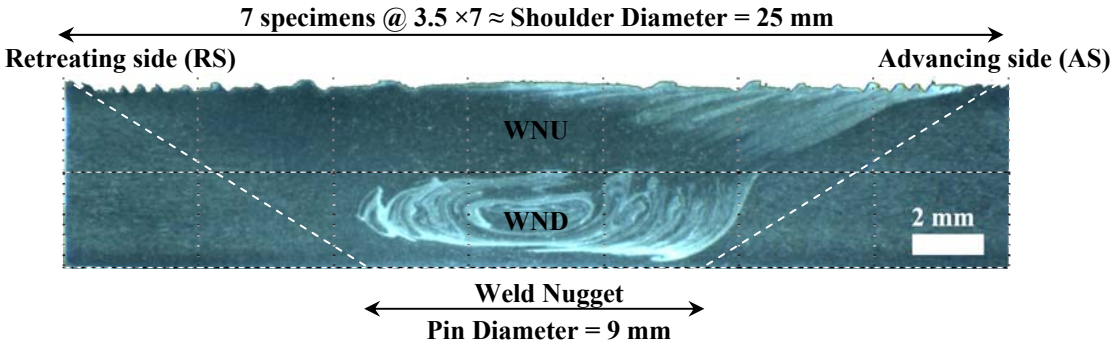

Fig. 4.7. Section through the 5251 weld (slightly etched in 10% H_3PO_4 solution) showing where DSC specimens were taken from (dashed black boxes) and selected notation (U 'upper' half of sheet and D 'down' or bottom half of sheet).

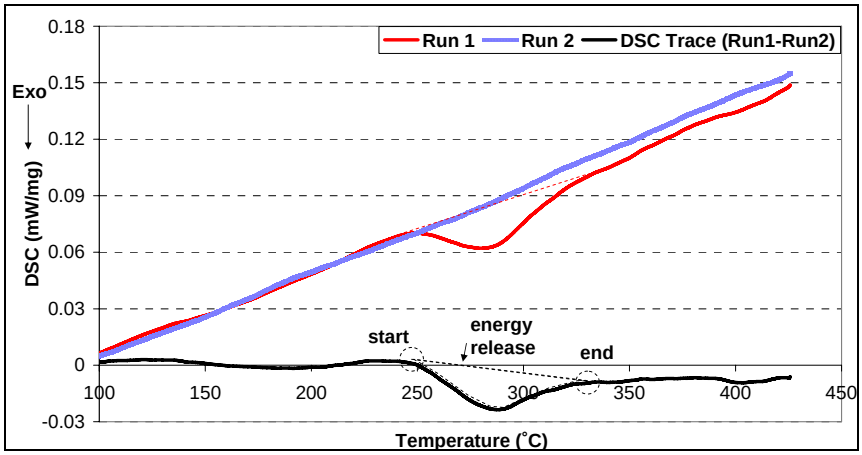

Fig. 4.8. Example DSC trace using the 2nd run approach

Table 4.4. Weld regions and reactions

Alloy	Conditions	Heat rate	Reactions
5251-H34/O	Basemetal, weld regions	20 ˚C/min	Recovery/Recrystallisation
2024-T351	Basemetal, selected weld regions	10 ˚C/min	Dissolution/precipitation
5083-H116	Basemetal, selected weld regions	20 ˚C/min	Recovery/Recrystallisation
5754-O DC/CC	Selected weld regions	20 ˚C/min	Recovery/Recrystallisation

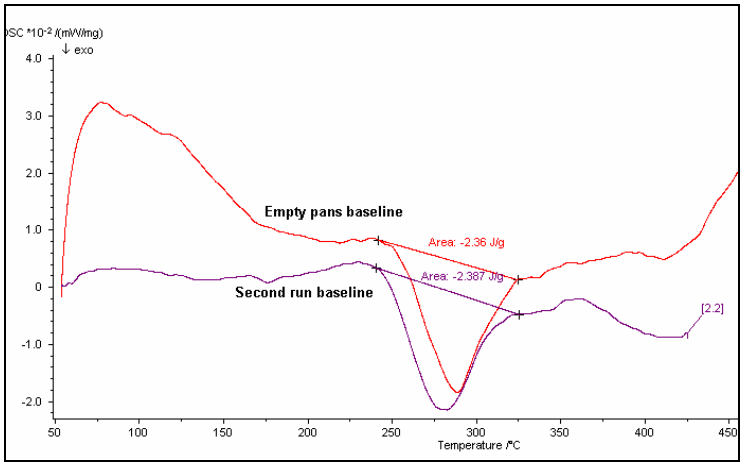

Fig. 4.9. DSC specimen traces using the empty pans baseline and using the double-run baseline (note the flatness of the double-run technique during the initial period)

4.5. Mechanical Testing

4.5.1. Hardness

Hardness measurements and contour mapping were carried out for the welds and the basemetal using a Mitutoyo microhardness tester on polished specimens. For the welds, hardness traces at mid-thickness and contour distributions were all carried out on the weld face. The contours and traces covered ± 20 mm from the weld centreline, thus virtually covering all the weld regions. Loads of 200 gf and 1000 gf for 8 seconds were used depending on the frequency and distance between indentations. As a general rule, the spacing between the indentations has to be 2-5 times larger than the diagonal of the indentation. To calculate the Vickers Hardness Number (VHN), an image analyser was used to accurately measure the size of the diagonals, and then the following formula was used:

$$VHN = \frac{1.854P}{d_{avg}^2} \tag{4.5}$$

where P is the load in kg, and d_{avg} is the average of the diagonals of the indentation in mm.

4.5.2. Tensile Testing

Tensile test specimens were machined from both the rolling and transverse directions of the basemetal, and in the transverse direction for the weldments. Due to size limitations, welded section specimens were machined with a shoulder-to-shoulder distance of 100 mm with the weld zone (25 mm shoulder diameter) centred, and width of 12.5 mm, Fig. 4.10. The basemetal specimens were machined with a gauge length of 25 mm, and width of 10 mm. Following both the ASTM E8/E8M [15], the gauge length (L_g) can be calculated as:

$$L_g = 5.65\sqrt{A} \tag{4.6}$$

Where the parallel length (L_c) can be calculated as:

$$L_C = L_g + 2\sqrt{A} \tag{4.7}$$

Testing was performed on a Zwick Z100 screw driven universal machine tester at a cross-head speed of 3 mm/min at room temperature. Load-extension curves were plotted using the machine software which recorded data running at a speed of 5 Hz. At least three tests were

performed for each condition. The 0.2% proof stress (0.2% PS) and tensile strength (TS) and percent elongation to failure were determined for each condition.

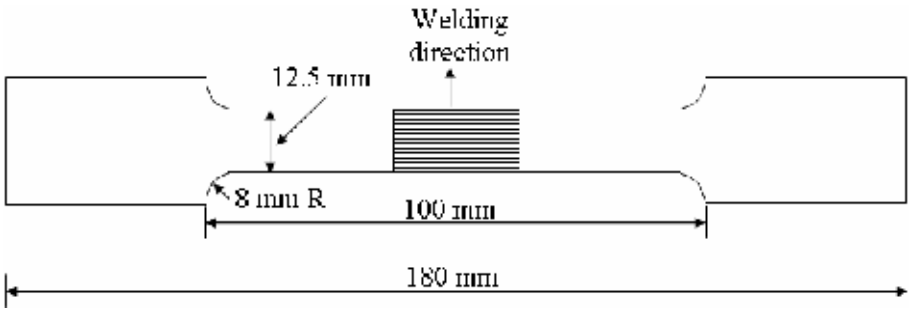

Fig. 4.10. Tensile specimen dimensions

4.6. Furnace Work & Heat Treatment

To study the recovery and recrystallisation behaviour of the work-hardened conditions studied (H34 and H116), isochronous annealing at various temperatures was carried out for 25×25×5 mm basemetal specimens in a laboratory oven controlled by means of a Eurotherm controller (±5 ˚C). In addition, basemetal specimens of the same dimensions in the O condition were further heat treated at temperatures above the annealing temperature to check the structure-property development based on the variation in the grain size using the Hall-Petch relationship. Other heat treatments were carried out for the 2024-T351 material to separate the various thermal effects. A list of the furnace work is available in Table 4.5.

Table 4.5. Heat treatments carried out for the basemetal

Material	Temperatures (˚C)	Time
5251-H34	140, 180, 225, 275, 325, 375, 425, 475, 525	1 hr
5251-O	375, 425, 475	1 hr
5083-H116	140, 180, 225, 275, 325, 375, 425, 475, 525	1 hr
2024-T351	525	1 hr
5754-DC/CC	375, 425	1 hr

4.7. Gleeble Thermo-Mechanical Simulator (GTMS)

The Gleeble® 3500 thermomechanical simulator (Dynamics Systems Inc.) is an important technique that provides materials scientists with the ability to simulate microstructure development associated with thermomechanical processing. The Gleeble utilises direct resistance heating by applying alternating current (50 Hz) through highly conductive grips to the specimen. The mechanical system enables *in-situ* mechanical testing (tension and compression), thus making it ideal to simulate high temperature deformation processes [16, 17]. The system's unique features include the ability to simulate heating and cooling at rates as high as 10,000 ˚C/s, which makes it ideal to simulate the transient thermal cycle during welding processes to specifically study the HAZ microstructural development or the effect of post-weld heat treatment [18].

In this research, GTMS was used to simulate the HAZ microstructural development and the recovery and recrystallisation behaviour of the basemetal for the 5251-H34 and 5083-H116 alloys, and the associated change in hardness. In addition, to simulate the microstructural development that takes place within the DSC for both the weld and basemetal, whole weld specimens (50×10×5 mm) and blocks of the basemetal (25×25×5 mm) were cycled at a heating rate of 20 ˚C/min as shown in Fig. 4.11. The maximum temperatures used during simulation corresponded to the beginning and the end of the maximum energy released peaks observed in the DSC for the weld specimens, whereas for the basemetal (H34), separate specimens were heated up to different temperatures (ranging from 140-525 ˚C) as listed in Table 4.6. For recrystallisation modelling, basemetal blocks were cycled at heating rates within the range of 0.33-175 ˚C/s to maximum temperatures of 400-525 ˚C.

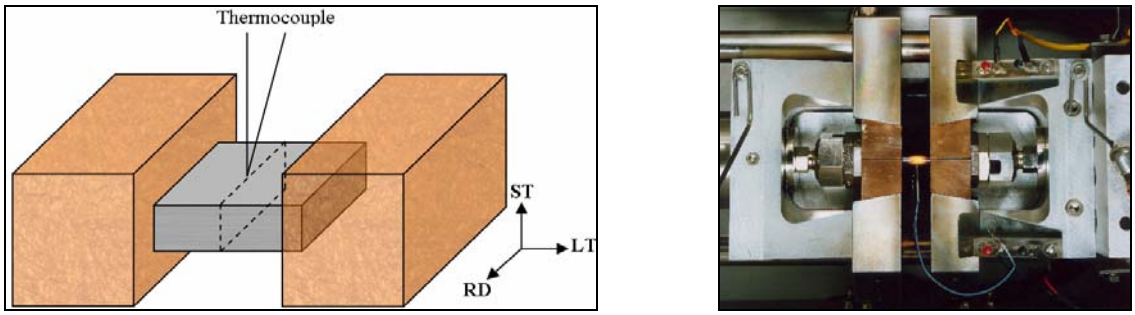

(a) (b)

Fig. 4.11. The use of GTMS showing a) configuration with the specimen (25×25 mm) located according to the shown microstructural directions, and b) image of the GTMS operating in the compression mode

Table 4.6. Conditions of the specimens thermally cycled in the GTMS

Specimen	Description	Peak Temperature	Heating Rates
BMH34	Basemetal, heated to different temperatures	140, 180, 220, 260, 300, 325, 350, 375, 400, 475, and 525 ˚C	20 ˚C/min
FSWH34-P	H34-FSW heated to re-xal onset	250 ˚C	20 ˚C/min
FSWH34-E	H34-FSW heated to re-xal end	375 ˚C	20 ˚C/min
FSWO-P	O-FSW heated to re-xal onset	250 ˚C	20 ˚C/min
FSWO-E	O-FSW heated to re-xal end	325 ˚C	20 ˚C/min
BMH34	Basemetal, heated to different temperatures and heating rates	400, 475, 550 ˚C	15, 25, 30, 50, 100, 150 ˚C/min

4.8. References

[1] J. E. Hatch, *Aluminum: Properties and Physical Metallurgy*. Ohio: American Society for Metals (ASM), 1984.

[2] L. F. Mondolfo, *Aluminum Alloys: Structure and Properties*. London: Butterworth, 1976.

[3] R. E. J. Sanders, "Technology Innovation in Aluminum Products," *JOM*, vol. 53, pp. 21-25, 2001.

[4] T. Zwieg, "A Universal Method for the Mechanical Preparation of Aluminium Alloy Specimens with High Edge Retention and their Subsequent Colour Etching," *Praktische Metallographie*, vol. 38, 2001.

[5] M. H. Loretto, *Electron Beam Analysis of Materials*. NY: Chapman and Hall, 1984.

[6] D. B. Williams and C. B. Carter, *Transmission Electron Microscopy*. NY: Plenum Press, 1996.

[7] F. J. Humphreys, "Grain and subgrain characterisation by electron backscatter diffraction," *Journal of Materials Science*, vol. 36, pp. 3833-3854, 2001.

[8] E. E. Underwood, *Quantitative Stereology*. Reading: Addison-Wesley Publishing Comp., 1970.

[9] M. J. Starink, "Analysis of aluminium based alloys by calorimetry: Quantitative analysis of reactions and reaction kinetics," *International Materials Reviews*, vol. 49, pp. 191-226, 2004.

[10] D. Vojtech, K. Saksl, J. Verner, and B. Bartova, "Structural evolution of rapidly solidified Al-Mn and Al-Mn-Sr alloys," *Materials Science and Engineering: A*, vol. 428, pp. 188, 2006.

[11] Y. J. Li and L. Arnberg, "Quantitative Study on the Precipitation Behavior of Dispersoids in DC-cast AA3003 Alloy during Heating and Homogenization," *Acta Materialia*, vol. 51, pp. 3415-3428, 2003.

[12] C. Garcia-Cordovilla and E. Louis, "A differential scanning calorimetry study of recrystallization and its interaction with precipitation in Al-Fe-Si commercial alloys (AA1145 and AA8011)," *Journal of Materials Science*, vol. 21, pp. 971-979, 1986.

[13] R. G. Kamat, "AA3104 can-body stock ingot: characterization and homogenization," *JOM*, vol. 48, pp. 34-38, 1996.

[14] R. Nicula, "Introduction to Differential Scanning Calorimetry," vol. 2006: Rostock University, 2002.

[15] *Metals-Mechanical Testing Standards*, vol. Vol. 3.01: AmericanSociety of Testing and Materials (ASTM).

[16] "http://www.gleeble.com."

[17] S. G. R. Brown, J. D. James, and J. A. Spittle, "3D numerical model of the temperature-time characteristics of specimens tested on a Gleeble thermomechanical simulator," *Modelling and Simulation in Materials Science and Engineering*, vol. 5, pp. 539-548, 1997.

[18] G. Oertelt, S. S. Babu, S. A. David, and E. A. Kenik, "Effect of thermal cycling on friction stir welds of 2195 aluminum alloy," *Welding Journal*, vol. 80, pp. 71-79, 2001.

Chapter 5

BASEMETAL CHARACTERISATION INFLUENCE OF THE PROCESSING ROUTE

In this chapter, the complete microstructural and mechanical characterisations of the basemetals are presented, identifying the influence of the processing route. The microstructural characterisation includes the grain structure, along with the grain substructure in the work-hardenable alloys, and the particle structure, identifying the phases; their sizes and number density distributions. Stereological studies of the through-thickness microstructural heterogeneities are also presented. The hardness testing results are included, as well as the microstructure-hardness development following isothermal and anisothermal heat treatments of the base alloys, to provide insight for the microstructural development in Chapter 7, and the structure-property relations in Chapter 8.

5.1. AA5251

AA5251 is the main material investigated in the present work. Thorough microstructural characterisation was performed to assist in characterising the microstructural-strength development associated with FSW.

5.1.1. H34 Condition: Grain Structure and Deformed Substructure

By definition, the H34-condition is half-hard and stabilised. Optically, the grain structure on the ST-RD plane was composed of pancake-shaped grains, elongated along the RD, Fig. 5.1. The grain morphology and size was found to vary across the thickness, Fig. 5.2, whereby in

the subsurface region of the sheet the grains were shorter (~150 μm), smaller in area, and contained deformation bands (DBs) inclined at 20-30˚ to the RD across the grains, Fig. 5.1-b,compared to longer (~250 μm) and larger area grains which did not contain many DBs within the central region of the sheet, Fig. 5.1-c. The average grain thickness (F_{min}) did not show a significant change across the thickness, with an overall average of 31±15 μm. DBs can arise due to non-uniform deformation in the high amount of cold work that occurs near the surface, which indicates a through thickness strain deformation gradient [1]. DBs are also known to nucleate due to the influence of non-deformable coarse intermetallic particles (>1 μm), which can alter the slipping of a portion of the grain containing them during deformation, causing it to slip in a different direction. This leads to the formation of a band of different orientation within the crystal [1].

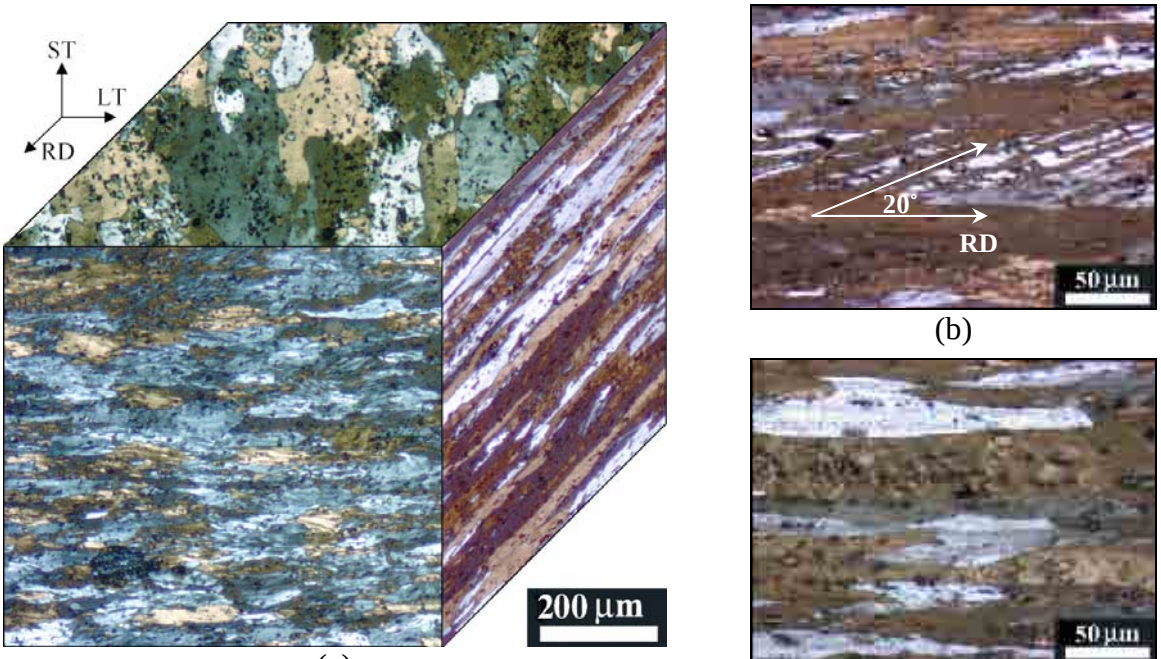

Fig. 5.1. Grain structure in 5251-H34 (a) 3D grain structure, (b) polarised light micrograph showing the near surface deformation bands (ST-RD plane) and (c) grain structure at the mid-thickness

The through-thickness variation in grain size (area and length) and morphology (DBs) is a direct outcome of the casting (DC or CC) and the rolling (hot or cold) processes respectively. The variation in the cooling rates across the thickness during casting results in the formation

of a fine grain structure near the surface (where rapid cooling occurs), with the grain size increasing towards the centreline [2]. This was manifested in the through-thickness variation in grain size, Fig. 5.2. Similarly, the cold rolling operations are associated with a through-thickness variation in deformation levels. The subsurface region experiences relatively higher strains compared to the sheet centre (i.e. higher deformation stored energy [3]), which explains the presence of the DBs near the sheet surface. In addition, the higher stored energy in the subsurface region makes it more susceptible for (or showing higher extent of) recovery after deformation than in the central region [3]. However, other microstructural and deformation factors [4, 5] could also influence the amount of recovery as previously discussed in section 2.5.2.

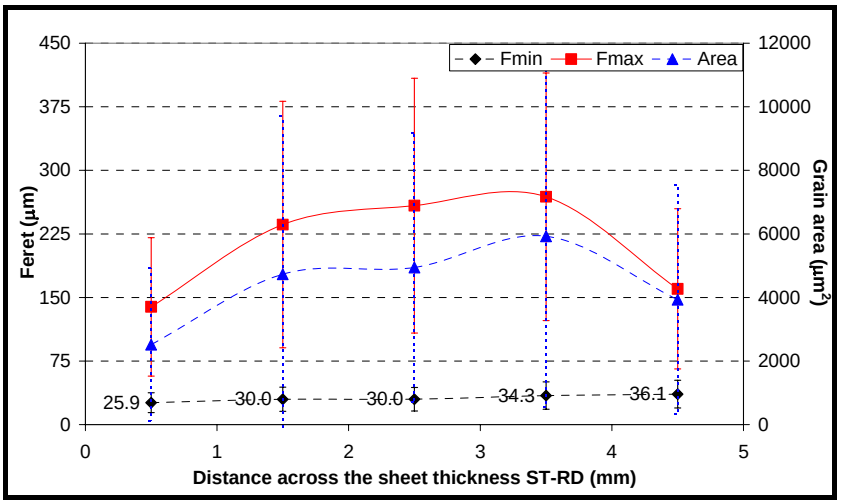

Fig. 5.2. Through-thickness variation in the ST-RD grain characteristics in 5251-H34

By observing the grain structure using the TEM (mostly from the central region), it was found that there was a substructure composed of dislocation cells with lamellar boundaries of grains and subgrains, (Fig. 5.3-a) elongated along the RD and highly deformed regions, Fig. 5.3-b. At higher magnification, two morphological trends were observed. Some regions showed trends of recovery (Fig. 5.4-a), with few dislocations existing within the subgrains, and boundaries composed of dislocation pile-ups (dense dislocation walls, Fig. 5.4-b). Other subgrains contained tangled dislocations, Fig. 5.4-c. This structure agrees with the description given by Hughes and Hansen (section 2.4.4.b) for materials exposed to large strains ($\varepsilon > 1$) [6], as well as the observations of Verdier *et al.* in deformed Al-2.5% Mg alloy [7, 8]. Further

quantitative characterisation of the subgrain structure was performed using EBSD, and will be discussed in Chapter 8.

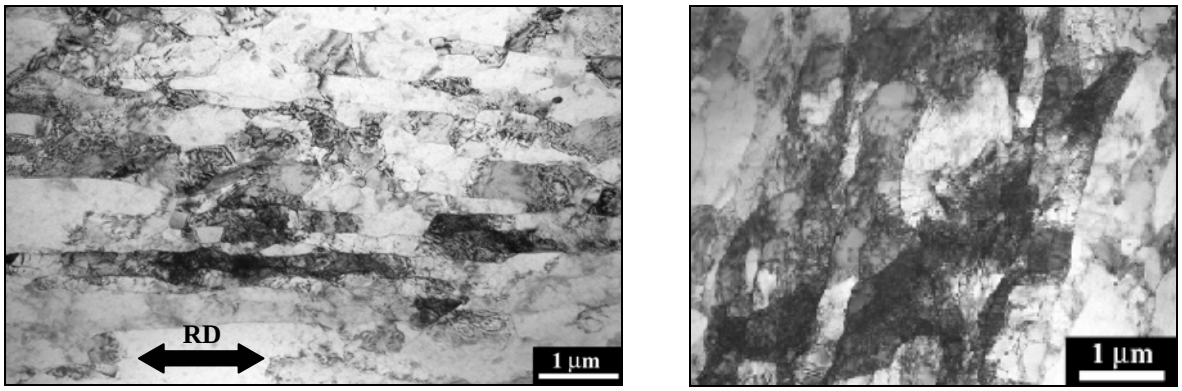

(a) (b)

Fig. 5.3. Grain substructure in 5251-H34 (a) lamellar boundaries along the RD and (b) the occurrence of recovery within the deformed microstructure

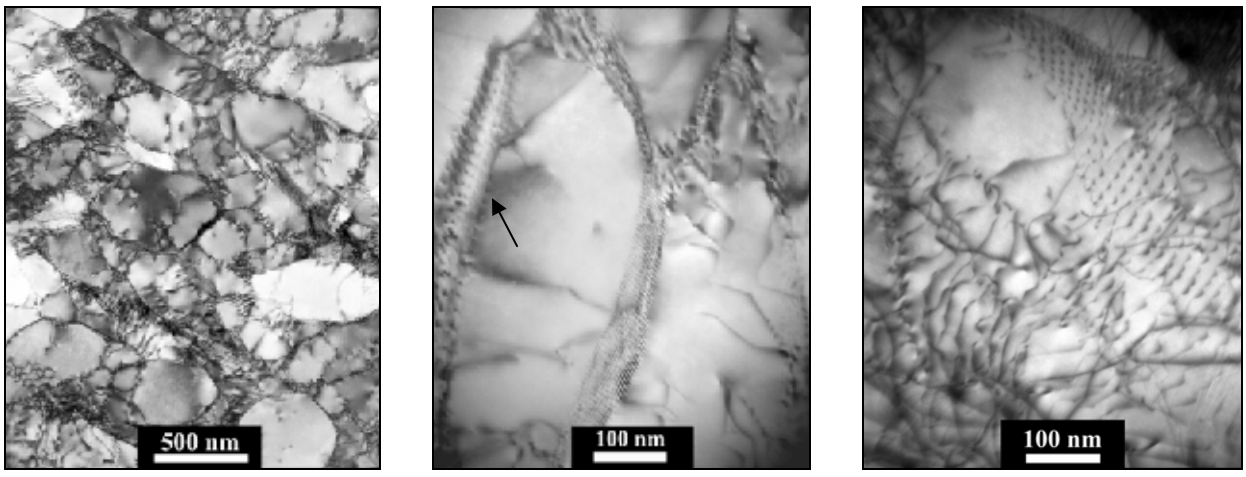

(a) (b) (c)

Fig. 5.4. Subgrain structure in 5251-H34 (a) recovered structure showing cells and subgrains of various sizes and shapes, (b) recovered subgrain showing a boundary with a dislocation pile-up (arrowed), (c) dense dislocation structure within a subgrain

5.1.2. O Condition: Annealed Grain Structure

The O-condition sheet was composed of irregularly-shaped relatively-flattened grains (viewed on the ST-LT plane), with an average aspect ratio of 0.55 ± 0.14. On average, F_{min} was found to be 24.1 ± 9.1 μm, while F_{max} was 46.9 ± 22.6 μm, and D_{Eq} was 29.8 ± 11.7 μm, Fig. 5.5. The variation in grain characteristics (F_{min}, F_{max}, F_{ratio}, and D_{Eq}) did not show a clearly consistent trend throughout the sheet thickness. The irregularity of the grain structure morphology is indicative of a discontinuous recrystallisation processes (i.e. PSN), which is driven by the local variations in stored energy within the deformed microstructure (e.g. due to the presence of non-deformable particles) [5]. During PSN, the sub-boundary migration consumes the deformed zones leading to such irregular grain morphology. Further quantitative characterisation of the grain structure was performed using EBSD to compare the measured sizes, and will be discussed in Chapter 8.

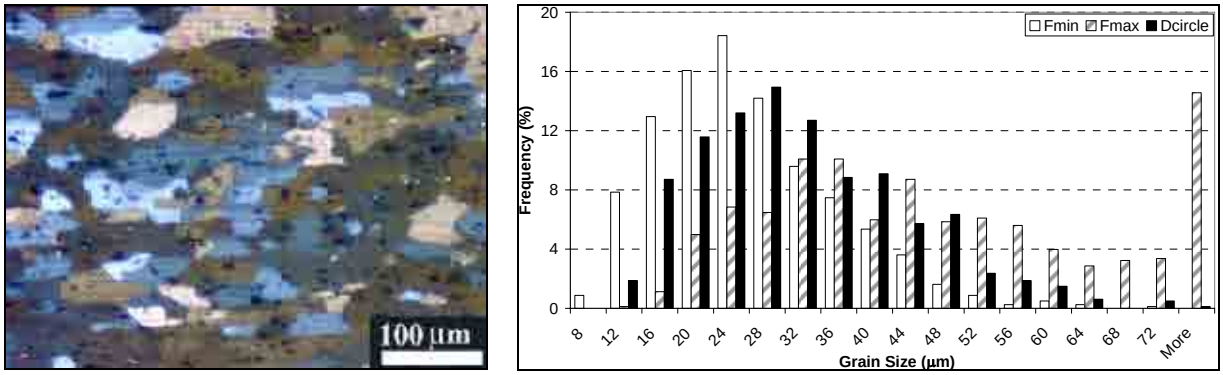

(a) (b)

Fig. 5.5. (a) Grain structure in 5251-O, (b) histogram for the grain characteristics (ST-LT)

Compared to the H34-condition, the dislocation substructure was easily resolvable in the TEM. It showed low $\rho_{Dislocation}$ regions within the grains with no subgrain structure, as well as submicron dispersoids of various morphologies (identification and quantification is discussed later), Fig. 5.6. $\rho_{Dislocation}$ was estimated at ~3.1±1.5 $\times 10^{13}/m^2$ using stereological analysis of 2-beam condition images. This value is intermediate between the literature values for fully annealed single phase materials (~10^{11} $/m^2$) and for work-hardened materials (10^{15} $/m^2$) [5, 9]. Compared to other Al-Mg alloys, it is ten times lower than $\rho_{Dislocation}$, measured by TEM, of an Al-2.9Mg alloy, subjected to a low deformation (e.g. 10% reduction) [10].

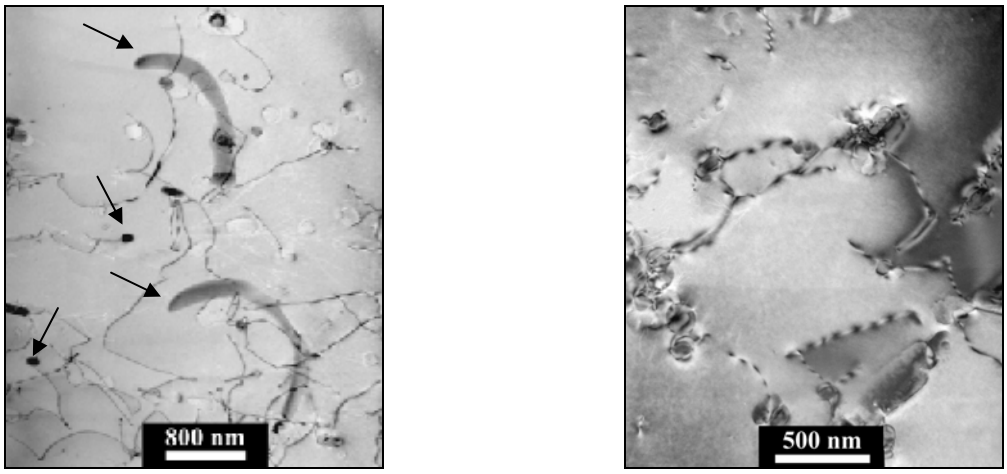

(a) (b)

Fig. 5.6. Dislocation substructure in 5251-O (a) low dislocation density with dispersoids of various shapes (arrowed), (b) 2-beam condition image for the dislocation structure

5.1.3. Constituent Particles and Dispersoids

Two types of constituent particles were identified in the microstructure of the H34 and O conditions, Fig. 5.7-a, (a) mid-grey faceted particles, and (b) dark more rounded particles. Using EDS analysis and mapping, they were identified as Fe-rich α-Al(Fe,Mn)Si {Fe/Mn ~7, (Fe+Mn)/Si ~3}, and Mg_xSi {Mg/Si~1} respectively. A summary of the area fraction, size, and number density of the intermetallic particles in both conditions is given in Table 5.1, and a histogram for the size distribution in the H34 condition is shown in Fig. 5.8.

The α-particles can be classified into two size ranges; fine particles (0.5-1 μm), and coarse particles (>1 μm). Such a classification considers their potential influence on recrystallisation (i.e. pinning or PSN). Most of the A_f of the α-particles were of coarse particles (0.018 and 0.016 for H34 and O respectively), with an average size of ~2 μm.

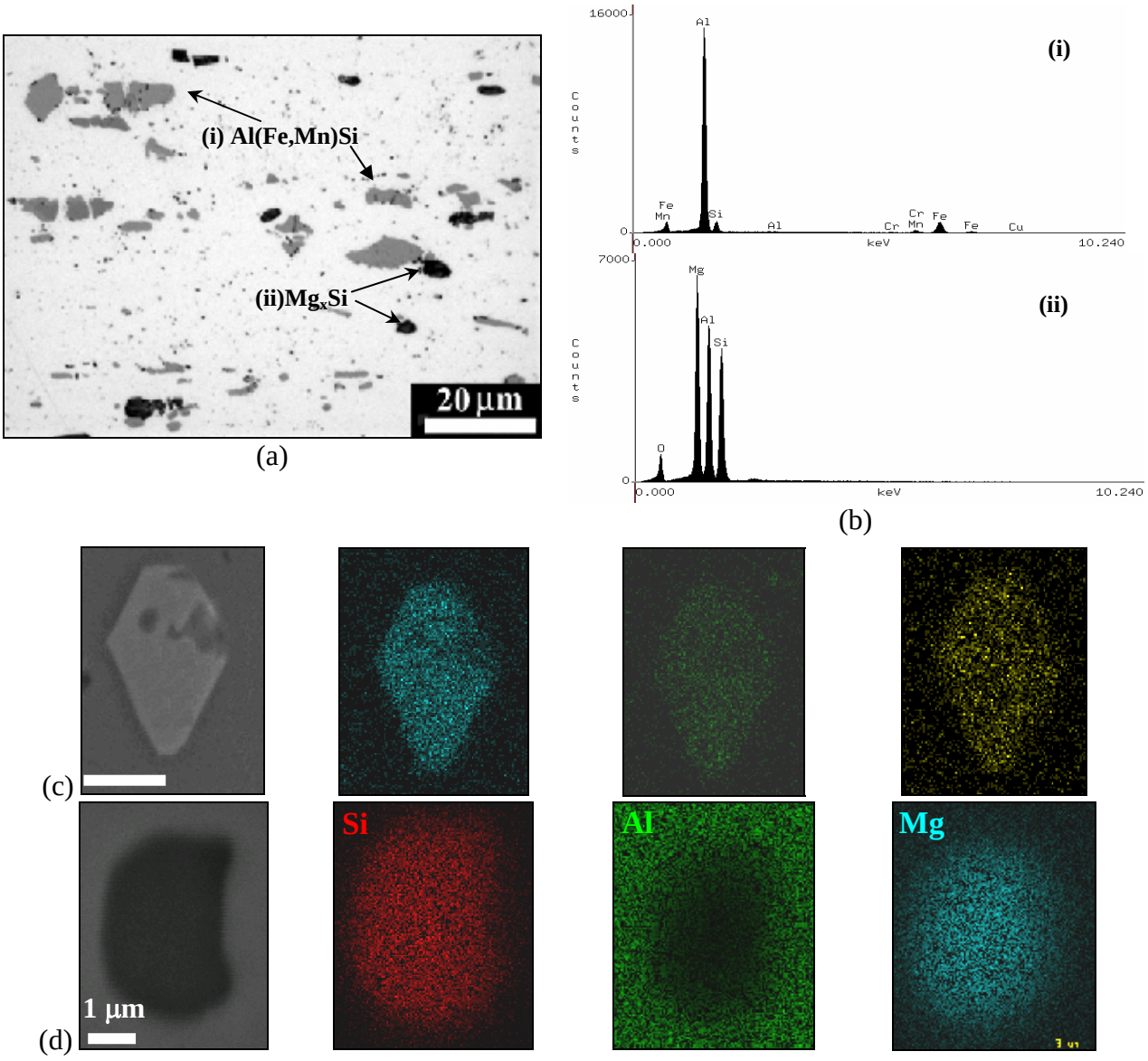

Fig. 5.7. (a) Micrograph for the constituent particle structure in 5251-O showing the observed types and (b) their corresponding EDS spectra, and the elemental maps for (c) Al(Fe,Mn)Si and (d) Mg_xSi

Table 5.1. Characteristics of the intermetallic particles in the H34 and O conditions

Alloy	Particles	Area Fraction	D_{Eq} (μm)	Number Density (#/mm^2)
H34	α-Al(Fe,Mn)Si	0.024 ± 0.004	1.1 ± 0.9	13,410
	Mg_xSi	0.0055 ± 0.0018	0.9 ± 0.6	6,365
O	α-Al(Fe,Mn)Si	0.027 ± 0.005	1.4 ± 0.9	8,735
	Mg_xSi	0.0049 ± 0.0016	0.8 ± 0.4	9,735

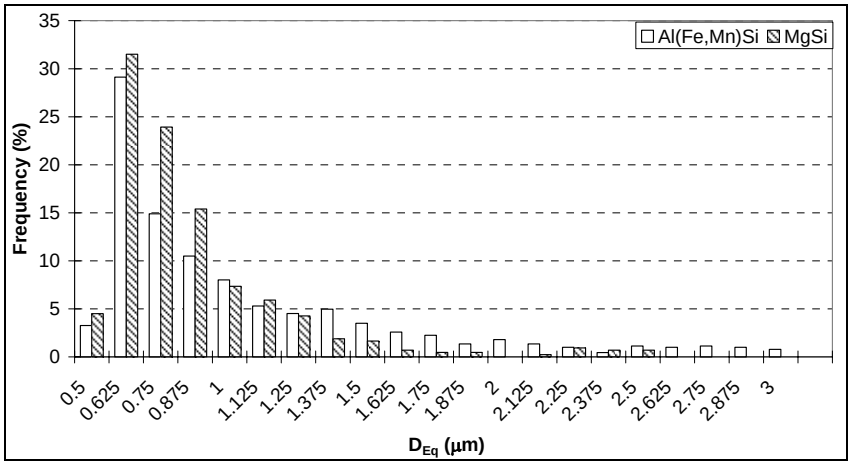

Fig. 5.8. Size distribution plot for the α-Al(Fe,Mn)Si and Mg_xSi particles in 5251-H34 covering the particles $D_{Eq} > 0.5\ \mu m$

Both conditions contained roughly similar amounts of both phases, which is as expected since the O and H34 conditions are from the same batch of material with different final heat treatments. However, the α-particles in the H34-condition were finer in size and larger in number density compared to the O-condition. In addition, the Mg_xSi had slightly lower number density in the H34-condition than in the O-condition. As the parameters of the annealing heat treatment were not provided, it is possible to suggest that this treatment led to the growth of the α-particles (by Ostwald ripening of the large particles at the expense of the fine particles), and accordingly decreasing the number density and slightly increasing the particle size and area fraction. Similar development of the α-particles during isothermal and dynamic annealing within a temperature range of 400-600 ˚C has been reported previously (section 2.1.2.c) [11-13]. Conversely, for the Mg_xSi particles, the thermal treatment of the H34-condition could dissolve some of the fine particles, which enriches the Mg-content, but this could also lead to re-precipitation of Mg_xSi during cooling if the solubility limit is exceeded, which could cause an increase in the number density. Further details on the development of the Mg_xSi and its influence on the hardness will be discussed later in this chapter.

In terms of their morphology, the α-particles were observed to form near-continuous bands of faceted particles along the RD in both conditions, Fig. 5.9-a. Linear intercept measurements of the bands did not show any trend in the inter-particle band spacing across

the thickness, with the spacing varying between 15 and 125 μm and an average spacing of ~38±22 μm in both conditions, Fig. 5.9-b. The banding of the α-particles along the RD is a typical feature of CC Al-Mg alloys, as observed in CC 5052 [14, 15], 5754 [16], and 5182 [15-18]. This banding is attributed to the fast cooling rates experienced during solidification, which results in the alignment of the constituent particles along the RD, normal to the maximum heat flux, while the *in-situ* (and successive) rolling fragments the particles due to their brittleness [19]. Non-uniform through-thickness thermal gradients in CC are known to lead to a through thickness variation in dendritic arm spacing, which is reflected in the variation in the particle band spacing [2].

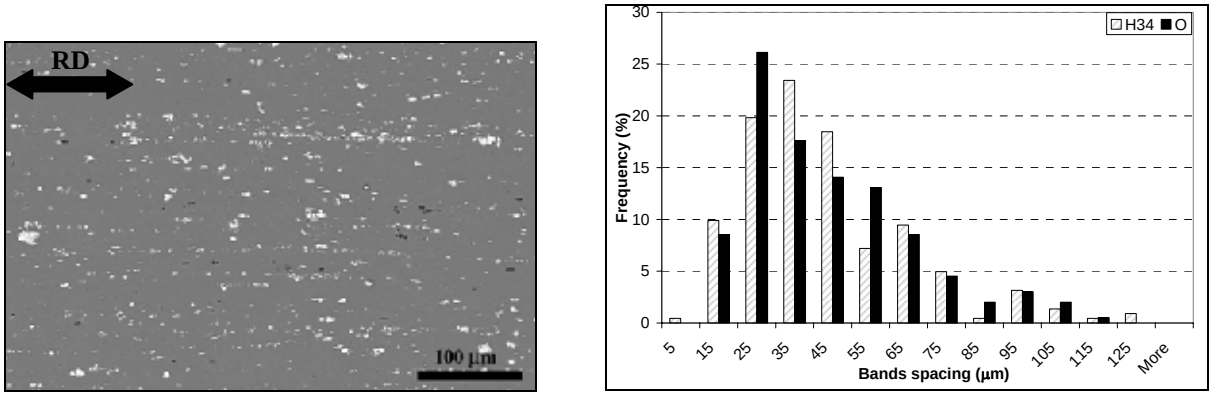

(a) (b)

Fig. 5.9. Distribution of the α-constituent particles in 5251-H34: (a) banding of particle stringers along the RD, (b) histogram of the inter-particle band spacing in H34 and O basemetal

In addition to constituent particles, TEM investigations revealed that both alloys contained submicron dispersoids (<0.5 μm) of the orthorhombic $Al_6(Fe,Mn)$ phase (Mn/Fe =~4, with some Cr occasionally observed), which is known to precipitate from the Mn in solid solution during homogenisation [20]. The particles were more frequently observed in the O-condition, and less frequently in the H34 condition. The particles appeared to nucleate on the remnants of the dislocation structure from the deformed state, Fig. 5.10. Various morphologies were observed: rod-like (Fig. 5.10-a), spherical, bowed (Fig. 5.6-a), and rhomboidal, similar to the morphologies observed in the literature [20, 21], as well as a wide size range (0.1-0.3 μm for spherical and rhomboidal particles, and 0.5-1 μm length and 0.05-0.2 μm width for rod-like particles).

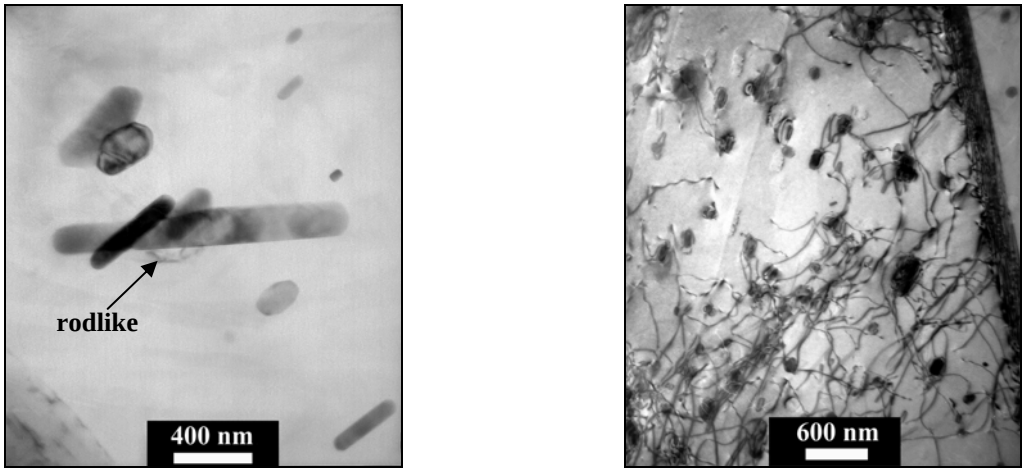

(a) (b)

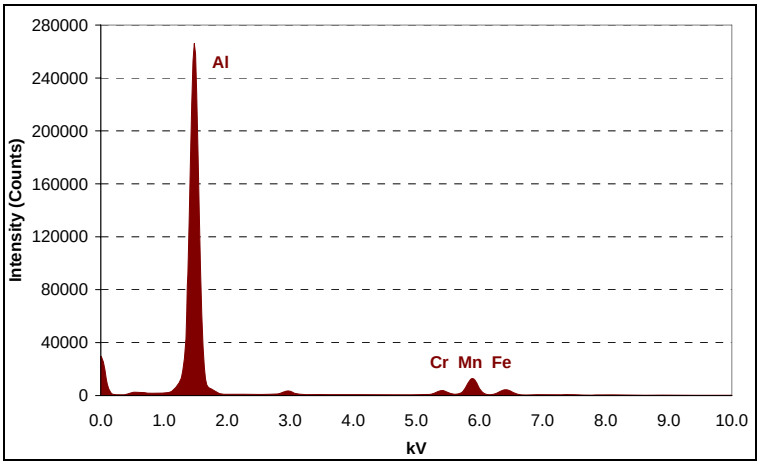

(c)

Fig. 5.10. 5251-O condition (a) $Al_6(Fe,Mn)$ rod-like dispersoids observed with the specimen tilted to a 2-beam invisibility condition, **g.b.** = 0 with **b** = $[011]$ and **g** = $(02\bar{2})$, (b) precipitation of the $Al_6(Fe,Mn)$ precipitates on the remnant dislocation structure, (c) corresponding EDS spectrum

5.1.4. Effect of Heat Treatments on Hardness & Microstructure

5.1.4.a. Basemetal Hardness

The basemetal hardness through-thickness variation was measured on both the ST-LT and ST-RD planes, Table 5.2. However, the ST-LT hardness data was correlated with the weld hardness since the weld face corresponds to the ST-LT plane. In the H34-condition, the ST-LT through-thickness variation was roughly symmetric, showing its minimum value (~76 H_V) close to the sheet surface. The hardness then increases to its maximum (~79-80 H_V) with a

larger standard deviation, and then decreasing again to ~76 H_V at mid-thickness which is probably associated with the larger grains in the central zone, Fig. 5.11-a. The ST-RD hardness was relatively higher and slightly less symmetric than the ST-LT. This higher ST-RD hardness was previously observed in rolled AA1xxx by Hilderbrandt, and suggested to be due to textural differences related to sheet rolling orientation [22]. It is important however to mention that the possible error in hardness measurements is ~ ±2 H_V, which could also explain the symmetry variation between both planes. In the O-condition, the hardness variation was also symmetric, decreasing from ~56 H_V near the surface to ~52-53 H_V at mid-thickness, with the ST-LT and ST-RD planes showing roughly similar trends, Fig. 5.11-b.

Table 5.2. Hardness in the different metallurgical directions

Condition	**5251-H34**		**5251-O**	
Orientation	**ST-LT**	**ST-RD**	**ST-LT**	**ST-RD**
Average	78.0	79.7	54.8	54.3
Stand. Deviation	1.9	1.5	1.9	1.6

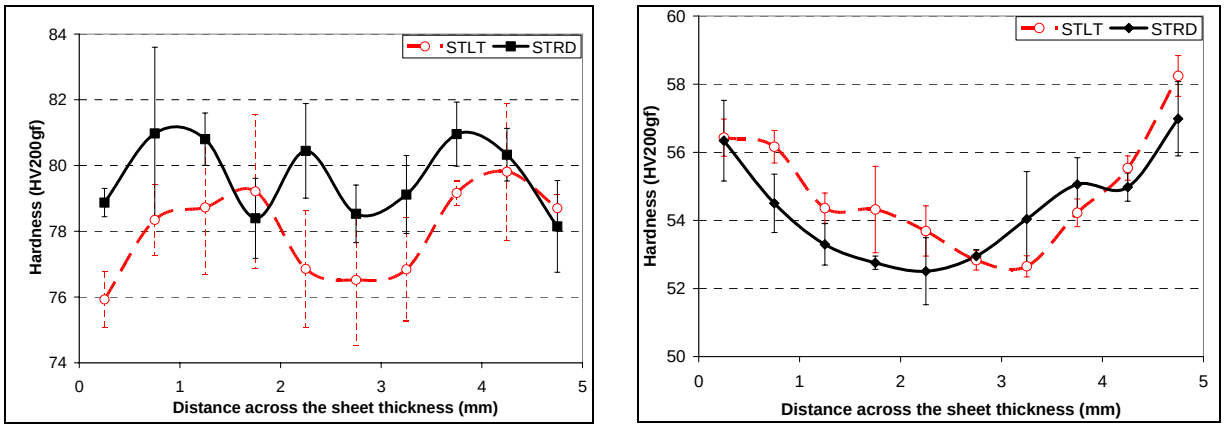

(a) (b)

Fig. 5.11. Through-thickness hardness variation in 5251 (a) H34-condition and (b) O-condition

5.1.4.b. Studying the microstructure-hardness development using the Gleeble & DSC

To study the hardness and microstructural development in the weld, notably within the HAZ, H34 basemetal samples were thermally cycled, using the Gleeble® thermomechanical simulator (TMS), to peak temperatures between 140 ˚C and 525 ˚C at a heating rate of 20

˚C/min, then water quenched. As this heating rate is the same as the DSC cycles, the traces for hardness variation with temperature were compared to the DSC trace, Fig. 5.12. Initially, the DSC trace showed that heating to temperatures up to 300 ˚C caused recovery (dislocation re-arrangement and some limited annihilation) to occur. This can be seen in the semi-continuous low energy releases 'A' (<0.1 J/g each) between 100 and 290 ˚C, which are accompanied by a decrease in hardness from the basemetal hardness of 78.0±1.9 H_V to 71.2±2.5 H_V at 300 ˚C. This was followed by the major energy release peak 'B' (0.5 J/g) between 300 and 360 ˚C, corresponding to the occurrence of recrystallisation, which resulted in a rapid decrease in the hardness to 52.0±0.8 H_V at 375 ˚C on completion of recrystallisation. This range of temperatures and energy releases is similar to what was observed for work-hardened commercially pure aluminium [23-25] and Al-Mg alloys [26].

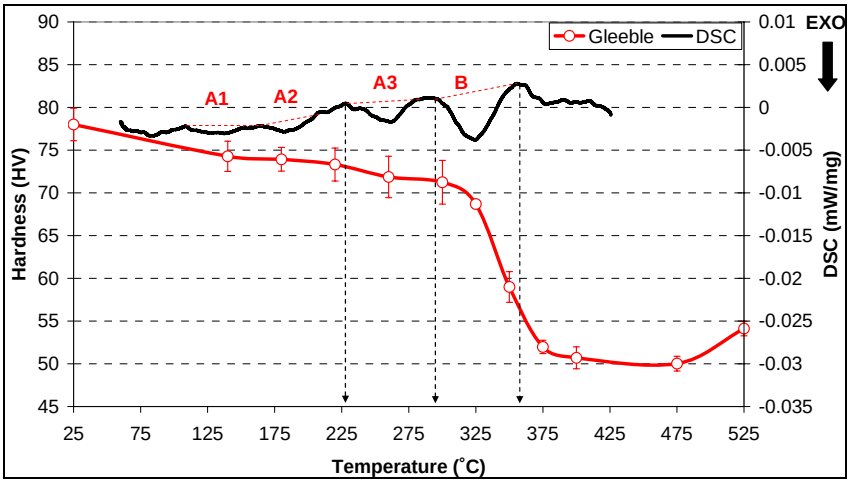

Fig. 5.12. Hardness development (ST-RD) for the 5251-H34 basemetal specimens thermally cycled at 20 ˚C/min to peak temperatures and quenched, along with a DSC trace performed at the same heating rate

By combining the DSC trace with microstructural investigations of the thermally cycled specimens, it was found that peak temperatures starting from 325 ˚C initiated recrystallisation (Fig. 5.13-a). Following completion of recrystallisation at 375 ˚C, grain growth was observed, with the average D_{Eq} growing from 24.3±10.2 μm at 375 ˚C (Fig. 5.13-b) to 40.2±14.8 μm at 525 ˚C (Fig. 5.13-c). Although such an increase in grain size would be expected to cause a decrease in hardness, it was found that this was the case only in the specimens cycled to 400

and 475 ˚C. At 525 ˚C, it was found that, despite grain growth, an increase of ~4 H_V was observed compared to the specimen cycled at 475 ˚C, Fig. 5.14.

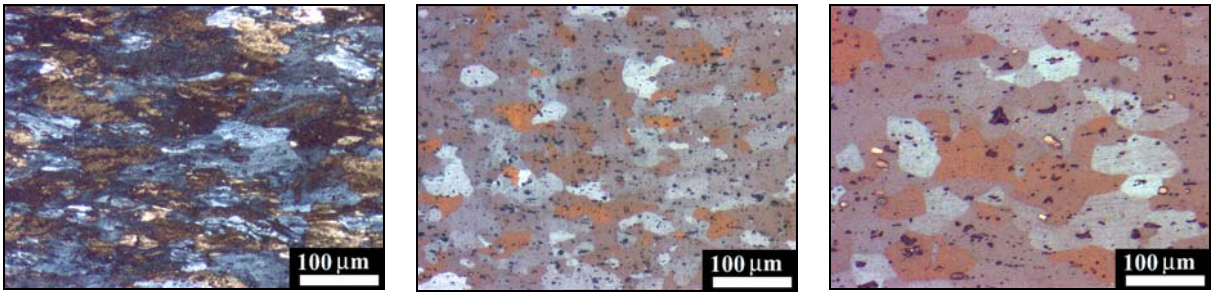

(a) 325 ˚C (b) 375 ˚C (c) 525 ˚C

Fig. 5.13. Micrographs of the Gleeble thermally cycled 5251-H34 basemetal at 20 ˚C/min

Image analysis of the Gleeble thermally specimens showed that the A_f of Mg_xSi particles remained roughly constant (~0.0047-0.0055) in the samples cycled to peak temperatures up to 375 ˚C, when it was found to slightly increase to ~0.0065 and then remained constant to temperature of ~475 ˚C until decreasing to ~0.0047 at 525 ˚C, Fig. 5.15-a. The slight increase at 375 ˚C is probably due to the dissolution of very fine Mg_xSi particles present in the basemetal (<0.5 μm, which are not quantified during image analysis), and then their re-precipitation on coarser particles starting from 375 ˚C. However, the dissolution/re-precipitation/coarsening effect is not clearly visible until 525 ˚C, where the decrease in A_f can be linked to the dissolution of the fine Mg_xSi particles, which causes the size distribution to be slightly shifted to larger sizes in the 525˚C specimen, Fig. 5.15-b, thus enriching the Mg and Si-content in solid solution, which led to the increase in hardness. Li and Arnberg [27] also observed that the average size of Mg_xSi does not significantly change during isothermal treatment of as-cast AA5182 (AlMg4.5Mn) at 520 ˚C, although at higher temperatures Mg_xSi completely dissolves. However, in the investigated alloy, the lower Mg-content could lead to the dissolution of Mg_xSi within the lower temperature range observed.

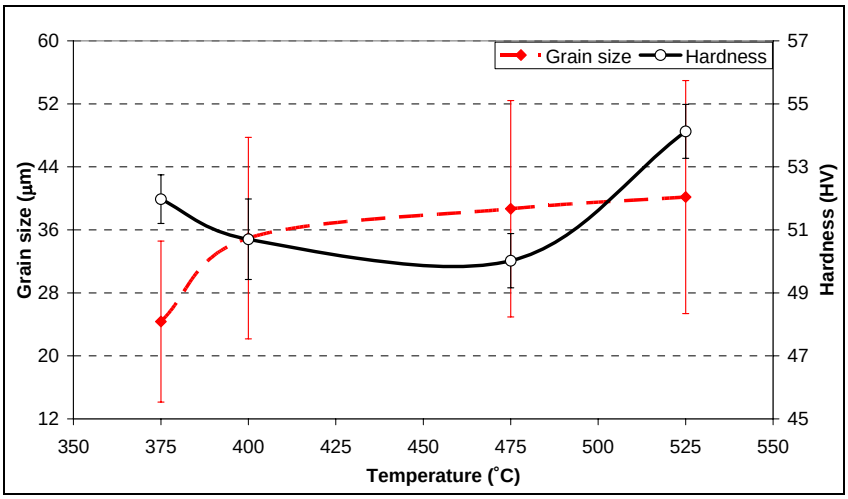

Fig. 5.14. Grain size and hardness development for the H34-basemetal specimens thermally cycled at 20 ˚C/min to peak temperature then quenched

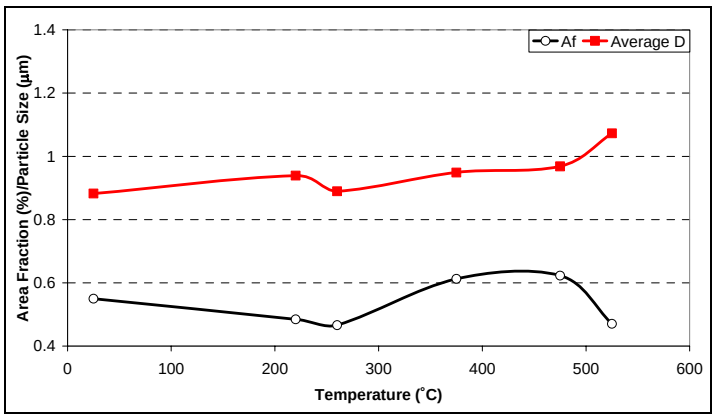

(a)

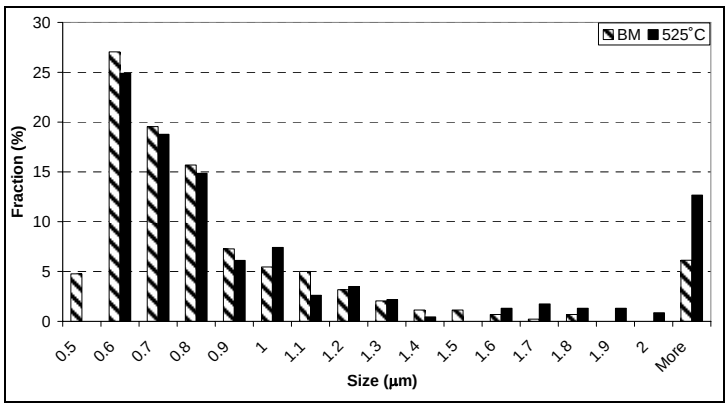

(b)

Fig. 5.15. The variation in Mg_xSi due to thermal cycling (a) size (particles >0.5 μm, average SD ~ 0.7 μm) and area fraction (average SD ~ 0.2 %), (b) size distribution for the H34-BM and the 525 ˚C specimen

5.2. AA5083

As a 5xxx-series alloy, this alloy was used to verify and compare some of the features investigated in the present work, especially with respect to the FSW microstructural development. Although both the AA5251 and AA5083 sheets have the same thickness, differences in their chemical composition and processing routes could lead to differences in the grain and particle structures. AA5083 is normally processed using DC casting, while low Mg content alloys (e.g. AA5251) are usually processed using CC [28], which was evident in the banded particle morphology in AA5251. The low freezing rates and smooth thermal gradients during DC casting, alongside the significant thickness reduction from the ingot to produce a plate, compared to a relatively smaller thickness reduction for CC products, are known to influence the resulting microstructure as discussed in section 2.3.2, affecting both the grain and intermetallic particle structures as will be also demonstrated in this section.

5.2.1. Grain Structure and Deformed Substructure

Similar to the 5251-H34 sheet, the grain structure of 5083-H116 sheet was composed of elongated flattened pancake-shaped grains along the RD. Compared to 5251-H34 sheet, the grains were longer (>0.5 mm), Fig. 5.16-a, finer in thickness (~9.5±4.8 μm), and did not show any morphological heterogeneities in terms of size or shape (e.g. DBs as in 5251-H34). There was no significant through-thickness variation in grain size.

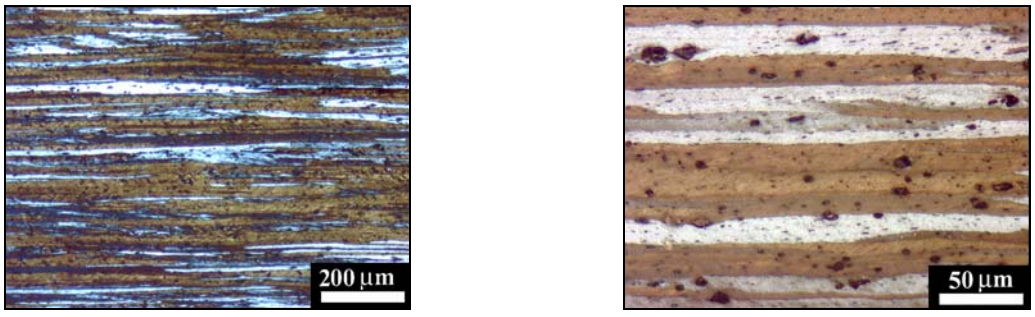

(a) (b)

Fig. 5.16. Grain structure (ST-RD) in 5083-H116 showing (a) elongated and (b) fine laths

The deformed substructure in 5083-H116 was composed of elongated grains and subgrains of lamellar boundaries oriented along the RD with a boundary spacing of 0.2-1 μm, Fig. 5.17-

(a,b). Some recovery can be observed in the deformed structure, which can be seen in the form of dislocation pile-up at the subgrain boundaries, although some dislocations can still be observed within the subgrains and grains, Fig. 5-17-c. Qualitatively, the extent of recovery is apparently higher than in 5251 (e.g. comparing Fig. 5.3 to Fig. 5.17-a). This is probably due to the higher Mg content of AA5083 (4.22 wt %), which is known to assist in energy storage during deformation, and accordingly enhance recovery after deformation at room temperature (section 2.5.2.a) [4]. Studying the effect of annealing (as a function of temperature) on the hardness development is expected to quantify the extent of recovery in 5083, which will be discussed in section 5.2.3.

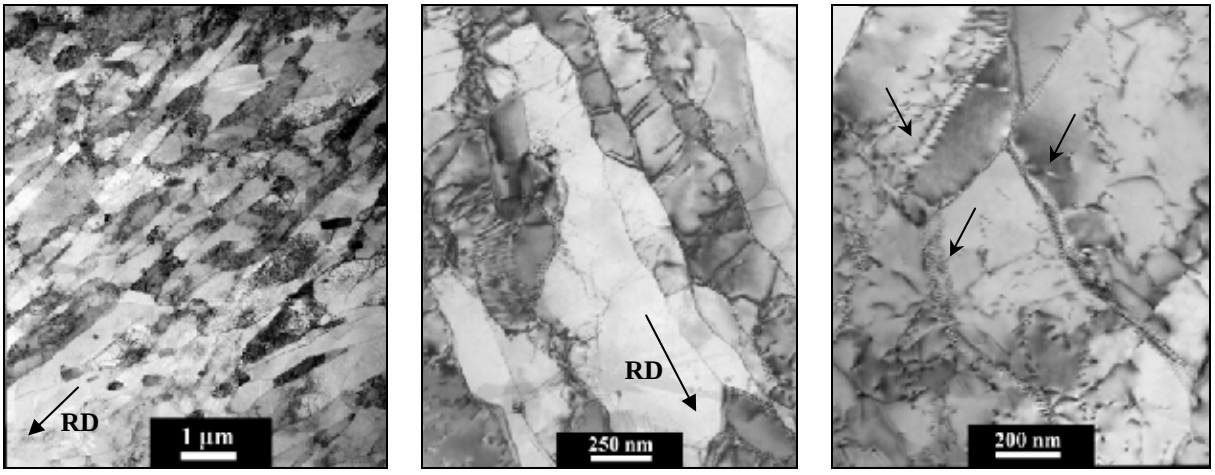

(a) (b) (c)

Fig. 5.17. Deformed substructure in 5083-H116 (a) elongated subgrains aligned along the RD, (b) recovered subgrains (c) with dislocation pile-up at the subgrain boundaries (arrowed) with some dislocations within the subgrains

5.2.2. Constituent Particles and Dispersoids

AA5083 contained similar constituent particles to those in 5251: the faceted Fe-rich $Al_6(Fe,Mn)$ or Al(Fe,Mn)Si, and the more rounded Mg_xSi. Due to the low Si-content in AA5083 (0.08 wt %, compared to 0.32 wt % in 5251), $Al_6(Fe,Mn)$ was more dominant than α-Al(Fe,Mn)Si, since the presence of sufficient Si (>0.3 wt %) is necessary for the $Al_6(Fe,Mn)$-to-α transformation [11-13, 27, 29-33]. Together, the Fe-rich phases constituted A_f = 0.02±0.002, compared to only 0.0015±0.0001 of Mg_xSi. The Fe-rich particles (>0.5 μm) were randomly distributed along the RD, Fig. 5.18-a, and were classified into three types: fine

submicron rod-like (low F_{ratio}) particles, fine rounded particles, and also coarse faceted particles, Fig. 5.18-b. The random distribution indicates that this alloy was produced by DC casting.

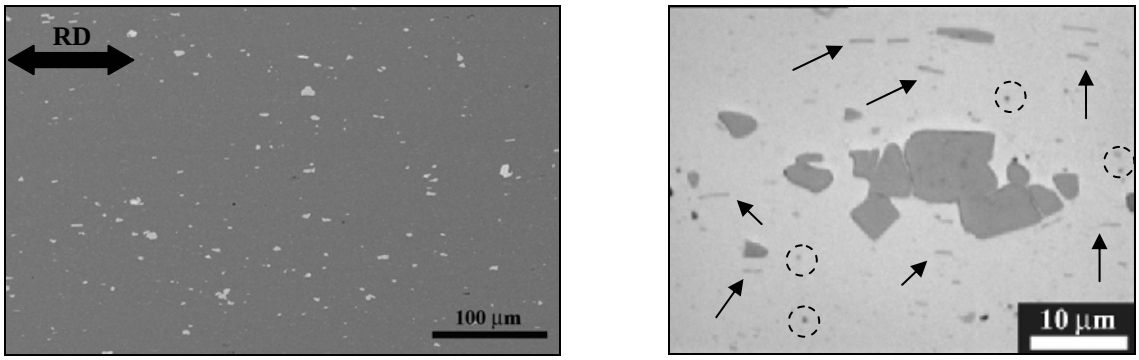

(a) (b)

Fig. 5.18. Particle structure in 5083-H116: (a) randomly distributed Fe-rich particles (ST-RD) (b) particle morphologies showing the fine rod-like particles (arrowed), rounded particles (circled), and the coarse faceted particles

The overall average particle size in 5083 is 1.2±1.1 μm for the Fe-rich particle size and 0.9±0.9 μm for the Mg_xSi particles, and the distribution is skewed to larger sizes, Fig. 5.19. The fine Fe-rich particles (0.5-1 μm) had an average D_{Eq} of 0.63 μm, compared to 2.3 μm for the coarse particles (>1 μm). However, the fine particles were more numerous than the coarse particles but less in A_f, with 8,581 /mm^2 and A_f ~0.003 for fine particles, compared to 3,284 /mm^2 and A_f ~0.017 for the coarse particles. The Mg_xSi particles were significantly lower than the Fe-rich particles in number density and A_f, with 915 /mm^2 for fine particles and A_f ~0.0002, compared to 250 /mm^2 A_f ~0.0013 for the coarse particles.

TEM investigations also revealed fine (length 0.3-1 μm, thickness <0.2 μm) mostly rod-like particles, identified as the $Al_6(Fe,Mn)$ dispersoids, which are known to precipitate from excess Mn in solid solution during homogenisation, Fig. 5.20. Although they have not been quantified, the $Al_6(Fe,Mn)$ particles were more frequently observed in 5083-H116 than in 5251-H34. These differences can be attributed to the differences in the processing routes, with the slow freezing rate and homogenisation associated with DC products, and also the repeated

annealing necessary for the significant thickness reduction, resulting in the precipitation of more Mn-rich dispersoids than those in the CC products (section 2.1.2.b).

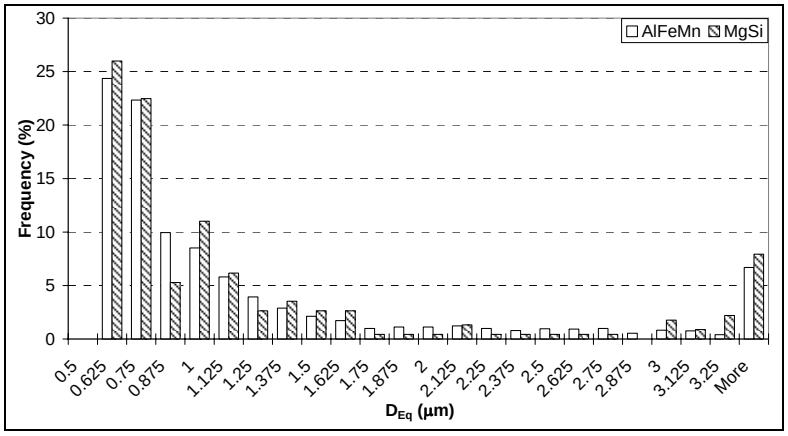

Fig. 5.19. Size distributions plot for the Fe-rich and Mg_xSi particles in 5083-H116 (> 0.5 μm)

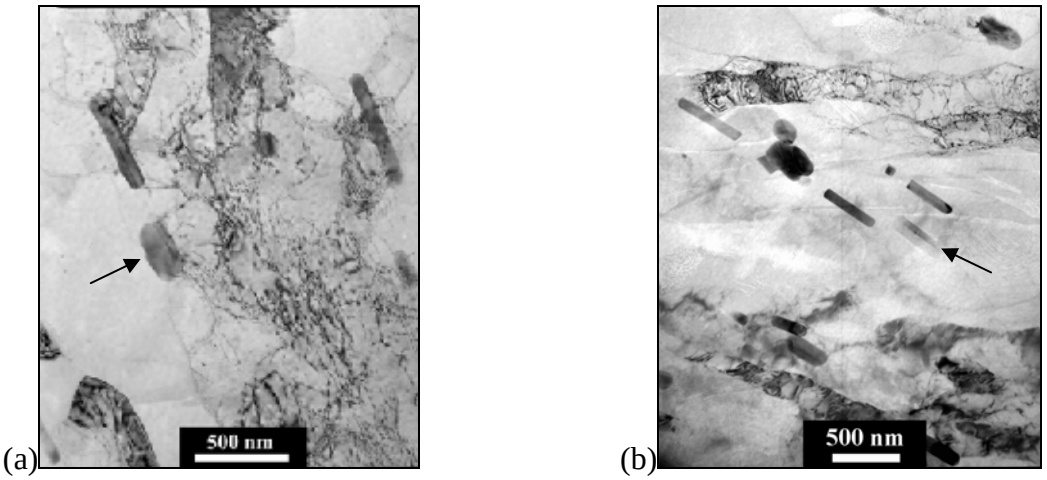

Fig. 5.20. $Al_6(Fe,Mn)$ dispersoids observed in 5083-H116

5.2.3. Effect of Heat Treatments on Hardness & Microstructure

The 5083-H116 basemetal hardness did not show a consistent variation across the thickness, with the hardness varying between 94.3 and 98 H_V, with an average of 97±1 H_V. Isothermal heat treatments were performed on the 5083-H116 basemetal to provide grain size data in the fully annealed condition, as well as hardness data for the recovered and fully recrystallised conditions. Temperatures up to 275 ˚C were found to slightly decrease the hardness to

93.6±0.9 H_V, Fig. 5.21. Temperatures above 275 ˚C led to a rapid decrease in hardness due to recrystallisation, reaching 77.2±1.1 H_V by 325 ˚C, and further decreasing to a minimum of 72.6±2.2 H_V at 425 ˚C. However, the hardness slightly increased beyond 425 ˚C, reaching 73.7±1.3 H_V by 525 ˚C. The amount of hardness drop prior to the initiation of recrystallisation in 5083-H116 (~3.4 H_V up to 275 ˚C) is almost half of that in 5251-H34 (~6.7 H_V up to 300 ˚C), which suggests that the extent of recovery after deformation at room temperature in 5083-H116 was higher than that in 5251-H34 due to the higher Mg-content, despite the differences in the extent of hardening (H34 is half-hard and H116 is quarter hard). This agrees well with previous work on recovery kinetics as a function of Mg-content as discussed in section 2.5.2.a [4].

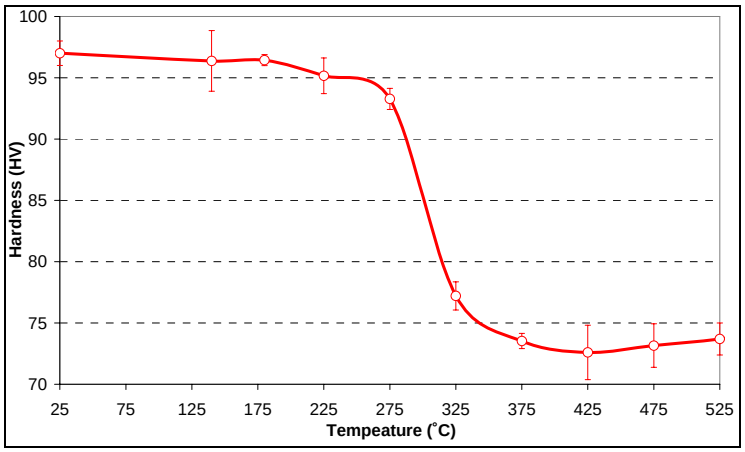

Fig. 5.21. Hardness (ST-LT) development due to isochronous (1hr.) heat treatments for the 5083-H116 basemetal specimens

The small hardness increase observed between 425 and 525 ˚C (~1.1 H_V) can also be correlated with the dissolution of Mg_xSi particles, as seen in 5251. This increase is lower than in 5251 due to the lower A_f of Mg_xSi particles in 5083 compared to 5251. In addition, the grain size did not show a significant increase by annealing beyond 375 ˚C (e.g. 19.8±6.3 μm at 375 ˚C and 20.5±7.2 μm at 425 ˚C, reaching 22±8.5 μm at 525 ˚C, Fig. 5.22). It is expected that the high number density of the submicron particles in 5083 assisted in grain size control during annealing, considering that they do not dissolve until ~575 ˚C ($Al_6(Fe,Mn)$ solvus temperature) [34].

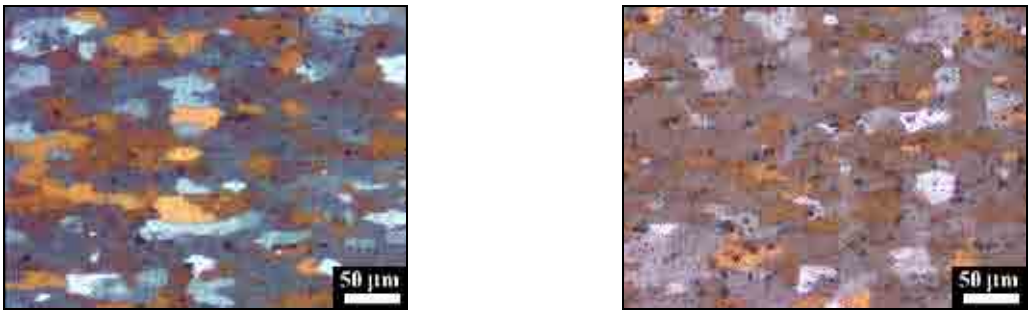

(a) (b)

Fig. 5.22. Micrograph for the 5083-basemetal annealed for 1 hr at (a) 375 ˚C, (b) 525 ˚C

5.3. AA5754-O

The CC and DC sheets were provided in the O-condition, having the same nominal chemical composition. This alloy was also used to verify and compare the FSW microstructure-property development features (e.g. onion rings), concentrating on the role of different basemetal grain and particle structures.

5.3.1. Grain Structure

The through-thickness grain size distribution showed a clear variation in the CC condition; where the grain structure within the outer section of the sheet was composed of nearly equiaxed grains (average F_{ratio} of ~0.65, with a grain size range 25-30 μm), compared to pancake-shaped coarser grains (average F_{ratio} of ~0.5, 35-45 μm) within the middle section, Fig. 5.23. On average, the F_{ratio} was found to be 0.58±0.14, and the D_{eq} was 32.2±14.9 μm, Fig. 5.24. The grain size distribution was found to have a significant influence on the hardness distribution in the sheet, whereby the outer section had a relatively high hardness (~60 H_V) compared to the middle section (~54 H_V). The study of the structure property relations, linking the grain size to hardness, for 5754 sheets will be presented in Chapter 8.

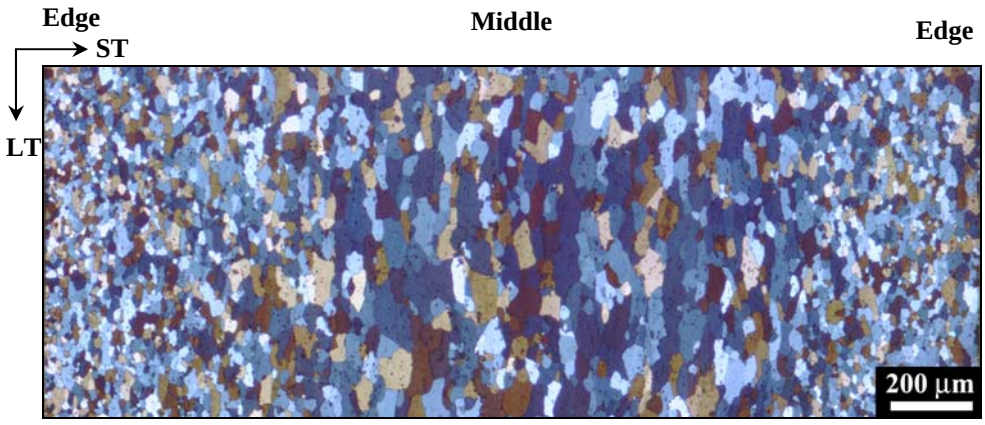

Fig. 5.23. Montage of the grain structure throughout the sheet thickness of the CC 5754-O

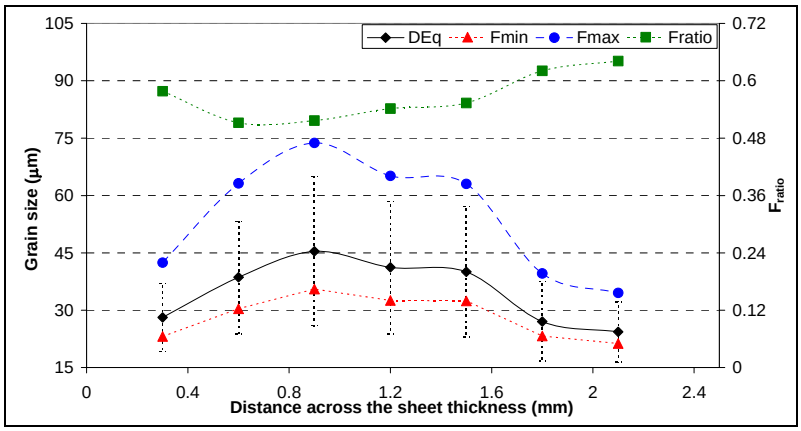

(a)

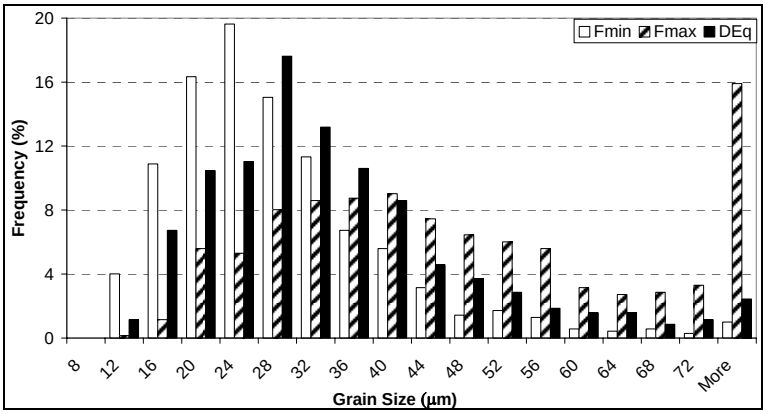

(b)

Fig. 5.24. (a) Through-thickness variation of grain characteristics in the CC 5754-O (Error bars for D_{Eq}), (b) histogram for the average grain characteristics (ST-LT)

In contrast with the CC condition, the DC condition grain structure distribution was uniform throughout the thickness of the sheet, showing a rather finer and a slightly elongated grain structure, Fig. 5.25. Average D_{Eq} grain size variations across the thickness varied between 20 and 26 μm, with an overall average grain size D_{Eq} of 23.12 μm, Fig. 5.26. The grain structure uniformity resulted in a constant hardness through thickness, with an average hardness of 58.9±1.0 H_V.

The difference in the grain structure between the CC and DC conditions is associated with two main factors; the manufacturing route and the thermomechanical treatment prior to annealing. DC sheets usually experience significant thickness reduction, compared to the CC sheets, which would typically result in a finer grain size.

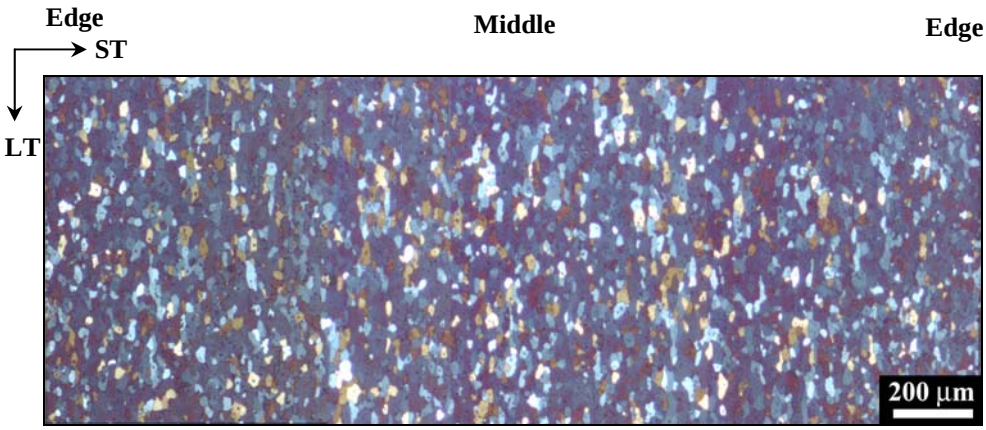

Fig. 5.25. Montage of the through-thickness grain structure in the DC 5754-O sheet

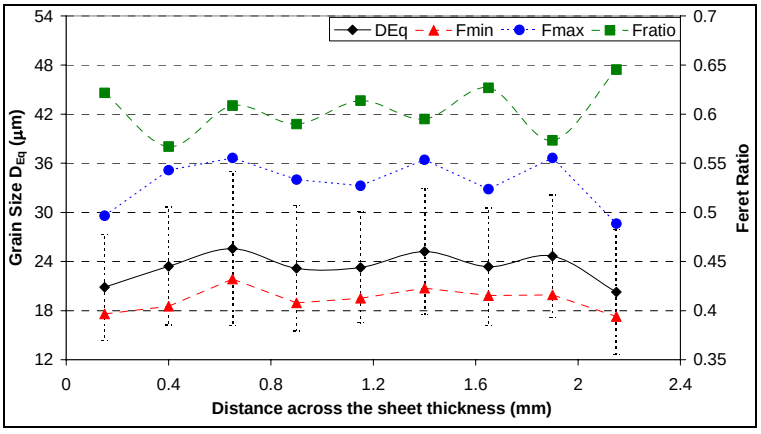

(a)

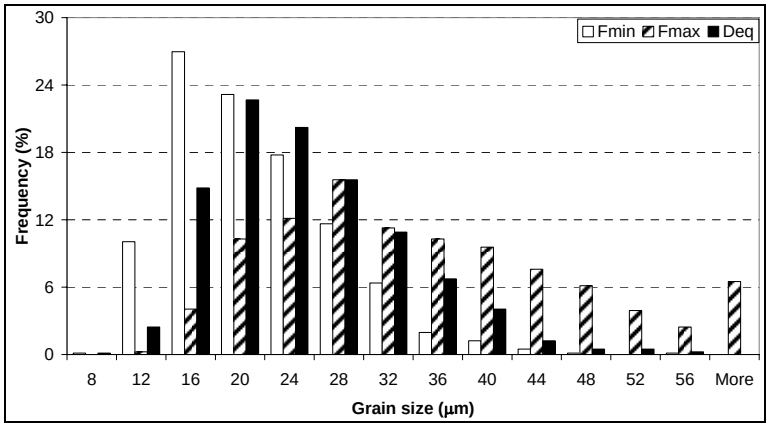

(b)

Fig. 5.26. (a) Through-thickness variation of grain characteristics in the DC 5754-O sheet (Error bars for D_{Eq}), (b) histogram for the grain characteristics (ST-LT)

5.3.2. Constituent Particles and Dispersoids

Both the DC and CC sheets contained the same types of intermetallic particles observed in 5251 or 5083; the faceted α-Al(Fe,Mn)Si and Al_6(Fe,Mn) (Fe/Mn = 3 to 5.5), and the more rounded Mg_xSi. The average area fraction and sizes of the Fe-rich particles were similar in the DC and CC sheets, Table 5.3, with the DC having a Fe-rich particle $A_f = 0.012 \pm 0.002$ compared to $A_f = 0.011 \pm 0.005$ in the CC condition, which is lower than the amount observed in 5083 and 5251. The Mg_xSi particle content in the DC sheet was less than that in 5251 and 5083, whereas the CC sheet contained less Mg_xSi than the 5251 but a similar amount to 5083.

The size distribution of the Fe-rich particles in both conditions was significantly different, Fig. 5.27. The CC condition had a higher number of the submicron particles, compared to a higher number of coarse particles in the DC condition. It is known that the Fe-rich particles in the DC sheets are typically coarser than in the CC sheets [2]. This is attributed to the low freezing rates and the prolonged heating during homogenisation in the DC sheets which leads to particle coarsening [12, 13, 30, 35], compared to the rapid cooling rates in the CC sheets which lead to the formation of finer particles, with the *in-situ* rolling breaking up the particles (section 2.3.2).

Table 5.3. Characteristics of the intermetallic particles in the 5754-O CC and DC sheets

Alloy	Phases Present	Area Fraction	D_{Eq} (μm)	Density (#/mm^2)
CC	Al_6(Fe,Mn) α-Al(Fe,Mn)Si	0.011 ± 0.005	1.15 ± 0.73	7,245
	Mg_xSi	0.0023 ± 0.0011	1.05 ± 0.52	2,031
DC	Al_6(Fe,Mn) α-Al(Fe,Mn)Si	0.012 ± 0.002	1.34 ± 0.75	6,657
	Mg_xSi	0.0008 ± 0.0004	0.81 ± 0.40	1,082

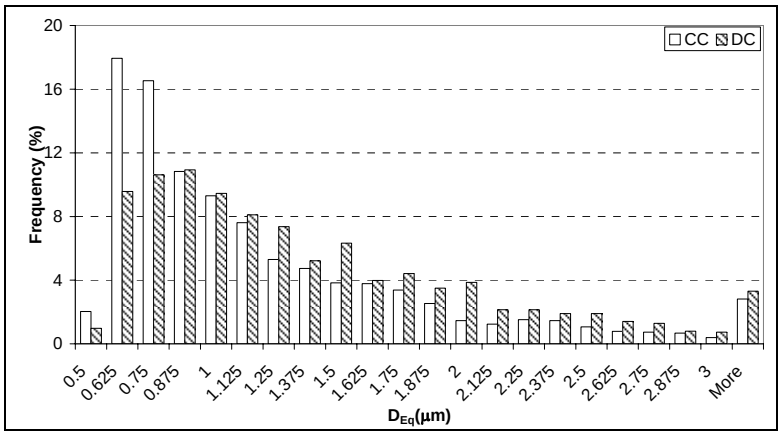

Fig. 5.27. Size distribution of the Fe-rich constituent particles in DC and CC 5754-O sheets

Similar to 5251, the CC sheets showed a clear banding of the Fe-rich particles along the RD, compared to a random distribution in the DC sheet, Fig. 5.28. By studying several through thickness traces for the inter-particle band spacing in the CC sheet, it was found to vary across the thickness; ~ 52 μm in the sub-surface regions and ~ 85 μm in the middle section, with an average band spacing of $\sim 75 \pm 25$ μm, Fig. 5.29-a. It should be noted that for the CC sheet the area fraction of the Fe-rich particles was not consistent through thickness with the near surface region (1/3rd of the sheet from each side) having an area fraction of ~0.012, the middle section (central 1/3rd) having an area fraction of ~0.006 but with a narrow centreline segregation region containing an area fraction of ~0.024. In contrast, the area fraction was roughly constant through thickness in the DC sheet, Fig. 5.29-b.

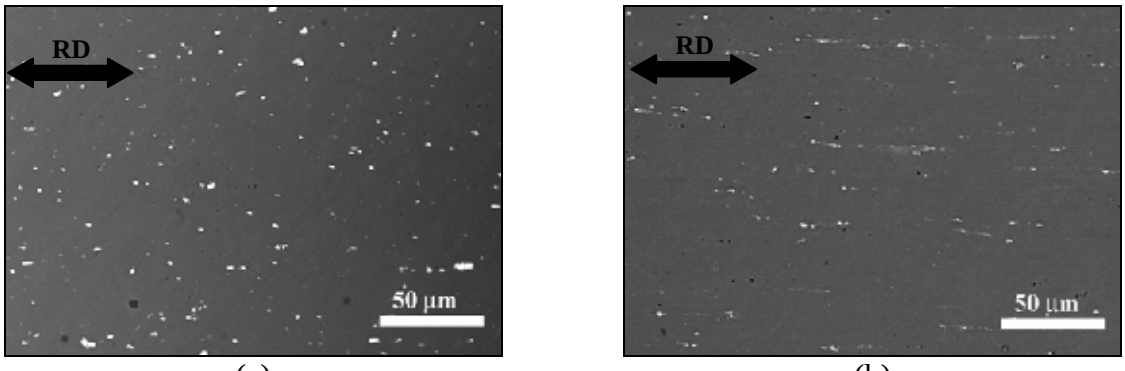

(a) (b)

Fig. 5.28. Distribution of the Fe-rich constituent particles in (a) 5754-DC, (b) 5754-CC

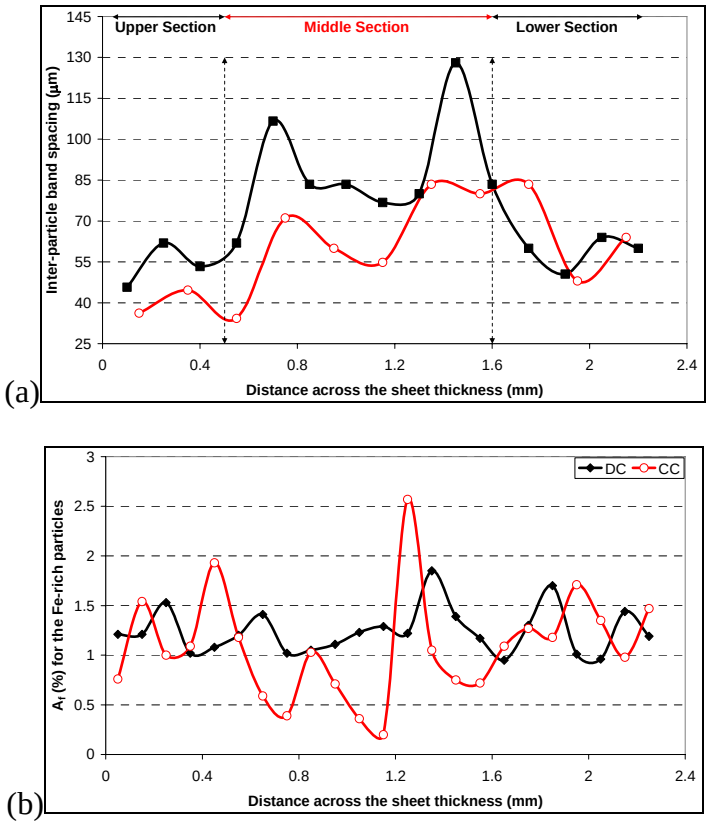

Fig. 5.29. (a) Two traces for the through-thickness variation in inter-particle band spacing in CC 5754-O (ST-RD), and (b) the area fraction of the Fe-rich particles in CC and DC 5754-O sheets

Fine $Al_6(Fe,Mn)$ dispersoids were also observed in both conditions. Although the numbers were not quantified, the particle density in both conditions was noticeably lower than that in 5251-O and 5083. In the CC sheet, the dominant morphology of the particles was the rhomboidal shape, with size range of 200-400 nm. In the DC sheet, the morphology was more of rod-like or nearly spherical, Fig. 5.30.

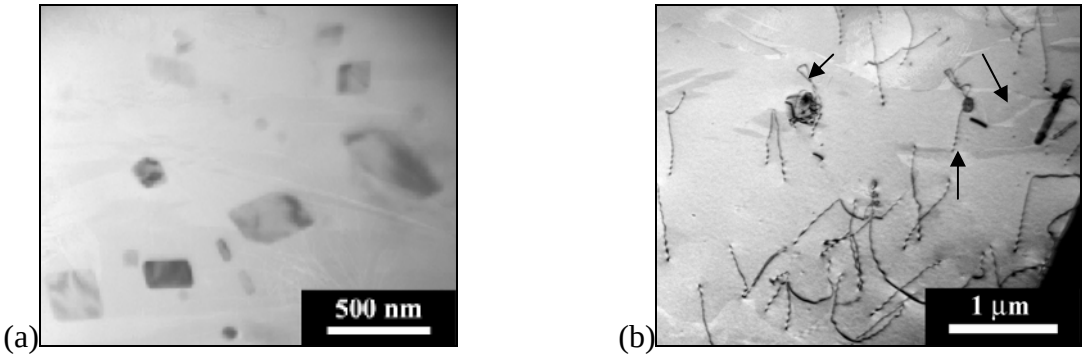

Fig. 5.30. (a) rhomboidal $Al_6(Fe,Mn)$ dispersoids observed in the CC 5754-O specimen tilted to a 2-beam invisibility condition, **g.b.** = 0 with **b** = $[001]$ and **g** = $(\bar{2}20)$, (b) in the DC 5754-O condition

5.4. AA2024-T351

As a heat-treatable alloy, AA2024 was used to study the influence of the alloy parameters (e.g. intermetallic particles, alloying elements, processing route) on the FSW microstructural development, in comparison to the development in work-hardenable 5xxx series alloys.

5.4.1. Grain Structure

The alloy was provided in the T351 condition (i.e. solution treated, stress relieved by stretching to 1.5-3%, followed by natural aging). The grain structure on the ST-RD plane was composed of elongated pancake-shaped grains along the RD, with F_{max} of ~150 μm near the surface, and increasing to >0.5 mm towards the middle of the sheet. On the ST-LT plane, the same pancake microstructure was also observed, with irregularly-shaped grains, with average F_{min} of 50 ± 21 μm, Fig. 5.31.

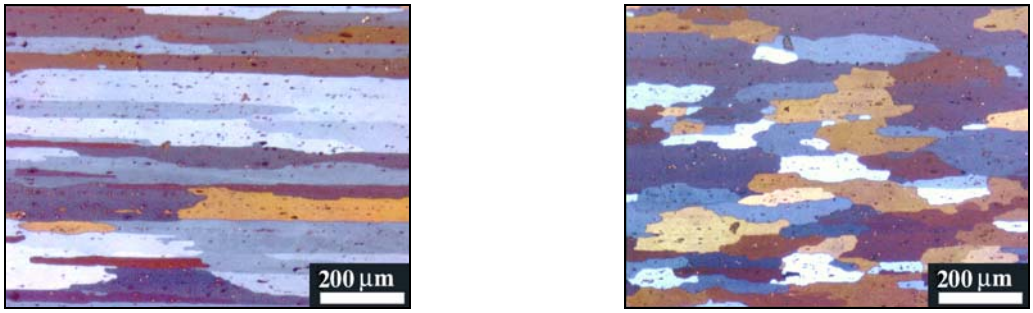

(a) (b)

Fig. 5.31. Grain structure in 2024-T351 showing (a) ST-RD plane, (b) ST-LT plane

5.4.2. Particle Structure

Four different particle types were identified by SEM/EDS: (Mg,Cu)-rich Al_2CuMg phase (equilibrium S-phase); Cu-rich Al_2Cu phase (equilibrium θ-phase); an (Fe,Mn,Cu)-containing phase, which is the α-constituent $(CuFeMn)_3Si_2Al_{15}$ (detected less frequently compared to S and θ); and Mg_xSi, Fig. 5.32. Optically, the S and θ-phases were found to form multi-phase particles. They could be distinguished by the difference in colour; where the S phase appeared grey in colour, compared to the θ, which was orange/pale pink, Fig. 5.33-a. Similar to 5251 and CC 5754-O, the Cu-rich particles were also banded along the ST-RD

plane as shown in Fig. 5.33-b. The average inter-particle band spacing was found to be ~95 ± 35 μm, with no specific variation trend (i.e. fluctuating between 70 and 200 μm across the thickness). The average band spacing in 2024 is about 2.5 times larger than that in 5251, but only 1.3 times larger than that in CC 5754.

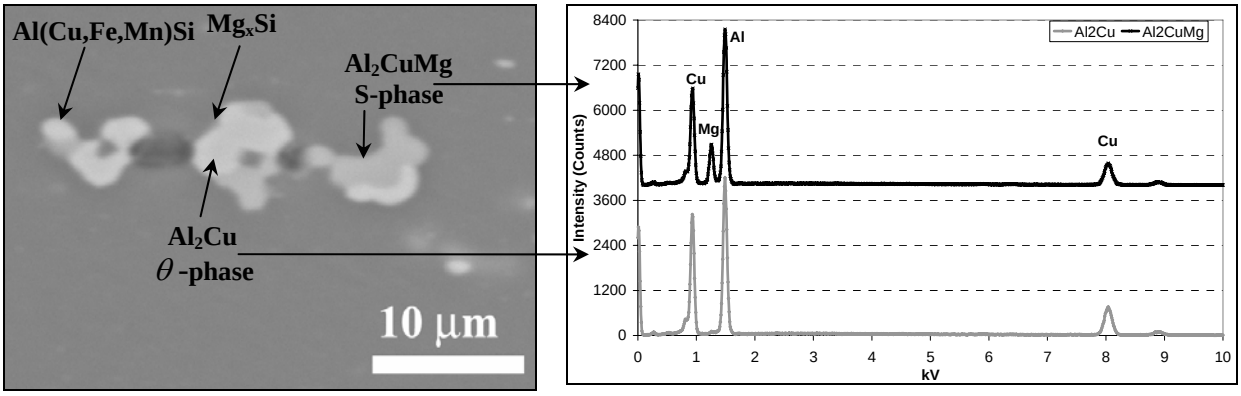

Fig. 5.32. Particle structure in AA2024-T351 with example corresponding EDS spectra

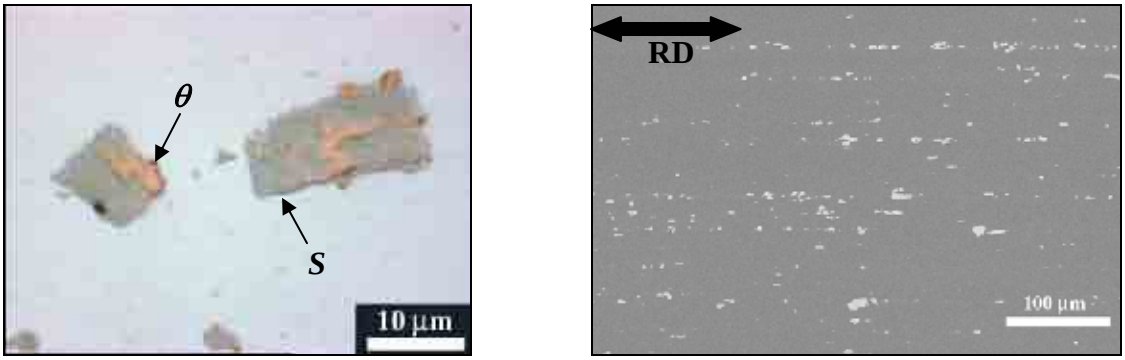

(a) (b)

Fig. 5.33. (a) particle structure observed under the optical microscope (the S phase is grey in colour, while the θ phase is orange/pink in colour), (b) Banding of the Cu-rich particles in 2024-T351 (ST-RD)

The three Cu-containing particle types (S, θ, and α) gave an area fraction of ~0.017 ± 0.006. They were coarser in size and lower in number density (3,106 /mm^2) than the Fe-rich particles in 5083 and 5251. The average particle size was $d_{avg}=2.1 \pm 1.7$ μm with ~47 % of the particles being > 2 μm in size, Fig. 5.34. The amount of Mg$_x$Si particles present was very small ($A_f=0.00037 \pm 0.00006$) compared to 5251, 5083 and 5754, which is expected because most of

the Mg present should combine with Cu to form the S-phase. 2024-T351 is also expected to contain hardening phases, because the sheet is in the naturally-aged temper, for which only GP (Guinier-Preston) zones are expected to be present, but they are too fine to be characterised in this study.

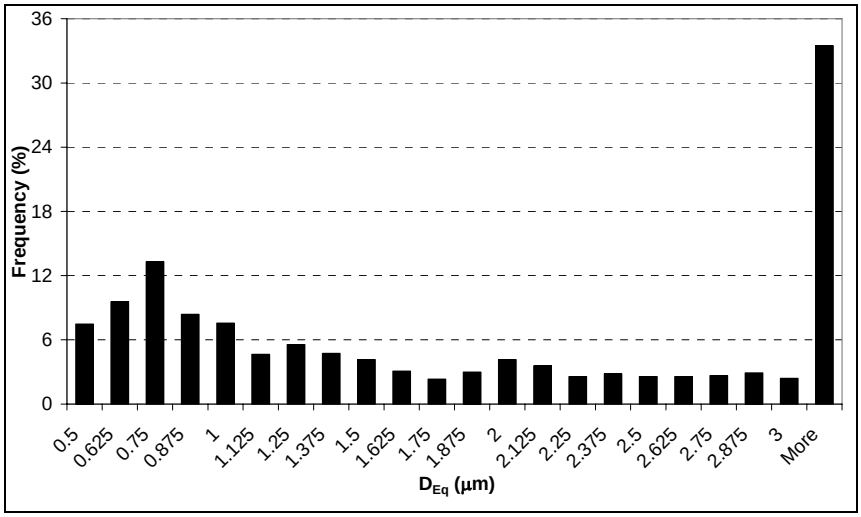

Fig. 5.34. Histogram for the D_{Eq} of Cu-containing particles in 2024-T351

5.4.3. Hardness

The average hardness of the T351-condition was 144.2 ± 4.2 H_V, with the hardness varying between 142 and 150 H_V. However, there was no specific variation observed across the thickness.

5.4.4. Dissolution and Precipitation Processes in 2024-T351

To distinguish the various effects that could happen during welding (precipitation, dissolution, and segregation), a basemetal specimen was cycled in the DSC at a heating rate of 10 ˚C/min from room temperature to 500 ˚C. A base line with empty pans was also measured and subtracted from the signal. As shown in Fig. 5.35, the 2024-T351 DSC trace is composed of three peaks as typically observed in the literature [36-38]. The first peak is an endothermic peak whose onset is at 150 ˚C and end at 250 ˚C, with an energy gain of 9.8 J/g. This peak is attributed to the dissolution of the GP zones, where the energy is proportional to their volume fraction. The second peak is an exothermic peak that starts 250 ˚C and ends at 310 ˚C, which

is attributed to the precipitation of the S/S' phase from the solid solution after the dissolution of the GP zones in peak A, with an energy release of -27.2 J/g. Finally, peak C which is endothermic peak indicating the dissolution of the S phase (finishes by 480 ˚C).

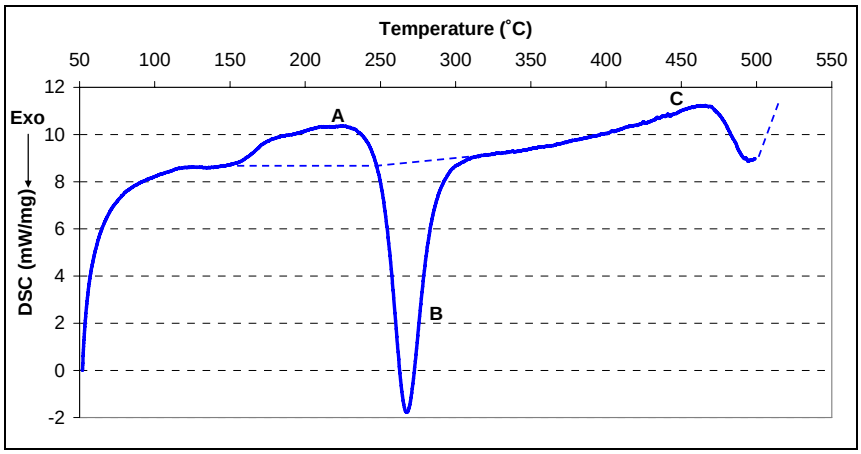

Fig. 5.35. DSC trace for the 2024-T351

5.5. Summary of the Basemetals Characteristics

Characterisation of the four basemetals was performed, including their particle and grain structures. It was found that the casting approach and thermomechanical processing route had a direct influence on the microstructural heterogeneity of the material, including the grain and particle structures. For the 5xxx series alloys processed by CC, the constituent particles were observed to form particle stringers, banded along the RD, compared to a random distribution in the DC 5xxx alloys. For the 2xxx series alloy, the equilibrium phases were also observed to be banded along the RD, with a larger inter-particle band spacing compared to the constituent particles in the CC 5xxx alloys. Such differences are caused by the difference in freezing rates during casting, and post-casting homogenisation. DC 5xxx and 2xxx alloys are homogenised, which ultimately results in the formation of a coarser particle structure and fine dispersoids which precipitate from excess elements in solid solution.

The information presented in this chapter will be used during the examination of the welds to achieve the following objectives:

- Studying the influence of the starting condition microstructure (work-hardened or annealed) on the microstructural development of the TMAZ/WN.
- Investigating the effect of the processing route of the basemetal, and accordingly the associated microstructural heterogeneity in the grain and particle distribution, on the weld microstructure.
- Identifying the basemetal microstructural parameters that control the joint microstructure, and accordingly its properties.

5.6. References

[1] F. J. Humphreys, "A unified theory of recovery, recrystallization and grain growth, based on the stability and growth of cellular microstructures--I. The basic model," *Acta Materialia*, vol. 45, pp. 4231-4240, 1997.

[2] B. Q. Li, "Producing thin strips by twin-roll casting - part I: process aspects and quality issues," *JOM*, vol. 47, pp. 29-33, 1995.

[3] D. Mandal and I. Baker, "Determination of the stored energy and recrystallization temperature as a function of depth after rolling of polycrystalline copper," *Scripta Metallurgica et Materialia*, vol. 33, pp. 645-650, 1995.

[4] E. Nes, "Recovery revisited," *Acta Metallurgica et Materialia*, vol. 43, pp. 2189-2207, 1995.

[5] F. J. Humphreys and M. Hatherly, *Recrystallization and Related Annealing Phenomena*. Great Britain: Pergamon, 1995.

[6] D. A. Hughes and N. Hansen, "High angle boundaries formed by grain subdivision mechanisms," *Acta Materialia*, vol. 45, pp. 3871-3886, 1997.

[7] M. Verdier, Y. Brechet, and P. Guyot, "Recovery of AlMg alloys: flow stress and strain-hardening properties," *Acta Materialia*, vol. 47, pp. 127-134, 1999.

[8] M. Verdier, M. Janecek, Y. Brechet, and P. Guyot, "Microstructural evolution during recovery in Al-2.5%Mg alloys," *Materials Science and Engineering A*, vol. 248, pp. 187-197, 1998.

[9] R. W. Hertzberg, *Deformation and Fracture Mechanics of Engineering Materials*, 4 ed. USA: John Wiley & Sons Inc., 1996.

[10] S. C. Wang, Z. Zhu, and M. J. Starink, "Estimation of dislocation densities in cold rolled Al-Mg-Cu-Mn alloys by combination of yield strength data, EBSD and strength models," *Journal of Microscopy*, vol. 217, pp. 174-178, 2005.

[11] W. B. Hutchinson, A. Oscarsson, and A. Karlsson, "Control of microstructure and earing behaviour in aluminium alloy AA 3004 hot bands," *Materials Science and Technology*, vol. 5, pp. 1118-1127, 1989.

[12] R. G. Kamat, "AA3104 can-body stock ingot: characterization and homogenization," *JOM*, vol. 48, pp. 34-38, 1996.

[13] Y. J. Li and L. Arnberg, "Evolution of Eutectic Intermetallic Particles in DC-cast AA3003 Alloy during Heating and Homogenization," *Materials Science and Engineering A*, vol. 347, pp. 130-135, 2003.

[14] J. Liu and J. G. Morris, "Recrystallization microstructures and textures in AA 5052 continuous cast and direct chill cast aluminum alloy," *Materials Science and Engineering A*, vol. 385, pp. 342-351, 2004.

[15] M. Slamova, M. Karlik, F. Robaut, P. Slama, and M. Veron, "Differences in microstructure and texture of Al-Mg sheets produced by twin-roll continuous casting and by direct-chill casting," *Materials Characterization*, vol. 49, pp. 231-240, 2002.

[16] X.-M. Cheng and J. G. Morris, "Texture, microstructure and formability of SC and DC- cast Al-Mg alloys," *Materials Science and Engineering A*, vol. 323, pp. 32-41, 2002.

[17] X. F. Yu, Y. M. Zhao, X. Y. Wen, and T. Zhai, "A study of mechanical isotropy of continuous cast and direct chill cast AA5182 Al alloys," *Materials Science and Engineering A*, vol. 394, pp. 376-384, 2005.

[18] W. C. Liu, T. Zhai, and J. G. Morris, "Comparison of recrystallization and recrystallization textures in cold-rolled DC and CC AA 5182 aluminum alloys," *Materials Science and Engineering A*, vol. 358, pp. 84-93, 2003.

[19] A. Baldacci, A. Bigot, H. Klocker, and J. H. Driver, "Constituent particle break-up during hot rolling of AA 5182," presented at Hot Deformation of Aluminum Alloys III, San Diego, CA, USA, 2003.

[20] P. Ratchev, B. Verlinden, and P. Van Houtte, "Effect of Preheat Temperature on the Orientation Relationship of $(Mn,Fe)Al_6$ Precipitates in an AA5182 Aluminium-Magnesium Alloy," *Acta Materialia*, vol. 43, pp. 621-629, 1995.

[21] P. Yang, O. Engler, and H.-J. Klaar, "Orientation Relationship between Al_6Mn Precipitates and the Al Matrix during Continuous Recrystallization in Al-1.3%Mn," *Journal of Applied Crystallography*, vol. 32, pp. 1105-1118, 1999.

[22] W. H. Hildebrandt, "Differential Scanning Calorimetry Evaluations of Recrystallization Behavior in Aluminum Sheet," *Metallurgical Transactions A (Physical Metallurgy and Materials Science)*, vol. 10A, pp. 1045-1048, 1979.

[23] C. Garcia-Cordovilla and E. Louis, "Differential Scanning Calorimetry Study of Recovery and Recrystallization in a Commercial Al-Fe-Si Alloy (AA1145)," *Scripta Metallurgica*, vol. 18, pp. 549-553, 1984.

[24] C. Garcia-Cordovilla and E. Louis, "A differential scanning calorimetry study of recrystallization and its interaction with precipitation in Al-Fe-Si commercial alloys (AA1145 and AA8011)," *Journal of Materials Science*, vol. 21, pp. 971-979, 1986.

[25] J. Lendvai, G. Honyek, A. Juhasz, and I. Kovacs, "Differential Scanning Calorimetry Study of the Release of Stored Energy in an Al-Fe Alloy," *Scripta Metallurgica*, vol. 19, pp. 943-946, 1985.

[26] M. Verdier, I. Groma, L. Flandin, J. Lendvai, Y. Brechet, and P. Guyot, "Dislocation densities and stored energy after cold rolling of Al-Mg alloys: Investigations by resistivity and differential scanning calorimetry," *Scripta Materialia*, vol. 37, pp. 449-454, 1997.

[27] Y. J. Li and L. Arnberg, "A Eutectoid Phase Transformation for the Primary Intermetallic Particle from $Al_m(Fe,Mn)$ to $Al_3(Fe,Mn)$ in AA5182 Alloy," *Acta Materialia*, vol. 52, pp. 2945-2952, 2004.

[28] R. E. J. Sanders, "Technology Innovation in Aluminum Products," *JOM*, vol. 53, pp. 21-25, 2001.

[29] D. T. L. Alexander and A. L. Greer, "Solid-State Intermetallic Phase Transformations in 3xxx Aluminium Alloys," *Acta Materialia*, vol. 50, pp. 2571-2583, 2002.

[30] Y. J. Li and L. Arnberg, "Quantitative Study on the Precipitation Behavior of Dispersoids in DC-cast AA3003 Alloy during Heating and Homogenization," *Acta Materialia*, vol. 51, pp. 3415-3428, 2003.

[31] M. Warmuzek and A. Gazda, "An Analysis of Cooling Rate Influence on the Sequence of Intermetallic Phases Precipitation in Some Commercial Aluminium Alloys," *Journal of Analytical Atomic Spectrometry*, vol. 14, pp. 535-537, 1999.

[32] F. H. Samuel, A. M. Samuel, H. W. Doty, and S. Valtierra, "Influence of Composition, Sr Modification, and Annealing Treatment on the Structure and Properties of Cast Al-4Pct Mg Alloys," *Metallurgical and Materials Transactions A*, vol. 34A, pp. 115-129, 2003.

[33] Y. J. Li and L. Arnberg, "Solidification Structures and Phase Selection of Iron-Bearing Eutectic Particles in a DC-cast AA5182 Alloy," *Acta Materialia*, vol. 52, pp. 2673-2681, 2004.

[34] Y. S. Sato, S. H. C. Park, and H. Kokawa, "Microstructural factors governing hardness in friction-stir welds of solid-solution-hardened Al alloys," *Metallurgical and Materials Transactions A: Physical Metallurgy and Materials Science*, vol. 32, pp. 3033-3042, 2001.

[35] A. L. Dons, "The Alstruc homogenization model for industrial aluminum alloys," *Journal of Light Metals*, vol. 1, pp. 133-149, 2001.

[36] C. Badini, F. Marino, and E. Verne, "Calorimetric study on precipitation path in 2024 alloy and its SiC composite," *Materials Science & Engineering A: Structural Materials: Properties, Microstructure and Processing*, vol. A191, pp. 185-191, 1995.

[37] C. Genevois, A. Deschamps, A. Denquin, and B. Doisneau-cottignies, "Quantitative investigation of precipitation and mechanical behaviour for AA2024 friction stir welds," *Acta Materialia*, vol. 53, pp. 2447-2458, 2005.

[38] L. F. Mondolfo, *Aluminum Alloys: Structure and Properties*. London: Butterworth, 1976.

Chapter 6

THERMAL MODELLING
A TOOL TO RATIONALISE THE HAZ DEVELOPMENT

Knowledge of the temperatures experienced during welding is crucial to explain the various microstructural phenomena associated with FSW, and their impact on the strength development. In this chapter, the mathematical formulation of a 3-D numerical model (adapted on MATLAB®) for the heat transfer during FSW is presented, alongside with the verification using thermocouple measurements for 2024-T351 and 5754-O welds. The model was used to provide the thermal cycles and steady-state thermal profiles for the investigated welds, which were compared against the hardness development and the HAZ microstructure. Gleeble thermal simulations of the thermal cycle for the 5251 weld were used to verify the model, and study the influence of the transient thermal cycle on the HAZ development.

6.1. Mathematical Modelling of Heat Flow

6.1.1. Constitutive Equations

The heat generation takes place during FSW at the interface between the tool shoulder/pin and the plasticised material as a result of the friction and plastic deformation taking place. The constitutive equation for the 3-dimensional unsteady-state heat flow with heat generation is given as [1]:

$$\frac{\partial}{\partial x}\left(k_x \frac{\partial T}{\partial x}\right)+\frac{\partial}{\partial y}\left(k_y \frac{\partial T}{\partial y}\right)+\frac{\partial}{\partial z}\left(k_z \frac{\partial T}{\partial z}\right)+q_V=\rho\, c \frac{\partial T}{\partial t} \qquad (6.1)$$

If the thermal conductivity (k) is assumed constant, the equation can be simplified to:

$$\frac{\partial^2 T}{\partial x^2}+\frac{\partial^2 T}{\partial y^2}+\frac{\partial^2 T}{\partial z^2}+\frac{q_V}{k}=\frac{1}{\alpha}\frac{\partial T}{\partial t} \tag{6.1-a}$$

6.1.2. Numerical Heat Flow Modelling

Several models have been established for the heat flow during welding by simplifying and analytically-solving equation (6.1) (e.g. the theory of moving source of heat by Rosenthal [2]). This requires a simplified geometrical representation for the heat source (e.g. point or line sources) and the weld geometry (e.g. thin and thick sheets), as summarised by Grong [3]. Obtaining analytical solutions for equation (6.1), though possible, results in complex formulations containing special functions, infinite series, and transcendental (non-polynomial) equations. Due to the geometrical complexity of the FSW heat source, it is more convenient and realistic to adopt a numerical formulation.

A numerical solution for the unsteady-heat transfer equation requires the formulation of the second derivatives of temperature in finite difference (FD) approximations in 3D-space, and the first derivative of temperature in time. FD solutions can be expressed in forward, centred, or backward difference depending on the spatial position of the node in 3D coordinates (e.g. interior or on the surfaces). Using centred difference, the first and second derivates of a general function *f(x)* can be *approximately* given as [4]:

$$f'(x_n)\cong\frac{f(x_{n+1})-f(x_{n-1})}{2\Delta x} \tag{6.2-a}$$

$$f''(x_n)\cong\frac{f(x_{n+1})-2f(x_n)+f(x_{n-1})}{(\Delta x)^2} \tag{6.2-b}$$

The numerical methods for solving the heat transfer equation can be *explicit* or *implicit*. In an explicit method, the spatial FD approximations are at the n^{th} time step while the time FD approximation provides a forward difference between the temperature in the $n+1$ *and* n^{th} time steps. Thus, a solution for the temperature at a specific node at the $n+1$ time step is *explicitly* expressed in terms of the other variables. There are concerns regarding the usage of explicit methods with regards to their stability, convergence, and accuracy. This requires the use of a small time step to avoid oscillation and improve the accuracy, which accordingly increases the computation time [4].

In an implicit method, the spatial FDs are approximated at the *n+1* time step, while the time derivative is approximated in the same way as the explicit solution. Accordingly, the temperature in all the nodes at the *n+1* time step can be solved as a single system of simultaneous equations, instead of solving the individual nodes in the explicit methods [1, 4]. Thus, implicit methods can provide an alternative time-efficient approach especially by using MATLAB® to solve systems of linear equations in tri-diagonal matrices (TDMAs).

The alternating direction implicit (ADI) scheme was used [4, 5]. In this method (Fig. 6.1), a single time increment is solved in three implicit 1D problems, instead of solving for each node in 3D. The three steps are numerically expressed in FDs for equation (6.1a) as:

Step I:

$$\frac{T_{i+1,j,k}^{n+1/3}-2T_{i,j,k}^{n+1/3}+T_{i-1,j,k}^{n+1/3}}{(\Delta x)^2}+\frac{T_{i,j+1,k}^{n}-2T_{i,j,k}^{n}+T_{i,j-1,k}^{n}}{(\Delta y)^2}+\frac{T_{i,j,k+1}^{n}-2T_{i,j,k}^{n}+T_{i,j,k-1}^{n}}{(\Delta z)^2}+\frac{q_V}{k}=\frac{1}{\alpha}\frac{T_{i,j,k}^{n+1/3}-T_{i,j,k}^{n}}{\Delta t} \quad (6.3\text{-a})$$

Step II:

$$\frac{T_{i+1,j,k}^{n+1/3}-2T_{i,j,k}^{n+1/3}+T_{i-1,j,k}^{n+1/3}}{(\Delta x)^2}+\frac{T_{i,j+1,k}^{n+2/3}-2T_{i,j,k}^{n+2/3}+T_{i,j-1,k}^{n+2/3}}{(\Delta y)^2}+\frac{T_{i,j,k+1}^{n+1/3}-2T_{i,j,k}^{n+1/3}+T_{i,j,k-1}^{n+1/3}}{(\Delta z)^2}+\frac{q_V}{k}=\frac{1}{\alpha}\frac{T_{i,j,k}^{n+2/3}-T_{i,j,k}^{n+1/3}}{\Delta t} \quad (6.3\text{-b})$$

Step III:

$$\frac{T_{i+1,j,k}^{n+2/3}-2T_{i,j,k}^{n+2/3}+T_{i-1,j,k}^{n+2/3}}{(\Delta x)^2}+\frac{T_{i,j+1,k}^{n+2/3}-2T_{i,j,k}^{n+2/3}+T_{i,j-1,k}^{n+2/3}}{(\Delta y)^2}+\frac{T_{i,j,k+1}^{n+1}-2T_{i,j,k}^{n+1}+T_{i,j,k-1}^{n+1}}{(\Delta z)^2}+\frac{q_V}{k}=\frac{1}{\alpha}\frac{T_{i,j,k}^{n+1}-T_{i,j,k}^{n+2/3}}{\Delta t} \quad (6.3\text{-c})$$

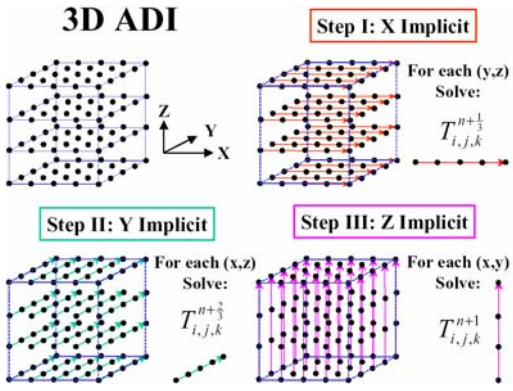

Fig. 6.1. Solution technique in the ADI method [5]

The equations are re-arranged to solve for the *n+1/3*, *n+2/3*, and *n+1* temperatures as unknowns in the three steps of equations (6.3) respectively. Although the ADI scheme is

'unconditionally stable', its stability is only restricted to being non-oscillating and finite. The accuracy and convergence can be further improved by selecting a time increment using:

$$\Delta t < \frac{(\Delta x)^2 + (\Delta y)^2 + (\Delta z)^2}{8\alpha_{\max}} \tag{6.4}$$

Following each time step, the temperature nodal values are stored in a 3-D array ($l \times m \times n$), which is used to calculate the temperatures in the following time step due to the moving heat source. To record the transient thermal cycle at given nodes, the temperature is recorded throughout the welding cycle. Yet, the entire 3-D temperature array is stored only at mid-weld path, as a representation of the steady-state temperature distribution. The graphical toolbox in MATLAB® is used to create 2D/3D temperature profiles for the weld.

Since the model uses a 3-D formulation, the model is thus ideal for medium thickness plates, where the transient heat transfer is three-dimensional. However, it can be used to solve the transient thermal cycle in thin plates, which are normally modelled as a two-dimensional heat transfer problem [3].

6.1.3. Heat Input Generation and Distribution

6.1.3.a. Heat Generation

The heat input was divided into three contributions (Fig. 6.2): a) the tool shoulder, $\boldsymbol{Q_S}$ (a flat annulus in contact with the workpiece surface), b) the tool pin lateral surface, $\boldsymbol{Q_p}$ (cylindrical or conical pin, regardless of the threading geometry or any re-entrant features), and the pin flat base, $\boldsymbol{Q_{pb}}$. The total heat input ($\boldsymbol{Q_{Total}}$) is thus given as:

$$Q_{Total} = Q_S + Q_P + Q_{pb} \tag{6.5}$$

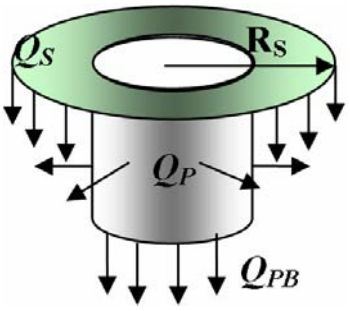

Fig. 6.2. FSW heat input contributions due to the shoulder (Q_S), pin lateral side (Q_p), and pin base (Q_{pb})

As mentioned in chapter 3, the FSW heat generation can result from the friction of the 'slipping' tool over the workpiece [6-8], or from the adiabatic-deformation of the material sticking to the tool [9, 10]. Although it is now believed that the latter case is the dominant condition [11, 12], the proposed algorithm considers both scenarios. A subroutine is included in the code to adjust the contact condition at the tool/welded metal interface based on Coulomb's friction law.

If the rotational work by the slipping tool shoulder over the metal surface is converted to frictional heat generation, the shoulder heat input can be expressed as [8]:

$$Q_S = \frac{2\pi}{3}\mu P \omega\left(R_S^3 - R_P^3\right) \tag{6.6}$$

where P is the pressure experienced under the tool shoulder:

$$P = \frac{F_N}{A_S} = \frac{F_N}{\pi\left(R_S^2 - R_P^2\right)} \tag{6.6-a}$$

The change from the friction-induced (slip) to the deformation-induced (stick) condition is governed by the modified Coulomb's friction law. As stated by this law [13], the friction shear stress (μP) due to the contact normal pressure (P) at a given temperature has a maximum limit value $\tau_{\max}(T)$, which is constant regardless of any increase in P. This maximum value is the limit of the sticking friction, and it starts when μP exceeds $\tau_{\max}(T)$. In this case, μP will be replaced in equation (6.6) by $\tau_{\max}(T)$, which is related to the material ultimate strength σ_{UTS} by (based on the Von Mises criterion between the yield stress in shear and yield stress in tension [13]):

$$\tau_{\max} = \frac{\sigma_{UTS}}{\sqrt{3}} \tag{6.7}$$

The friction coefficient will be estimated during the fitting stage using the torque and normal force measurements during FSW, using the approach followed by Schmidt and Hattel [9], based on the torque-based model by Khandkar *et al.* [14]. This approach will also provide an estimate for the average shear stress ($\tau_{\max}$), which can be also used to rationalise the dominant contact condition (slip or stick).

Due to the stirring action by the pin, its heat generation will always be deformation-induced. The heat input of the pin lateral surface and base can be added together, such that:

$$Q_P = \frac{2\pi}{3}\tau\omega\left(3R_P^2 H_P + R_P^3\right) \tag{6.8}$$

6.1.3.b. Spatial Distribution of the Heat Sources

The heat input is distributed in the form of an annular heat flux under the shoulder, and a volumetric heat source for the pin heat input (Q_P+Q_{pb}), Fig. 6.2. The shoulder heat input gets dissipated as a heat flux (q) which is a function of the radius as suggested by Chao *et al.* [15]:

$$q(r) = \frac{3Q_S\, r}{2\pi\left(R_S^3 - R_P^3\right)} \tag{6.9}$$

such that $R_P \le r \le R_S$.

By substituting (6.9) into (6.6), the heat flux at any node under the tool shoulder at a radius (r) can be expressed by:

$$q(r) = \mu P\, v \tag{6.10-a}$$

where v is the resultant speed at a radius r, which is given as:

$$v = \sqrt{\left(f + \omega r\cos\theta\right)^2 + \left(\omega r\sin\theta\right)^2} \tag{6.10-b}$$

where θ is the angle between the tangential component and the feed direction. Since the feed speed (f) is generally much lower than the tangential speed of the tool (ωr), v can be approximated as:

$$v \cong \omega r \tag{6.10-c}$$

For the pin, its heat input contribution can be represented as a volumetric heat source (q_V) within the cylindrical volume occupied by the pin ($2\pi R_P H_P$), such that:

$$q_V = \tau\omega\left(3 + \frac{R_P}{H_P}\right) \tag{6.11}$$

Equation (6.10-a) is in the slip (friction) condition. On reaching the stick condition, μP is replaced by τ as discussed earlier.

6.1.4. Boundary Conditions

Radiation heat losses were not considered in the model due to the minimal surface emissivity by aluminium. In the absence of artificial cooling on the surface (e.g. by air blowing or liquid N_2 or water sprinkling), natural (free) convection can be assumed on the exposed surfaces (the 4 vertical planes and the surface), except at the nodes where the shoulder heat input is applied. The contact conductance at the base plane in contact with the machine anvil was also modelled as equivalent to a convection boundary.

The (Neumann) convection boundary condition is formulated as:

$$-k\frac{\partial T}{\partial x} = h_x\left(T_\infty - T\right) \tag{6.12}$$

which can be represented using FD as:

$$-k\left[\frac{T_{i+1,j,k} - T_{i-1,j,k}}{2\Delta x}\right] = h_x\left(T_\infty - T_{i,j,k}\right) \tag{6.12-a}$$

Simplified empirical equations were used to calculate temperature-dependent convection heat transfer coefficients to air from the vertical and horizontal surfaces [1], such that:

$$h = C\left(\Delta T/L\right)^{1/4} \tag{6.13}$$

where C is a constant (~1.4), ΔT is the difference between the sheet and the ambient temperatures, and L is the vertical or horizontal dimension. The coefficients are calculated in each time step based on the temperature profile of the previous step. For the base plane in contact with the backing plate, a constant or varying convection heat transfer coefficient (h_C) was used to simulate the heat flow through the contact boundary using equation 6.12, with T_∞ as the backing plate temperature (assumed constant). The fitting of the contact conductance is discussed in section 6.2, and compared to other models.

6.1.5. Material Properties

6.1.5.a. Thermomechanical Properties

To model the heat generation and transfer, the model requires the thermomechanical and thermophysical properties of the alloys. The thermomechanical (i.e. σ_{UTS} variation with

temperature) properties are obtained from the ASM Handbook [16]. The σ_{UTS} -temperature data between ~>150 ˚C and ~400 ˚C are fitted to an exponential equation of the form:

$$\sigma_{UTS}(T) = A\exp(-BT) \tag{6.14}$$

Good fit (with R^2 >0.95) can be obtained, e.g. as in Fig. 6.3. The equation can be extrapolated beyond the fitted limit to estimate σ_{UTS} of the material up to the solidus temperature (i.e. incipient melting). The value of σ_{UTS} is fixed as zero at incipient melting and beyond in the code (compared to ~5-10 MPa if the fitted function is used). This is because, at incipient melting, a liquid film will form at the tool/matrix interface, which is the heat generation interface and also the maximum temperature path, lubricating the tool and minimising the heat input to almost zero [6]. For the alloys whose thermomechanical properties are unavailable or incomplete (mainly 5754 or 5251), data are interpolated from other 5xxx-series alloys assuming a linear relation of the strength with the Mg-content.

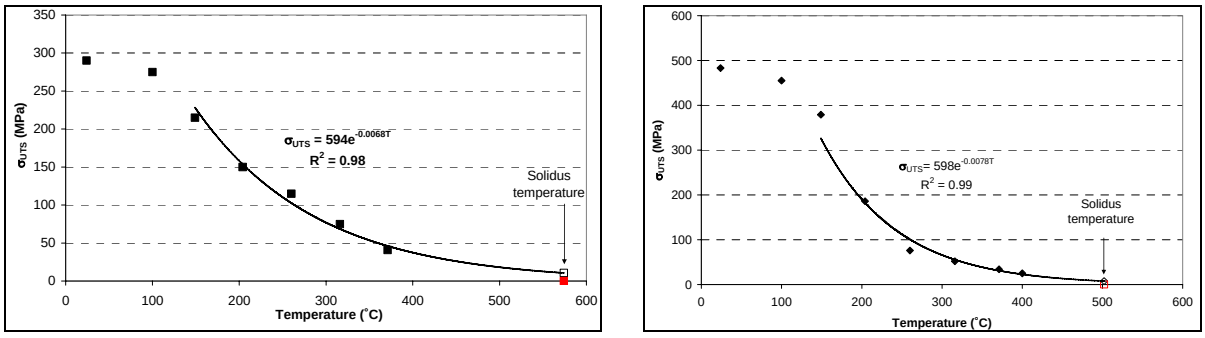

(a) AA5083 (b) AA2024

Fig. 6.3. An example for the fitted temperature-dependent tensile strength (ASM data)

It is important to admit that there are some concerns with using the ASM temperature-dependent data, and with the validity of the exponential thermomechanical data fit. First, the ASM σ_{UTS} data were measured following 10,000 h hold time, compared to the transient thermal exposure during welding thermal cycles which are of the order of 10-100 s. This effect could be more significant in heat-treatable alloys, where the dissolution and aging/over-aging processes are rate/time-dependent, which could result in different microstructural development ahead of the moving tool compared to that in the ASM experiments. Second, the

ASM data were measured using a slow strain rate (0.001 s^{-1}) typical for mechanical testing, compared to the high strain rates experienced during weld, which are of the order of 100-500 s^{-1} [17]. Thus, there are two factors; the transient thermal exposure during weld and the strain-rate dependence, which are expected to result in the actual $\sigma_{UTS}(T)$ being higher than the ASM data. It is not the first time that these concerns have been raised [18-20] (section 3.3.2.b), although the ASM data has been used for some time to establish thermomechanical models for FSW (e.g. [11, 13]). These effects were highlighted in the CFD models by Colegrove and Shercliff [17, 18], notably in their work which compared various models for material constitutive behaviour [18].

However, as the scope and aim of the present model is to present a simplistic approach for modelling the thermal fields to help rationalise the microstructural development, the suggested approach could be acceptable for a number of reasons. First, σ_{UTS} data were used instead of σ_{YS}, providing an upper bound estimate for the shear stress in Coulomb friction law as in the work of Xu and Deng [13], to minimise the strain rate-dependence effect. Second, it was noticed from the 2024-T3 temperature-dependent data performed by Alcan, following 10 s hold in the range 150-400 ˚C [19], that using the ASM data would significantly underestimate the strength development during FSW. With the increase in temperature, the effect of the hold time (10 s versus 10,000 hr) on the strength decreases, though being still present. It is important to highlight that the estimated $\tau_{\max}$ using the exponential fit represents an average value for the flow stress along the tool/matrix interface, with all the variations in strain rate and temperatures (between 400-500 ˚C). In fact, early weld thermal models have previously used estimates of $\tau_{\max}$ (e.g. [15, 21]), although their estimates were either arbitrary or fitted using thermal measurements. In the present model, $\tau_{\max}$ is calculated using the most commonly available thermomechanical properties database. This is the main hypothesis of this model; whether acceptable thermal predictions can be obtained using this simple approach or not.

6.1.5.b. Thermophysical Properties

The thermophysical properties (k, C_P, ρ) were also obtained from the literature as a function of temperature [16, 22]. The temperature-dependent thermophysical properties are usually

unavailable in the literature. A few studies [19, 23] have investigated the possibility of using room temperature data, as an alternative, in terms of accuracy and reliability of computer welding simulations. Zhu and Chao [23] performed a sensitivity analysis for the influence of the temperature-dependent properties on the transient thermal cycles during welding of AA5xxx. They showed that using room temperature values for the specific heat and the density have a minimal effect on the model accuracy. However, there is some effect for the thermal conductivity. They indicated though that reasonable results can be obtained using either room-temperature or average properties over the welding cycle temperature range, as the variation in *k* in non-heat treatable alloys (e.g. 5754, Fig. 6.4-a) is not significant. For heat treatable alloys (e.g. 2024), Preston *et al.* [19] indicated that the thermal conductivity is considerably affected by the dissolution and precipitation reactions that take place during welding, Fig. 6.4-b. This variation in *k* is also dependent on the time of thermal exposure, which controls the types and sizes of the precipitates formed or solute fraction retained. Depending on the availability of the properties, either average values or temperature-dependent values were used. In the latter case, the values were calculated in the code in each step based on the temperature profiles of the previous time step.

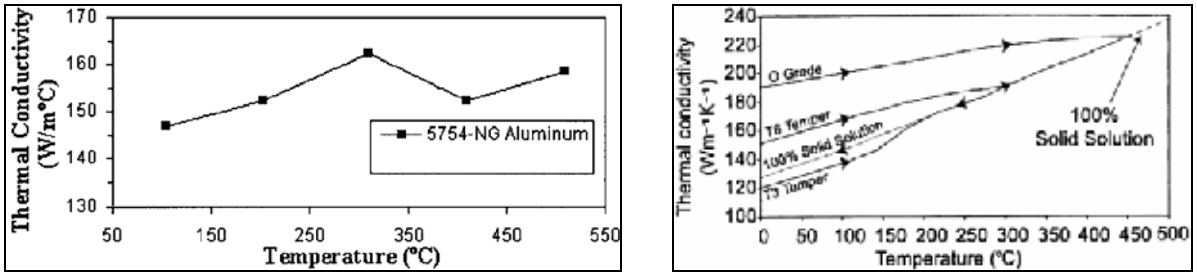

(a) (b)

Fig. 6.4. Variation of the thermal conductivity with temperature of (a) AA5754 [24], and (b) AA2024, showing a more significant variation and the effect of the initial temper [19]

6.2. Fitting & Validation of the Thermal Model

The thermal model was fitted (for the friction coefficient and contact conductance) using the thermocouple and machine data (torque, tool forces, and power) for a 2024-T3 weld (W1) obtained from the weld-Benchmarks website [25]. The validation was later performed using the thermocouple measurements for the 2024-T351 weld (W2) obtained from the work of M. Jariyaboon, who studied the corrosion behaviour of the same weld [26]. Further validation was performed using the thermocouple measurements performed for the 5754-O welds (W3). Nonetheless, machine data were only available for W1 and W3. The welding parameters of the welds used for fitting and validation are shown in Table 6.1.

Table 6.1. The welding parameters for the welds used for fitting and validation of the model

#	Alloy	Rotation Speed (RPM)	Feed Rate (mm/min)	Z-Force (kN)	Sheet Thickness mm	Tool	Tool dim. (mm)			Source
							D_S	D_P	H_P	
W1	2024-T351	600	80	22	5.85	Threaded	18	6	5.3	[25]
W2*	2024-T351	468	75	24	6.35	Threaded	24	10	5.5	[26]
W3	5754-O	500	500	14.9	2.3	MX-Triflute	15	6	2	--

*: Also referred to as HW (section 4.2)

6.2.1. Fitting: W1:2024-T351

6.2.1.a. Analysis of Experimental Data

To identify the contact condition (slip or stick) and also to provide an estimate for the friction coefficient to be used in the model, the torque and plunge force data were studied with the same approach followed by Schmidt and Hattel [9], based on the torque-based model by Khandkar *et al.*[27]. According to Schmidt and Hattel, a fully sliding or sticking heat input can be represented respectively as:

$$Q_{Sliding} = \frac{2\pi}{3}\mu P\left(R_S^3 + 3R_P^2 H_P\right)\omega \tag{6.15.a}$$

$$Q_{Sticking} = \frac{2\pi}{3}\tau\left(R_S^3 + 3R_P^2 H_P\right)\omega \tag{6.15.a}$$

where $P = F_N / \pi R_S^2$.

The average welding power input ($Q_{Welding}$), based on the total torque is given by:

$$Q_{Welding} = T\omega \tag{6.16}$$

By relating equations (6.15) and (6.16), it becomes predictable that there is a proportional relation between the torque and flow stress, and the torque and μP (or F_N provided that μ remains constant). These relations will be used to rationalise the contact condition (slip or stick) in W1.

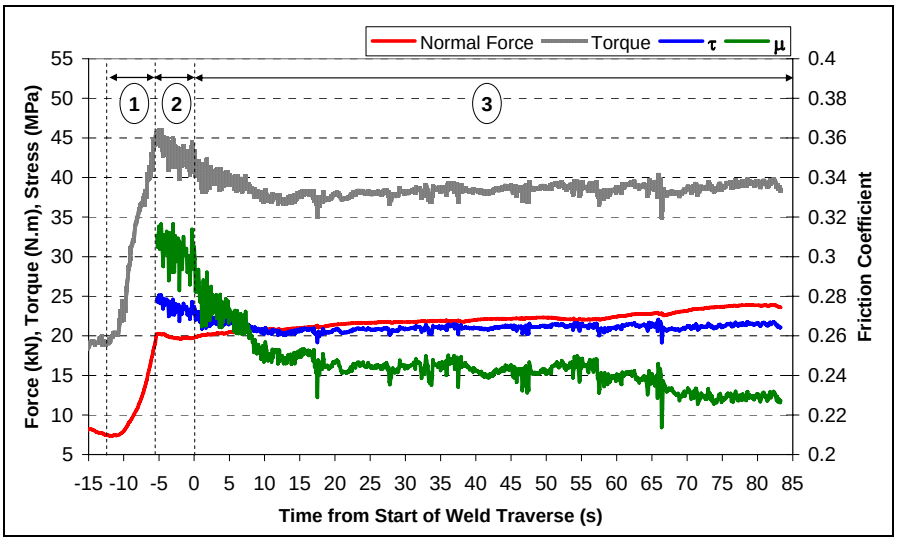

Fig. 6.5. Torque and normal force measurements for the 2024-T3 weld (W1), and the calculated shear stress (τ) and friction coefficient (μ) based on [9, 14]. The numbers 1, 2, and 3 refer to the process stages; plunging, dwell, and welding.

As shown in Fig. 6.5, the process is divided into three stages; (1) plunging from -12.3 to – 5.3 s, (2) dwell from -5.3 to 0, and (3) welding. Within the plunging stage, both the normal force and torque increased with the increase in the plunging depth to maximum values of 19.9 kN and 45.6 N.m respectively. As the tool is not entirely plunged, this period cannot be used to estimate the shear stress or friction coefficient. Within the dwell stage, as the tool was fully plunged, the torque slightly decreased to an average of 43.2 ± 1.4 N.m. However, the normal force remained roughly constant, with an average of 19.9 ± 0.2 kN. Since the force/torque proportionality should hold in a fully-sliding condition, it is thus possible to assume a sliding condition in the dwell stage, with an average friction coefficient of 0.3 ± 0.008.

Following the dwell stage, the torque further decreased until it stabilised at a roughly constant level at 38.5 ± 0.8 N.m after 10 s from the weld start, while the normal force increased reaching 23.6 kN at the end of the welding cycle, with an average of 22 ± 1 kN. The average heat input in this stage was 2418 ± 52 W. The stabilisation of the torque (and heat input) in the welding stage can be considered as an indication of a sticking condition, since it remained roughly constant regardless of the increase in the normal force observed throughout this period. If the contact condition had been of sliding type, then the friction coefficient should have varied from 0.3 to 0.23 as shown in Fig. 6.5, which is unlikely to be called a steady state. Using the analytical equations, the average shear stress can thus be estimated at 21.1 ± 0.5 MPa. This value is similar to other estimates in the literature (20.8 MPa in 2024-T3 weld [9], 14 MPa in 6061-T6 weld [14], and in a range between 15 to 38.5 MPa in dissimilar 5083-6082 welds [28]). Thus, it can be suggested that the contact condition starts as sliding and eventually becomes sticking, which also follows the concept of Coulomb friction law. In the model, a friction coefficient of 0.3 will be used to represent the slipping heat input, with the change from slip to stick occurring according to the approach described in section 6.1.3.a.

6.2.1.b. Fitting of the Thermal Measurements

The experimental details for the thermocouple measurements for this weld are obtained from the weld-Benchmarks website [25]. The weld (W1) was performed on a weld-adapted milling machine, with the sheets mechanically clamped to the anvil using 2 steel bars, bolted by three 8 mm diameter bolts. K-type thermocouples (wire Ø 0.25 mm) were inserted in to Ø 0.8 mm × 0.6 mm deep holes drilled at the top and bottom surfaces of the sheet, at 4 mm and 15 mm from the butting faces of the sheets, at different positions along the travel direction, Fig. 6.6-a.

The thermophysical data used in the model are given in Table 6.2, based on the data from Touloukian [22]. Due to the significant variation in k with temperature (Fig. 6.4-b), a value of k = 190 W/m.˚C was selected which is an average value within the range of temperatures experienced.

Table 6.2. Thermophysical properties and equation (6.14) constants for 2024-T351 [16, 22]

k (W/m.˚C)	C_P (J/kg.˚C)	ρ (kg/m^3)	Solidus temperature (˚C)	A (MPa)	B (˚C^{-1})
190	875	2770	502	598	0.0078

The simulated thermal cycles for both contact conditions were compared against the thermocouple data at 4 mm (below the tool shoulder at the weld root face, labelled TC7), and at 15 mm on the sheet surface (outside the shoulder periphery, 6 mm from the shoulder periphery, labelled TC3) from the weld centreline, Fig. 6.6-a. As the model was only limited to the sheet itself, it was not possible to use the anvil thermocouple (TC2) for validation.

Fitting was performed to determine the contact conductance (h_C) between the sheet lower surface and anvil. The thermal cycle was simulated using two simple scenarios:

1. Perfect contact: with h_C = 1000 W/m^2.˚C the whole time during the welding process.
2. Imperfect contact: partial loss of contact takes place, changing h_C from 1000 W/m^2.˚C in front of the tool to 500 W/m^2.˚C behind the tool due to the distortion occurring during tool motion.

The quality of the fit for both contact scenarios was analysed with respect to the influence on the peak temperature and the cooling section of the thermal cycle, Fig. 6.6. For the peak temperature, the contact condition did not have a significant influence in either thermocouple positions, although the small overshoot (8-14 ˚C) observed at 4 mm (Fig. 6.6-b) for both contact scenarios changed to undershoot of -12 ˚C for the perfect contact condition at 15 mm (Fig. 6.6-c). Considering the possible experimental error range in thermocouple experiments (~±10-20 ˚C) due to the thermocouple accuracy or positioning errors, it can be argued that the contact condition did not significantly influence the peak temperature.

On the other hand, the influence of the contact condition was more significant for the cooling section of the thermal cycle, with the perfect contact scenario causing a more rapid cooling compared to the imperfect contact. A deviation of -70 ˚C was observed at 4 mm by the end of the thermal cycle, compared to -25 ˚C for the imperfect contact. At the 15 mm thermocouple position, the deviation was -60 ˚C by the end of the cycle for the perfect contact condition (compared to -20 ˚C in case 2), combined with slower heating (starting from ~35 s), and slightly lower peak temperature (by 12 ˚C).

(a)

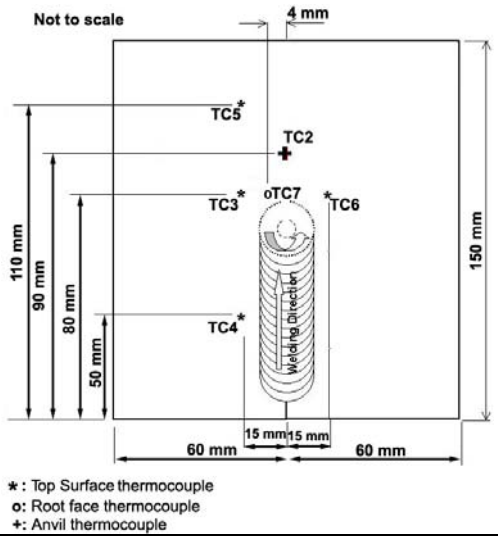

(b)

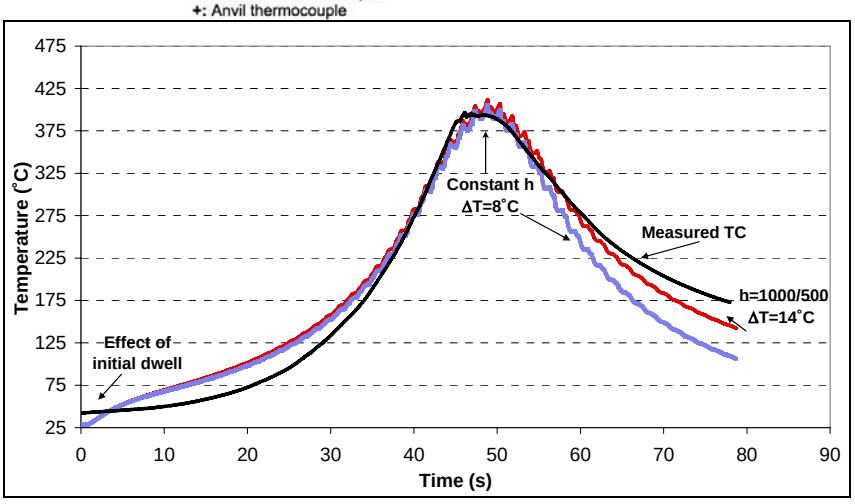

I

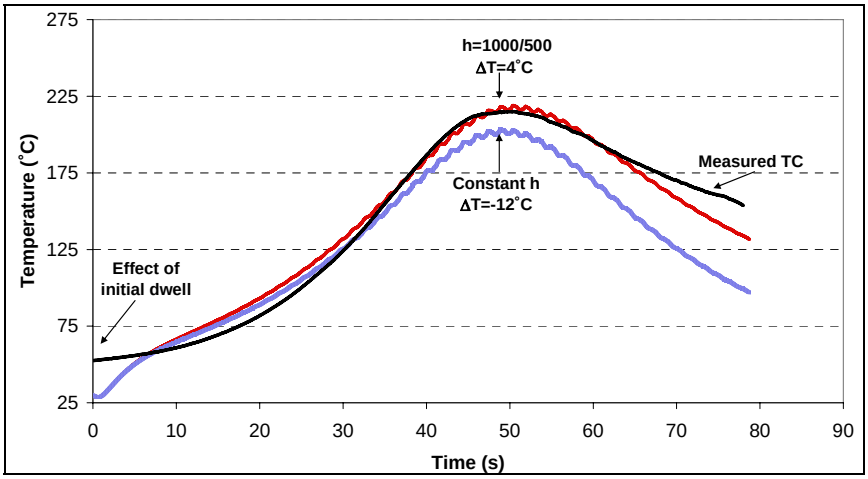

Fig. 6.6. (a) The thermocouple positions in the weld benchmark experiments [25], and the W1 simulated thermal cycles for both contact conditions and the thermocouple measurements (b) TC7: 4 mm from the weld centreline at the root face, and (b) TC3: 15 mm from the weld centreline on the sheet surface (ΔT: peak temperature over/undershoot). The initial undershoot in the simulated cycle results from the initial heating dwell in the measured cycle.

It is clear that the imperfect contact scenario was thus capable of providing a more accurate fit for the thermal cycle, notably the cooling section. Nonetheless, the simulated thermal cycles using this scenario still deviated from the actual cycle by -20 ˚C by the end of the thermal cycle. This deviation was observed to start from ~275 ˚C (Fig. 6.6-b) and ~180 ˚C (Fig. 6.6-c). This deviation could be attributed to either precipitate development (GP-zones or θ''), which decreases the thermal conductivity compared to the average value used, or due to extra heat being lost from the system through contact (i.e. the assumed contact conductance is slightly higher than the actual). It is expected that the heat input would initially dissolve the GP-zones in the T351 condition (increasing the thermal conductivity). Then, depending on the maximum temperatures experienced, re-precipitation may occur during cooling, which could decrease the thermal conductivity.

The results suggest that the contact condition behind the tool has an influence on the quality of fit of the thermal cycle. During welding, the sharp thermal gradients caused by the moving heat source (i.e. the tool) lead to rapid expansion and contraction in the clamped sheet. As a result, distortion takes place, slightly lifting the sheet, which accordingly decreases the contact conductance. As shown in the simulation, such an influence is clearly visible in the cooling section of the thermal cycle, which actually represents the measurements behind the tool. This explains why the contact conductance does not notably influence the peak temperature. It is expected that the imperfect contact condition is the dominant case in mechanically-clamped welds. However, the contact conductance might change in presence of special cooling/clamping effects, or for relatively different thicknesses or alloys.

6.2.2. Validation: W2:2024-T351

Validation was performed by predicting the thermal cycle and temperature profile in another thermocoupled weld (W2). The sheets were slightly thicker (6.35 mm for W2 compared to 5.85 in W1), and welding was performed on a different machine, yet mechanically-clamped as well. Thermocouples were embedded at 6, 8, 10, 16, 20 mm from the weld centreline at the plate mid-thickness. Although the torque and force versus time data for this weld were not provided, the heat input (eq. 6.15) due to pure sliding (μ = 0.3) can be estimated at ~4615 W, and ~3500 W for pure sticking (τ = 21 MPa). These values are quite higher than the typical FSW heat input [29], which could be due to lower τ, suggesting a sticking condition.

Using the same imperfect contact model for W1, reasonable predictions were obtained for the thermal cycle (Fig. 6.7-a) and the peak temperatures (Fig. 6.7-b), at different distances from the weld centreline. The predicted maximum temperatures were slightly lower than the measured temperature (between 0.5 to 30 ˚C), which is reasonable considering the measurement errors. The simulated thermal cycle at 6 mm cooled faster than the measured cycle below 275 ˚C (similar to W1), deviating by ~25 ˚C undershoot at the end of the thermal cycle. For the thermal cycle at 16 mm, the undershoot was ~10 ˚C at the end of the thermal cycle.

(a)

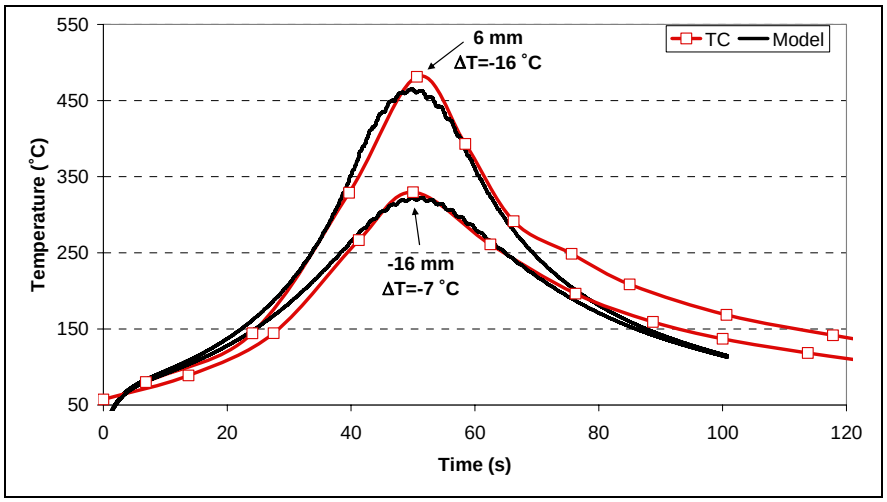

(b)

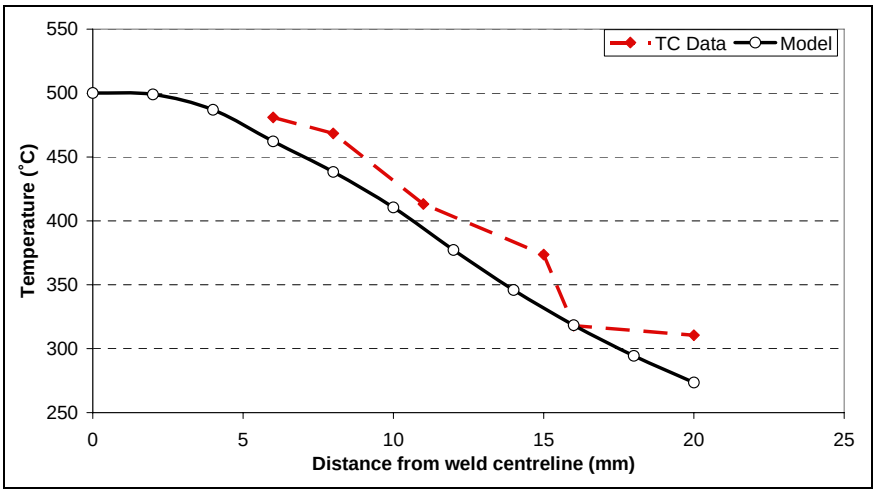

Fig. 6.7. Comparison between the simulated and measured temperature data (a) the thermal cycles in the 2024-T351 W2 at 6 mm from weld centreline at mid-thickness, (b) the maximum temperature as a function of the distance from the weld centreline (TC data obtained from [26])

6.2.3. 5754-O weld: SPECIAL COOLING OF THIN PLATES

Further validation for the model was performed using thermocoupled 5754-O welds, which were welded on the TWI's ESAB machine, Cambridge. The sheets were thinner (2.3 mm), and vacuum clamping was used to grip the sheets to the machine anvil, which is expected to alter the contact condition. In general, the contact conductance below the sheet can be either enhanced by special cooling/clamping effects (e.g. vacuum clamping, water or liquid N_2 cooled anvils), or reduced by the distortion during welding, notably in the case of thin sheets which experience more distortion [30]. This validation stage was thus essential to provide information on the model's sensitivity to variations in the contact condition. The thermophysical and mechanical properties for 5754 were obtained from the literature [24].

6.2.3.a. Analysis of Experimental Data

Similar to W1, the welding cycle for the 5754-O weld was divided into plunging, dwell, and welding stages, Fig. 6.8. In the forging stage (-9 to -4.5 s), both the force and torque steadily increased to 10.4 kN and 28.5 N.m respectively. During the short dwell (-4.5 to 0 s), the torque increased and subsequently stabilised at ~32 N.m until 5 s of the welding stage, where it increased again to finally stabilise at 8 s until the end of the weld at 38.6 ± 0.7 N.m. On the other hand, the force remained constant for 2 s during the dwell, and then shortly decreased prior to the welding stage to increase again steadily until the end of the welding cycle.

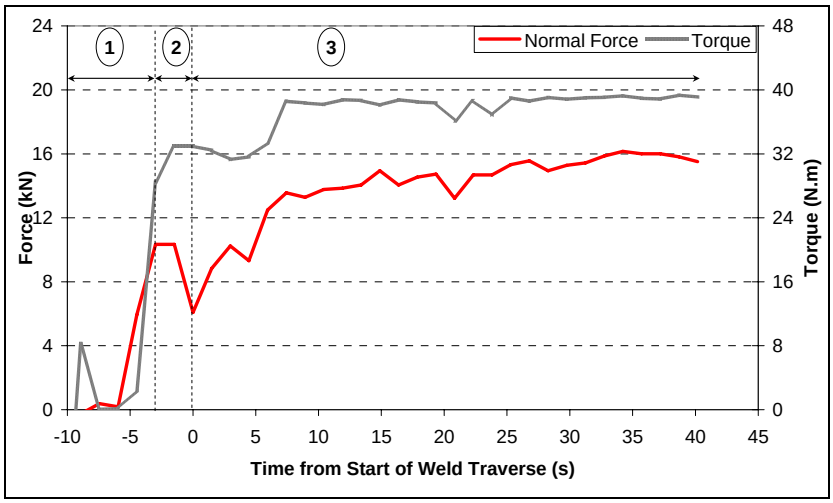

Fig. 6.8. Torque and normal force measurements for the 5754-O weld. The numbers 1, 2, and 3 refer to the process stages; plunging, dwell, and welding.

The torque measurements indicated that the average power input was ~2020 ± 45 W. Quantitative estimates for the welding condition reveal that, for a purely sliding contact, an average μ of 0.46 ± 0.03 is required to deliver this heat input, or τ of 38.7 ± 0.7 MPa for a sticking condition. These values are relatively larger than the estimate obtained for 2024-T3, although they are within the limits found in the literature [28], and consistent with the range of flow stress for this material within the welding temperature range (400-500 ˚C). It can be argued that the higher shear stress results from the higher Mg-content in 5754, which is expected to result in higher shear stresses during deformation as discussed in section 2.5.4. It can be argued that, noting the relative stability in welding torque between 8 to 40 s, that sticking was the dominant condition. For this purpose, the friction coefficient used in the model will be kept at 0.3.

6.2.3.b. Fitting the Thermocouple Measurements

The thermocouples were fixed, on the sheet surface, at 10, 15 and 20 mm from the weld centreline (process parameters are present in Table 6.1). Using the same values for h_C of the imperfect contact condition in 2024-welds, the model was initially used to predict the thermal cycle at the thermocouple positions. Although the peak temperature showed 22 ˚C overshoot, rapid cooling was observed later in the cooling section of the thermal cycle, starting after the peak temperature, and reaching 140 ˚C undershoot by the end of the thermal cycle, Fig. 6.9. Despite the vacuum clamping, significant distortion apparently took place, further decreasing h_C. Nonetheless, when the contact conductance behind the tool was lowered to 10 W/m^2.˚C and 0 W/m^2.˚C (perfect insulation), the perfect insulation scenario showed a good fit, except for a 40 ˚C overshoot at the peak temperature, higher than the other contact conditions.

Figure 6.9 shows that obtaining a good fit for the cooling section of the thermal cycle, by decreasing h_C behind the tool, led to peak temperature overshoot. Decreasing the contact conductance means that less heat will be transferred through the sheet/anvil interface, until the extreme case of perfect insulation where the only outlet for the heat transfer becomes through the exposed surfaces. The only way to correct this overshoot is through increasing the contact conductance at the sheet/sheet interface below the tool shoulder.

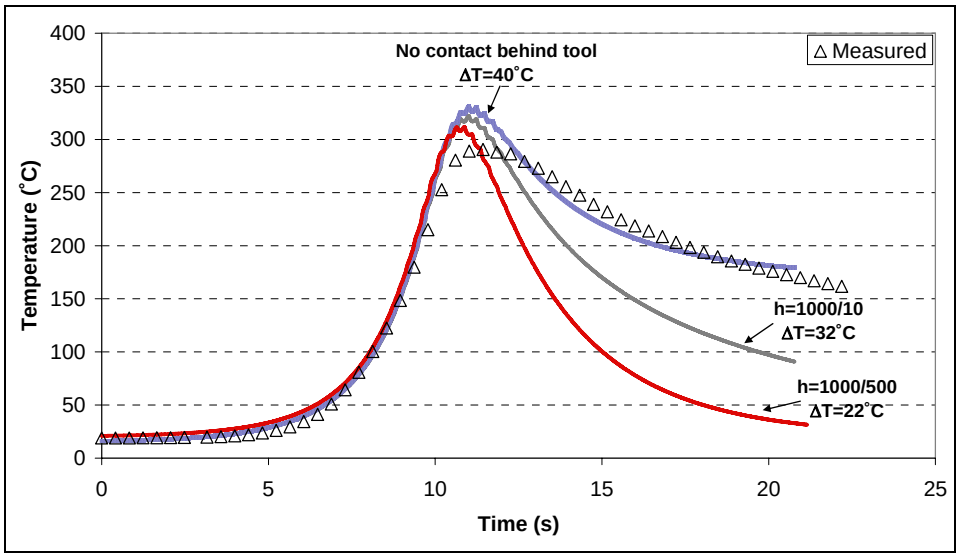

Fig. 6.9. The influence of the contact condition on the simulated thermal cycle compared to the thermocouple measurements for 5754-O weld at 10 mm position (ΔT: peak temperature over/undershoot).

Further fitting of the thermal cycle resulted in a contact condition dividing the sheet/anvil interface into three zones below, behind and in front of the tool, with h_C = 4000, 1000 and 50 W/m^2.˚C respectively. Using this condition, the simulated thermal cycles showed closer fits of the peak temperature and cooling section, despite deviating higher than the peak temperatures by ~ 10, 23, 29 ˚C at 10, 15 and 20 mm from the weld centreline respectively, Fig. 6.10.

It can be observed that the deviation in the cooling section changes from undershoot at 10 mm and 15 mm to overshoot at 20 mm, which indicates that the contact conductance is possibly non-uniform at the sheet/anvil interface. The undershoot at 10 and 15 mm implies that the actual conductance is lower than the assumed value, and vice versa for the overshoot at 20 mm. This means that the actual contact conduction increases with the distance from the weld centreline, while the distortion decreases. Although the model can allow for local variations in the contact conductance, such a modification would contradict the attempted simplicity of the model. The peak temperature data retrieved from four identical 5754-O welds (Fig. 6.10-b) show that the model can provide reliable predictions with the simple contact condition used, considering the uncertainty in thermocouple measurements.

(a)

(b)

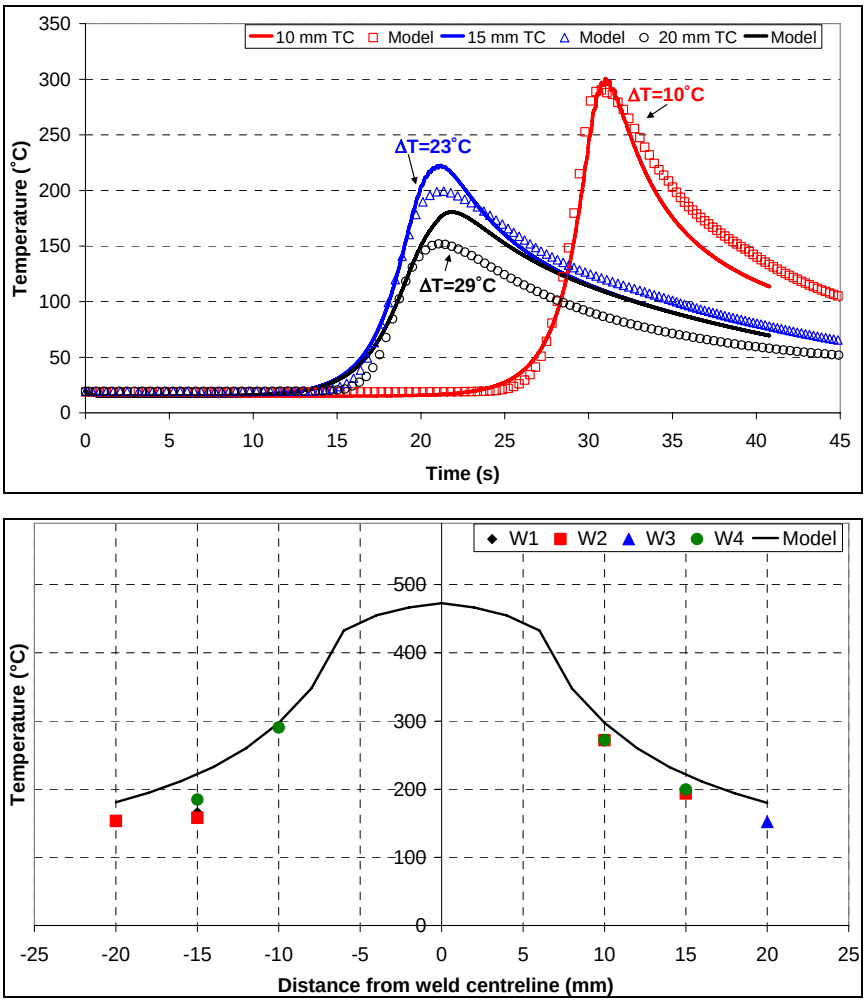

Fig. 6.10. Correlation between the model and (a) measured thermal cycles and (b) the maximum surface temperatures measured by the thermocouples in four identical weld runs (h_C values of 4000, 1000 and 50 W/m^2.˚C were used for conductance below, behind and in front of the moving tool respectively)

6.2.3. Model Assessment

6.2.3.a. Numerical FD Models

To assess the proposed model, compared to the existing FD thermal models of FSW, the assessment will focus on the fitting parameters, quality of prediction, and the numerical scheme adopted. It is not possible to consider the computation speed due to the differences in the computational power of the computers used by the various models, as well as the model-specific values (e.g. time and spatial steps). However, identifying the type of the numerical scheme (i.e. explicit or implicit) could give an indication of the computational speed.

Currently, there are two FD models for FSW available in the literature; the model by Frigaard *et al.* [6], and the model by Song and Kovacevic [31, 32].

The Frigaard *et al.* model used a friction-induced heat generation scheme, assuming a constant friction coefficient of 0.4. Heat generation was provided through the friction of the rotating circular shoulder, and distributed across the thickness in square sources of uniform heat flux. Thus, the heat input contribution due to the pin was not analytically considered, although it was accounted for through the distribution of the heat sources. On reaching a specific temperature, heat generation was fixed at zero. However, the choice of this temperature was not alloy-specific, with a temperature of 555 ºC chosen for both 6xxx and 7xxx series alloys. The model used an explicit numerical scheme (i.e. each node was calculated separately), which implies a long processing time. The contact conductance condition was not provided, and constant room temperature thermophysical properties were used. In terms of the quality of its predictions, the thermal cycle was found to show an overshoot of 20-50 ºC in the peak temperature compared to the actual measurements, with the cooling section showing a deviation of ± 20 ºC in the HAZ, and increasing to up to 70º C in the measurements performed close to the TMAZ.

The other model by Song and Kovacevic also used a friction-induced heat generation approach, with a fixed friction coefficient and an explicit numerical scheme. Heat generation was provided through the rotating tool shoulder, as well as due to the friction of a cylindrical pin (no plastic deformation). However, the shoulder heat generation was a function of the radius, similar to the one adopted in the proposed model. The quality of predictions was relatively better than the predictions Frigaard *et al.*, with both the measured and simulated thermal cycles having the same shape and temperatures predicted. However, the simulated thermal cycle was ~10 s out of phase with the measured one. The contact conductance was assumed constant across the plate/anvil interface.

In the proposed model, a mixed deformation-friction heat generation scheme was introduced, which simulates the best available description of heat generation during FSW, and considers the pin heat generation. The use of the implicit numerical approach boosted the computation speed, although the speed can be further improved by using an adaptive (non-uniform) grid. The use of arbitrary model variables (e.g. the friction coefficient, incipient melting

temperature, or the contact conductance) was avoided by using actual material data, which can accordingly minimise the fitting effort.

6.2.3.b. FE and CFD Models

Compared to FE and CFD models, the proposed model provides thermal predictions of a quality similar to that obtained by FE thermal models [15, 20, 31, 33, 34]. However, FE and CFD models represent the additional advantage of predicting other process parameters. Even in early uncoupled FE thermal models (e.g. the model by Shi *et al.* [20] for the FSW benchmark weld), accurate predictions for the thermal cycle could be obtained, except for a small shift in time for the peak temperature, and undershoot in the final temperature (which was also experienced in the present model as explained earlier). The same concerns with the contact conductance were also earlier addressed in FE uncoupled modelling by Khandkar *et al.* [14] and Simar *et al.*[34], resulting in fitting parameters similar to those obtained by the present model, and better modelling of the thermal cycle. Moreover, thermomechanical FE and CFD models are capable of predicting additional process variables (e.g. residual stresses and tool forces, plastic strains, strain rates), which is not possible in the proposed model. Such an advantage in thermomechanical models enables the prediction and the application of a more complex distribution of the contact conductance, which can be seen in the work of Kovacevic *et al.* [33], as previously discussed in section 3.3.2. Recent CFD models by Colegrove and co-workers [17, 35] probably represent the state of the art in thermal modelling, as well as material flow and deformation, because of the multitude of process parameters that can be predicted with a high level of accuracy. Still, one shortcoming for the FE and CFD model is the computational burden they require, and sometimes the processing time when re-meshing is applied. This is the strength of the present model, where reasonable predictions can be obtained with less computational burden. A short comparison between the proposed model and the other models in the literature is available in Table 6.3.

Table. 6.3. Comparing the various models with the proposed model

Model	Type	Heat Generation	Contact conductance	Prediction Quality
Frigaard *et al.* [6]	FD	Friction	Not provided	±20-70 ˚C
Song *et al.* [31, 32]	FD	Friction	Convection boundary	Cycles out of phase
Kovacevic *et al.* [33]	FE	Friction	Variable, stress dependent	Almost match
Shi *et al.* [20]	FE	Power Input	Variable, temperature dependent	Cycles out of phase
Simar *et al.* [34]	FE	Deformation	Decreasing beyond the tool	±20 ˚C
Colegrove *et al.* [17, 35]	CFD	Deformation	Constant	Almost match
Schmidt & Hattel [11]	FE	Mixed	Constant (h=1000 W/m^2.˚C)	No thermal cycle
Khandkar *et al.*[14]	FE	Power Input	Constant, fitted	±20 ˚C
Colegrove *et al.* [7]	FE	Friction	Constant (h=1000 W/m^2.˚C)	±10-40 ˚C
Russell and Shercliff [21]	Analytical	Deformation	Not provided	±10 ˚C (HAZ only)
The Proposed Model	FD	Mixed	Variable, 3 regions	±20-30 ˚C

6.2.3.c. Contact Condition

In principle, the thermal conductance between two materials in contact is a function of the temperature and hardness of the materials, the size of the gap between the interfaces, which is related to the surface roughness and flatness/curvature of the surfaces in contact, the average interface temperature, and the pressure applied [11, 33, 36]. However, the sharp thermal gradients that occur during welding and the associated thermal expansion and contraction, as well as the forces due to the moving tool, create residual stresses and distortion in the weld, which results in considerable fluctuations in the contact conductance across the weld. As a result, the contact conductance becomes more dependent on additional material-related parameters (e.g. elastic modulus and thermal expansion coefficient) as well as the sheet thickness.

The results of this study highlight the difficulty in fitting the contact conductance using thermal modelling due to the variable nature of the contact condition. However, the proposed approach in modelling the contact conductance represents a simplified approach for simulating the actual contact conductance, based on the findings of other models that attempted to estimate the variation in contact conductance across the weld. It is possible to consider in the model a more complex distribution of the contact conductance across the weld, by defining the contact conductance as a weighted function of the distance from the weld centreline. However, such modifications in the algorithm would contradict the attempted simplicity in the model, and would increase the fitting parameters for the model.

6.3. Thermal Fields and HAZ Development

Using the thermal model, the thermal fields for the 5251-H34, 5083-H116 and 2024-T351 welds were generated and compared to the HAZ microstructure and hardness. These welds were chosen because they are work-hardened or aged. Accordingly, the correlation of the thermal fields to hardness/microstructure can be easily determined.

6.3.1. 5251-H34-weld

6.3.1.a. Analysis of Experimental Results

Figure 6.11 shows the normal and torque measurements for the 5251-H34 and O welds. An interesting aspect of the measured data is that both welds had almost identical torque and force data with average values of 97.0 ± 3.4 N.m and 14.2 ± 1.2 kN in the H34-condition, and 99.7 N.m ± 2.9 and 14.4 ± 1.3 kN in the O-condition respectively. This result indicates that the thermomechanical deformation during FSW treats both conditions similarly, which suggests that the material ahead of the moving tool in the H34 weld experiences some extent of recrystallisation, resulting in a similar power input of ~ 5200 W for both welds. The stability in the welding torque also suggests that sticking was the dominant condition, with an average τ of ~20 MPa. The τ estimate is lower than that for 5754, although both welds were welded using the same parameters, probably due to the lower Mg-content in 5251.

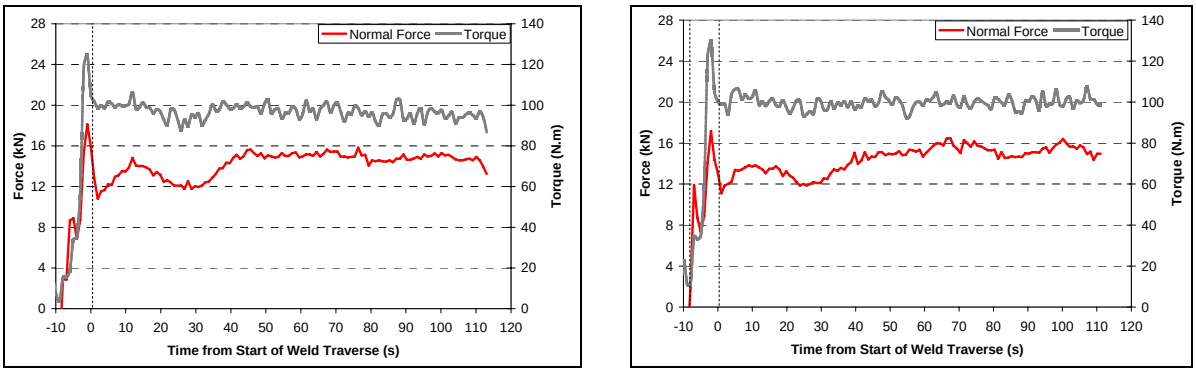

(a) 5251-H34 (b) 5251-O

Fig. 6.11. Torque and normal force measurements for (a) 5251-H34 weld, and (b) 5251-O.

6.3.1.b. Predicted Thermal Fields

To predict the thermal fields experienced in the 5251-H34 weld, the thermal model was used assuming the imperfect contact scenario used for the 2024-T3 welds. As the thermomechanical and thermophysical properties for 5251 are unavailable in the literature, the properties were estimated from alloys of similar compositions, Fig. 6.12. The temperature-dependent mechanical properties were interpolated from the properties of 5050 (AlMg1.4) and 5052 (AlMg2.5), assuming a linear proportionality of the strength with the Mg-content [16]. For the thermophysical properties, the properties for 5052 (AlMg2.5) were used [23].

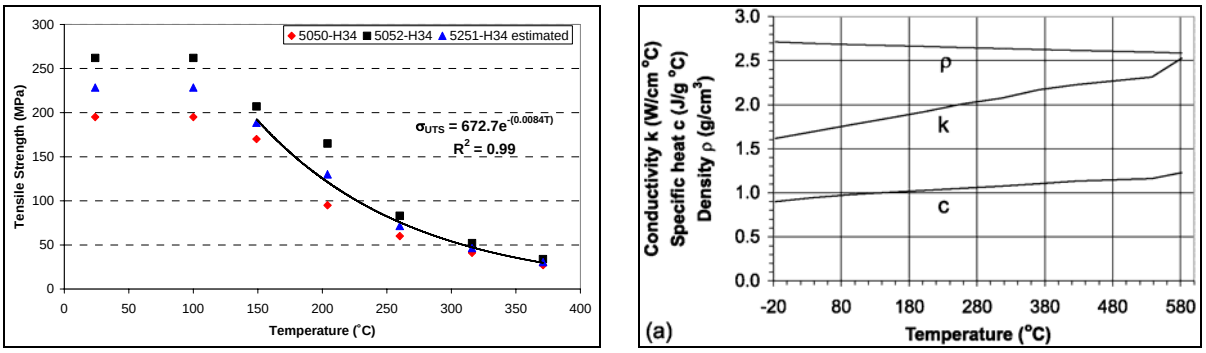

(a) (b)

Fig. 6.12. (a) The thermomechanical and (b) thermophysical properties used in the model [23]

The model predicted a maximum temperature of ~500 ˚C, which occurred at the surface of the weld, and decreasing towards the weld base, Fig. 6.13. The temperature was uniform within the TMAZ (roughly between 450 and 500 ˚C). Beyond the TMAZ, sharp thermal gradients existed, with the temperature decreasing within the HAZ from 450 ˚C to ~300 ˚C at ~ ±15 mm from the weld centreline.

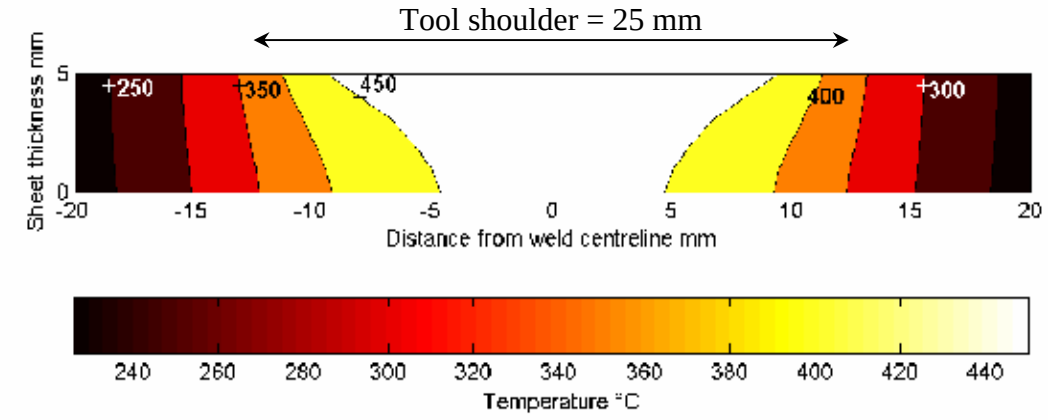

Fig. 6.13. Temperature distribution in the 5251-H34 weld

6.3.1.b. HAZ Microstructure and Microhardness

To obtain a more quantitative representation for the influence of the thermal fields on the microstructure, microstructural investigations and microhardness measurements were performed to determine the HAZ width, and compare it with the results of the thermal model. The HAZ in the 5251-H34 weld appeared as a narrow band, which is inclined through thickness (Fig. 6.14), along the direction of the heat flow from the sheet surface (exposed to free convection) to the base of the sheet (in contact with the anvil) as visualised in the temperature distribution contour (Fig. 6.13).

Based on the weld microstructure and the microhardness distribution, the HAZ can be classified into two regions: the statically recrystallised (SRX) zone (~3-5 mm thick inclined band beyond the TMAZ), where the thermal exposure led to the initiation of recrystallisation. Recrystallisation can be observed microscopically at different fraction recrystallised depending on the proximity to the TMAZ (e.g. fully recrystallised structure only adjacent to the TMAZ, Fig. 6.14-a, and partially recrystallised structure, Fig. 6.14-b). Within the SRX zone, the recrystallised grain size was found to vary between 26 and 39 μm (compared to 29.8 μm in the O-BM), depending on the proximity of the location to the TMAZ. Beyond the SRX zone, a recovered (REC) zone existed within a 2-7 mm wide region, Fig. 6.14-c, where thermal effects were insufficient to initiate recrystallisation.

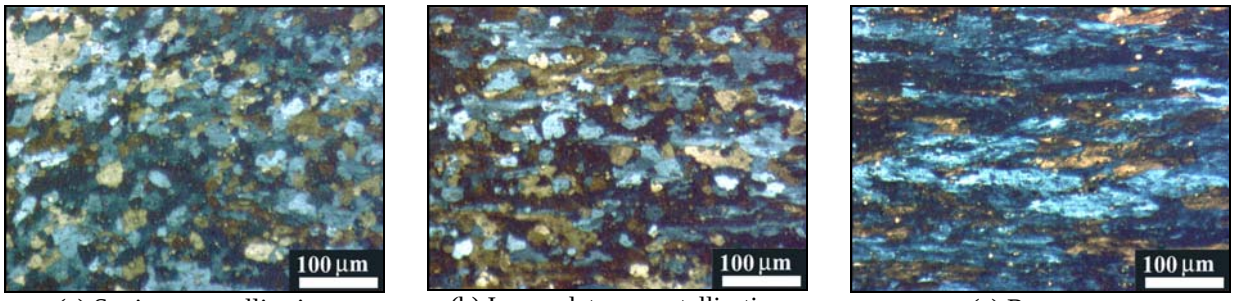

(a) Static recrystallisation (b) Incomplete recrystallisation (c) Recovery

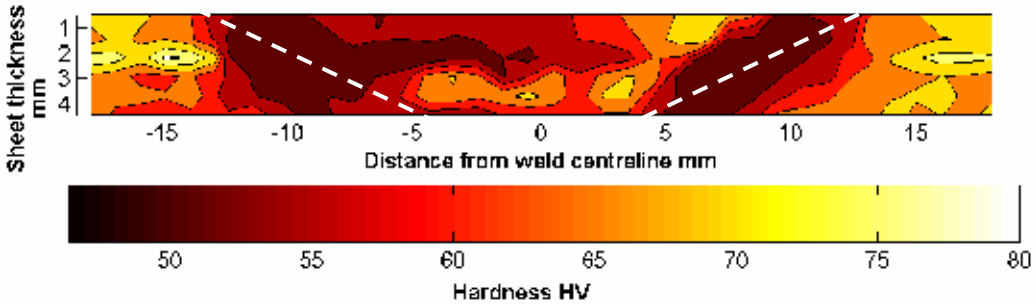

(d) Microhardness profile (the dashed lines show the width of the TMAZ)

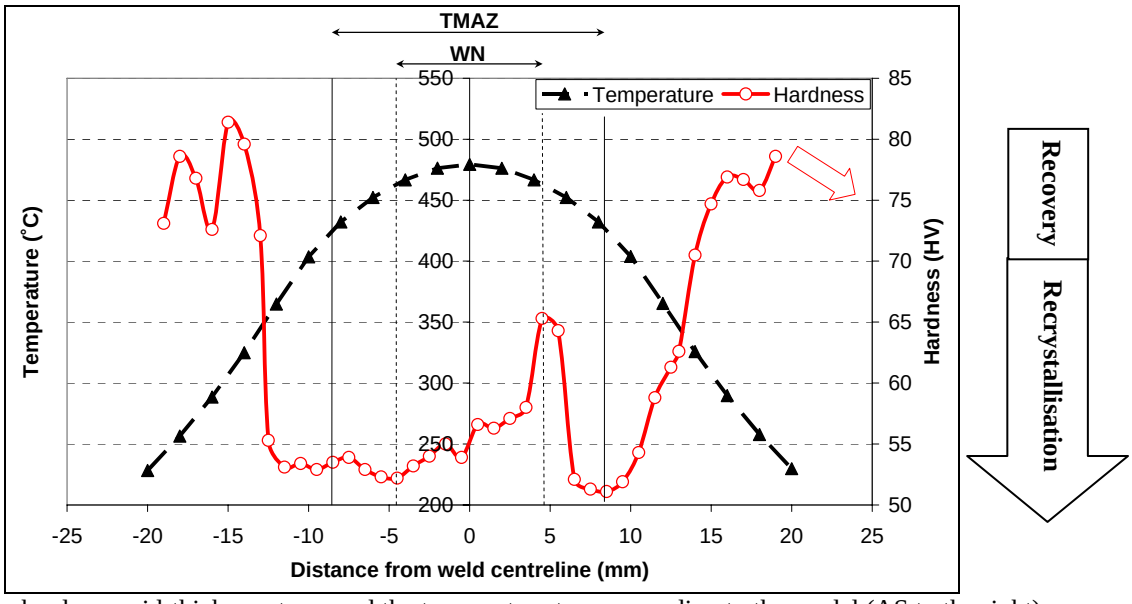

(e) microhardness mid-thickness trace and the temperature trace according to the model (AS to the right)

Fig. 6.14. The 5251-H34 weld HAZ microstructure and microhardness distribution

Due to recrystallisation, the hardness in the SRX dropped to a range between 65 H_V (partially recrystallised) and 51-54 H_V (fully-recrystallised). Within the REC zone, the hardness was found to be in a range between 70 to 75 H_V, before reaching to the basemetal hardness (~78 H_V). Based on the temperature predictions of the model, the HAZ-SRX zone experienced temperatures between 350 and 425 ˚C, which led to a drop in hardness to <70-72 H_V (which is the recovery completion hardness), Fig. 6.14-e. Compared to the recrystallisation temperature range obtained using the DSC and the Gleeble thermal simulations (325 to 375 ˚C), the recrystallisation start temperature in the weld is slightly higher. It is important to highlight the transient nature of the thermal exposure, compared to the longer exposure in the DSC or Gleeble experiments. Rapid heating rates, as during welding, are known to influence recovery and recrystallisation kinetics, as clearly reported in the literature [37-41].

6.3.1.c. Simulating the HAZ Microstructural Development using Gleeble TMS

Within the HAZ, thermal cycling of the material leads to different annealing microstructures depending on the maximum temperature experienced and cooling rate. Using the thermal model for the 5251-weld, the heating rate in the weld was predicted to fluctuate between 30 to 150 ˚C/s. It has been reported [37-39] that heating rate fluctuation could have an impact on the temperature at which recovery or recrystallisation initiates, as well as the extent of grain growth. Accordingly, the Gleeble TMS was used to understand the HAZ microstructural development, by performing thermal simulations within the range of heating rates and temperatures experienced within the HAZ.

It was found that the heating rate had a major influence on the recrystallisation start temperature (T_{Start}). By heating the H34-basemetal specimens to 400 ˚C, where recrystallisation is known to occur during static annealing for 1 hr, two ranges of heating rates resulted in different recrystallisation regimes.

1. Regime (A): At low-to-moderate heating rates (15-25 ˚C/s), only recovery occurred, Fig. 6.15-a. As this was a dynamic heating process, time was insufficient for complete recrystallisation to occur. However, it was sufficient for recovery processes to occur, resulting in a re-ordered lower energy dislocation structure, thus reducing the driving force for recrystallisation.
2. Regime (B): Above a critical heating rate (~>30 ˚C/s), recrystallisation occurred, Fig. 6.15-b. The rapid heating reduces the time available to release a portion of the stored

energy during recovery. Accordingly, all the stored energy present in the basemetal acts as the driving force for recrystallisation, consuming the deformed substructure from the pre-existing nuclei, and thus decreasing T_{Start}, Fig. 6.15-c.

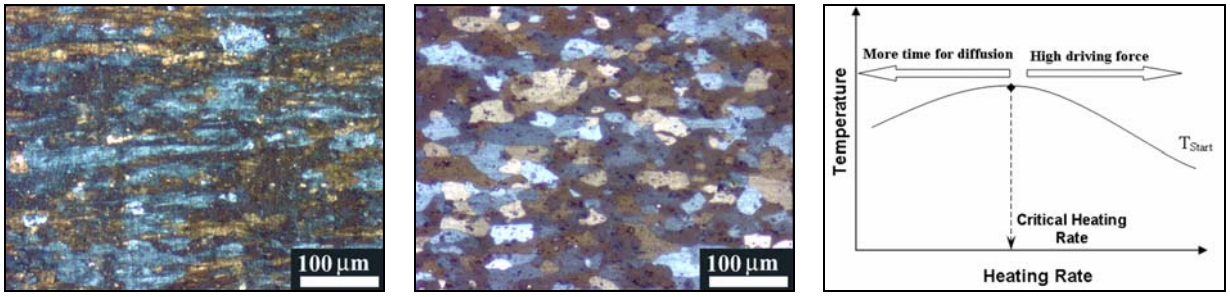

(a) Rate=15 ˚C/s, T_C = 397˚C (b) Rate=50 ˚C/s, T_C = 405 ˚C (c)

Fig. 6.15. (a,b) The influence of the heating rate on recovery/recrystallisation due to Gleeble simulation (T_C: thermocouple temperature), (c) schematic for the heating rate model

This microstructural development is certainly associated with hardness development. It was found that, for a peak temperature of 400 ˚C (±5 ˚C), it is possible to thermally cycle the material, while only losing a minor portion of the basemetal hardness (due to recovery), Fig. 6.16. However, on increasing the peak temperature (e.g. to 475 ˚C), the influence of the heating rate becomes insignificant in controlling the hardness development as the material will undergo full recrystallisation regardless of the heating rate. It is important to indicate that the heating rates and the temperatures at which recrystallisation initiates are expected to also depend on the extent of pre-existing deformation, and the intermetallic particle distribution (i.e. nucleating sites for PSN).

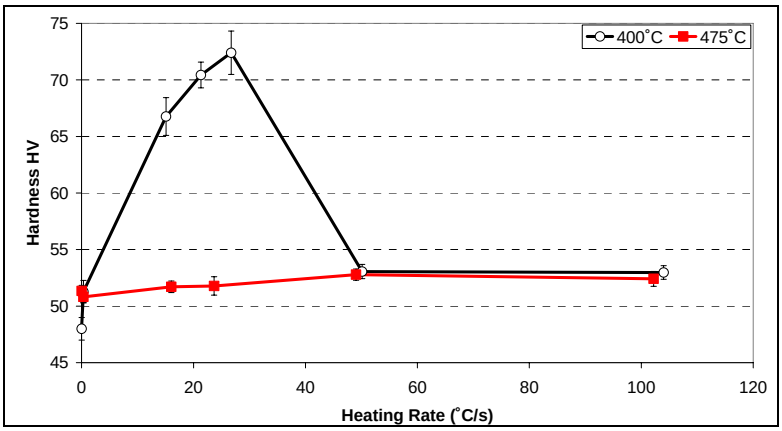

Fig. 6.16. The influence of the heating rates during Gleeble simulations on the hardness at different peak temperatures

The Gleeble TMS was used to simulate the thermal cycle within the HAZ of the 5251-H34 weld to peak temperatures of 350 ˚C and 385 ˚C, based on a HAZ thermal cycle predicted by the model to provide an additional microstructural verification for the model. As shown in Fig. 6.17, heating took place on both ranges of heating rates, with regime (A) rates occurring within the recovery range (~150-200 ˚C), followed by increasing to regime (B) rates within the recrystallisation range (~>300 ˚C), reaching a maximum of 135 ˚C close to the peak temperature. Based on the suggested hypothesis, it is expected that recovery will be induced during the low-rate section of the thermal cycle. The release of an amount of the deformation stored energy will accordingly reduce the available driving force for recrystallisation, which will cause recrystallisation to initiate at temperatures higher than those required for static recrystallisation to occur. This can be visualised in a specimen thermally cycled using a HAZ cycle to 350 ˚C, resulting in a recovery only (Fig. 6.17-b). However, on heating to 385 ˚C, recrystallisation initiated, resulting in a partially recrystallised microstructure, Fig. 6.17-d.

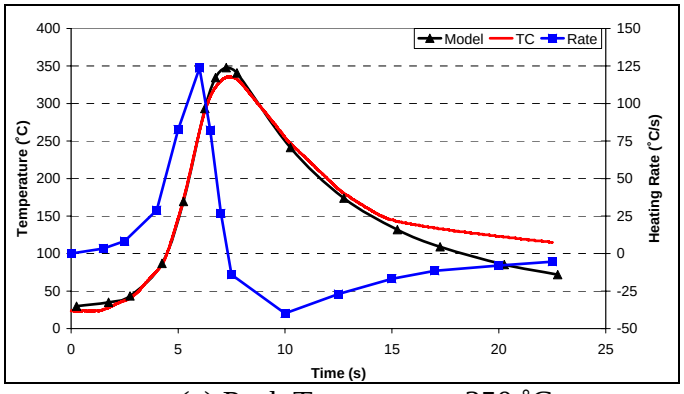

(a) Peak Temperature 350 ˚C

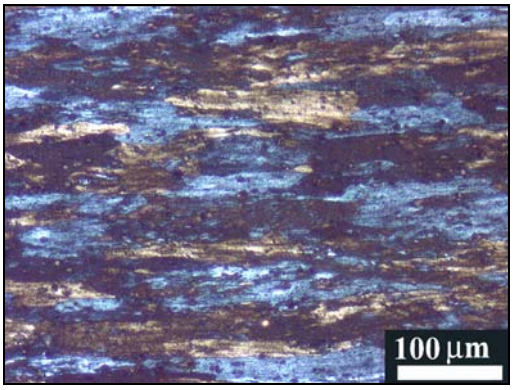

(b) Recovered microstructure

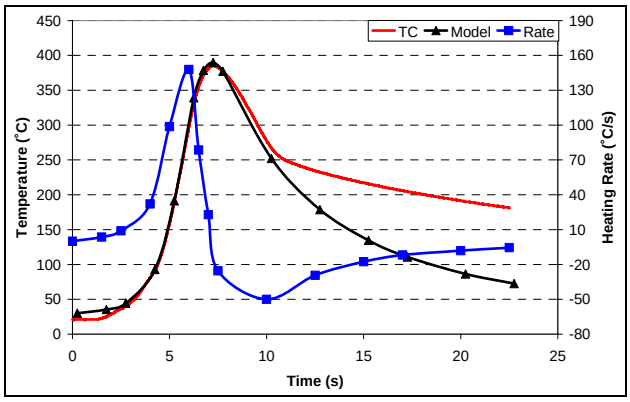

(c) Peak Temperature 385 ˚C

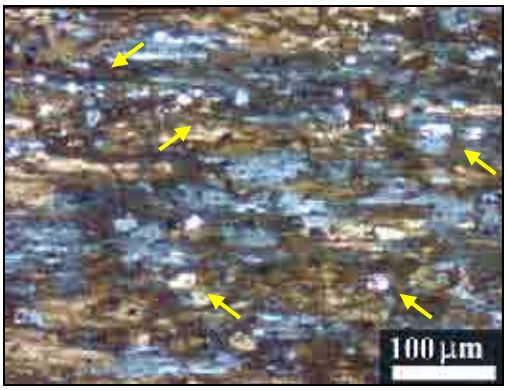

(d) Recrystallisation initiated (recrystallised grains arrowed)

Fig. 6.17. Typical HAZ thermal cycles from the model to a peak temperatures 325 ˚C (a,b) and 385 ˚C (c,d), compared to simulated cycle (T_C) using Gleeble on a H34-basemetal specimen, and the corresponding microstructure

Although static heating or slow dynamic heating (e.g. in the DSC) to both temperatures resulted in the initiation of recrystallisation by ~325 ˚C and the completion of the process by 375 ˚C, the initial heating in regime (A) resulted in the dissipation of a portion of the driving force available for recrystallisation, which accordingly retarded recrystallisation to higher temperatures. These results also show that the model predictions were close to the actual temperatures experienced, as confirmed through the microstructural development in the thermally cycled specimens.

6.3.2. 5083-H116-weld

The model was also used to predict the thermal fields associated with the 5083-H116 weld to assist in explaining the HAZ microstructural development, and also the range of temperatures investigated in the weld.

6.3.2.a. Predicted Thermal Fields

The thermal model was also used assuming the imperfect contact scenario of the 2024-T351 weld due to the comparable thickness of the sheet (5 mm). The thermomechanical and thermophysical properties for 5083 were obtained from the literature [16, 42]. The model predicted a maximum temperature of ~425 ˚C (Fig. 6.18), which is lower than that in the 5251-H34 weld. This can be attributed to the low rotation speed and smaller tool used in the 5083 weld, which is expected to reflect on the weld creating a localised HAZ.

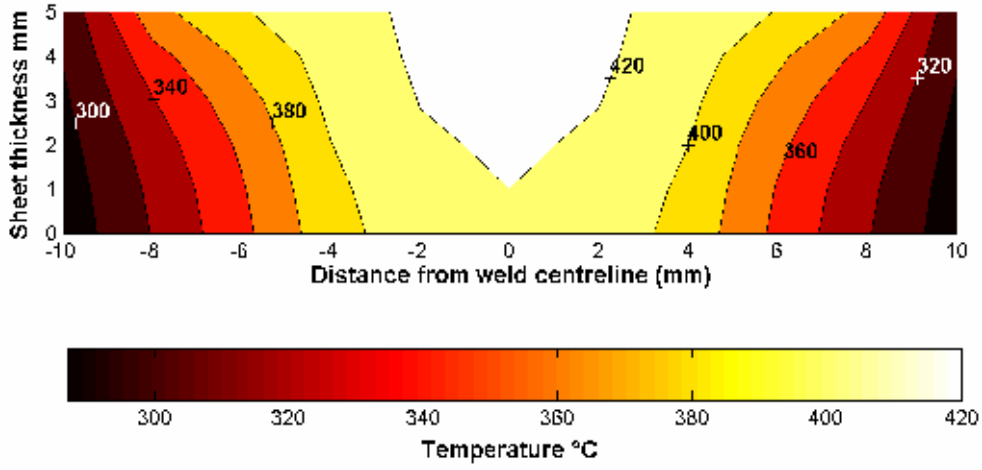

Fig. 6.18. Temperature distribution in the 5083-H116 weld according to the thermal model

6.3.2.b. Microhardness Contours and HAZ microstructure

The macrostructural zones in the HAZ of the 5083-H116 resembled the classification for the 5251-H34 weld, with SRX and REC zones. Nonetheless, due to the differences in the process parameters, the range of temperatures experienced and the parent metal condition, the HAZ was relatively more localised in this weld, with the HAZ ceasing to exist beyond ± 10 mm from the weld centreline, Fig. 6.19. Full recrystallisation (Fig. 6.19-a) was only observed in a thin band along on the HAZ/TMAZ boundary, resulting in a drop in hardness to 75-80 H_V.

According to the predictions of the model, the SRX-HAZ experienced temperatures within the range of 290 to 365 ˚C. Recrystallisation in this alloy was found to occur when statically annealed at temperatures > 275 ˚C as shown in section 5.2.3, which is close to the range suggested by the model to overlap with the formation of the SRX-HAZ region. This indicates that heating in the weld thermal cycle occurred at relatively lower heating rates compared to the 5251-H34 weld, which accordingly avoided the delay of recrystallisation to higher temperatures. In fact, the simulated thermal cycles for the HAZ indicate that heating in the recovery range occurred at rates < 50 ˚C/s, with a maximum heating rate of 65 ˚C/s occurring at the peak temperature, Fig. 6.20.

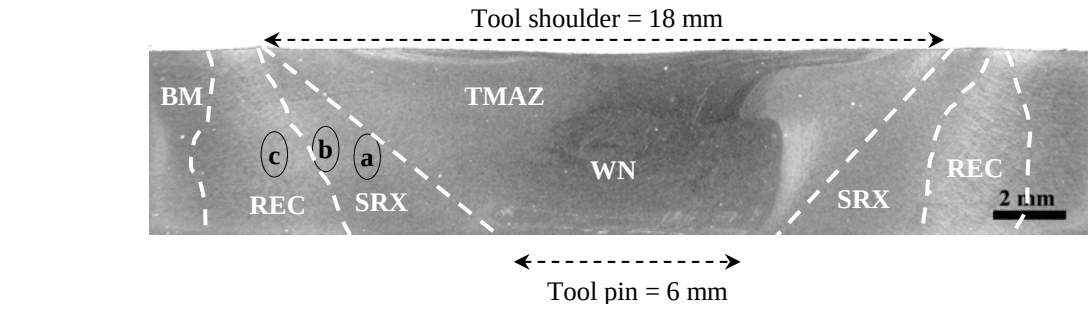

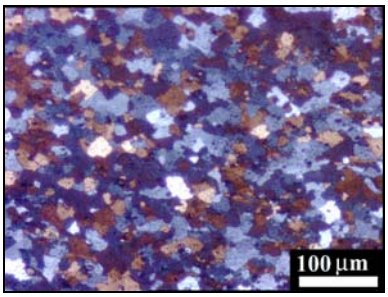

(a) Static recrystallisation

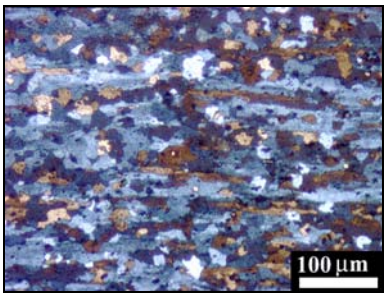

(b) Incomplete recrystallisation

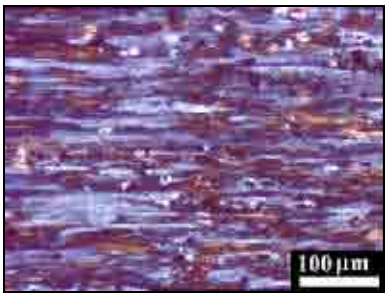

(c) Recovery/ recrystallisation initiates

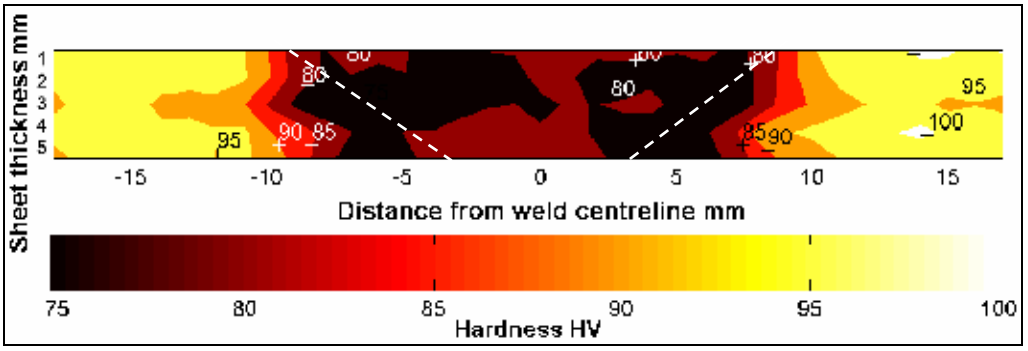

d) Microhardness profile (the dashed lines show the width of the TMAZ)

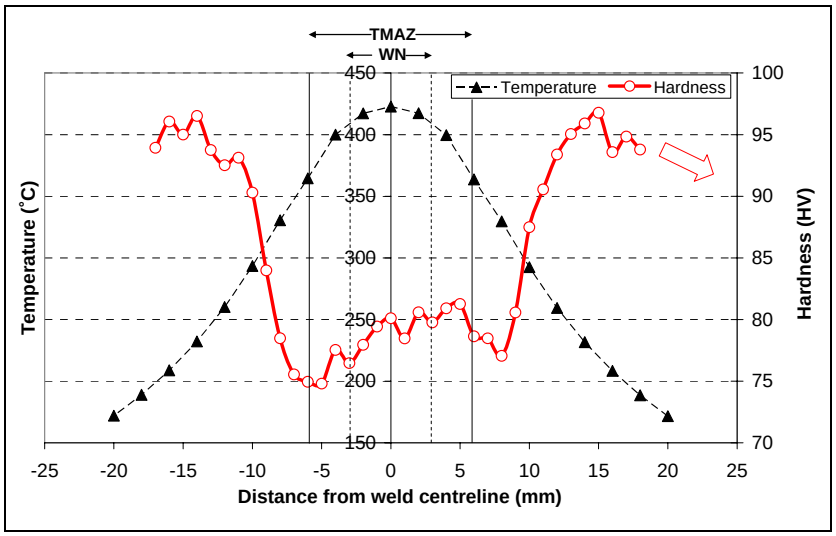

(e) microhardness mid-thickness trace and the temperature trace according to the model (AS to the right)

Fig. 6.19. The 5083-H116 weld HAZ microstructure and microhardness distribution

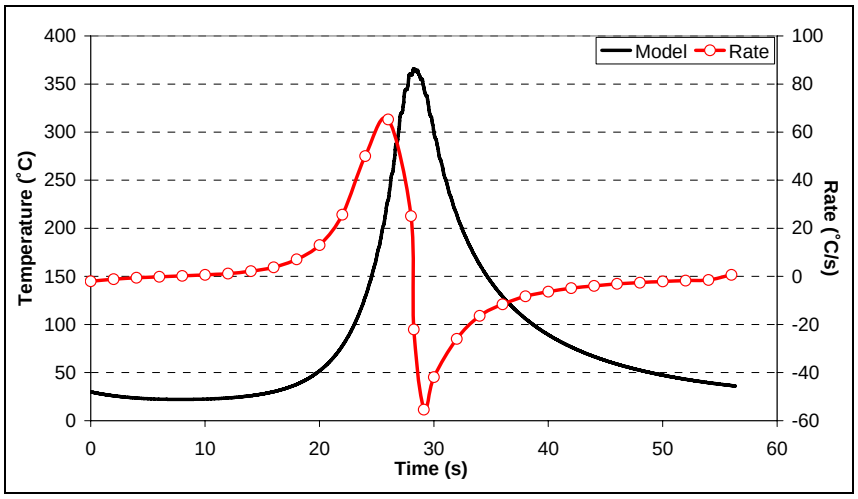

Fig. 6.20. SRX-HAZ thermal cycle from the 5083-H116 model to a peak temperatures 360 ˚C

6.3.3. 2024-T351

6.3.3.a. Predicted Thermal Fields

The thermal model was used to predict the thermal cycles of the 2024-T351 welds (set 4, CW and HW, section 4.2). The maximum temperature in HW was ~500 ˚C (~80 ˚C higher than that in the CW), Fig. 6.21.

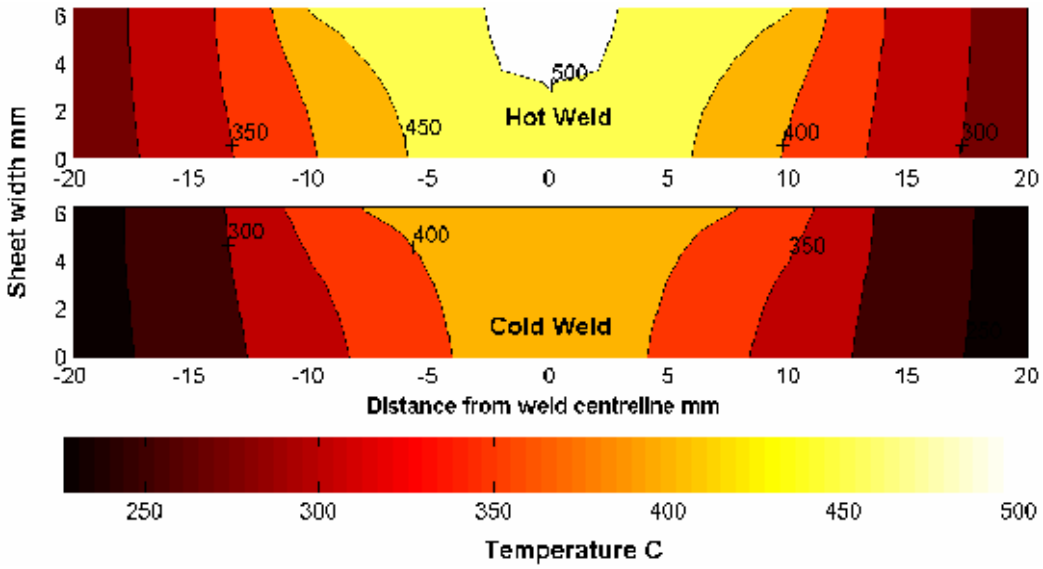

Fig. 6.21. Temperature distribution in the 2024-T351 welds according to the thermal model

6.3.3.b. Microhardness Development

The complexity of the natural aging (NA) response in 2024 makes it difficult to rationalise the microhardness development based on the thermal fields, noting that the microhardness measurements were obtained more than 2 years after welding. However, with the help of the isothermal hold experiments performed for 2024-T3 by Preston *et al.* [43], it is possible to discern the possible impact of transient heating, followed by NA, on the hardness development. As shown in Fig. 6.22, isothermal hold between 175 to 500 ˚C for ~10 s (to simulate the transient thermal exposure during welding) resulted in a hardness drop (as-quenched), with the extent of drop increasing with the increase in temperature. However, following 1 week of NA, strength recovery was found to vary depending on the isothermal hold temperature. For the specimen held close to the solidus temperature (~500 ˚C), 90 % of the T3 strength was regained after NA. However, for specimens experiencing temperatures ~400 ˚C, only 80 % of the T3 strength was recovered by NA, which indicates that full dissolution was not achieved, and only non-hardening phases formed due to the thermal exposure, decreasing the solute content. Following, for the specimens held at 250 and 300 ˚C, the T3 was almost fully retained, which suggests that thermal exposure led to partial dissolution of the GP zones, then their re-precipitation by NA. Finally, thermal exposures at 200 ˚C and lower resulted in limited change in hardness, with the T3 strength fully retained following NA.

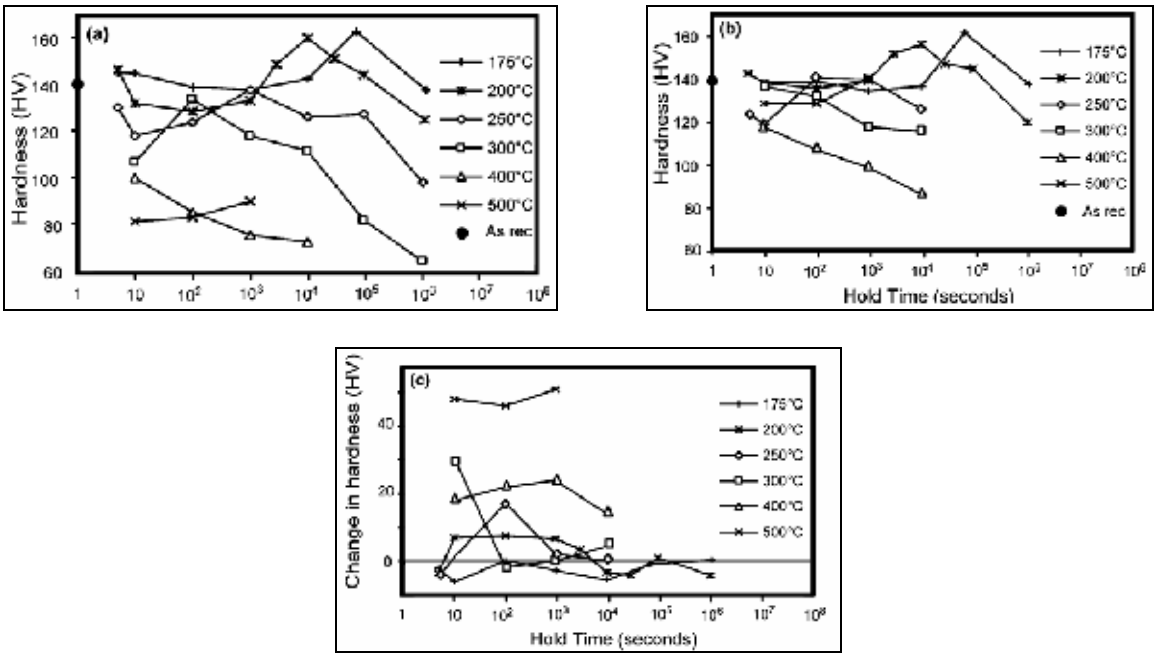

Fig. 6.22. Hardness variation due to isothermal holds in salt bath (a) as-quenched hardness, (b) after 1 week natural aging, (c) hardness change between (b) and (a) [43]

To apply the previous correlations on the 2024-T351 HW and CW, the hardness traces for both welds were plotted, alongside the temperatures predicted by the thermal model, Fig. 6.23. Within the HW-WN, high hardness values close to that of the basemetal (T351) (135-147 H_V) were observed, Fig. 6.23-a. This indicates that the temperature within HW-WN was high enough to allow for dissolution of some of the precipitates present (GP, S and θ) into the solid solution, followed by their re-precipitation by NA in the form of GP zones, which increases the hardness to this level (i.e. naturally aged). The predictions of the thermal model agreed to a large extent with this development, where temperatures of ~475-500 ˚C were predicted within the WN, which is expected to dissolve the present GP precipitates, and fragment/dissolve some of the constituent S and θ particle by the action of stirring.

In the HW-HAZ, the predicted temperature (~400 ˚C) was insufficient to cause the dissolution/re-precipitation effect, which accordingly resulted in the observed decrease in the hardness to ~115-120 H_V, which is the minimum level in the HW. Similarly, within the CW-WN, the hardness values showed similar low hardness levels (120 H_V) since this region experienced temperatures ~400-425 ˚C, Fig. 6.23-b. Within the CW HAZ, and with the fading out of the thermal effects from the weld centreline, the over-aging level decreases as the distance from the weld centreline increases. These correlations agree with the findings of Preston *et al.* [43], and give some evidence on the validity of the model. At some distance from the weld centreline in both welds, the hardness reaches a peak value of ~155 H_V, which is probably related to achieving a peak-aging (T6-like) condition with the transient thermal cycle during welding, and the long natural-aging period following welding. Similar trends were observed in 2024-T351 welds [44, 45] as discussed in chapter 3.

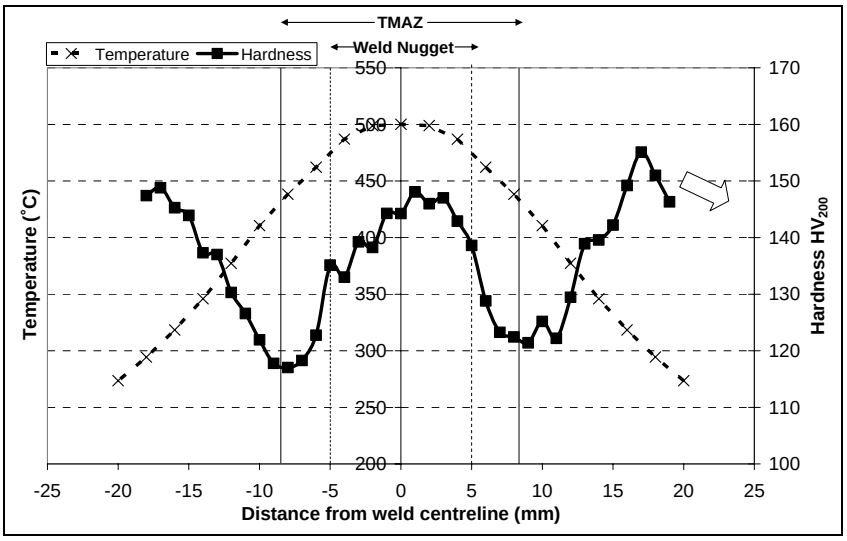

(a) Hot weld

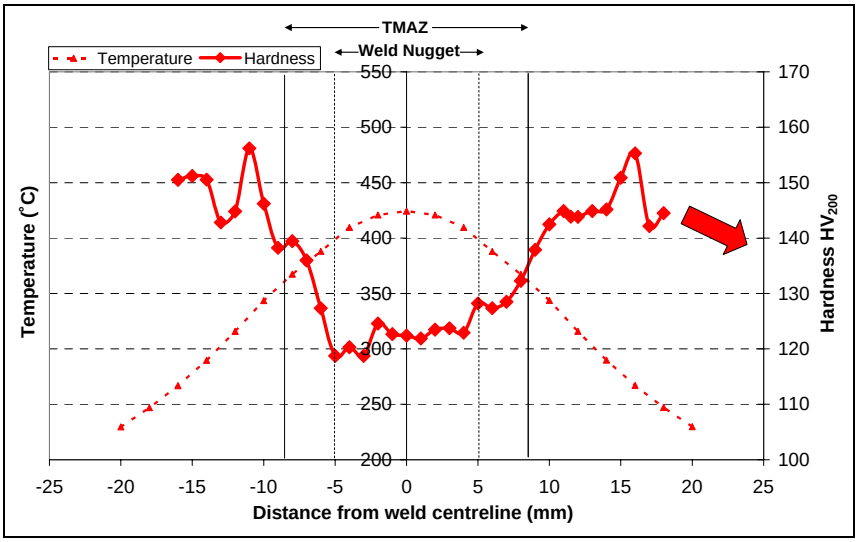

(b) cold weld

Fig. 6.23. The hardness distribution in the 2024-T351 hot and cold welds at mid-thickness (following 2 years aging), with the temperature predictions from the thermal model (WN ± 5mm, TMAZ ± 9mm)

6.4. Conclusions

In this chapter, the construction, fitting and experimental validation of a simple numerical model for heat transfer during weld was presented. Fitting was performed for 2xxx and 5xxx series alloys using experimental torque, force, and thermocouple data. Additional correlation was performed using microstructural investigations for the HAZ and hardness measurements, alongside with thermocouple measurements. Based on this, the following conclusions can be drawn:

1. The ADI-technique is a simple numerical FD approach for modelling the heat flow and the thermal cycle during FSW. This approach provides reasonable predictions close to the experimental thermocouple data, within the range of experimental error of ±30 ˚C, and similar to the prediction accuracy of other FSW models.
2. The model calibration is limited to the friction coefficient and the contact condition between the workpiece and the machine anvil. The warping which happens following welding minimises the conductivity behind the tool, depending on the sheet thickness. In general, the contact condition can be simplified by assuming different contact conductance for in front and behind the moving tool.
3. FSW results in a localised thermal field, which accordingly creates a narrow HAZ, with temperatures lower than the melting point within the TMAZ. In the work-hardened conditions, it is apparent that the transient nature of the thermal cycle affects the recrystallisation kinetics, which were found to be highly dependent on the heating rate with full recrystallisation needing a critical heating rate to avoid recovery during initial heating.

6.5. References

[1] J. P. Holman, *Heat Transfer*, 8th ed. New York: McGraw-Hill, Inc., 1997.

[2] D. Rosenthal, "The Theory of Moving Source of Heat and its Application to Metal Transfer," *Transactions ASME*, vol. 43, pp. 849-866, 1946.

[3] Ø. Grong, *Metallurgical Modelling of Welding*, 2nd ed. London: The Institute of Materials, 1997.

[4] S. C. Chapra and R. P. Canale, *Numerical Methods for Engineers*, 3rd ed. Singapore: McGraw-Hill, Inc., 1998.

[5] T.-Y. Wang, Y.-M. Lee, and C. C.-P. Chen, "3D thermal-ADI - An efficient chip-level transient thermal simulator," presented at the International Symposium on Physical Design, Monterey, CA, United States, 2003.

[6] Ø. Frigaard, Ø. Grong, and O. T. Midling, "A process model for friction stir welding of age hardening aluminum alloys," *Metallurgical and Materials Transactions A: Physical Metallurgy and Materials Science*, vol. 32, pp. 1189-1200, 2001.

[7] P. A. Colegrove, M. Painter, D. Graham, and T. Miller, "3-dimensional flow and thermal modelling of the friction stir welding process," presented at 2nd International Symposium on Friction Stir Welding, Gothenburg, Sweden, 2000.

[8] H. R. Shercliff and P. A. Colegrove, "Modelling of Friction Stir Welding," in *Mathematical Modelling of Weld Phenomena*, vol. 6, H. Cerjak and H. K. H. D. Bhadeshia, Eds. London: Maney Publishing, 2002, pp. 927–974.

[9] H. Schmidt, J. Hattel, and J. Wert, "An analytical model for the heat generation in friction stir welding," *Modelling and Simulation in Materials Science and Engineering*, vol. 12, pp. 143-157, 2004.

[10] P. Heurtier, M. J. Jones, C. Desrayaud, J. H. Driver, F. Montheillet, and D. Allehaux, "Mechanical and thermal modelling of Friction Stir Welding," *Journal of Materials Processing Technology*, vol. 171, pp. 348-357, 2006.

[11] H. Schmidt and J. Hattel, "A local model for the thermomechanical conditions in friction stir welding," *Modelling and Simulation in Materials Science and Engineering*, vol. 13, pp. 77-93, 2005.

[12] H. N. B. Schmidt, T. L. Dickerson, and J. H. Hattel, "Material flow in butt friction stir welds in AA2024-T3," *Acta Materialia*, vol. 54, pp. 1199-1209, 2006.

[13] S. Xu and X. Deng, "A Three-Dimensional Model for the Friction-Stir Welding Process," presented at 21st Southeastern Conference on Theoretical and Applied Mechanics (SECTAM XXI), Orlando, Florida, 2002.

[14] M. Z. H. Khandkar, J. A. Khan, and A. P. Reynolds, "Prediction of Temperature Distribution and Thermal History during Friction Stir Welding: Input Torque Based Model," *Science and Technology of Welding and Joining*, vol. 8, pp. 165-174, 2003.

[15] Y. J. Chao and X. Qi, "Heat Transfer and Thermo-Mechanical Modeling of Friction Stir Welding Joining of AA6061-T6 Plates," presented at the First International Symposium on Friction Stir Welding, Rockwell Science Center, Thousand Oaks, CA, 1999.

[16] J. R. Davis, *Aluminum and Aluminum Alloys*. Ohio: American Society for Metals (ASM), 1993.

[17] P. A. Colegrove and H. R. Shercliff, "CFD modelling of friction stir welding of thick plate 7449 aluminium alloy," *Science and Technology of Welding and Joining*, vol. 11, pp. 429, 2007.

[18] P. A. Colegrove and H. Shercliff, "Modelling the Friction Stir Welding of Aerospace Alloys," presented at 5th International Symposium on Friction Stir Welding, Metz, France, 2004.

[19] R. V. Preston, H. R. Shercliff, P. J. Withers, and S. D. Smith, "Finite element modelling of tungsten inert gas welding of aluminium alloy 2024," *Science and Technology of Welding & Joining*, vol. 8, pp. 10-18, 2003.

[20] Q. Shi, T. Dickerson, and H. Shercliff, "Thermo-mechanical FE Modelling of Friction Stir Welding of Al-2024 Including Tool Loads," presented at The 4th International Symposium on Friction Stir Welding, Park City, Utah, USA, 2003.

[21] M. J. Russell and H. R. Shercliff, "Analytical Modelling of Microstructure Development in Friction Stir Welding," presented at the First International Symposium on Friction Stir Welding, Rockwell Science Center, Thousand Oaks, CA, 1999.

[22] Y. S. Touloukian and E. H. Buyco, *Theromophysical Properties of Matter*, vol. 4. London: IFI Plenum, 1970.

[23] X. K. Zhu and Y. J. Chao, "Effects of temperature-dependent material properties on welding simulation," *Computers & Structures*, vol. 80, pp. 967-976, 2002.

[24] S. K. Khanna, X. Long, W. D. Porter, H. Wang, C. K. Liu, M. Radovic, and E. Lara-Curzio, "Residual stresses in spot welded new generation aluminium alloys Part A - thermophysical and thermomechanical properties of 6111 and 5754 aluminium alloys," *Science and Technology of Welding & Joining*, vol. 10, pp. 82-87, 2005.

[25] T. L. Dickerson, "The Friction Stir Welding Benchmarks, http://www-materials.eng.cam.ac.uk/FSW_Benchmark/," 2nd ed, 2003.

[26] M. Jariyaboon, "PhD Thesis: Corrosion of Friction Stir Welds in High Strength Aluminium Alloys," in *Department of Metallurgy and Materials, University of Birmingham, UK*, 2005.

[27] M. Z. H. Khandkar, J. A. Khan, and A. P. Reynolds, "Input Torque Based Thermal Model of Friction Stir Welding of Al-6061," presented at Trends in Welding Research, Phoenix, AZ, United States, 2002.

[28] M. J. Peel, A. Steuwer, P. J. Withers, T. Dickerson, Q. Shi, and H. Shercliff, "Dissimilar friction stir welds in AA5083-AA6082. Part 1: process parameter effects on thermal history and weld properties," *Metallurgical and Materials Transactions A (Physical Metallurgy and Materials Science)*, vol. 37A, pp. 2183-2193, 2006.

[29] T. U. Seidel and A. P. Reynolds, "A 2-D friction stir welding process model based on fluid mechanics," *Science and Technology of Welding and Joining*, vol. 8, pp. 175-183, 2003.

[30] C. L. Tsai, S. C. Park, and W. T. Cheng, "Welding distortion of a thin-plate panel structure," *Welding Journal (Miami, Fla)*, vol. 78, pp. 156-165, 1999.

[31] M. Song and R. Kovacevic, "Numerical and experimental study of the heat transfer process in friction stir welding," *Proceedings of the Institution of Mechanical Engineers, Part B: Journal of Engineering Manufacture*, vol. 217, pp. 73-85, 2003.

[32] M. Song and R. Kovacevic, "Thermal modeling of friction stir welding in a moving coordinate system and its validation," *International Journal of Machine Tools and Manufacture*, vol. 43, pp. 605-615, 2003.

[33] R. Kovacevic, V. Soundararajan, and S. Zekovic, "Thermo-mechanical model with adaptive boundary conditions for friction stir welding of Al 6061," *International Journal of Machine Tools & Manufacture*, vol. 45, pp. 1577-1587, 2005.

[34] A. Simar, T. Pardoen, and B. d. Meester, "Influence of the friction stir welding parameters on the power input and temperature distribution in Aluminium alloys,"

presented at 5th International Symposium on Friction Stir Welding, Metz, France, 2004.

[35] P. A. Colegrove, "Modelling the Heat Generation, Temperature and Microstructure of Friction Stir Welds using Comsol Multiphysics," presented at Comsol Users Conference, Birmingham, UK, 2006.

[36] W. M. Rohsenow, J. P. Hartnett, and E. N. Ganic, *Handbook of Heat Transfer Fundamentals*, 2nd ed. ed. New York: McGraw-Hill, Inc., 1985.

[37] M. Ferry and D. Jones, "High-rate annealing of single-phase and particle-containing aluminium alloys," *Scripta Materialia*, vol. 38, pp. 177-183, 1997.

[38] J. Go, W. J. Poole, M. Militzer, and M. A. Wells, "Modelling recovery and recrystallisation during annealing of AA 5754 aluminium alloy," *Materials Science and Technology*, vol. 19, pp. 1361-1368, 2003.

[39] W. S. Miller, A. Burger, D. Sampath, and M. R. van der Winden, "Temperature compensated time concept as a tool for the modelling of aluminium alloys," *Materials Science Forum*, vol. 331, pp. 757-762, 2000.

[40] M. Atkinson, "Bifurcation of thermal restoration processes in deformed iron and steel," *Materials Science and Engineering A*, vol. 262, pp. 33-38, 1999.

[41] M. Atkinson, "On the credibility of ultra rapid annealing," *Materials Science and Engineering A*, vol. 354, pp. 40-47, 2003.

[42] H. Ahmed, M. A. Wells, D. M. Maijer, B. J. Howes, and M. R. v. d. Winden, "Modelling of microstructure evolution during hot rolling of AA5083 using an internal state variable approach integrated into an FE model," *Materials Science and Engineering A*, vol. 390, pp. 278-290, 2005.

[43] R. V. Preston, H. R. Shercliff, P. J. Withers, and S. Smith, "Physically-based constitutive modelling of residual stress development in welding of aluminium alloy 2024," *Acta Materialia*, vol. 52, pp. 4973, 2004.

[44] J. C. Ehrstrom, A. Bigot, L. Cervi, and H. Gerard, "Microstructure and properties of aluminum alloys friction stir welds for aircraft application," Leganes, Madrid, Spain, 2003.

[45] C. Genevois, A. Deschamps, A. Denquin, and B. Doisneau-cottignies, "Quantitative investigation of precipitation and mechanical behaviour for AA2024 friction stir welds," *Acta Materialia*, vol. 53, pp. 2447-2458, 2005.

Chapter 7

INFLUENCE OF THE BASEMETAL ON THE MICROSTRUCTURAL DEVELOPMENT

The thermomechanical deformation associated with FSW is known to result in a complex microstructural development, which is expected to be influenced by the basemetal type, condition and microstructure, especially since FSW is a solid-state joining method. The aim of this chapter is to determine the influence of the basemetal microstructural factors on the microstructural development, specifically the grain and particle structures, as well as the formation of the characteristic onion rings structure. Quantitative characterisation of the microstructural development in several 5xxx-series alloys is presented, and compared to that in a 2xxx alloy. The characterised welds can be divided into three groups; the first group contains the 5251 and 5754 welds, which were welded using the same welding parameters but the base alloys had different processing routes; the second was the 5083 weld, which was welded using different welding parameters; and thirdly the 2024 weld, which is used to explain the influence of alloy and constituent particles types on the weld microstructure. This chapter also provides insight for the structure-property modelling in Chapter 8.

7.1. AA5251 (H34 and O)

7.1.1. Weld Macrostructure

To reveal the TMAZ/WN structure and the details of the onion rings zone (ORZ), a 10 % H_3PO_4 solution was used to etch polished 5251-welds (H34 and O conditions). Digital macrographs for the etched welds showed a sharp TMAZ/HAZ boundary towards the advancing side (AS), compared to a more diffuse boundary towards the retreating side (RS). A preferentially-etched ORZ was also revealed showing bands of alternating contrast within the lower half of the sheet, and extending across the WN width (i.e. the width of the tool pin),

Fig. 7.1-a. The preferentially-etched region was also found to extend from the ORZ along the flow arm towards the AS, which has also been seen in other welds (e.g. [1]). The ORZ bands were irregular, with the thicknesses/spacings varying between 10 and 100 μm across the weld face, thus differing from the typical concentric ellipse morphology observed in other reports [1-3]. This difference in the ORZ morphology could be attributed to the tool geometry. The effect of the tool shape on the weld profile has been investigated in several studies [4-6]. It is known that cylindrical threaded tools cause the flow fields surrounding the tool to be mostly tangential to the tool, whilst current designs (as the MX-Triflute® tool used for the 5251 weld) are frustum-shaped, containing re-entrant features (e.g. helix-like flutes), which would disturb the tangential flow [4, 5]. By sectioning along the welding direction (WD) at the weld centreline, it can be seen that the ORZ represents a section through a uniformly repeated etching trend along the WD, Fig. 7.1-b, occurring every 1 mm, which is consistent with the advance per revolution (APR). This repeated trend has been previously observed in several studies [3, 6, 7]. The same trend was also observed in the O-weld.

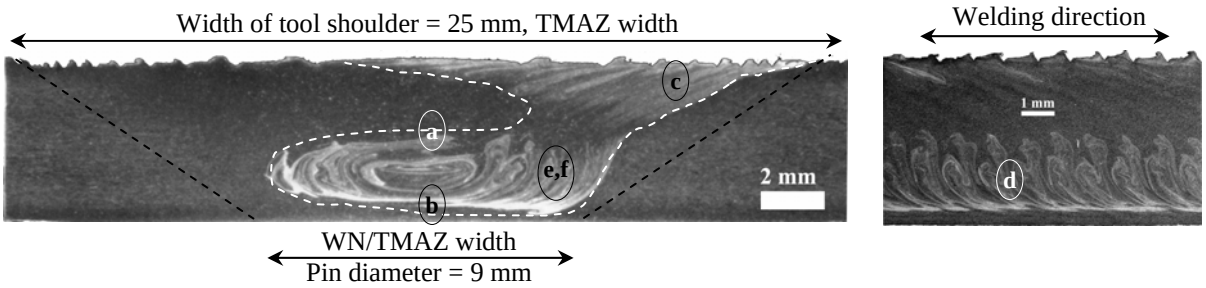

Fig. 7.1. Macrograph of 5251H34-weld etched in 10 % H_3PO_4 solution showing (a) the weld face (the AS is to the right), (b) full longitudinal section along the WD at the weld centreline

7.1.2. Weld Microstructure

The microstructural development due to FSW is associated with two microstructural aspects; the grain structure, which is known to experience dynamic recrystallisation (DRX) within the WN, and the intermetallic particles, which could break up, precipitate or dissolve as a consequence of thermomechanical stirring. Using the 5251-H34 and O welds, the influence of the starting condition on the microstructural development (if any) can be established.

7.1.2.a. Microstructural Development (Qualitative)

Within the WN of the H34-weld, Fig. 7.2, and parts of the TMAZ (as spatially defined in Fig. 7.1), grain refinement by DRX was the common feature, showing equiaxed grains with sizes within a range of 3-8 μm, Fig. 7.2-a. Yet, the grain structure was not uniform throughout, notably in the ORZ bands, showing a heterogeneity in grain sizes exhibited in the form of bands containing coarse grains of size 7-10 μm, and fine grains of size 2-5 μm within the ORZ (Fig. 7.2-b) and the AS flow arm (Fig. 7.2-c). It is important to note that the banding was restricted to the selectively-etched regions. On the sectional view (Fig. 7.1-b), the repeated etching trend, at the lower half of the sheet, was also found to correspond to coarse and fine grain bands of varying thicknesses, Fig. 7.2-d. Coarse Fe-rich particles, which were identified using EDS as α-Al(Fe,Mn)Si, were also found to segregate in the lower part of the WN, forming semi-continuous bands (Fig. 7.2-e), with the particles mostly segregated on the grain boundaries, Fig. 7.2-b. These features have been previously observed in the ORZ of AA2xxx and AA7xxx welds (section 3.5.3). The fine grain bands were also found to overlap with the presence of fine Mn-containing grain boundary precipitates, which were identified by diffraction and EDS as the Al_6(Fe,Mn) dispersoids, Fig. 7.2-f. Although, optically, the grain boundary precipitates appeared to be continuous along the grain boundaries as in Fig. 7.2-(a,b), it was found using TEM that the precipitates were not actually continuous, Fig. 7.3. Different morphologies were observed (e.g. rod-like, spherical, and globular, size <0.5 μm), which are similar to those observed in the literature [8, 9]. However, they did not appear to be causing a significant pinning effect as the grain boundaries did not appear bowed around them. Moreover, the Al_6(Fe,Mn) dispersoids were observed using the TEM within the grains, indicating a potential strengthening contribution as will be discussed in following sections.

In the O-weld, similar features were observed within the TMAZ/WN regions (e.g. grain refinement by DRX (Fig. 7.4-a), banding of coarse and fine grains with roughly similar size ranges as in the H34-weld (Fig. 7.4-b), and GB precipitation (Fig. 7.4-c) within the ORZ bands. Alternating bands of coarse and fine particles, coinciding with the coarse and fine grain bands respectively, were also observed within the ORZ bands. As shown in Fig 7.4-d, the upper band, which was selectively etched, was found to contain finer particles and a relatively high hardness (~74 H_V), compared to the region below which contained coarser particles and a lower hardness (~68 H_V).

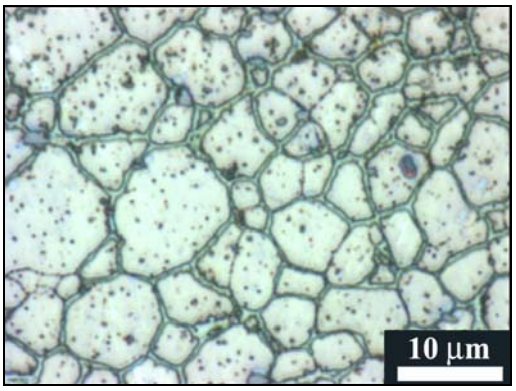

(a) Dynamic recrystallisation

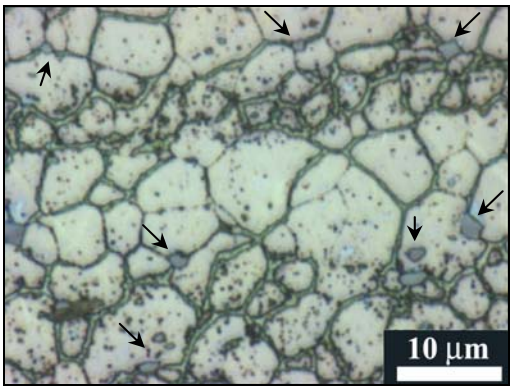

(b) WN grain size banding and precipitation (segregated α -particles arrowed)

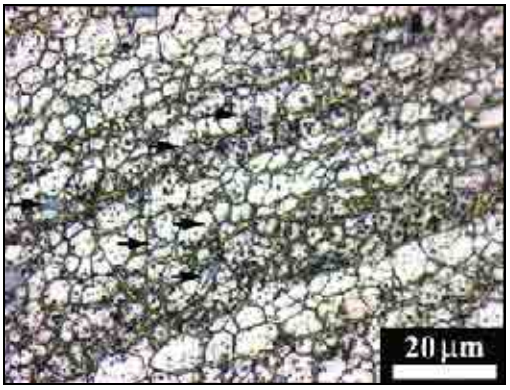

(c) AS grain size banding and precipitation (segregated α -particles arrowed)

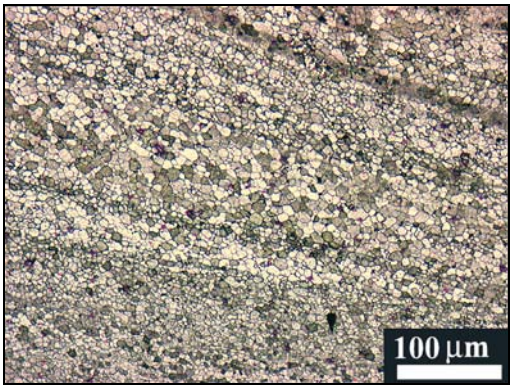

(d) Grain size banding on the sectional view

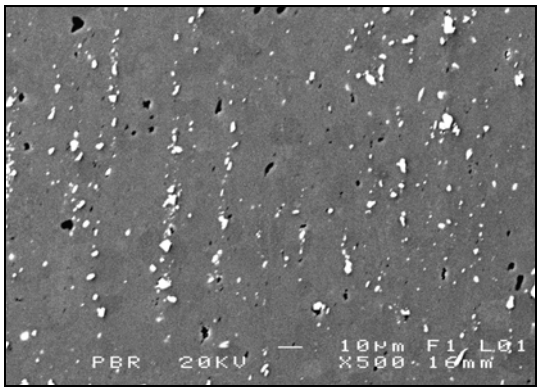

(e) α -particle bands in the WN

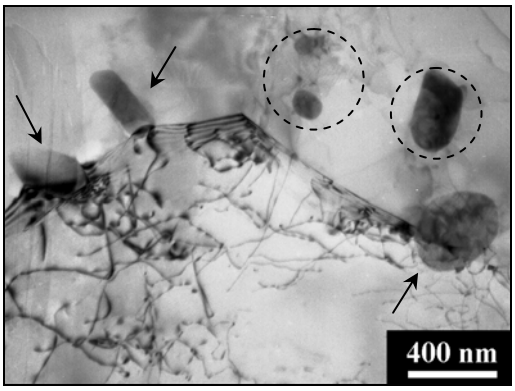

(f) $Al_6(Fe,Mn)$ GB precipitates (arrowed) and within the grains (circled)

Fig. 7.2. Micrographs for the 5251-H34 weld (positions according to Fig. 7.1)

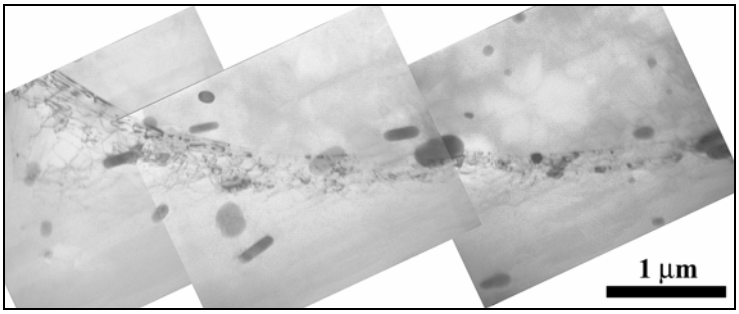

Fig. 7.3. $Al_6(Fe,Mn)$ precipitates along the grain boundary in the WN of 5251-H34 weld (TEM specimen extracted from region (b) in Fig. 7.1-a)

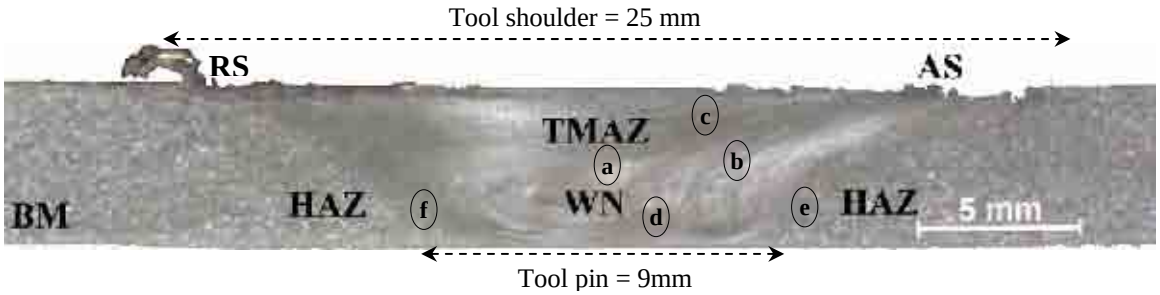

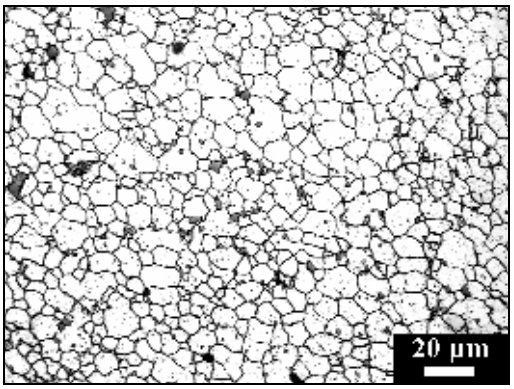

(a) WN dynamic recrystallisation

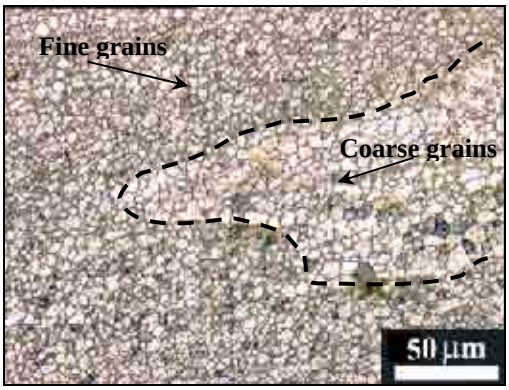

(b) coarse and fine grain regions

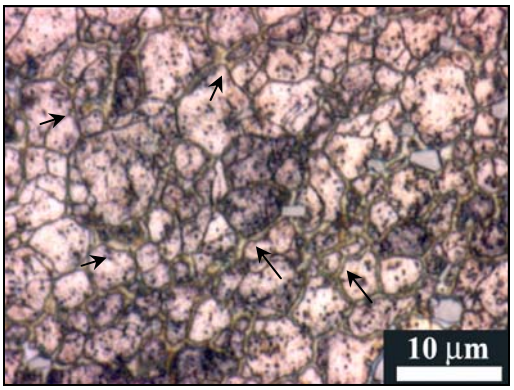

(c) GB precipitation (thick GBs arrowed)

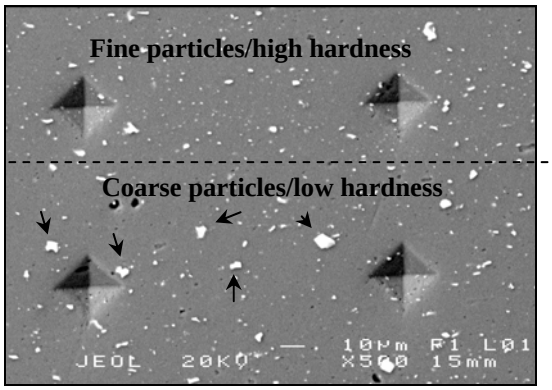

(d) ORZ bands (coarse α -particles arrowed)

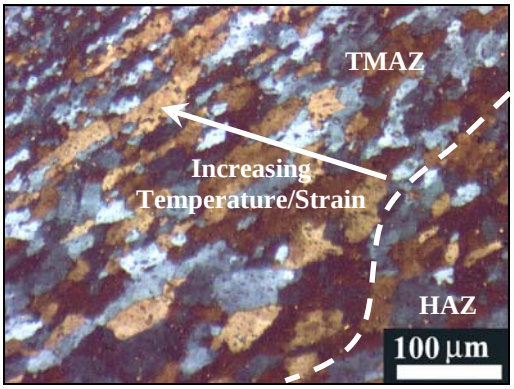

(e) HAZ/TMAZ at AS

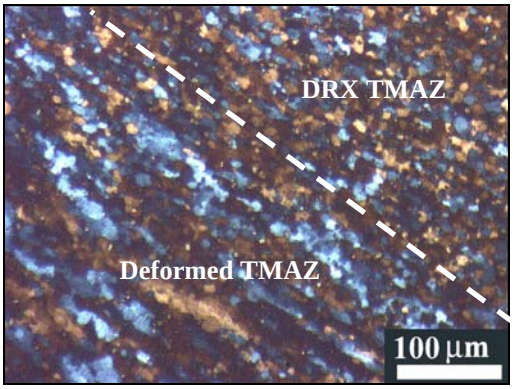

(f) TMAZ at RS

Fig. 7.4. Optical micrographs from various weld regions in the 5251-O weld

As the starting condition was the O-temper, observing the microstructural development within the TMAZ can be performed by tracing the development across the WN/TMAZ and TMAZ/HAZ boundary regions. Within the TMAZ (as defined by the trapezoidal region whose edges are the tool shoulder and pin diameters), the occurrence of DRX was found to decrease moving across the TMAZ from the WN edge towards the region at the vicinity of the HAZ. The recrystallised grain structure of the basemetal (~30 μm) appeared to be thermomechanically deformed within the TMAZ close to the boundary with the HAZ, Fig. 7.4-e, where the grains appeared elongated and flattened (~100 μm long). As the intensity of the thermomechanical deformation parameters (temperature and strain) increases closer to the WN, the elongated grains gradually develop into DRXed equiaxed grains, Fig. 7.4-f, thus dividing the TMAZ into two regions; a deformed TMAZ, where the temperature and strain are insufficient to induce DRX, and a DRXed TMAZ in the vicinity of the WN.

7.1.2.b. Quantitative Metallography

Both welds showed similar trends in grain size variation within the TMAZ/WN. Generally, the grain size increases from the AS towards the RS, and increases from the surface downwards, until the mid-thickness, where it then decreases again within the ORZ, Fig. 7.5 and 7.6. The average grain size in the image fields (96 × 72 μm) taken in the TMAZ was finer at the AS, compared to coarser grains at the RS. The maximum grain refinement was observed under the tool shoulder towards the flow arm at the AS (Fig. 7.2-c), with an average grain size of ~ 3.3±1.3 μm in the O-weld and 3.7±1.2 μm in the H34-weld.

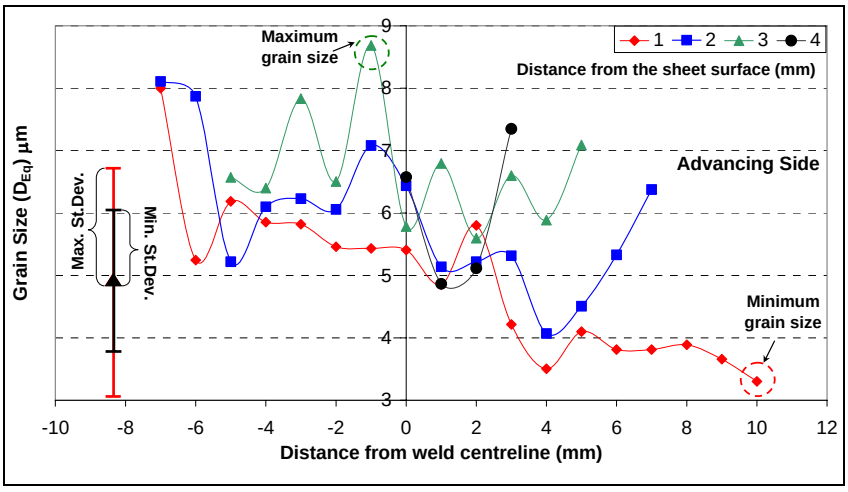

Fig. 7.5. Grain size distribution with the TMAZ/WN of 5251-O weld
Each point corresponds to the average grain size in an image field. Standard deviation (St.Dev.) range is shown.

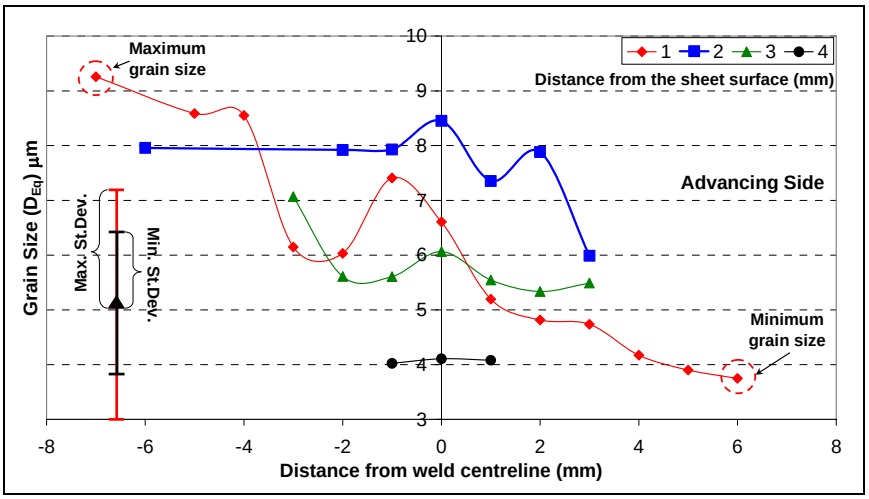

Fig. 7.6. Grain size distribution with the TMAZ/WN of 5251-H34 weld

The largest grain sizes were generally observed in the image fields taken in the middle traces (2 and 3 mm) and towards the RS, with a maximum grain size of 8.7±2.9 μm in the O-condition, and 9.2±2.9 μm in the H34-condition. Further details are presented in Chapter 8.

It can be inferred from the grain size measurements that the thermomechanical deformation in the TMAZ/WN removed any effect of the starting conditions (H34 and O), which resulted in a roughly similar range of grain sizes. This can also be correlated with the similar power input in both welds (i.e. torque and force measurements, section 6.3.1.a), which indicates that the thermal field in front of the moving tools possibly softened the H34 material, and accordingly removed the possible influence of the starting condition. However, spatially, the grain size variation in both conditions (either in size or trends) does not seem to exactly match, except in the trace at 1 mm below the sheet surface, which shows a roughly similar trend and sizes (considering the standard deviation). This can be attributed to the large grain size variability within a single image field due to the bimodality in grain size, which seemed to increase in intensity away from the surface (e.g. comparing Fig. 7.2-a and 7.2-b taken at mid-thickness and in the ORZ respectively, which show grain sizes of up to ~15 μm and down to 2 μm, and Fig. 7.2-c taken at the top of the weld towards the AS). Because of this, only the regions which showed clear size differences (i.e. AS, RS, and WN) were later considered to establish the Hall-Petch relation in Chapter 8.

It is also important to note that the grain size range in the H34 and O welds is similar to the range normally observed in welds (section 3.5.1), although the spatial grain size distribution is different from other published trends in the literature [10-12], where the grain size was found to increase near the top of the weld, and decrease on either side of the weld, with the finest sizes reported in the WN or towards the RS. However, as was also indicated, the spatial grain size distribution (e.g. location of the most fine or coarse grains) was highly dependent on the material and welding parameters (e.g. the alloy type, sheet thickness, starting grain size, process parameters, and tool geometry), showing to some extent inconsistent trends [10]. In addition, the previous weld grain size studies were performed mainly on heat-treatable alloys (compared to the present study which investigated work-hardenable alloys), using cylindrical tools (compared to the frustum-shaped MX-Triflute tool used in this study), and in thicker sections which are known to result in a larger temperature variation across the weld [13]. Accordingly, a universal spatial grain size distribution in all welds does not possibly exist.

With regard to the intermetallic particles, as previously shown, the stirring action influences the distribution of constituent particles and the fine dispersoids. In the H34-weld WN (±4.5 mm from the weld centreline), the area fraction (A_f) of the α-particles (>0.5 μm) decreased to 0.0175±0.005, compared to 0.024±0.005 in the H34 basemetal, and also the Mg_xSi A_f decreased to 0.0017±±0.0015, compared to 0.0055±0.0018 in the basemetal. Similar decrease in both types was also observed in the O-weld; the α-particles decreased to 0.021±0.01, compared to 0.027±0.005 in the basemetal, and the Mg_xSi A_f decreased to 0.0016±±0.002, compared to 0.0049±0.0016 in the O-basemetal. However, the variations in size and number density of the particles showed a large local variability in the images taken within the WN, such that no trend compared to the basemetal could be determined experimentally. Due to the tool stirring action, the particles, of either type, are expected to be stirred and re-distributed, fragmented, or dissolved within the TMAZ/WN (section 3.5.2), depending on the particle characteristics (e.g. dissolution temperature and hardness) and the matrix characteristics (flow and load transfer during high temperature deformation). For the constituent α-particles, this type is known to dissolve and melt at about 635-700 ˚C [14-16] (and similarly for the $Al_6(Fe,Mn)$ dispersoids). As this temperature range is appreciably above the maximum temperatures observed in FSW (400-525 ˚C) [17, 18], the measured decrease in A_f can be attributed to a refinement of a fraction of particles to below that of the microscopic resolution (0.5 μm), thus decreasing the overall A_f. Nonetheless, for the Mg_xSi particles, as dissolution

can start at temperatures as low as 450 ˚C [14], the decrease in A_f is probably linked to the dissolution of a fraction of the particles, assisted by the fragmentation that takes place.

Thus, during heating in the weld thermal cycle, dissolution of the Mg_xSi is expected to occur, followed by some re-precipitation during cooling to room temperature. The dissolution of Mg_xSi particles is expected to have a strengthening influence by enriching the Mg and Si-content of the matrix, thus causing local improvements in strength by solid solution strengthening. The creation of fine submicron α-particles and the precipitation of the $Al_6(Fe,Mn)$ particles are similarly expected to cause local improvements in strength through blocking the dislocation movement (Orowan mechanism). It is also possible that the creation of fine particles (by precipitation or fragmentation) can also influence the grain and dislocation structures. These influences have been investigated using TEM.

7.1.2.c. Dislocation Structure and Precipitates

By investigating the microstructure of the different weld regions under the TEM, it was observed that there were a considerable number of dislocations within the TMAZ. Although it was not quantified, the dislocation density appeared to be more intense towards the AS of the TMAZ (Fig. 7.7-a) and in the WN (Fig. 7.7-c), showing tangled dislocations, compared to a relatively lower density towards the RS of the TMAZ (Fig. 7.7-e). The tangled dislocations were often associated with fragmented α-particles (Fig. 7.7-b), or submicron $Al_6(Fe,Mn)$ dispersoids (Fig. 7.7-d). Different weld regions were also found to show different levels of dispersoid area fraction and number density, where the micrographs of the RS grains showed a significantly lower number density of particles (Fig. 7.7-f), and dispersoid-free grain boundaries, compared to those in the WN (Fig. 7.3). This suggests a possible link between the presence of the dispersoids or particles and the dislocation density, although it is difficult to confirm this link based on the TEM observations. As previously mentioned, $Al_6(Fe,Mn)$ dispersoids were occasionally observed to precipitate along the GB in the WN (as in Fig. 7.3), although not as continuous as the optical micrograph might indicate.

The observed structures differ from the dislocation-free grains observed in the TMAZ by Murr *et al.* [19] in AA1100 weld or by Sato *et al.* [20] in AA1080 weld, which is consistent with DRX in the previous studies decreasing the dislocation density. This appears to depend on alloy composition, as well as the impurity level, which is reflected in the presence of

intermetallic particles and dispersoids. The dislocation structure observed in this study was similar to that observed previously in 5083 weld, which contained dispersoids (section 3.6.2, Fig. 3.30-b) [20]. It is possible that the existence of the submicron dispersoids and particles in the grains could increase the dislocation density by creating geometrically-necessary dislocations during deformation (section 2.5.1.b) [21]. Yet, the dislocation density could also increase during plastic deformation due to the formation of statistically-stored dislocations in the regions which did not experience DRX (section 2.5.1.a). Calorimetric measurements were performed to estimate the dislocation density in various regions, and their influence on strength, which will be described in Chapter 8.

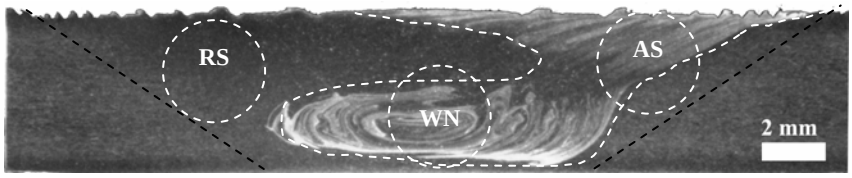

Advancing Side

(a)

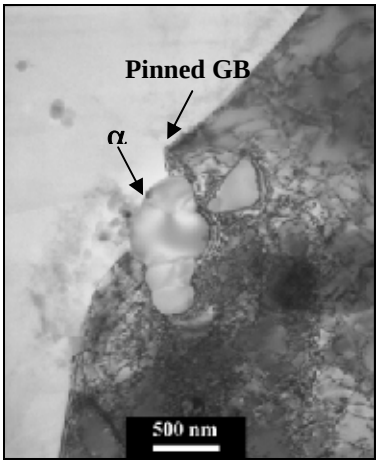

(b)

Weld Nugget

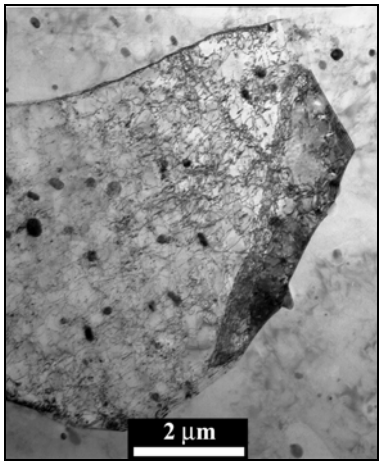

(c)

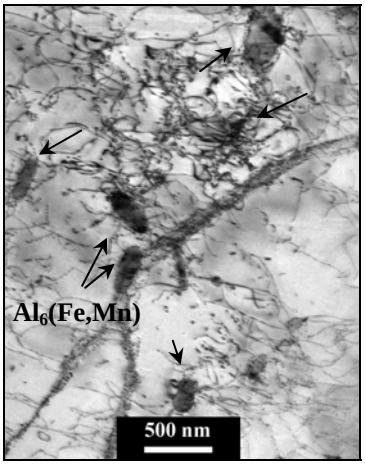

(d)

Retreating Side

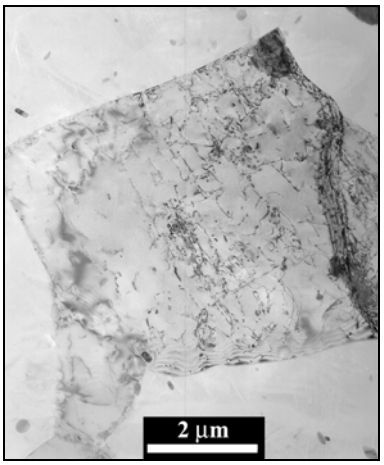

(e)

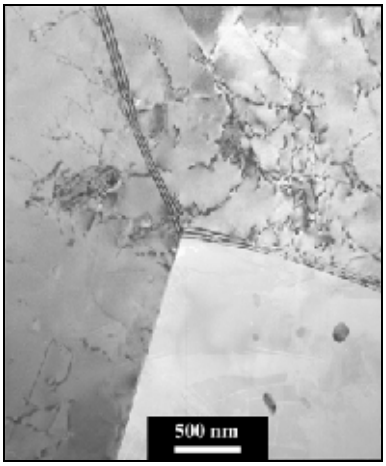

(f)

Fig. 7.7. Multi-beam TEM micrographs from different locations of the 5251-H34 weld (as shown using the dashed circles on the macrograph)

7.2. AA5754 (DC and CC)

Three 5754-O welds were characterised. The welds were performed using the same welding parameters and tool type as the 5251 weld. However, two welds (DC1 and CC1) were performed with the WD parallel to the RD. The third weld (CC2) was welded with the WD normal to the RD. The aim of this work was to investigate the influence of the sheet processing route and the weld orientation on the weld microstructure, especially the ORZ.

7.2.1. Weld Macrostructure

The etching trends in the three welds were generally weak compared to 5251 weld, even with increasing the etching time. The welds were further sensitised at 150 ˚C for 120 hours to try to precipitate grain boundary β phase from Mg in solution. However, the etching contrast did not improve, possibly due to precipitation of the β-phase only occurring significantly in alloys with higher Mg-content (>3 wt % Mg).

7.2.1.a. DC1 (WD || RD)

On etching the DC 5754 weld with the 10% H_3PO_4 solution, only the kissing-bond was revealed. However, on etching with Keller's reagent for 3 minutes, the TMAZ was selectively etched, showing a region (3 × 0.5 mm) with an etching contrast at the bottom of the WN, Fig. 7.8-(a,c), yet without showing the characteristic ORZ morphology. Sectioning along the WD showed the kissing bond. However, no repeated etching trends, as seen in Fig. 7.1-b for 5251 weld, were observed.

7.2.1.b. CC1 (WD || RD)

On etching the CC1 5754 weld, with either the 10% H_3PO_4 solution or Keller's reagent, a small region (3.5 × 0.7 mm) at the base of the WN showed an etching contrast with a translated series of rings (i.e. ORZ), some of which are concentric, Fig. 7.9-(a,c). However, the ORZ etching intensity was lower compared to the 5251 and 2024 welds. Excessive etching for 3 minutes was required to reveal the ORZ bands, which were elliptical in shape with varying widths (0.2 - 1.4 mm wide), i.e. similar in nature to the 5251 weld ORZ. Along the WD, a repeated etching contrast was also visible, occurring every 1 mm corresponding to the APR, Fig. 7.9-b.

7.2.1.c. CC2 (WD ⊥ RD)

Etching this weld showed a continuous region (4 × 0.7 mm) with an etching contrast observed at the bottom of the WN. However, the concentric ORZ rings were not observed, Fig. 7.10.

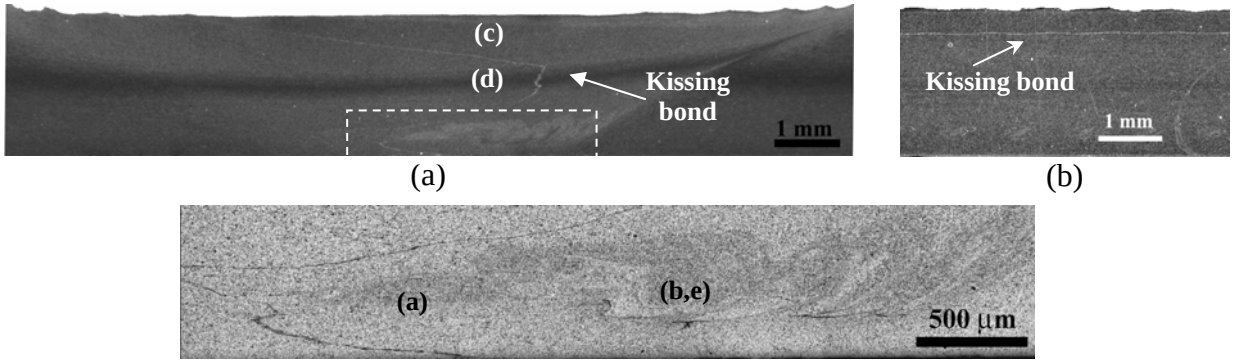

Fig. 7.8. Macrographs for the DC1 weld etched in Keller's reagent showing (a) the weld face, (b) longitudinal section along the weld centreline, (c) magnified view of the dashed box in (a)

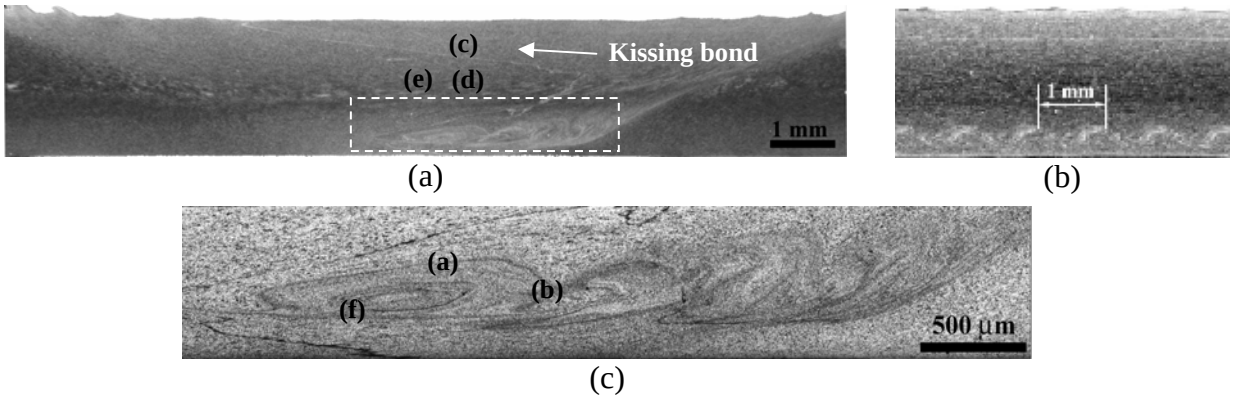

Fig. 7.9. Macrographs for the CC1 weld etched in Keller's reagent showing (a) the weld face, (b) longitudinal section along the weld centreline, (c) magnified view of the dashed box in (a)

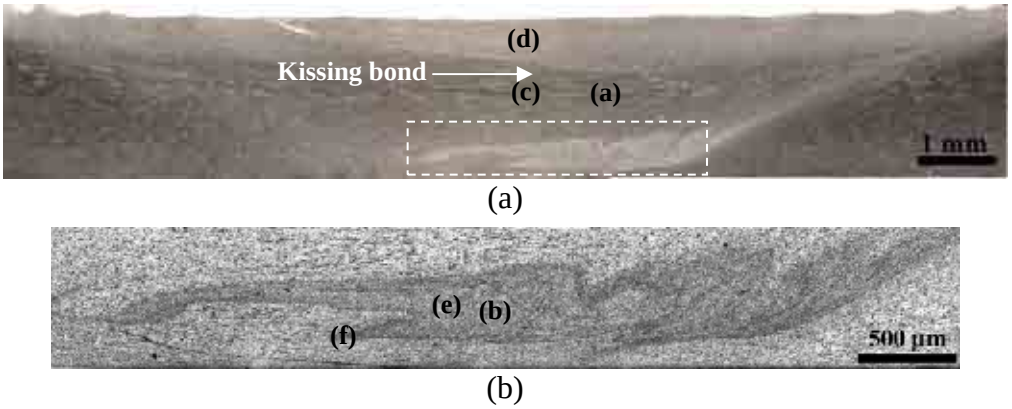

Fig. 7.10. Macrographs for the CC2 weld etched in Keller's reagent showing (a) the weld face, (b) magnified view of the dashed box in (a)

7.2.2. Weld Microstructure

7.2.2.a. Microstructural Development (Qualitative)

In the DC1 weld, the selectively etched region at the WN base (shown in Fig. 7.8-c) did not show the same banding observed in the 5251 weld. Instead, the WN base was found to contain a localised heterogeneity in the grain size, showing a mixture of fine and coarse grains regions, Fig.7.11-a, with a slightly finer average grain size within the preferentially-etched region, Fig. 7.11-b. In this region, the fine grains were within a range of 8-10 μm, alongside regions of coarser grains of sizes 12-15 μm, with an overall average size of 10.2±2.3 μm. Elsewhere in the weld, the grain size distribution was roughly homogeneous, with the size increasing from the weld top (the finest size of 6.8±1.7 μm, Fig. 7.11-c) to the mid-thickness (coarser, 8.7±2.5 μm Fig. 7.11-d). With respect to the particle distribution, this weld showed a weak or almost no banding of the Fe-rich particles or precipitates within the preferentially-etched region, as observed in 5251, Fig. 7.11-e. Generally, a more random distribution of the constituent Fe-rich particles was found within the TMAZ/WN.

In the CC1 weld, the dark ellipses in the etched region (Fig. 7.9-c) were found to correspond to localised variations of marginal significance in grain size, containing fine grains with an average size of ~6.5±1.6 μm, surrounded by coarser grains, with a size of ~7.8±2 μm, Fig. 7.12-a, hence the low significance given the standard deviation. However, in most cases, the selectively etched (dark) bands in the CC 5754 weld were only a few grains thick (i.e. ~20-50 μm, Fig. 7.12-b). It is important to note that the grain structure heterogeneity in these three welds was restricted to the preferentially-etched regions. Elsewhere in the welds, the grain structure was roughly homogeneous. Size variation trends similar to those in DC1 weld were observed, with the grain size slightly increasing from 6±2 μm at the top, Fig. 7.12-c, until the region above the ORZ (average size of 7.6±1.9 μm), Fig. 7.12-d, followed by the local heterogeneity in the ORZ. Similar to the 5251 weld, bands of relatively fine Fe-rich particles (< 1 μm) were observed throughout the WN/TMAZ, Fig. 7.12-e, with non-uniform spacings across the thickness and more disintegrated compared to the CC basemetal, , Fig. 7.12-g,. However, within the ORZ, the particle bands ceased to exist, Fig. 7.12-f.

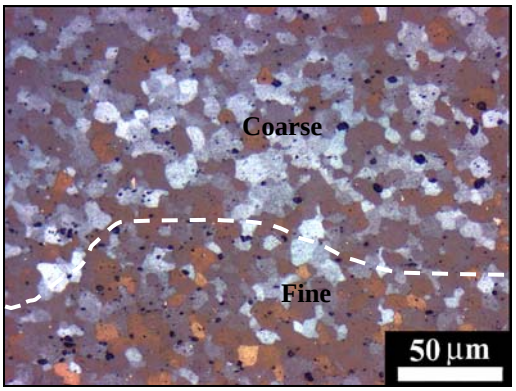

(a) The edge of the etched zone

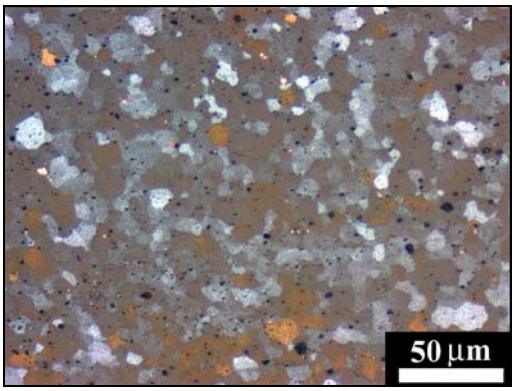

(b) The selectively etched zone

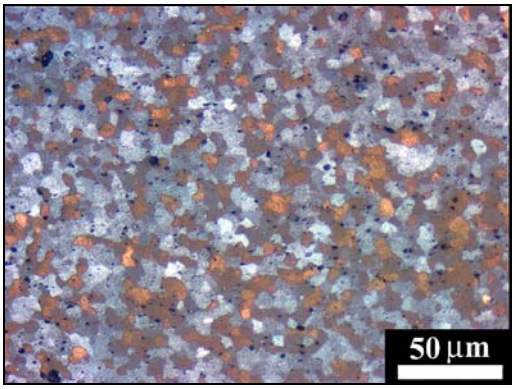

(c) Microstructure at the weld top

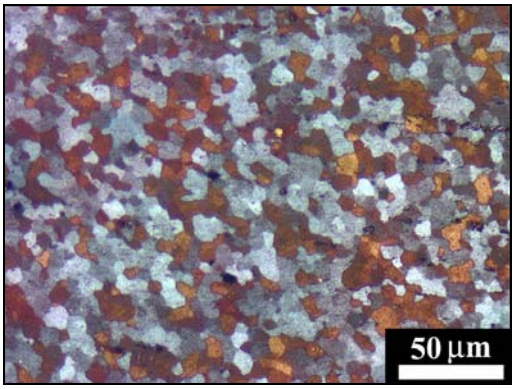

(d) Microstructure at mid-thickness

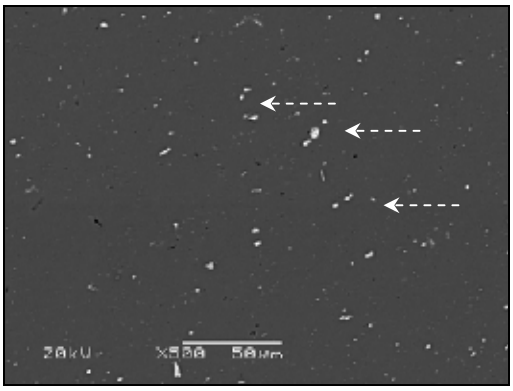

(e) Particle structure in the WN (weak banding trends arrowed)

Fig. 7.11. Micrographs for the 5754-O DC1 weld (positions according to Fig. 7.8)

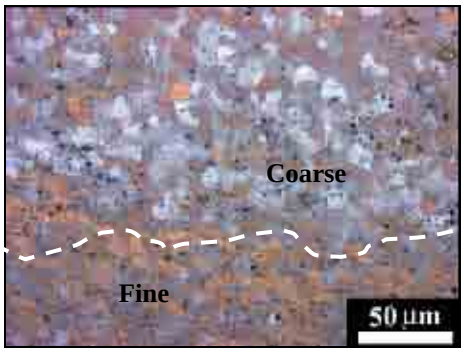

(a) Edge of the etched region

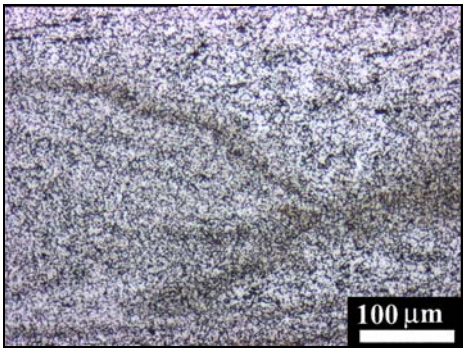

(b) The etched bands in the ORZ

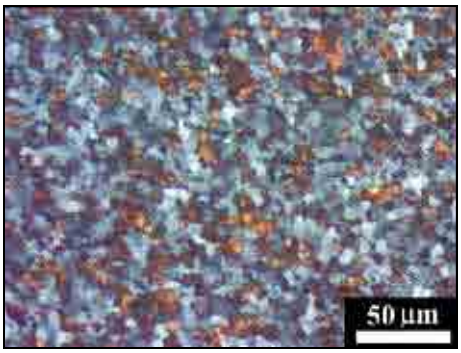

(c) Microstructure at the weld top

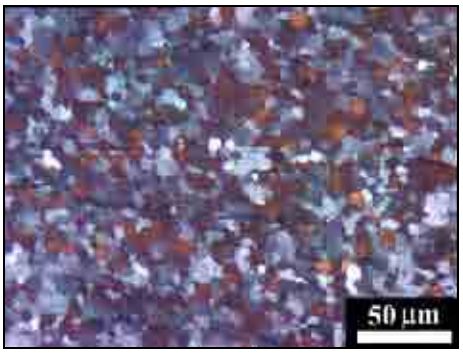

(d) Microstructure at mid-thickness

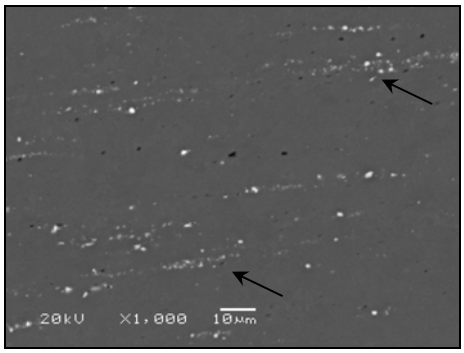

(e) Particle bands (arrowed) at mid-thickness

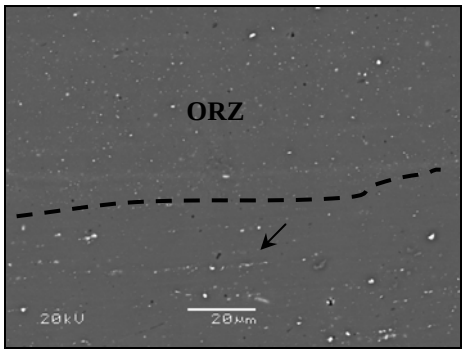

(f) Particle structure at the ORZ edge (bands arrowed outside the ORZ)

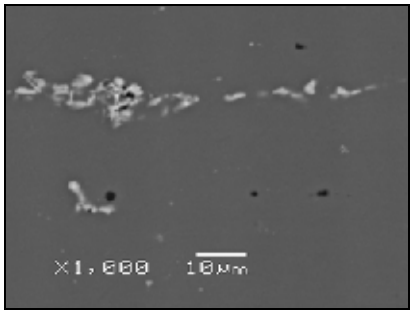

(g) Particle bands in the CC basemetal

Fig. 7.12. Micrographs for the 5754-O CC1 weld (positions according to Fig. 7.9)

Finally, in CC2 weld, intermetallic particle bands were observed throughout the TMAZ/WN with inter-particle bands spacing of ~20-50 μm, Fig. 7.13-a, except in the preferentially etched region which showed a weak banding of intermetallic particles Fig. 7.13-b. This range is almost half the range of the band spacing in the basemetal. Despite the existence of particle bands within the TMAZ (Fig. 7.13-a), the grain structure did not seem to be affected by particle banding as the grain structure was approximately uniform, Fig. 7.13-c. Similar to the other welds, the grain size only slightly increased from 7±1.5 μm the top of the weld (below the shoulder, Fig. 7.13-d), to 8.5±1.8 μm at mid-thickness. Similar sizes were observed within the etched zone, Fig. 7.13-e. However, at the edges of the zone, a localised microstructural heterogeneity was observed, showing coarser grains to exist outside the etched region, Fig. 7.13-f. The coarse regions contained grains within the range 10-12 μm, compared to 6-9 μm for the fine grains. It is important to note that the degree of particle banding was determined using the same criteria specified for the basemetal (section 4.3.4), which required the existence of semi-continuous particle bands. Although particle bands were observed in DC1 weld (Fig. 7.11-e), these were less extensive. In CC1 weld (Fig. 7.12-e) and CC2 weld (Fig. 7.13-a), the bands become more defined and more numerous throughout the TMAZ, except for the ORZ in CC1 weld, or the preferentially etched zone in CC2 weld, which contains sporadic limited banding.

The microstructural development across the WN/TMAZ and TMAZ/HAZ boundary regions was similar to that observed in 5251-O weld, with the grains starting to deform from the TMAZ/HAZ edge, Fig. 7.14-a. The plastic strains associated with stirring also caused the grains to elongate within the TMAZ (~50 μm long), prior to the occurrence of DRX in the TMAZ and WN, Fig. 7.14-b.

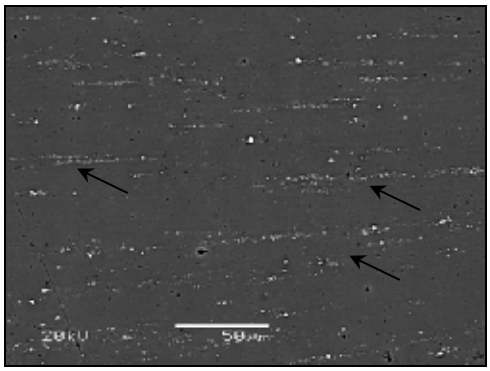

(a) Particle bands in the TMAZ/WN

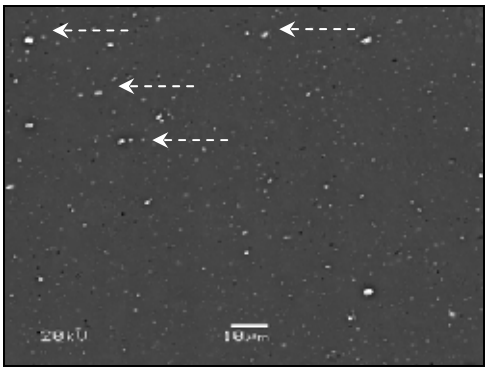

(b) Weak banding (arrowed) in the etched region

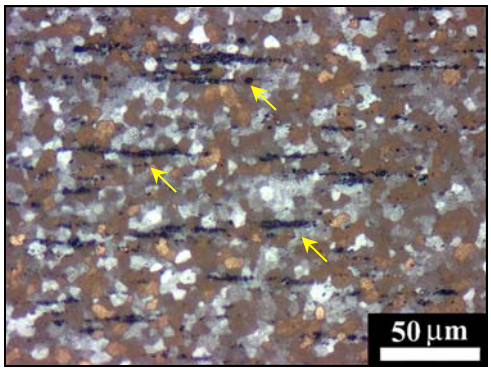

(c) grains at mid-thickness showing particle bands (arrowed), the band thickness is due to anodising

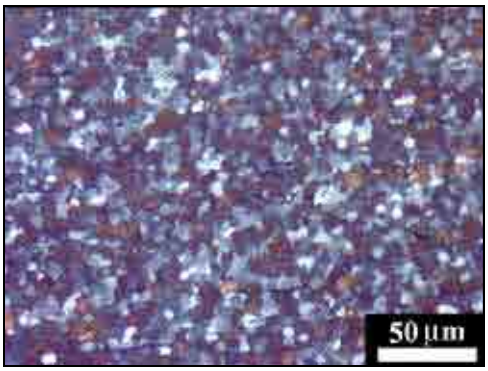

(d) grain structure under the tool shoulder

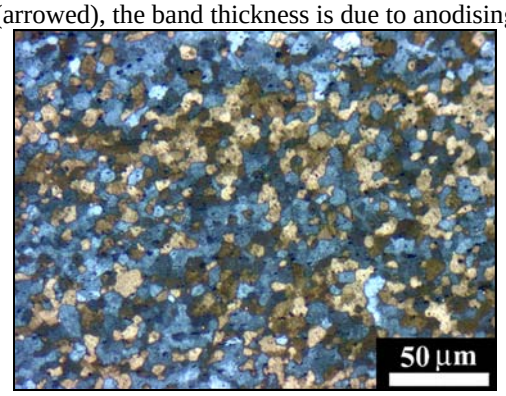

(e) grain structure in the etched region

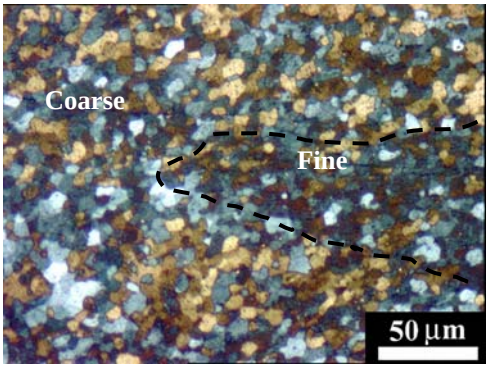

(f) at the periphery of the etched zone

Fig. 7.13. Micrographs for the 5754-O CC2 weld (positions according to Fig. 7.10)

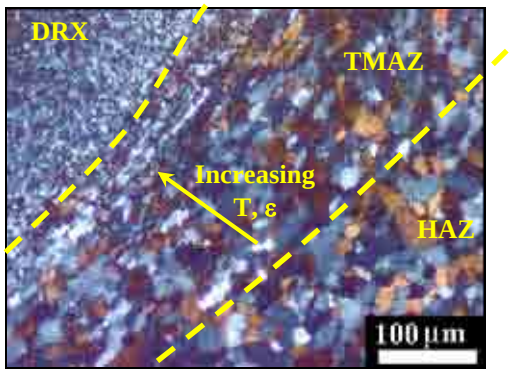

(a) The interface between the DRXed region and TMAZ at the top of the weld

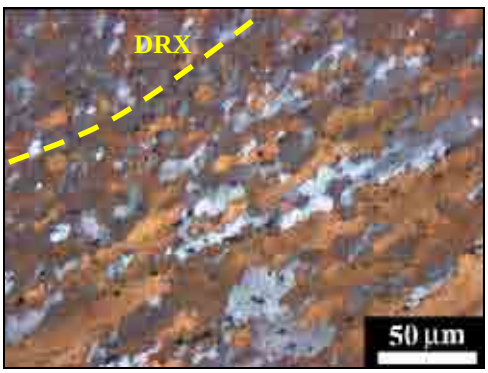

(b) Recrystallised grains at the edge of the deformed region of the TMAZ

Fig. 7.14. Dynamic recrystallisation in the WN of the CC1 5754-O welds

7.2.2.b. Quantitative Metallography

As qualitatively shown, the 5754-O welds showed a similar grain size variation, with the finest grain size occurring within the upper region of the weld, then increasing in size towards mid-thickness prior to any local heterogeneity observed within the preferentially-etched regions. The differences in average sizes in the different regions were very small (~2-4 μm difference). On average, the WN grain size in CC1 was 7.8 μm, compared to 8.7 μm in DC1, with a standard deviation in the measurements of ~ ±2 μm. Thus, as can be seen in Fig. 7.15, the WN grain size in the different conditions does not show any noticeable differences, which is as might be expected considering that the three welds were produced with exactly the same welding parameters. Moreover, the starting condition (grain or particle structure) did not have a noticeable influence on the WN grain size, although significant differences can be seen in the sizes beyond the WN in the TMAZ.

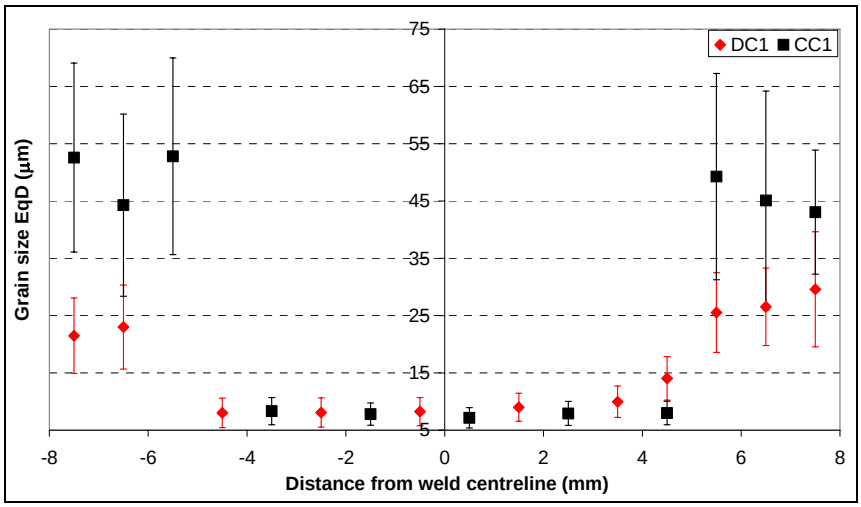

Fig. 7.15. Grain size trace at the mid-thickness of the DC1 and CC1 welds

Both the CC and DC basemetal conditions initially contained roughly similar sizes and amounts of the Fe-rich particles. However, due to the originally low Fe-rich particle content in the 5754 sheets, the variations in the particle characteristics in the weld, Table 7.1, are not as clear as in 5251 weld. In DC1, the particle size and A_f in the WN was roughly similar to the DC basemetal. However, in the DC1 etched zone at the bottom of the WN, the particle size, A_f and number density slightly decreased from the WN or basemetal levels, which is probably due to a refinement of a fraction of particles to below the microscopic resolution (0.5 μm),

thus decreasing the overall A_f, as previously observed in 5251 weld. Nonetheless, considering the standard deviation, this change cannot be considered significant.

Table 7.1. Characteristics of the Fe-rich intermetallic particles in the 5754-O welds

Region	Area Fraction	D_{Eq} (μm)	Density (#/mm^2)
DC-basemetal	0.012 ± 0.002	1.34 ± 0.0.75	6,657
DC1-WN*	0.013 ± 0.006	1.16 ± 0.84	8,100
DC1- bottom (etched zone)	0.008 ± 0.003	1.23 ± 0.76	4,837
CC-basemetal	0.0011± 0.005	1.15± 0.73	7,245
CC1-WN	0.005 ± 0.002	0.90 ± 0.41	7,357
CC1- ORZ	0.010 ± 0.004	0.99 ± 0.47	10,717
CC2-WN	0.011 ± 0.004	0.96 ± 0.39	13,592
CC2- bottom (etched zone)	0.010 ± 0.005	0.88 ± 0.29	13,945

* WN: above the ORZ or etched zones

In the CC1-WN and ORZ, a decrease was observed in the particle size and A_f compared to the CC basemetal, although this decrease is less significant in the ORZ (almost similar). It is expected that the stirring action could cause some disintegration of the particle bands in the CC weld (Fig. 7.12-e) compared to the CC basemetal (Fig. 7.12-g), which led to the decrease in the A_f in CC1-WN due to the fragmentation of the Fe-rich particles to sizes smaller than the quantified particle range (>0.5 μm). Generally, the CC1 WN was found to contain larger numbers of fine Fe-rich particles (0.5-1 μm) compared to the DC1 weld, Fig. 7.16. It is worth mentioning that the variation of the Mg_xSi particles was not considered due to the very low content in the basemetal.

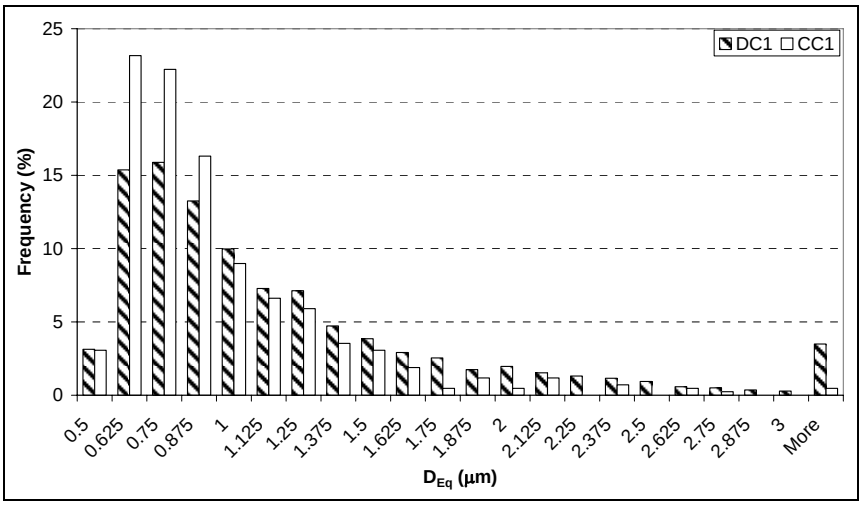

Fig. 7.16. Size distribution of the Fe-rich constituent particles in the DC1 and CC1 WN

Finally, in CC2, no significant changes in A_f were observed throughout the thickness, although the size slightly decreased. This is probably due to the different weld orientation, with the banded Fe-rich particles oriented normal to the WD in CC2, compared to parallel to the WD in CC1. As observed in previous marker studies (section 3.4.1), the presence of the markers parallel to the WD (copper foils or SiC composite thin rods) resulted in a significant disruption of the marker material, which is sheared and periodically deposited in a streaky fashion at the weld base due to the thread action [22]. However, for markers placed normal to the WD (copper foil), although deformation around the tool occurred, foil markers were found to remain continuous and intact in almost half the weld nugget towards the RS [23]. Accordingly, similar influences could happen to the banded particles in the basemetal. In CC1 (WD || RD), the particle bands in the basemetal (Fig. 7.12-g) are deformed by the shear field surrounding the tool, before depositing behind it. Shearing results in band disintegration (Fig. 7.12-e), which results in a decrease in the A_f and size. On the other hand, in CC2 WN (WD $\perp$ RD), the particle bands do not experience a massive disintegration, (Fig. 7.13-a). However, the notable elongation of the bands could also cause particle break-up, which decreases the particle size, but not markedly below the microscopic resolution. These trends are probably more significant in alloys with higher A_f than the present alloy.

7.2.2.c. Dislocation Structure and Precipitates

To explain the particle development in the CC1 weld, TEM specimens from the etched region in Fig. 7.9-c were examined, and showed that the grain boundary substructure shows two trends; the first is the existence of precipitate-clean grain boundaries with grains of low dislocation density, Fig. 7.17-a, and the second is the segregation of constituent particles (0.1-0.5 μm) along the boundaries, Fig. 7.17-(b,c). The majority of the particles were α-particles, which can be visually distinguished by their faceted morphology, as opposed to the more rounded or rod-like morphology of the $Al_6(Fe,Mn)$ dispersoids. Fine grain boundary $Al_6(Fe,Mn)$ precipitates were also infrequently observed (Fig. 7.17-d), with sizes < 200 nm.

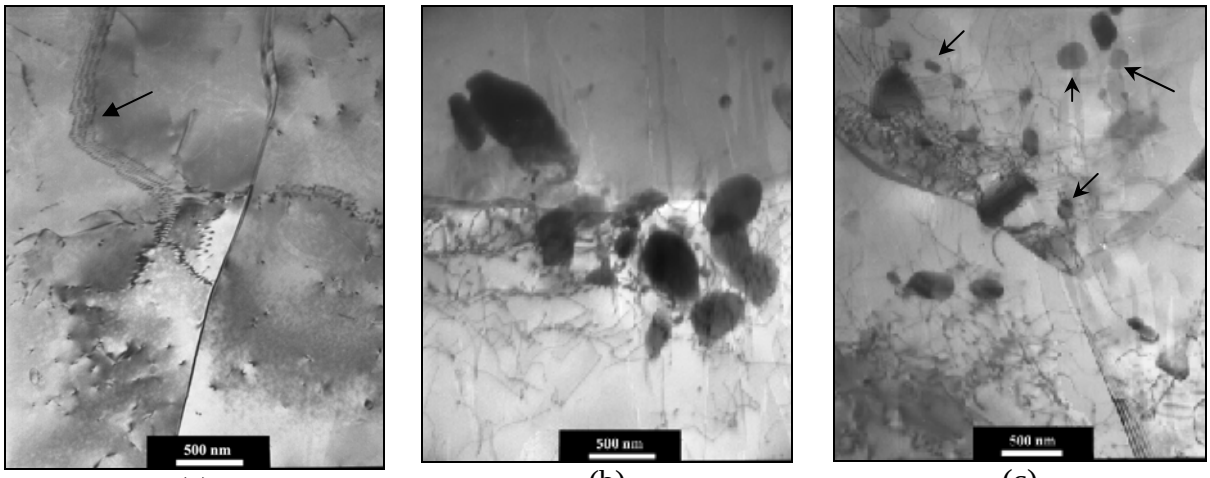

(a) (b) (c)

Fig. 7.17. Grain boundary structure in the 5754-O CC1 ORZ weld, showing (a) precipitate-clean low-dislocation grain boundary and a sub-grain boundary (arrowed), (b) the segregated Fe-rich particles along grain boundaries, (c) $Al_6(Fe,Mn)$ dispersoids (arrowed) and α-particles scattered near a grain boundary

7.3. AA5083

7.3.1. Weld Macrostructure

To reveal the weld macrostructure, etching of the polished weld face was performed using the 10% H_3PO_4 solution and Weck's reagent. Although a major part of the TMAZ/WN was preferentially etched, the onion rings structure was not be revealed by either reagent. As in 5251 weld, the TMAZ/WN boundary was also characterised by a sharp transition towards the AS, compared to a more diffuse transition towards the RS, Fig. 7.18-a. On the longitudinal section, a preferentially-etched profile was observed ~ 1 mm below the weld surface, Fig. 7.18-b. However, no repeating bands were observed along the WD.

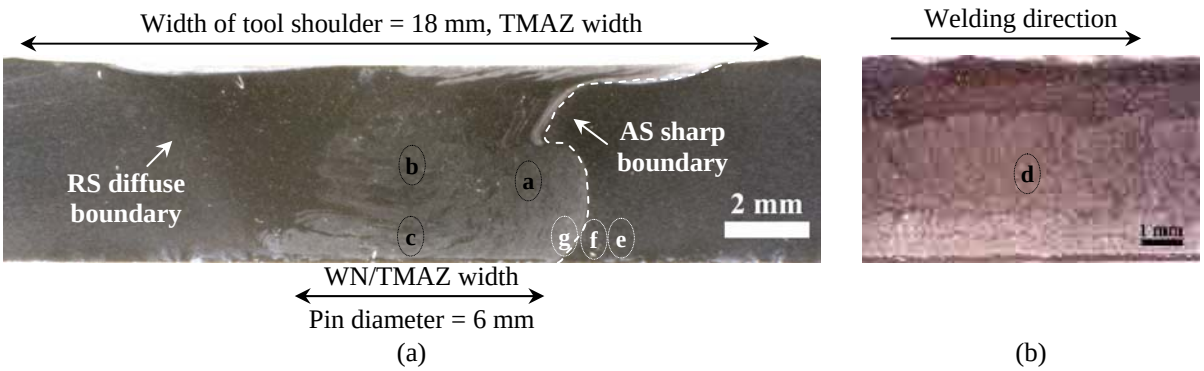

Fig. 7.18. Macrographs for the 5083-H116 weld etched in 10% H_3PO4 solution showing (a) full weld micrograph, (b) longitudinal section along the weld centreline

7.3.2. Weld Microstructure

The different welding parameters in this weld (compared to the previous welds) and also the low temperatures experienced (as shown in the thermal model discussed in chapter 6) should have a significant effect on the weld microstructure. Studying the microstructural developed in the TMAZ/WN should shed light on the nature of the ORZ structure and the influence of the welding and basemetal microstructural parameters.

7.3.2.a. Microstructural Development (Qualitative)

In the WN, the grain structure in the 5083 weld was composed of DRXed equiaxed grains, Fig. 7.19-a. No grain size banding, particle banding, or continuous grain boundary precipitation was observed within the WN throughout, Fig. 7.19-(b,c), not even on the longitudinal section (Fig. 7.19-d), and the microstructure was generally homogeneous.

In the TMAZ, three regions can be distinguished moving across the weld face from the HAZ to the WN. First, a region existed adjacent to the HAZ/TMAZ interface where a deformed partially-recrystallised structure was observed, Fig. 7.19-e, with the recrystallised fraction dependent on its position with respect to the shoulder. With the increase in temperature and strain in the TMAZ in the direction to the WN, a second region was observed with elongated grains (~100 μm long), where recrystallisation was observed to initiate forming grains of sizes similar to the WN grain size, Fig. 7.19-f. With further increase in the thermomechanical conditions at the TMAZ/WN boundary, the deformed grains develop into fully DRXed grains, Fig. 7.19-g. This development differs from that in the weldments of annealed sheets, which only show the latter two microstructure development regions within the TMAZ.

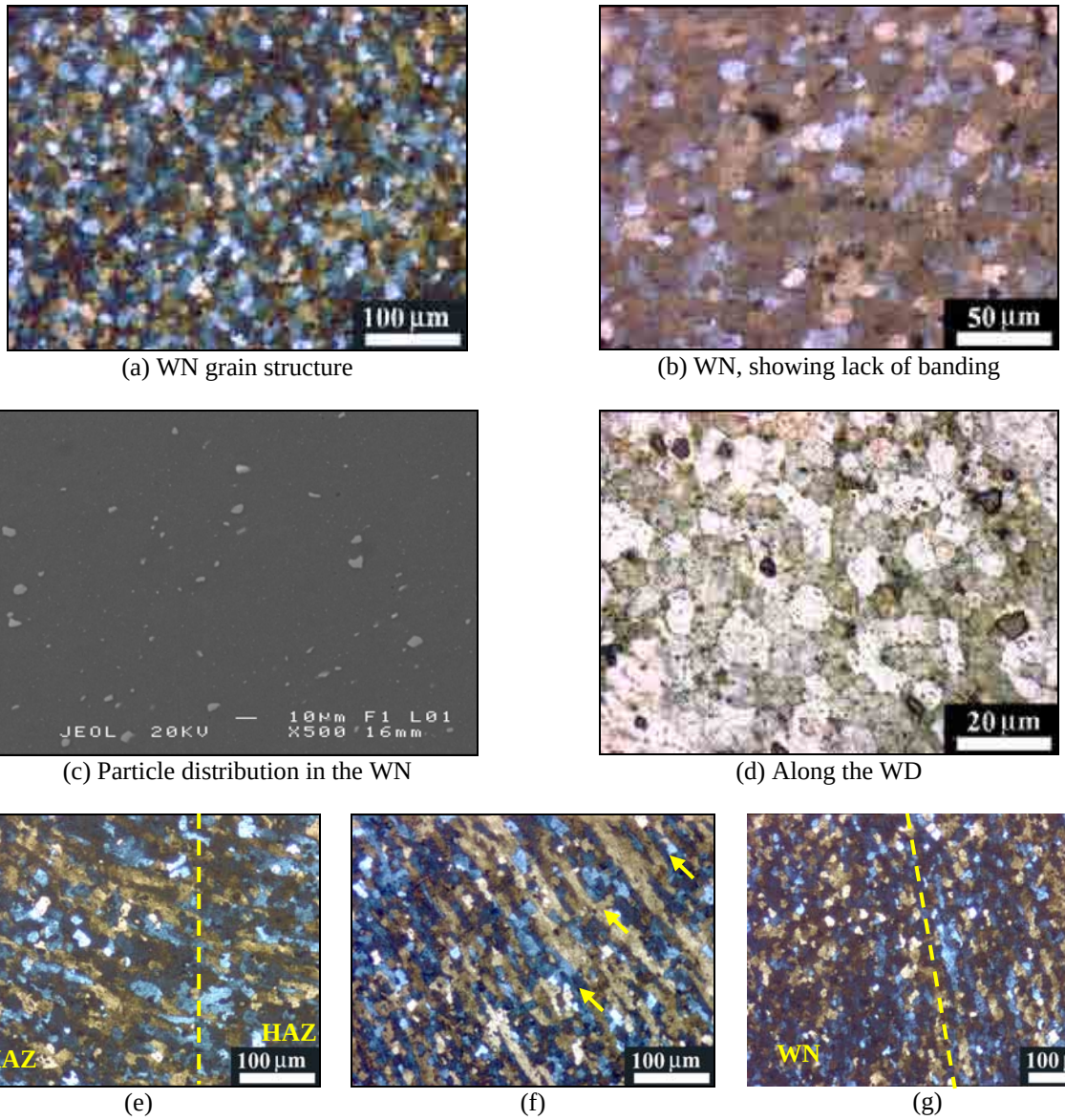

(a) WN grain structure

(b) WN, showing lack of banding

(c) Particle distribution in the WN

(d) Along the WD

(e) (f) (g)

The grain structure development across (e) the HAZ/TMAZ boundary, (f) TMAZ, and (g) TMAZ/WN boundary

Fig. 7.19. Microstructure in 5083-H116 weld (positions according to Fig. 7.18)

7.3.2.b. Quantitative Metallography

Within the WN (± 3 mm from the joint centreline), the grain size was roughly constant with an average grain size of ~14.9 ±4.6 μm, Fig. 7.20. This size is coarser than that observed in the rest of the welds in this study. As this weld was welded using a lower rotation speed than the other welds (and accordingly lower temperatures, as also predicted by the thermal model), it would be expected that a finer grain structure was generated. However, by considering the differences in the plastic strain rates associated with FSW at 500 rpm in 5251 and 5754 welds, compared to 200 rpm in 5083, such a difference can probably account for the difference in grain sizes. An increase in the strain rate during hot deformation would result in an increase in the Zener-Hollomon parameter, which is inversely proportional to the recrystallised grain size [21]. This correlation can explain the grain size variation between the different 5xxx-series welds, but it fails to explain the lack of banding in this weld. Towards the AS TMAZ/HAZ boundary, Fig. 7.18-(f,g), the grain size was relatively coarser, but with a larger standard deviation too, which is due to the existence of both deformed and recrystallised grains within this region.

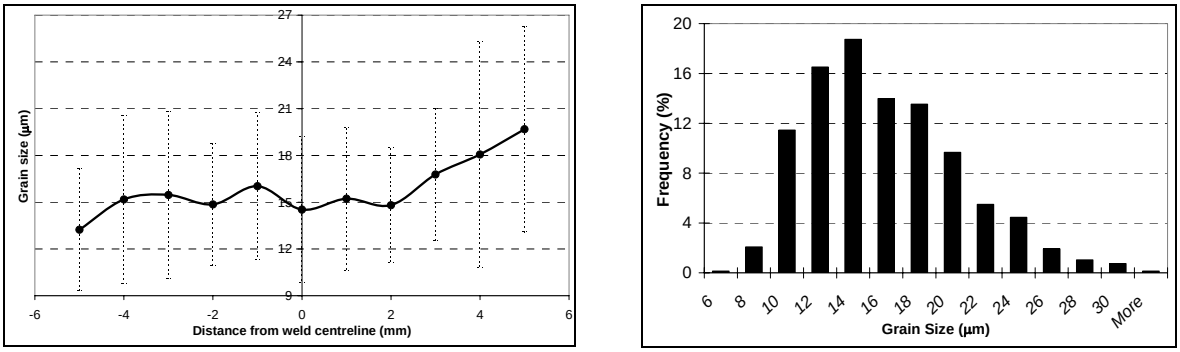

(a) (b)

Fig. 7.20. The grain structure characteristics in the 5083-H116 weld: (a) grain size at mid-thickness (TMAZ width ± 6 mm) (b) histogram for the grain size in the WN

Moreover, the area fraction of the Fe-rich particles in the weld decreased from 0.020 ± 0.002 in the basemetal to 0.016 ± 0.005 in the WN, which is expected to be due to the fragmentation of some of the particles to sizes below the microscope resolution limit (< 0.5 μm). This also resulted in a drop in the overall particle number density to 3,482 /mm^2 from 11,829 /mm^2 in the basemetal.

7.3.2.c. Dislocation Structure and Precipitates

Similar to the development observed in the 5251 weld, the microstructure of the different TMAZ regions was found to be composed of tangled dislocations and $Al_6(Fe,Mn)$ dispersoids, Fig. 7.21. This observed structure resembles the morphology normally observed in 5083 weld [20]. However, the dislocation density (qualitatively) appeared to be uniform throughout the TMAZ, compared to the non-uniform distribution observed in the 5251 weld. Different sizes of the $Al_6(Fe,Mn)$ dispersoids were observed, mostly ranging from ~50 to 500 nm, with no noticeable number density or area fraction variations within the TMAZ. The dispersoids, especially the finer ones (0.1-0.3 μm), were mostly present within the grains, while the coarser ones were found to be segregated along the grain boundaries, e.g. Fig. 7.21-(b,c). However, the majority of the investigated grain boundaries showed a lower number density of grain boundary precipitates than those in 5251 weld. Subgrains were observed within some parts of the weld, Fig. 7.21-d, which are occasionally observed in AA5xxx welds [24, 25], indicating subgrains which did not evolve to DRXed grains.

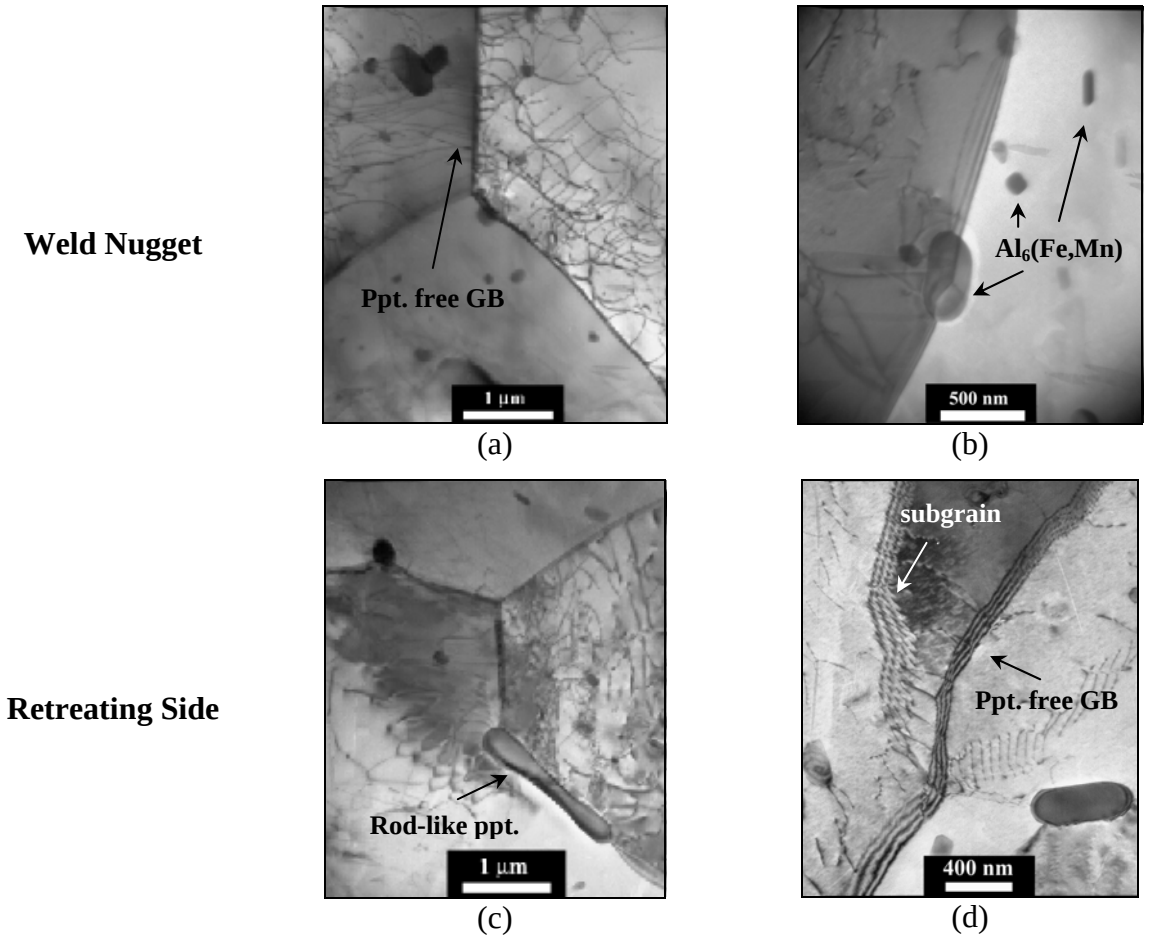

Fig. 7.21. TEM micrographs from different locations of the 5083-H116 weld

7.4. AA2024-T351

7.4.1. Weld Macrostructure

Etching was performed for polished 2024-T351 weld using Weck's reagent to reveal the weld macrostructure. Digital macrographs for the etched weld showed a preferentially-etched TMAZ, extending over a trapezoidal region whose bases are the shoulder and pin diameters. The ORZ was revealed by etching as an elliptical region showing bands of alternating contrast, centred across the sheet thickness at ~3 mm from either surfaces, and having the width of the tool pin (10 mm), Fig. 7.22-a. The thickness/spacing of the selectively-etched bands varied across the ORZ width, with the inter-band spacing decreasing from ~100 μm at the centre to ~50 μm near the edge. This morphology is similar to other welds reported in the literature [1-3], probably due to the use of a threaded tool. On etching the longitudinal section along the WD at the weld centreline, curved bands of alternating contrast (thick/dark and thin/light bands) were observed, with a uniform spacing of ~160 μm at the mid-thickness (which is equivalent to the APR of this weld). The light band thickness increases upwards or downwards through the thickness, at the expense of the dark band whose thickness decreases, Fig. 7.22-b.

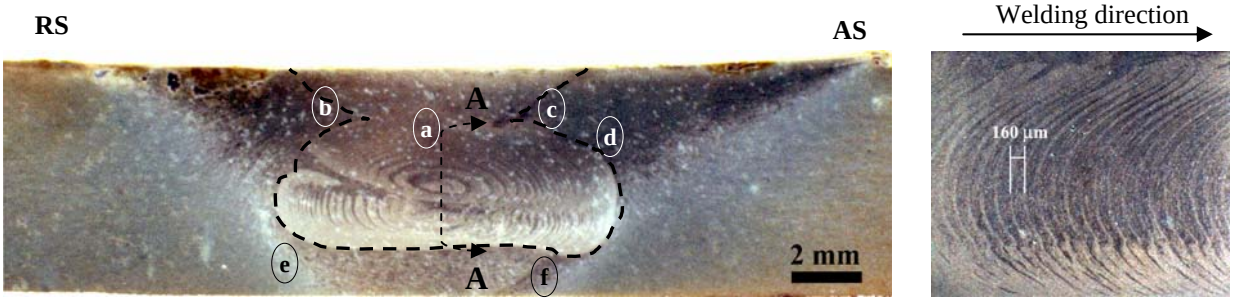

(a) (b)

Fig. 7.22. Macrograph of 2024-T351 weld etched in Weck's reagent showing: (a) the weld face (dashed lines refer to the DRX WN), (b) longitudinal A-A section along the weld centreline

7.4.2. Weld Microstructure

As a heat-treatable alloy, the microstructural development in 2024-T351 differs from the 5xxx-series welds due to the differences in the solutes and intermetallic particles present. These differences could impact the recrystallisation mechanism, as well as the stirring-assisted dissolution/precipitation/break-up processes.

7.4.2.a. Microstructural Development (Qualitative)

Microstructural characterisation of the weld revealed that DRX was restricted to the WN/ORZ, within the boundaries of the dashed region in Fig. 7.22-a, creating a fine grain structure with an average size of 3.4±1.3 μm. The grain structure was not uniform throughout, showing a size bimodality, combined with the formation of a grain boundary precipitate, Fig. 7.23-a, notably in the ORZ. Beyond the WN boundaries, the TMAZ was observed to contain highly elongated grains with lengths of up to ~1 mm and thicknesses of ~10 μm, Fig. 7.23-b. The TMAZ grains were deformed and rotated along the deformation flow fields surrounding the tool, Fig. 7.23-(c,d), showing a morphology which resembles that of dynamically recovered (DRVed) grains [21]. The transformation from DRV to DRX took place at the WN/TMAZ boundary as shown by the dashed line in Fig. 7.22-a, where the thickness of the excessively elongated grain boundaries further decreases prior to developing into DRXed grains within the stirred zone. Moreover, the grain structure seems to experience rotation, notably at the regions close to the shoulder, Fig. 7.23-(c,d), before eventually recrystallising inside the WN.

It is interesting to point out the differences between the HAZ/TMAZ boundary in the work-hardened 5xxx-series conditions (Hxx) welds compared to the 2024 weld. In the 5xxx-series welds, the HAZ/TMAZ boundary exhibits the fading out of the strain fields in the TMAZ, until the material becomes only thermally-affected in the HAZ, showing signs of the recrystallisation phenomenon. In 2024, the TMAZ (outside the WN) experiences DRV, whose extent is controlled by the amount of strain experienced with the TMAZ, as well as the temperature. The intensity of elongation in the TMAZ, and also the TMAZ width, decreases from the top of the weld (Fig. 7.23-(b,c,d)), which experiences large strains by the rotating shoulder, to the base of the weld (Fig. 7.23-(e,f)), where the amount of strain is minimum, and accordingly the grain morphology is relatively less affected.

In the ORZ, it was observed that the preferentially-etched bands corresponded microscopically to coarse grain bands (CGBs) and fine grains bands (FGBs), with the FGBs containing grains of size range 2-4 μm, while within the CGBs the grain size was 5-7 μm, Fig. 7.24-a. The CGBs were found to coincide with micron-sized Cu-rich particles, segregated within the bands, and fewer grain boundary precipitates, Fig. 7.24-(b,c). On the other hand, the FGBs were found to coincide with the existence of submicron discontinuous grain

boundary precipitates, Fig. 7.24-d. EDS point analyses for this GB-phase revealed that it is Cu-rich, with small amounts of Mg and Mn. It was observed that the relative thickness of the CGBs and FGBs was not spatially uniform along the weld face; towards the AS of the WN (Fig. 7.24-(b,f)), they were roughly similar in thickness. However, towards the RS of the WN, the CGB thickness decreased and the FGBs became dominant, Fig. 7.24-e.

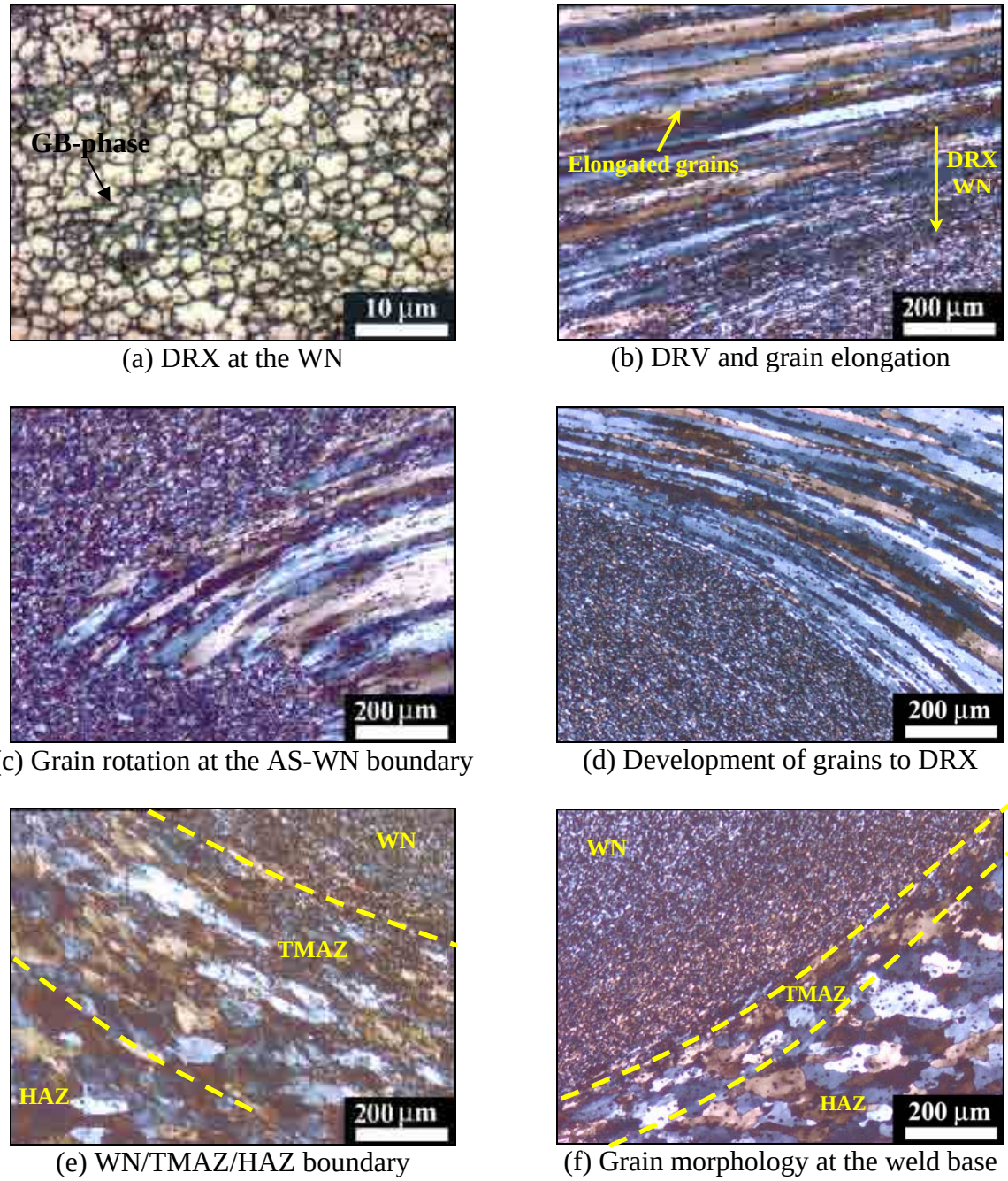

Fig. 7.23. Microstructure of the 2024-T351 weld (positions according to Fig. 7.22)

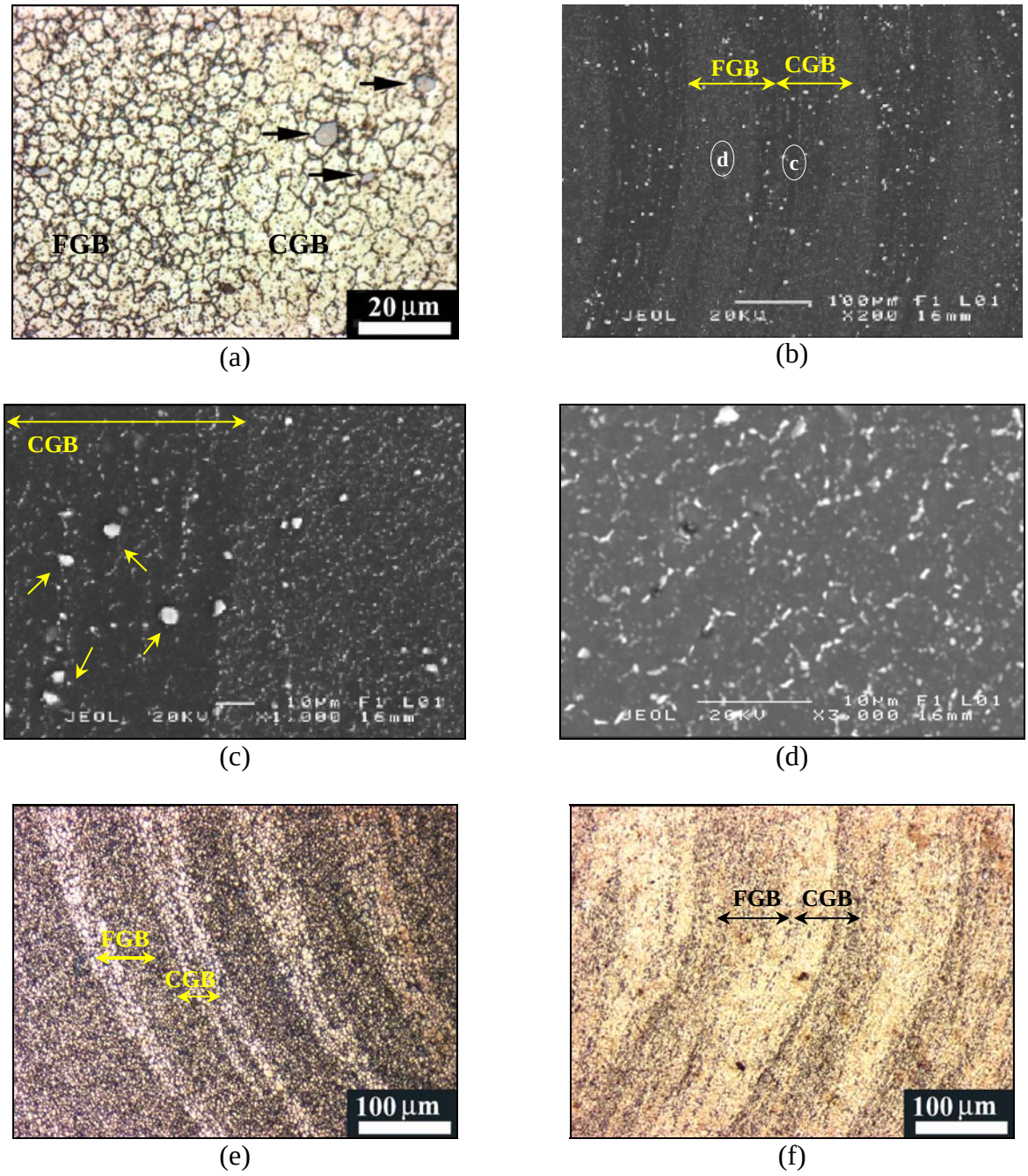

Fig. 7.24. ORZ microstructure in 2024-T351 weld, showing (a) the alternating fine and coarse grains bands, with GB precipitation and segregated coarse particles (arrowed), (b) SEM-BSE image of the ORZ bands across the WN, (c) fewer grain boundary precipitates and more coarse particles (arrowed) in the CGB, (d) more precipitates in the FGB, (e) the ORZ bands at the RS of the WN, showing the dominance of the FGBs, (f) the ORZ bands at the AS of the WN

The trend of preferentially-etching bands was also observed on the longitudinal section of the weld, showing a repeated trend of fine grained precipitate-rich bands, and bands of coarse grains with segregated coarse particles. The thickness of the FGBs was ~35 μm, compared to

~125 μm for the CGBs at the mid-thickness position, Fig. 7.25-a. Moreover, the coarse particles in the CGBs were observed to trail behind a trace of GB precipitates, causing refinement of the grains along this trail, Fig. 7.25-b, or in the grains surrounding the coarse particles. Thus, despite the differences with the 5xxx-series welds, the microstructural features in the ORZ resembled to some extent the features previously observed in 5251 weld, and to a lesser extent in 5754 CC1 weld.

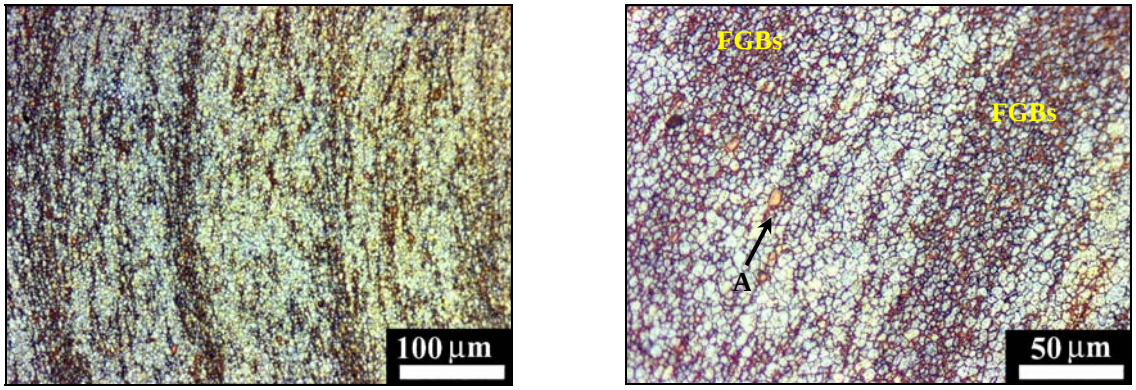

(a) (b)

Fig. 7.25. Microstructure along the longitudinal section for the 2024-T351 weld, showing (a) coarse and fine grained bands at mid-thickness repeated every APR, (b) the formation of fine grains along the precipitate trail above particle A, and in the precipitate containing FGBs

7.4.2.b. Quantitative Metallography

Within the WN, the DRXed grain size was roughly uniform in the image fields taken at the weld mid-thickness, Fig. 7.26. The histogram for the grain size distribution shows a variation in grain size between 1.5 and 8.5 μm, with the overall average of 3.4±1.3 μm.

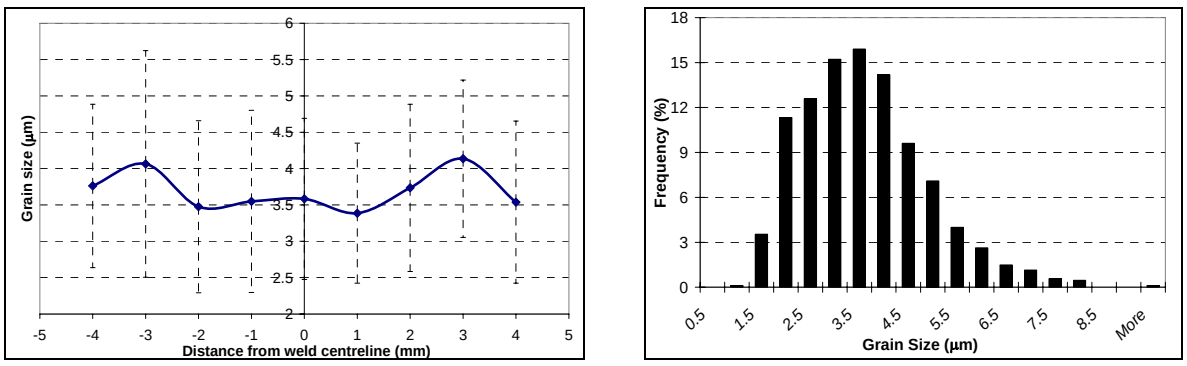

(a) (b)

Fig. 7.26. Grain structure in 2024-T341 weld (a) DRXed grain size across the WN, (b) histogram for grain size distribution in the WN

For the Cu-rich intermetallic particles, the particle structure within the weld showed three different trends. First, in the TMAZ (beyond the WN/ORZ), the A_f of the particles slightly increased to 0.020±0.002, compared to 0.017±0.006 in the basemetal (roughly similar considering the standard deviation), with the banded particles along the RD in the basemetal carried to the weld face by the stirring effect to become inclined in the direction of the flow field. The inter-particle band spacing was smaller than in the basemetal at the proximity of the WN (e.g. 68±18 μm in Fig. 7.27-a, compared to 95±35 μm in the basemetal, Fig. 7.27-d). Second, in the top 2 mm of the WN, the A_f increased to ~0.025±0.009 due to the existence of a heterogeneous re-distribution of particles, which causes them to appear segregated, or re-precipitate the hardening phases in the form of continuous GB precipitates, (Fig. 7.27-b). Third, on average within the ORZ, the A_f of the particles decreased to 0.012 ±0.005, with the A_f decreasing as a function of depth, reaching 0.007±0.001 at the bottom of the ORZ (Fig. 7.27-c). However, in most parts of the ORZ, coarse particle-rich and poor bands were observed as previously shown in Fig. 7.24-(a-d).

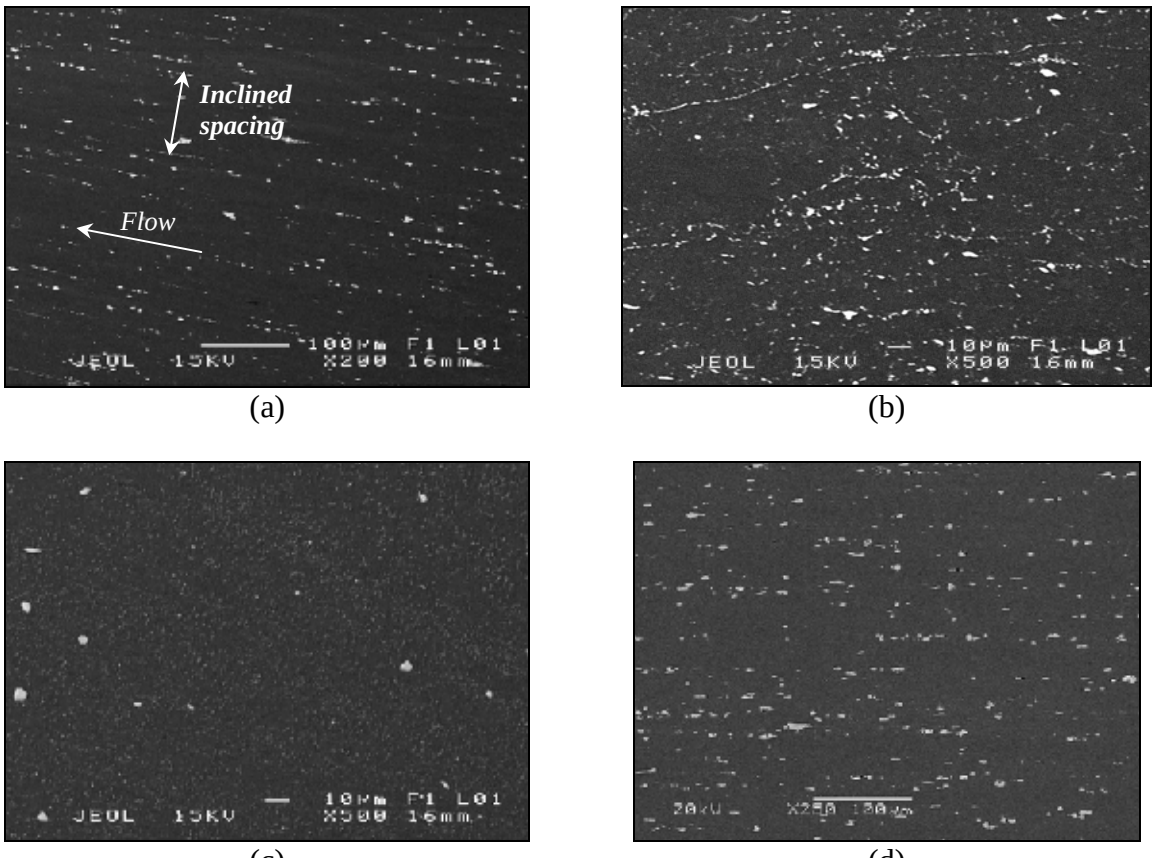

(a) (b)

(c) (d)

Fig. 7.27. Particle structure in 2024-T351 showing (a) particle bands in the TMAZ top (outside the WN/ORZ), (b) high density of particles and continuous GB precipitation at the WN top, (c) low density of coarse particles at the WN bottom, (d) basemetal particle structure (RD-ST plane)

7.5. Analysis of Results and Discussion

The in-depth microstructural characterisation of the 5xxx and 2xxx series welds has revealed several microstructural features that could be linked to the influence of the basemetal microstructure, one of which is the formation of the ORZ and its associated microstructural features (e.g. grain and particle size banding, and grain boundary precipitation). Moreover, the investigations also highlighted the microstructural differences between FSW of 2xxx and 5xxx series alloys. Although the present investigation attempted to decouple the effects of the basemetal and process-related parameters on the microstructural development, it was found that the relationship is quite complex, and would require a more systematic study. The correlations between these effects and the observed microstructural features will be discussed in this section.

7.5.1. Defining the Onion Rings Structure: Morphology and Parameters

As noted in the previous sections, the ORZ was found to occur in the 5251 and 2024 welds, showing a strong etching response with concentric irregular bands of varying contrast across the WN, and with a weaker etching response in the 5754-CC1 weld and localised to the WN base. In the 5754-DC, 5754-CC2 (WD $\perp$ RD), and the 5083 welds, preferentially-etched regions were also observed, covering parts of the WN with a dark profile, yet without showing the characteristic ORZ bands morphology. In the 5083 weld, the dark etch profile covered most of the WN, whereas a localised region at the WN base was selectively etched in the 5745-DC and CC2 welds. Bands of alternating contrast were also observed only, in the etched sections along the WD at the weld centreline, in the welds which showed an ORZ with the repeated etching trend occurring every APR.

On the microstructural scale, the banded preferential-etching response of the ORZ and also along the WD in the 5251 and 2024 welds was found to result from the existence of coarse and fine grained bands, with banded grain boundary precipitation and segregated particles segregation. These features were previously observed by other researchers as typical weld features [12, 26-28], but not directly associated with the ORZ. The occurrence of the microstructural heterogeneities was also found to be dependent on the welded material, where only grain size banding was observed in the ORZ of the 5754-CC1 weld. The presence of preferentially-etched non-banded regions in 5745-DC and CC2 was due to a heterogeneity in the grain size.

It was expected that since the 5251, and 5754-DC and CC1 welds were all welded using the same welding parameters (APR, tool type, and welding orientation), all of them would show the ORZ, with similar etching intensity and morphology. With the absence of this correlation, the APR was ruled out as a controlling parameter for the formation of the ORZ, which was indicated in a previous study [3]. However, it is apparent that the APR could be linked to the ORZ morphology, since it controls the spacing between the bands observed along the WD, and accordingly on the weld face. It is also possible that the tool profile could affect the ORZ morphology and location within the WN. This can be explained by noting the differences between the irregular bands morphology created by the MX-Triflute tool in the base of the 5251 and 5754-CC1 welds, and the concentric ellipses centred across the sheet thickness in the 2024 weld which was welded by a threaded tool. This correlates with previous flow visualisation studies investigating the effect of the tool profile using marker materials (e.g. [5, 6]), which showed that different tool geometries resulted in different flow fields.

In fact, the complexity of explaining the causes of the ORZ is attributed to the various parameters that were previously suggested to lead to its occurrence. However, the present microstructural investigations clarified that the ORZ should be defined as an etching phenomenon that results from the microstructural heterogeneities in the WN of some alloys, which lead to the selective etching effect of the bands with varying contrast. Since the selective etching effect was still observed in the absence of grain boundary precipitation in the 5754-CC1 weld, it is more likely that this effect was linked to a microstructural heterogeneity only in grain size. However, there is an important correlation between the presence of coarse particle bands in the ORZ, and the presence of banded particles in the 5251 and 2024 basemetals. It is possible that the microstructural development in the welds can be related to the basemetal microstructure. Since FSW is a solid-state welding process, it is possible that some of the basemetal microstructural features could be carried along to appear in the weld. The segregation of intermetallic particles, precipitates, and the banded grain structure in the ORZ imply a possible influence for the basemetal particle structure on these features.

7.5.2. Influence of the Basemetal Microstructure on the "Onion Rings" Formation

The presence of coarse particles bands within the ORZ bands in the welds of 5251 (e.g. Fig. 7.2-e), 5754-CC1 (Fig. 7.12-e), and 2024 (Fig. 7.24-b) was linked to the presence of particle bands in the basemetal. As previously shown in chapter 5, the basemetal sheets were prepared

with different processing routes, which has resulted in microstructural features specific to the processing routes (e.g. banding of intermetallic particles in the 5xxx CC sheets, and in the 2024 sheet). A summary of the particle characteristics in the investigated alloys is shown in Table 7.2 and Fig. 7.28. These indicate that, in 2024 and 5251, which are the alloys whose welds showed a strong ORZ etching response with clearly distinguishable microstructural features, the Cu-containing particles (S, θ and $Al_{15}(CuFeMn)_3Si_2$) or the Fe/Mn-containing constituent particles (respectively) formed bands of faceted particle stringers along the RD. However in DC 5754 and 5083, which did not show a clear ORZ, a more random distribution of the constituent particles was observed. A localised ORZ with a weak etching intensity was observed in CC1 5754, which also showed banded particles in the basemetal. However, on changing the orientation to CC2 (WD $\perp$ RD), a continuous etched band was observed. This would suggest that there is a relationship between the existence of banded intermetallic particles in the basemetal and the formation of the ORZ. As previously discussed in chapters 2 and 5, the banding of constituent particles is an indication of processing by continuous casting, and it also indicates a higher degree of microstructural heterogeneity that was created during casting due to the high cooling rates, compared to direct chill casting.

Table 7.2. Intermetallic particles in the investigated alloys and their properties

Alloy	Particles	Type	Dissolution range* [15]	Area Fraction‡	D_{avg} (μm)
5251	α -Al(Fe,Mn)Si	Constituent	635-700 ˚C	0.024 ± 0.004	1.1 ± 0.9
	Mg_xSi		449-595 ˚C	0.0055 ± 0.0018	0.9 ± 0.6
	$Al_6(Fe,Mn)$	Dispersoids	657-710 ˚C	--	0.1-0.5
5754 DC	α -Al(Fe,Mn)Si	Constituent	635-700 ˚C	0.011 ± 0.005	1.34 ± 0.75
	$Al_x(Fe,Mn)$		635-700 ˚C		
	Mg_xSi		449-595 ˚C	0.0008 ± 0.0004	--
	$Al_6(Fe,Mn)$	Dispersoids	657-710 ˚C	--	--
5754 CC	α -Al(Fe,Mn)Si	Constituent	635-700 ˚C	0.012 ± 0.002	1.1 ± 0.7
	$Al_x(Fe,Mn)$		635-700 ˚C		
	Mg_xSi		449-595 ˚C	0.0023 ± 0.0011	--
	$Al_6(Fe,Mn)$	Dispersoids	657-710 ˚C	--	--
5083	α -Al(Fe,Mn)Si	Constituent	635-700 ˚C	0.02 ± 0.002	1.2 ± 1.1
	$Al_x(Fe,Mn)$		635-700 ˚C		
	Mg_xSi		449-595 ˚C	0.0015 ± 0.0001	--
	$Al_6(Fe,Mn)$	Dispersoids	657-710 ˚C	--	--
2024	S-Al_2CuMg	Equilibrium phases	507-518 ˚C	0.017 ± 0.006	2.1 ± 1.7
	θ-Al_2Cu		515-547 ˚C		
	$Al_{15}(CuFeMn)_3Si_2$	Constituent	635-700 ˚C		
	Mg_xSi		449-595 ˚C	0.0004 ± 0.0006	--
	GP-Zones	Hardening	150-250 ˚C	--	--

* Temperature ranges are approximate as they depend on the alloy/particle composition and heating rate.
‡ Particles of close contrast (e.g. Cu or Fe-containing) were grouped together during image analysis.

By relating the constituent particles type and characteristics in 5251, CC 5754 and 2024 to the formation of the ORZ, it is possible to point out that the banded particle type did not appear to affect the formation of the ORZ, as both the banded Fe-rich constituent particles in the 5xxx series alloys and the Cu-rich constituent and equilibrium particles in 2024 led to the formation of an ORZ. However, it should be noted that the lower dissolution temperatures of the Cu-rich particles in 2xxx series alloys (Table 7.2) would mean that their development would be dependent upon the heat input. This was highlighted in the work of Biallas *et al.* [29], which showed that the ORZ morphology tended to vanish with the increase in rotation speed and feed rate in 2024-T3 welds, despite maintaining a constant APR.

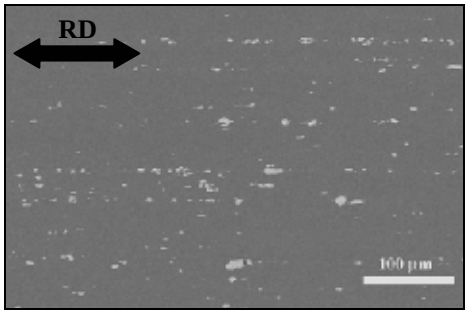

(a) 2024-T351 (Cu-rich particles A_f = 0.017, ORZ ✓)

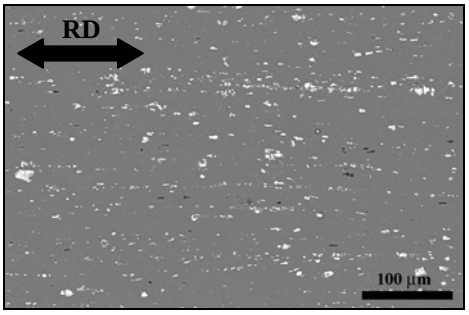

(b) 5251-H34 (Fe-rich particles A_f = 0.024, ORZ ✓)

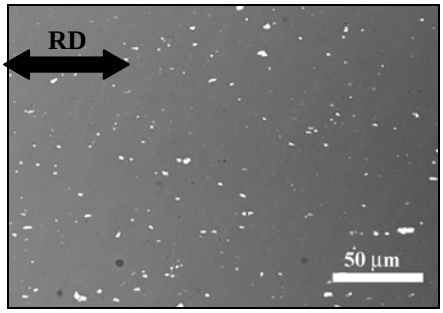

(c) DC 5754-O (Fe-rich particles A_f = 0.011, ORZ ×)

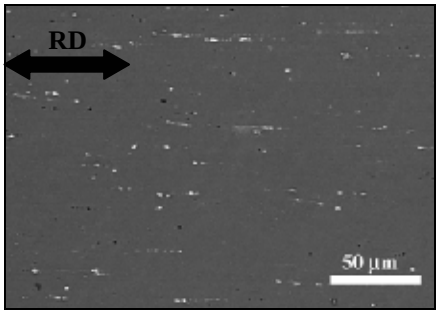

(d) CC 5754-O (Fe-rich particles A_f = 0.012, ORZ ✓)

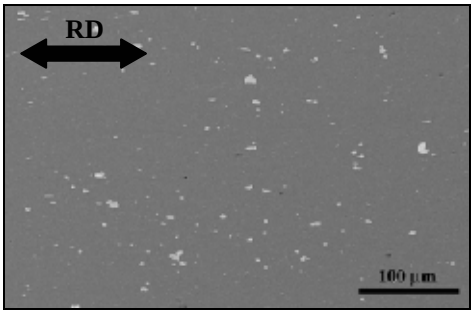

(e) 5083-H116 (Fe-rich particles A_f = 0.02, ORZ ×)

Fig. 7.28. Constituent particle structures in the investigated alloys (ST-RD plane)

It was also found that the area fraction of the banded particles affected the etching intensity, as the higher A_f of Fe-rich constituent particles in 5251 led to a stronger etching response, compared to CC 5754, which contained approximately half the particle content of 5251. Nonetheless, it is important to indicate that the A_f in itself does not control the formation of the ORZ as roughly similar amounts of the Fe-rich particles in 5251 (banded) and 5083 (more random) led to the formation of the ORZ in the former only, while CC 5754 formed an ORZ with a lower intermetallic particle A_f. Another factor that was investigated was the influence of the inter-particle band spacing on the ORZ. However, it was found that there was no direct relation between the banding in the basemetal and that in the weld, as in the weld no single spacing was observed with variation across the weld face. In 2024, the band spacing was ~2.5 times larger than that in 5251 ($95 \pm 35\ \mu m$ in 2024, compared to $38 \pm 22\ \mu m$ in 5251), and slightly larger than CC 5754 ($75 \pm 25\ \mu m$). However, all of them showed ORZs.

Thus, this study clarified the possible role of the intermetallic particles characteristics on the ORZ formation, as summarised in Table 7.3. These characteristics are a direct outcome of the alloy's processing history, and have to be thought about when considering FSW of a new alloy. Among these factors, it was found that the formation of the ORZ is directly correlated with the presence of particle banding in the basemetal.

Table 7.3. Summary of the intermetallic particle characteristics associated with the ORZ and their influences within the range of process parameters studied

Particle Factor	Influence	Effect & Evidence
Particles Banding	Evident	• Affects the formation of the ORZ. • The presence of banding in the basemetals of 5251, 5754-CC, and 2024 resulted in the formation of the ORZ.
Particle Content (A_f)	Evident	• Higher A_f of banded particles in 5251 resulted in more pronounced ORZ. • Does not affect the formation of the ORZ; both 5083 and 2024 had roughly similar A_f, but ORZ only formed in 2024.
Banded Particle Type	None	• Either Fe/Mn-rich or Cu-rich particles led to the ORZ formation.
Inter-particle Band Spacing	None	• No correlation was found with the ORZ bands.

The etching intensity, which is a qualitative indication of the extent of microstructural heterogeneity in grain size, is affected by the A_f of the constituent particles or the equilibrium phases in the 5xxx and 2xxx series alloys. The type of the banded particles (constituent Fe/Mn-rich in 5xxx or Cu-rich particles in 2xxx) was not found to affect the formation of the

ORZ, as long as they are banded along the RD in the basemetal, and provided that the heat input does not lead to their full dissolution in 2xxx series alloys. Other particle characteristics (e.g. particle size, inter-particle banding spacing, and number density) were not found to affect the ORZ formation.

7.5.3. Influence of the Process Parameters on the "Onion Rings" Formation

There are three process-related parameters that were previously associated with the formation of the ORZ, which are: the tool type, APR, and the welding orientation. It is clear that there is an influence of the tool type on the ORZ morphology. This can be seen in the 5251 weld welded using MX-Triflute, which resulted in randomly-oriented bands on the lower half of the weld face, compared to the centred concentric ellipses in 2024 weld welded using a threaded tool. This factor, along with the influence of the intermittent material deposition every APR associated with FSW, has been previously suggested to be the cause for the formation of the ORZ [3, 6]. It is widely accepted that an intermittent material deposition occurs during FSW as verified by several studies [2, 3, 6, 22, 23]. However, the presence of microstructural heterogeneities to reveal this motion upon etching is what actually causes the ORZ pattern to be observed. As previously noted, welds having the same APR values do not necessarily have similar ORZ morphologies, with the rings pattern vanishing with the increase in the rotation/travel speeds [29]. This can be explained since the increase in rotation speed would also result in an increase in temperature, which could also cause full dissolution, especially in the less thermally-stable Cu-rich particles, or severe particle break-up. This results in changing the etching profile of the ORZ. From the results of the present work, it can be concluded that the material flow is certainly not the only reason for the formation of the ORZ as defined before. Whilst there is intermittent material deposition behind the tool during FSW, in the absence of any microstructural heterogeneity, it is impossible to reveal the ORZ morphology by etching. The welding orientation also resulted in the formation of a continuous etch band in CC2 5754 weld, which was attributed to a microstructural heterogeneity in grain size as in DC1 weld. Within the WN, the inter-particle band spacing within the weld decreased to half the range observed in the basemetal. A brief summary of the factors associated with ORZ is given in Table 7.4.

Table 7.4. Summary of the process-related factors associated with the ORZ and their influences within the range of process parameters studied

Factor	Influence as found by the present study
Process Parameters (e.g. APR)	Affects the repeated ORZ trend along the WD
FSW Tool type	Affects the ORZ morphology
Welding Orientation (WD / RD)	ORZ forms when welded WD || RD only

7.5.4. Controlling the Formation of the ORZ and the Weld Microstructure

For some time, the ORZ has been considered as an interesting microstructural phenomenon. However, with the results of the present investigation, highlighting the microstructural heterogeneities associated with the ORZ, it is important to consider the possible impact of these features on the structural integrity of the welds. For instance, the occasional presence of grain boundary precipitation or segregation of constituent particles could be a concern for the corrosion properties of the weld since they act as preferential sites for corrosion initiation [30]. Moreover, the presence of grain size bimodality in the ORZ bands, alongside the segregation of intermetallic particles, could be another concern for the fracture toughness and fatigue properties since they initiate crack growth paths [12, 27, 28, 31].

In 5xxx-series alloys, the elimination of the microstructural heterogeneities associated with FSW would require the utilisation of DC-cast alloys, or CC alloys with low constituent particles fraction (A_f ~<0.01). In the DC-cast alloys, the slow cooling rates during casting leads to the formation of a homogeneous non-banded particle structure, while the subsequent homogenisation removes the solute atoms in solution (e.g. Mn) by precipitating them in the form of dispersoids, or by transforming them to other types as explained in section 2.1.2. In the CC alloys, constituent particles banding cannot normally be avoided due to the nature of the process. However, by the reduction of the constituent particle content, the extent of microstructural heterogeneity can be reduced, as observed in the 5754-CC weld.

There is an additional parameter that can be used to control the ORZ, which is the APR. Although this study did not attempt to systematically investigate the influence of the APR on the ORZ, there are some conclusions that can be drawn regarding its influence. In general, an increase in the APR would result in an increase in the thickness of the bands which form behind the tool along the WD (e.g. Fig. 7.22-b). Thus, to minimise the bands observed on the weld face, it is necessary to use relatively high APR values (>1 mm/min). This can be shown

in Fig. 7.29, which predicts the possible influence of the APR and the A_f of banded constituent particles on the intensity of the ORZ in 5xxx-series alloys. For a given APR, the increase in the A_f of banded constituent particles would result in more intense ORZ, whilst the increase in the APR for a given A_f would result in a less intense ORZ.

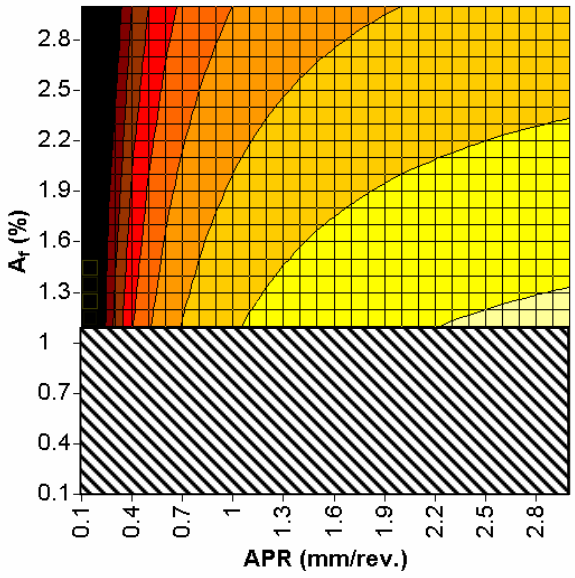

Fig. 7.29. Suggested qualitative relationship for the influence of the banded particle fraction and the APR on the ORZ intensity in 5xxx-series alloys (the darker regions indicate higher ORZ intensity (the hatched region is speculative).

It is important to mention that this relationship is only hypothetical, especially that the number of characterised welds was not sufficient to predict the full image, which could raise some concerns. First, there is no quantitative definition of the ORZ intensity, but possibly qualitative, based on the extent of microstructural heterogeneity and the etching response. Moreover, the region with $A_f < 1$ % has not been investigated. It is also possible that the tool type could be influential, noting the lack of uniformity in the bands morphology created by the MX-Triflute tool (Fig. 7.1-b), compared to the uniform bands created by a threaded tool (Fig. 7.22-b). Finally, applying the above relationship to 2xxx-series alloys could be relatively difficult, since the varying the APR by varying the rotation speed would result in a change in the heat input, which could affect the extent of precipitation or break-up of particles.

7.5.5. Microstructural Differences between 2xxx and 5xxx series alloys

The present investigation showed that there are significant microstructural differences between the weld microstructural zones (HAZ, TMAZ, and WN) of 2xxx and 5xxx-series alloys, as summarised in Table 7.5.

Table 7.5. Summary of the microstructural differences between 2xxx and 5xxx welds

Region		AA2xxx	AA5xxx
WN	Grains	• Dynamic recrystallisation. • Grain size banding within the ORZ.	• Dynamic recrystallisation. • Grain size banding within the ORZ in the welds of CC alloys only.
	Particles	• Formation of Cu-rich grain boundary precipitates coinciding with the ORZ fine grains. • Segregation of coarse Cu-rich particles within the ORZ coarse grain bands.	• Stirring-assisted dissolution of the Mg_xSi particles. • In CC alloys welds, formation of Mn-rich grain boundary precipitates coinciding with the ORZ fine grains, and coarse Fe/Mn-rich particles segregated within the ORZ coarse grain bands. • In DC alloys welds, formation of a random distribution of the Fe/Mn-rich particles, with no grain boundary precipitates.
TMAZ**	Grains	• Dynamic recovery, observed in the form of elongated grains.	• Dynamic recrystallisation.
	Particles	• Partial/full dissolution of the GP-zones/hardening phases occur*	• Partial/full dissolution of the Mg_xSi particles.
HAZ	Grains	• Almost no change in grain structure due to the originally coarse grains.	• Recovery and recrystallisation occur in the work-hardened conditions*.
	Particles	• Partial/full dissolution of the GP-zones/hardening phases occur*	• Partial/full dissolution of the less thermally-stable Mg_xSi phase. No change occurs in the Fe/Mn-rich particles.

*: Depending on the temperatures experienced.
**: TMAZ outside the WN

As clear from the above comparison, the microstructural development in 5xxx-series welds is dependent on the starting condition, specifically with the respect to the development of the particle structure. For example, the distribution of the $Al_6(Fe,Mn)$ dispersoids was roughly homogenous and mostly within the grains in the 5083 weld, whereas in the 5251 weld a higher number density of $Al_6(Fe,Mn)$ precipitates was observed towards the AS and in the WN, precipitating along the grain boundaries and within the grains, compared to a lower number density in the RS of the weld. The uniformity of the dispersoids distribution in the 5083 is most likely attributed to the fact that homogenisation was performed for this sheet,

precipitating the Mn-atoms, while precipitation of the $Al_6(Fe,Mn)$ possibly occurred *in-situ* during FSW of 5251, resulting in a heterogeneous distribution.

TEM investigations have also revealed a noticeable dislocation activity in the 5251 and 5083 welds, and to a lesser extent in the 5754 CC1 weld. In addition, fragmented constituent α-particles and $Al_6(Fe,Mn)$ dispersoids were also observed within the TMAZ of the weld, with roughly similar amounts in the 5251 and 5083 welds, and with lower quantity in the 5754 CC1 weld. This suggests a potential correlation between particle content and dislocations, although TEM investigations are insufficient to establish this. In Chapter 8, quantitative investigations for the dislocation density and particles will be performed to establish the structure-property relations.

7.6. Conclusions of Chapter 7

As shown in this chapter, the microstructural development in FSW is dependent on the starting condition, which was linked to FSW's most unique microstructural feature; the onion rings. The existence of banded constituent or equilibrium particles in the basemetal has resulted in the formation of an ORZ in the welds performed with the RD parallel to the WD. Some process parameters (e.g. orientation, tool type) and material parameters (e.g. area fraction) were found to influence the intensity or the morphology of the ORZ.

The chapter highlighted the microstructure differences between the welds of 2xxx and 5xxx series alloys. It chapter also clarified the microstructural characteristics of the ORZ, which are related to a microstructural heterogeneity in the grain and particle structures. Moreover, the influence of the basemetal and process parameters on the formation and intensity of the ORZ was discussed, highlighting the relative significance of these parameters. In fact, it could be possible to control the ORZ formation or morphology by manipulating those parameters, in order to optimise the in-service properties that could be affected by the presence of the microstructural heterogeneities in the ORZ.

7.7. References

[1] P. Threadgill, "Friction Stir Welds in Aluminium Alloys: Preliminary Microstructural Assessment," *TWI Bulletin*, vol. 38, pp. 30-33, 1997.

[2] M. Guerra, C. Schmidt, J. C. McClure, L. E. Murr, and A. C. Nunes, "Flow patterns during friction stir welding," *Materials Characterization*, vol. 49, pp. 95-101, 2002.

[3] K. N. Krishnan, "On the formation of onion rings in friction stir welds," *Materials Science and Engineering A*, vol. 327, pp. 246-251, 2002.

[4] P. A. Colegrove and H. R. Shercliff, "3-Dimensional CFD modelling of flow round a threaded friction stir welding tool profile," *Journal of Materials Processing Technology*, vol. 169, pp. 320-327, 2005.

[5] P. A. Colegrove, H. R. Shercliff, and P. Threadgill, "Modelling and Development of Trivex^{TM} Friction Stir Welding Tool," presented at The 4th International Symposium on Friction Stir Welding, Park City, Utah, USA, 2003.

[6] R. Zettler, S. Lomolino, J. F. d. Santos, T. Donath, F. Beckmann, T. Lippman, and D. Lohwasser, "A Study on Material Flow in FSW of AA2024-T351 and AA6056-T4," presented at 5th International Symposium on Friction Stir Welding, Metz, France, TWI, Cambridge, 2004.

[7] Y. Li, L. E. Murr, and J. C. McClure, "Solid-state flow visualization in the friction-stir welding of 2024 Al to 6061 Al," *Scripta Materialia*, vol. 40, pp. 1041-1046, 1999.

[8] P. Ratchev, B. Verlinden, and P. Van Houtte, "Effect of Preheat Temperature on the Orientation Relationship of (Mn,Fe)Al_6 Precipitates in an AA5182 Aluminium-Magnesium Alloy," *Acta Materialia*, vol. 43, pp. 621-629, 1995.

[9] P. Yang, O. Engler, and H.-J. Klaar, "Orientation Relationship between Al_6Mn Precipitates and the Al Matrix during Continuous Recrystallization in Al-1.3%Mn," *Journal of Applied Crystallography*, vol. 32, pp. 1105-1118, 1999.

[10] M. Mahoney, R. S. Mishra, T. Nelson, J. Flintoff, R. Islamgaliev, and Y. Hovansky, "High strain rate, thick section superplasticity created via friction stir processing," Indianapolis, IN, United States, 2001.

[11] Y. Li, L. E. Murr, and J. C. McClure, "Flow visualization and residual microstructures associated with the friction-stir welding of 2024 aluminum to 6061 aluminum," *Materials Science and Engineering A*, vol. 271, pp. 213-223, 1999.

[12] M. W. Mahoney, C. G. Rhodes, J. G. Flintoff, R. A. Spurling, and W. H. Bingel, "Properties of friction-stir-welded 7075 T651 aluminum," *Metallurgical and Materials Transactions A: Physical Metallurgy and Materials Science*, vol. 29A, pp. 1955-1964, 1998.

[13] R. S. Mishra and Z. Y. Ma, "Friction stir welding and processing," *Materials Science and Engineering: R: Reports*, vol. 50, pp. 1-78, 2005.

[14] J. E. Hatch, *Aluminum: Properties and Physical Metallurgy*. Ohio: American Society for Metals (ASM), 1984.

[15] L. F. Mondolfo, *Aluminum Alloys: Structure and Properties*. London: Butterworth, 1976.

[16] I. J. Polmear, *Light Alloys: Metallurgy of the Light Metals*. Bristol: St. Edmundsbury Press Ltd., 1995.

[17] W. Tang, X. Guo, J. C. McClure, L. E. Murr, and A. Nunes, "Heat input and temperature distribution in friction stir welding," *Journal of Materials Processing and Manufacturing Science*, vol. 7, pp. 163-172, 1998.

[18] Y. S. Sato, M. Urata, and H. Kokawa, "Parameters Controlling Microstructure and Hardness during Friction-Stir Welding of Precipitation-Hardenable Aluminum Alloy 6063," *Metallurgical and Materials Transactions A*, vol. 33, pp. 625-635, 2002.

[19] L. E. Murr, G. Liu, and J. C. McClure, "Dynamic recrystallization in friction-stir welding of aluminum alloy 1100," *Journal of Materials Science Letters*, vol. 16, pp. 1801-1803, 1997.

[20] Y. S. Sato, S. H. C. Park, and H. Kokawa, "Microstructural factors governing hardness in friction-stir welds of solid-solution-hardened Al alloys," *Metallurgical and Materials Transactions A: Physical Metallurgy and Materials Science*, vol. 32, pp. 3033-3042, 2001.

[21] F. J. Humphreys and M. Hatherly, *Recrystallization and Related Annealing Phenomena*. Great Britain: Pergamon, 1995.

[22] B. London, M. Mahoney, W. Bingel, M. Calabrese, R. H. Bossi, and D. Waldron, "Material flow in friction stir welding monitored with Al-SiC and Al-W composite markers," presented at Friction Stir Welding and Processing II. 2003, San Diego, CA, USA, 2003.

[23] H. N. B. Schmidt, T. L. Dickerson, and J. H. Hattel, "Material flow in butt friction stir welds in AA2024-T3," *Acta Materialia*, vol. 54, pp. 1199-1209, 2006.

[24] H. Jin, S. Saimoto, M. Ball, and P. L. Threadgill, "Characterisation of microstructure and texture in friction stir welded joints of 5754 and 5182 aluminium alloy sheets," *Materials Science and Technology*, vol. 17, pp. 1605-1614, 2001.

[25] M. Peel, A. Steuwer, M. Preuss, and P. J. Withers, "Microstructure, mechanical properties and residual stresses as a function of welding speed in aluminium AA5083 friction stir welds," *Acta Materialia*, vol. 51, pp. 4791-4801, 2003.

[26] W. Baeslack, K. Jata, and T. Lienert, "Structure, properties and fracture of friction stir welds in a high-temperature Al-8.5Fe-1.3V1.7Si alloy (AA-8009)," *Journal of Materials Science*, vol. 41, pp. 2939-2951, 2006.

[27] M. A. Sutton, B. Yang, A. P. Reynolds, and R. Taylor, "Microstructural studies of friction stir welds in 2024-T3 aluminum," *Materials Science and Engineering A*, vol. 323, pp. 160-166, 2002.

[28] B. Yang, J. Yan, M. A. Sutton, and A. P. Reynolds, "Banded microstructure in AA2024-T351 and AA2524-T351 aluminum friction stir welds. Part I. Metallurgical studies," *Materials Science and Engineering A*, vol. 364, pp. 55-65, 2004.

[29] G. Biallas, R. Braun, C. Dalle Donne, G. Staniek, and W. A. Kaysser, "Mechanical Properties and Corrosion Behavior of Friction Stir Welded 2024-T3," presented at 1st International Symposium on Friction Stir Welding, Thousand Oaks, CA, USA, 1999.

[30] A. Afseth, J. H. Nordlien, G. M. Scamans, and K. Nisancioglu, "Filiform Corrosion of Binary Aluminium Model Alloys," *Corrosion Science*, vol. 44, pp. 2529-2542, 2002.

[31] M. A. Sutton, B. Yang, A. P. Reynolds, and J. Yan, "Banded microstructure in 2024-T351 and 2524-T351 aluminum friction stir welds. Part II. Mechanical characterization," *Materials Science and Engineering A*, vol. 364, pp. 66-74, 2004.

Chapter 8

STRUCTURE-PROPERTY RELATIONS IN AA5XXX FRICTION STIR WELDS

The complex microstructural development associated with FSW is expected to result in a heterogeneous local mechanical property (microhardness) distribution in the welds. In this chapter, the structure-property relations in the 5xxx-series welds are established, using the models discussed in Chapter 2 to link the quantified microstructural features (e.g. grain sizes, intermetallic particles and dislocations) to strength. Differential Scanning Calorimetry (DSC) was used to measure the stored energy in the welds. Optical and electron microscopy were utilised to quantify the strengthening contribution due to grain size (Hall-Petch) and particles.

8.1. AA5251 Welds

In order to establish the microstructure-property relations, microstructural investigations (using optical and electron microscopy), calorimetric measurements and hardness traces were performed in specific locations of the weld, which are: the advancing side (AS), retreating side (RS), weld nugget up (WNU), weld nugget down (WND), and thermomechanically-affected zone down (TMAZD), as indicated in Fig. 8.1. Average microhardness and grain sizes were obtained by measuring at least 8 hardness points and 6 image fields within those regions (dashed boxes), thus obtaining average values for those regions rather than any localised variation within.

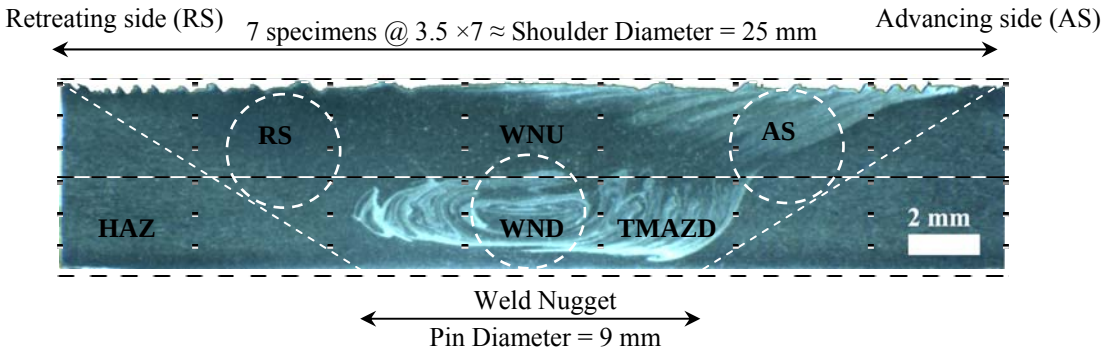

Fig. 8.1. Macrograph for the 5251-H34 weld, showing the specific locations of weld (AS, RS, WNU, WND, TMAZD) for the microstructural investigations, and the TEM specimens (dashed circles), and the DSC specimens (dashed black boxes).

8.1.1. Hardness Distribution

The hardness measurements were performed for the O and H34 5251 welds on two traces located at 1.5 mm (up) and 3.5 mm (down) from the weld surface. As shown in Fig. 8.2, the location of the maximum hardness in the 'up' trace (~72-74 H_V) was found at the AS in both welds, with the hardness decreasing beyond this location, reaching a minimum hardness of 50-55 H_V at the TMAZ/HAZ boundary. In the H34-weld HAZ, the hardness increases with the decrease in the thermal fields experienced during welding, and accordingly decreasing extents of recovery and recrystallisation. In the O-weld HAZ, the hardness decreases gradually until it reaches the O-basemetal hardness (54±2 H_V). Thus, it can be seen that the 'up' traces in both conditions show similar trends, with a hardness peak of 70-75 H_V on the AS, decreasing to a hardness of 55 H_V at the RS-HAZ.

The 'down' traces for both conditions also show similar trends, with the peak hardness forming a plateau of 66-72 H_V within the H34 WN (±4.5 mm from the weld centreline), precisely in the onion rings region, before decreasing to its minimum in the HAZ. Conversely, in the O-weld 'down' trace, the hardness was found to decrease across the onion rings, from 73 H_V at the weld centreline, to 64 H_V at the WN edge, followed by a sharp decrease to 50-55 H_V within the HAZ.

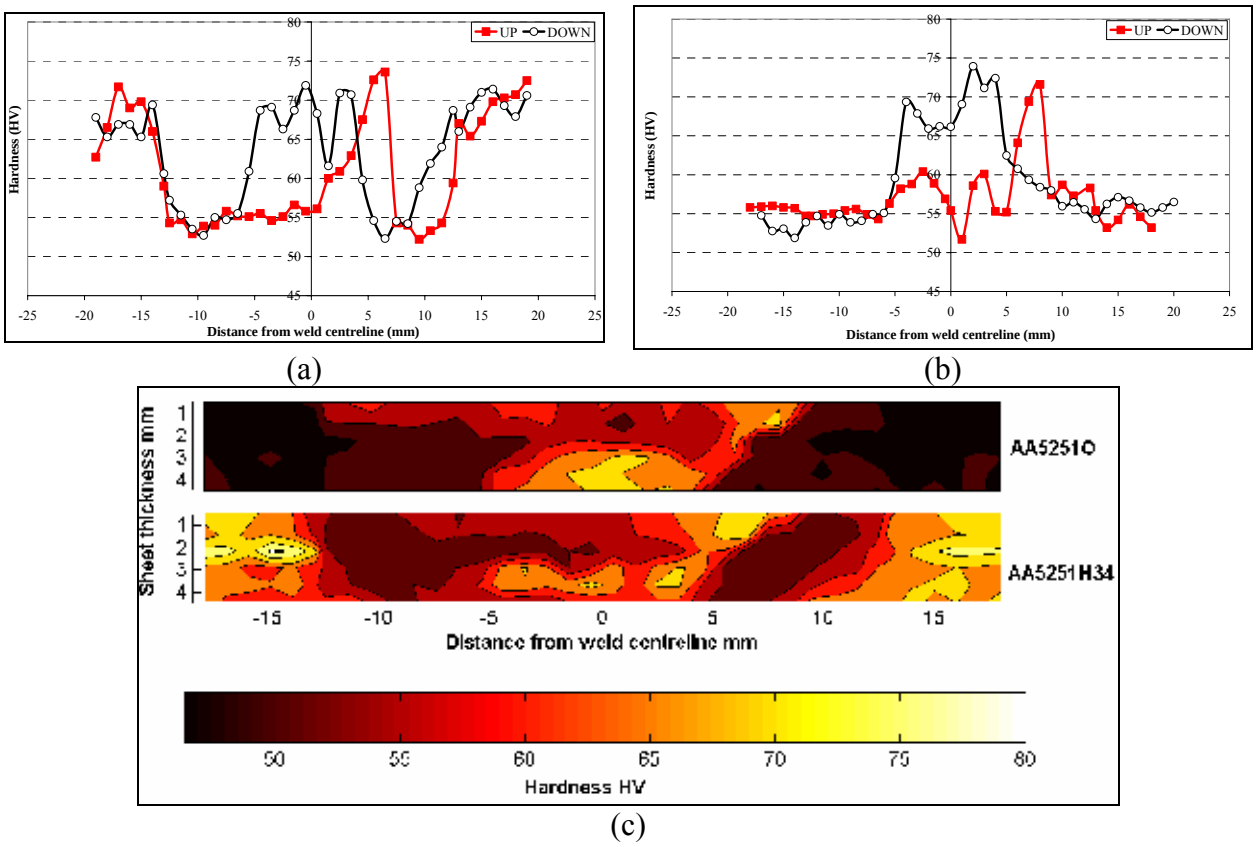

Fig. 8.2. Hardness traces for (a) the H34-weld and (b) the O-weld, taken at 1.5 mm (up, TMAZ width ±10.1 mm) and 3.5 mm (down, TMAZ width ±6.9 mm) from the surface (the AS of the weld is to the right in each graph), (c) complete microhardness contours for both welds

Due to the similarity in the hardness traces within the TMAZ of both welds, notably the peak at the AS of the 'up' traces and in the onion rings region in the 'down' traces, it is clear that the starting condition does not influence the TMAZ microstructure, and accordingly the hardness development, although its influence can be easily identified in the HAZ and beyond. Compared to the previously reported welds, these hardness traces differ from the centreline traces reported for welds in work-hardened and annealed temper 5xxx-alloys [1-4], which show a roughly uniform hardness within the TMAZ (section 3.6.2). However, by looking into full weld hardness contours in the literature, a high hardness region has been reported towards the AS close to the sheet surface (e.g. in 2095 weld [5] and 1050 weld [6]). The local variation in the hardness development in different weld regions suggests that a more thorough microstructural investigation is required to explain this variation.

8.1.2. Hall-Petch

To separate the various strengthening mechanisms, Hall-Petch plots were used to establish the grain size strengthening contribution. Grain size data were obtained for Gleeble thermally cycled H34 specimens, cycled at 20 ˚C/min (similar to the DSC rate) to peak temperatures of 375, 400, 475, and 525 ˚C (i.e. after full recrystallisation, as determined from the hardness and DSC measurements), to establish a Hall-Petch relation for the basemetal. Additional data points were plotted for the specified positions in the O-weld (AS, RS, WNU, and WND), as well as from an O-weld thermally cycled to 375 ˚C (i.e. complete recrystallisation), and for both the H34 and O-basemetal (BM) specimens.

By plotting the thermally-cycled H34 data points, it was found that grain growth in the three specimens cycled to 375, 400, and 475 ˚C and the associated decrease in hardness provided a Hall-Petch fit, which is given by: $H_V = 43+44d^{-1/2}$ as shown in Fig. 8.3. Following thermal cycling to 525 ˚C, and despite the grain growth, there was an increase in hardness of ~4 H_V, which was linked to the dissolution of the Mg_xSi particles [7] (also consistent with the decrease in the area fraction of the Mg_xSi particles in this condition, section 5.1.4.b). The dissolution of Mg_xSi enriched the Mg-content in solid solution, which accordingly caused the increase in strength. The O-BM data point was found to be out of the Hall-Petch fit by ~+3 H_V. Since it was statically annealed by the material provider from the H34-BM (using an unspecified treatment), it is expected that such a treatment could have dissolved some of the Mg_xSi particles, especially as the area fractions of Mg_xSi in the O-BM and the 525 ˚C heat treated specimens are roughly similar (section 5.1.4.b).

Using the Hall-Petch data of Al-Mg alloys performed by Furukawa *et al.* [8, 9] and Sato *et al.* [10, 11], the relationship for 5251 can be interpolated assuming a linear relationship between the Mg-content and the Hall-Petch slope (K_H) and intercept (H_{VO}), giving $H_V = 38+45d^{-1/2}$. This assumption has been established based on several experimental reports which showed a roughly linear relation between the Mg-content trend and frictional stress and K_Y (e.g. [10-15], section 2.4.2). The estimated relationship is close to the one calculated for 5251, although the calculated relation had an H H_{VO} value 5 H_V greater. Since H_{VO} is linked to solid solution and precipitate strengthening [16] (section 2.4.1), it is possible to attribute the discrepancy in H_{VO} to differences in the solute content of other alloying elements or the constituent particles and dispersoids content between 5251 in this study and the published data for other Al-Mg

alloys. It is known that Fe and Mn solutes have the most significant strengthening effect in Al-based alloys even when they are present at low quantities [13, 14, 17, 18].

Figure 8.3 also shows that while the hardness of some locations in the TMAZ (RS and WNU) can be explained by the grain size effect, other locations (WND and AS) show higher hardness levels (~4-8 H_V higher than the upper limit fit) that cannot be explained by the grain size or solid solution strengthening effects. Moreover, the hardness of the H34-BM also shows a significantly high hardness (~29 H_V higher than the fitted Hall-Petch relation using the feret minimum (F_{min}) of the H34 elongated grains as the grain size).

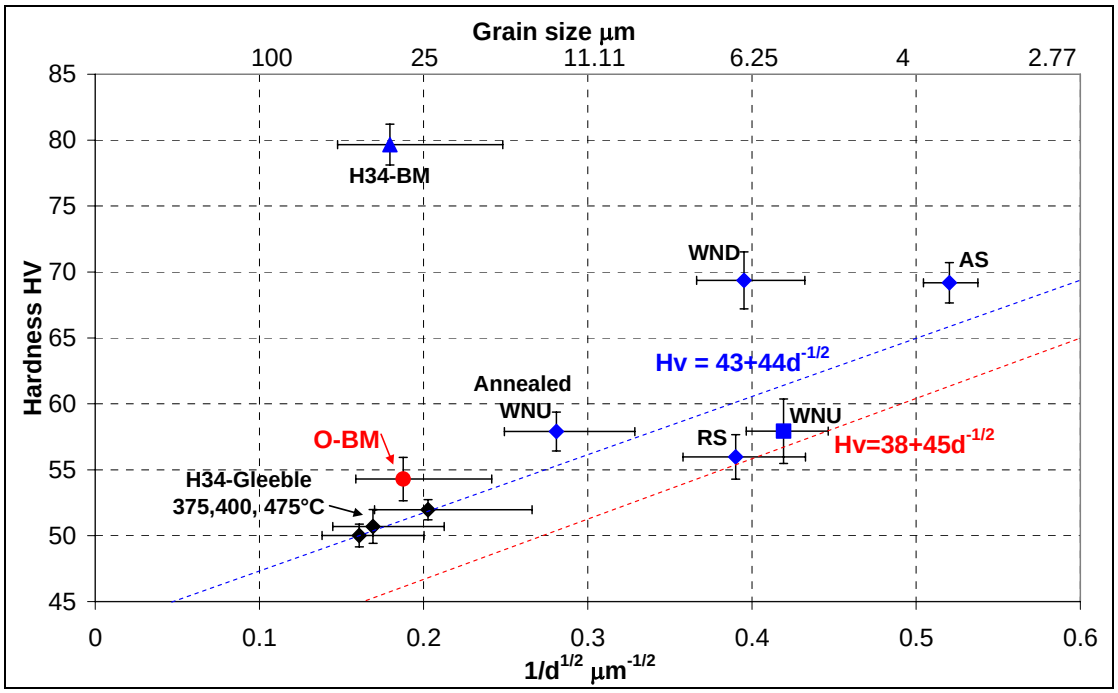

Fig. 8.3. Hall-Petch plot showing the contribution of the grain size to hardness for some of the weld positions and thermally-cycled H34 and welded specimens. Error bars are based on the standard deviation in measured hardness and grain size values.

To study the influence of the change in grain size on the strength, it was found that Gleeble thermal cycling of the H34-BM to 375-400 ˚C (fully recrystallised) resulted in ~27-29 H_V decrease in the hardness, changing the grain morphology from the elongated low-aspect ratio grains to more rounded grains. However, the grain size (equivalent circle diameter in the case of the annealed structures) was roughly similar to the H34-BM F_{min}. Conversely, on thermal-cycling of a WNU specimen, the hardness still did not change despite the change in grain size from 5.7 μm to 12.7 μm after annealing. Although thermal cycling in both cases resulted in

the release of stored energy, as will be discussed in section 8.1.4, the H34-BM specimen showed a significant change in hardness while the WNU specimen did not. This highlights the need for a more thorough investigation of other strengthening mechanisms, which will be presented in subsequent sections.

The previous analysis of the Hall-Petch plot reveals that there are two Hall-Petch relations, with roughly similar slope but different H_{VO}; the lower one includes the RS and WNU sites from the weld, whose strength is primarily controlled by the grain size strength, and the upper one includes the Gleeble-cycled H34 and WNU, and O-BM specimens. The upper limit relation includes the specimens that may be affected by the relatively longer thermal exposure during thermal cycling or static annealing, compared to the transient thermal cycles in the weld specimens in the lower limit relation. The longer thermal exposure possibly led to the dissolution of Mg_xSi particles, which enriched the Mg-content in the matrix, causing the 5 H_V offset in the Hall-Petch intercept. This also explains why the hardness of the WNU specimen did not drop following thermal cycling. The superposition of the thermal-stirring effect during welding, followed by further thermal cycling in the Gleeble, enriched the Mg-content in the matrix, which compensated the decrease in strength due to grain growth. However, the aforementioned correlations fail to account for the hardness levels in the AS, WND, and H34-BM specimens by grain size and solid solution strengthening only.

Such discrepancies in the hardness-grain size relationship suggest that there are additional strengthening parameters that could contribute to the basemetal and weld strength. Most of the other parameters are measurable using other experimental tools (e.g. the grain substructure using EBSD, dislocation stored energy using the DSC, and particle strengthening using the TEM). Hence a quantitative representation for their strengthening contribution can be obtained.

8.1.3. Grain substructure

Microstructural analysis of the H34-BM (using polarised light microscopy, section 5.1.1) showed that it was composed of elongated pancake-shaped grains with an average grain thickness (F_{min}) of ~31±14.8 μm, which resulted in a microhardness of 79.7±1.6 H_V. By plotting this data point on the Hall-Petch plot, it was found to be ~29 H_V above the fitted relation. However, on using the TEM to investigate the grain structure, it was found to contain

elongated subgrains (0.3-1 μm thick) within the grain structure. Accordingly, it was thought that considering the strengthening contribution of the grain substructure could correct such a discrepancy. Hansen *et al.*'s model (section 2.4.4.b) states that the dislocations in deformed materials rearrange themselves into subgrains with low angle boundaries (LAB, θ<15 $^{\circ}$), which can provide a strengthening contribution that can exceed the Hall-Petch contribution [19-24].

To distinguish the LAB from the high angle grain boundaries (HAGB), EBSD mapping was performed for the conditions which showed a poor Hall-Petch fit (H34-BM and WND), as well as O-BM. EBSD is known to provide a better sampling capability, as well as ease of use compared to the other possible approach using the TEM. EBSD is considered an intermediate technique in terms of resolution and the extent of microstructural details obtained. However, the quality of the microstructural details obtained extensively relies upon the post-processing of the EBSD data, and pixel area (resolution) which indicates the size of the smallest area whose orientation is being resolved [25].

8.1.3.a. 5251-H34 basemetal

EBSD mapping for the H34-BM was performed using 512 square pixels maps with two pixel areas of 0.23 μm^2 (low resolution, Fig. 8.4) and 0.0574 μm^2 (high resolution, Fig. 8.5) at the mid-thickness of the RD-ST plane. On the low resolution map, the grain structure appeared elongated, with a size range for the grain thickness of ~10-30 μm which is similar to the size range observed optically. However, because of the low resolution, measuring the subgrain size was not possible.

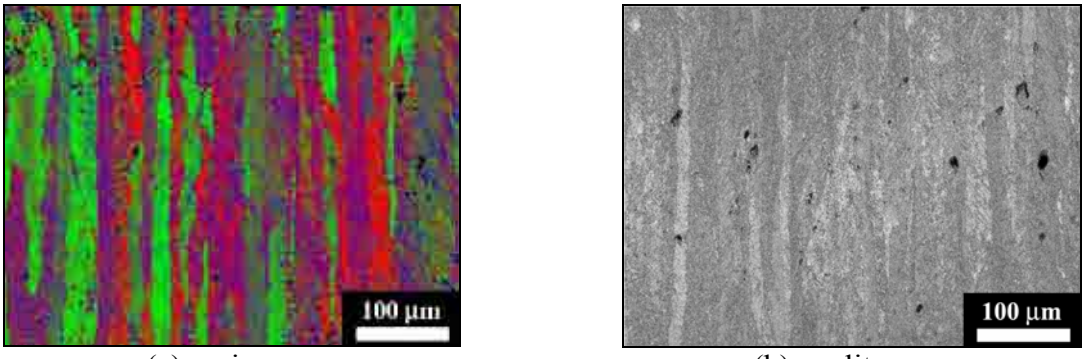

(a) grain map (b) quality map

Fig. 8.4. Low resolution EBSD maps for 5251-H34 (RD-ST) plane

On the high resolution map, HAGBs can be seen on the orientation map having different colours which correspond to the inverse pole figure (Fig. 8.5-a). On analysing the boundary misorientation distribution for the grain map (Fig. 8.5-b), LABs with misorientation angles <15 ˚ were observed to exist within the grains. These LABs are expected to correspond to the boundaries of the subgrains observed in the TEM. The most important feature is that the LABs represented ~70% of the observed boundaries (Fig. 8.5-c). It can be observed in the EBSD map that some grains were found to contain a high density of LABs, while some grains contained a lower density of LABs. This is indicative of the occurrence of recovery in the grains with a high density of LABs.

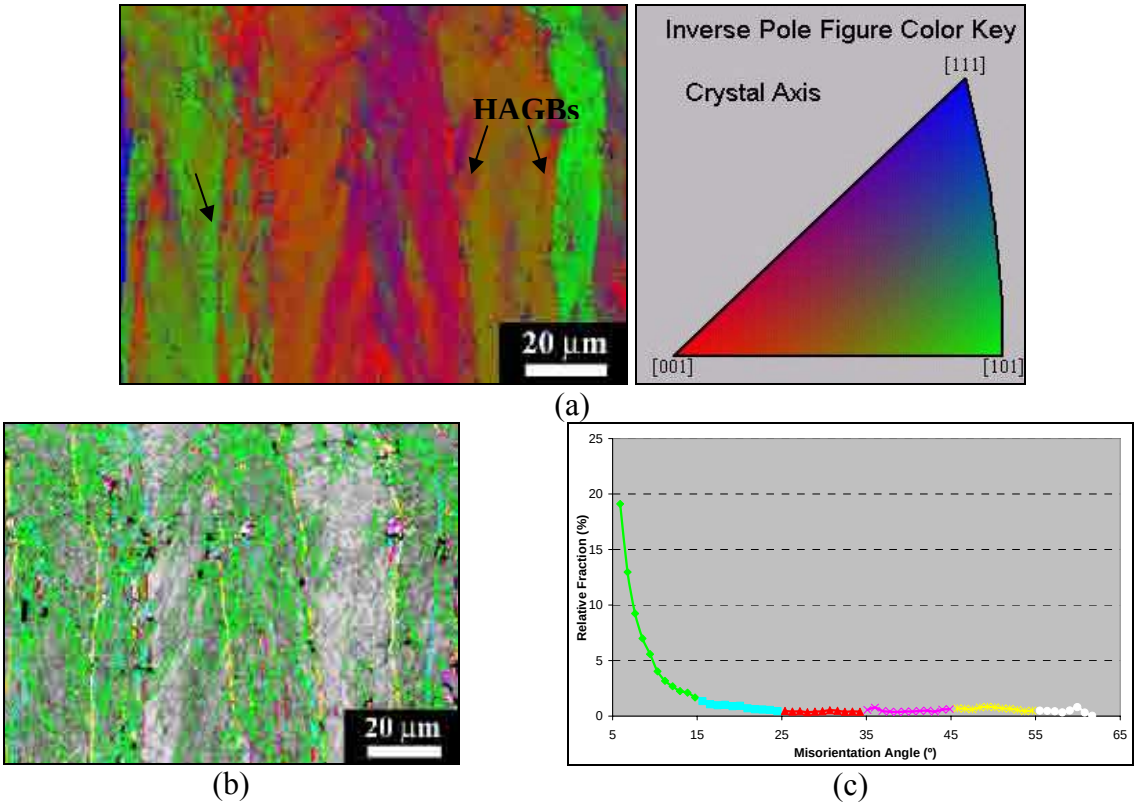

Fig. 8.5. EBSD map for the 5251 H34-BM (RD-ST plane, mid-thickness), showing (a) grain orientation map, (b) boundaries with misorientation angle range of 5 to 60˚ superimposed on the quality map, and (c) the boundary misorientation distribution with the same colour code as in (b)

To quantify the strengthening contribution due to the LABs, the average boundary intercept distance ($\overline{L}_{XY\,LAGB}$) was calculated as 3.4±0.3 μm from the average boundary intercept spacings for the LABs (calculated from the LABs with misorientations in the range between 2

and 15 °), with an average misorientation angle ($\overline{\theta}_{LAB}$) of 8.25°. It is important to mention that $\overline{L}_{XY\,LAGB}$ is a stereological parameter that is not directly related to the subgrain size as measured by the TEM.

Hansen *et al.*'s model was then used to calculate the yield stress of the material using the following equation:

$$\sigma_{YS} = \sigma_O + kd^{-1/2} + M\alpha Gb\sqrt{\frac{3\overline{\theta}_{LAB}}{\overline{L}_{XY\,LAB}b}} \tag{8.1}$$

According to Burger *et al.* [12], the frictional stress component (σ_O) for Al-Mg alloys is proportional to the Mg-content such that:

$$\sigma_O = 15.5\,(wt.\%)\ \text{Mg (MPa)} \tag{8.2}$$

The Hall-Petch slope (*k*) was estimated at ~0.16 MPa.m$^{1/2}$ using Burger *et al.*'s data, with grain size (*d*) equivalent to the measured F_{min} of 31 μm. For deformed Al-Mg alloys, a value of Taylor factor (M) ~3.06 can be used [15], and α is given as 0.24 [19]. The shear modulus of aluminium of 26 GPa was used, and *b* is the Burger's vector of aluminium, 2.86 Å. Using these values, the yield stress for 5251-H34 was calculated as ~175 MPa. Using the hardness conversion relation for Al-based alloys [26], this value is equivalent to 74.4 H_V, which is slightly lower than the measured H34-BM hardness. This value is also slightly lower than the value obtained using mechanical (tensile) testing, with the specimen axis positioned along the rolling (RD) and transverse (TD) directions, Fig. 8.6, giving an average yield stress of ~192±4 MPa.

It was found that the calculated strength by Hansen *et al.*'s model is slightly lower than the measured strength by an error of ~6-9%. However, this error can be considered reasonable due to several reasons. First, Hansen *et al.*'s model was fitted using high-purity aluminium alloys. Accordingly, it does not consider the possible solute-dislocation interactions, which might have an influence on the constants used in the third term of equation (8.1). Second, it is possible that other solutes present in solution (e.g. Mn) could have a significant influence on the frictional stress component. Court *et al.* [14, 17] estimated this contribution to be ~115-145 MPa/wt % Mn in AA5754 (AlMg3). For 5251, 0.3 wt % Mn is present in its chemical composition, however, it is not expected that this entire amount is retained in solution. Court

et al. found that that only 0.12 wt % Mn is retained in solution for a bulk content of 0.3 wt % Mn in AA5754. Assuming that this relation is also applicable for 5251, the presence of 0.12 wt % Mn in solution could increase the frictional stress component by ~14-17 MPa, which could correct the error noted above. Finally, the deviation in the calculated yield stress was not considered, as it is based on the average values for *d* and $\overline{L}_{XY\,LAGB}$, without considering the standard deviation. These reasons could explain the difference between the calculated and measured yield stress.

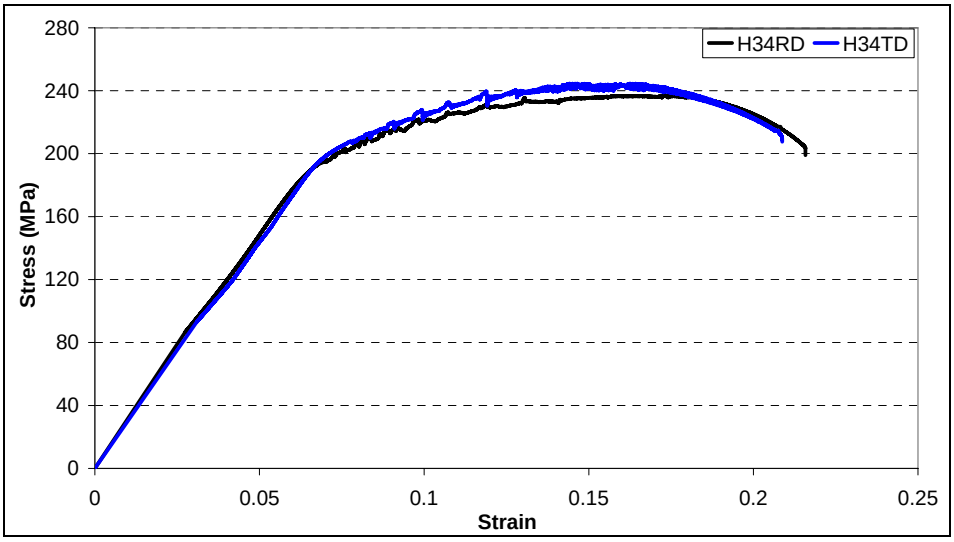

Fig. 8.6. Engineering stress-curves for the H34-BM tested on both the transverse and rolling directions (strain calculation is based on crosshead displacement)

8.1.3.b. 5251-O basemetal

EBSD mapping for the O-BM revealed an annealed grain structure with irregularly-shaped flattened grains, Fig. 8.7-a, with size range similar to that obtained using optical microscopy.

The most important feature revealed by EBSD was the boundary misorientation angle distribution in this condition compared to H34-BM. The majority of the resolved boundaries (~91%) were found to be HAGBs (>15 ˚ misorientation), which is indicated on the quality map (Fig. 8.7-a) using the colour of the boundaries which refer to the misorientation angle range as shown in Fig. 8.7-b. The resolved LABs were actually sections of the GBs of low misorientation angles, as opposed to the continuous LABs observed in the H34-BM sample.

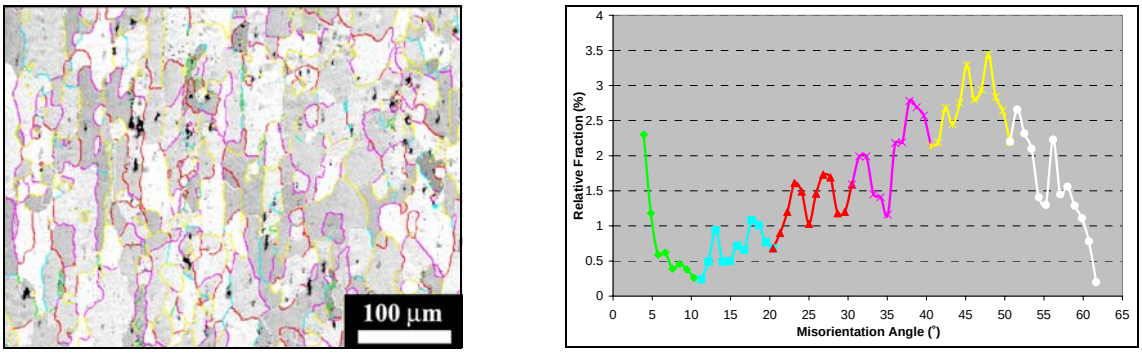

(a) (b)

Fig. 8.7. EBSD map for the 5251 O-BM (RD-ST plane), showing (a) boundaries with misorientation range 2 to 61˚ superimposed on the quality map, and (b) the distribution of boundary misorientation angles with the same colour code as in (a)

To verify the fitting used for the H34-BM, tensile tests were performed on the O-BM, giving an average σ_{YS} of 73±7 MPa, Fig. 8.8. The Hall-Petch relation (for σ_{YS}) was used to calculate a theoretical σ_{YS} for the O-BM, with the same values used for σ_O and k as in the H34-BM, and with d of 29.8±11.7 μm. The calculated σ_{YS} falls within the range of 56-68 MPa (considering the standard deviation in grain size), with 63 MPa yield stress corresponding to $d_{average}$. The differences between the measured and calculated σ_{YS} could be attributed to the same reasons indicated in the previous section for H34-BM.

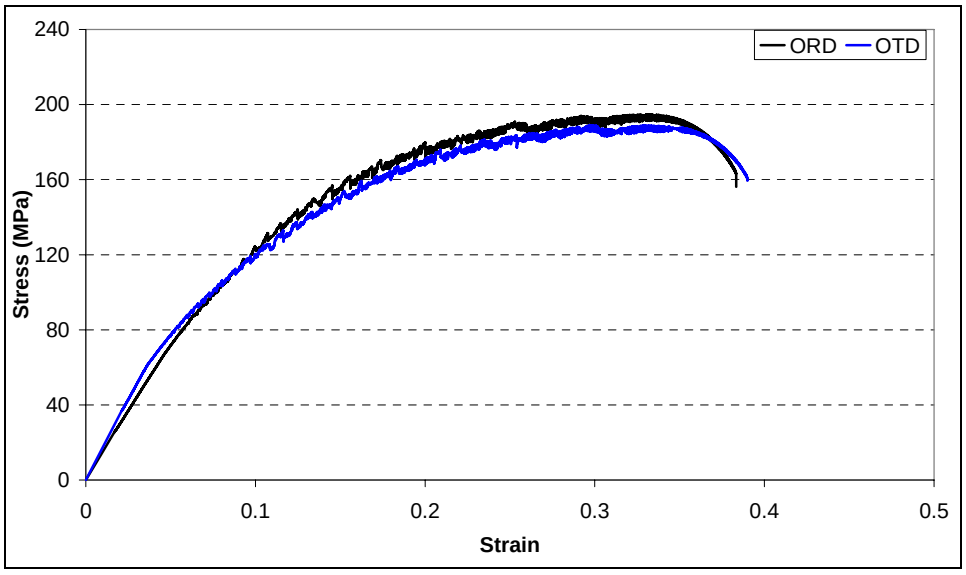

Fig. 8.8. Engineering stress-strain curves for the O-BM tested on both the transverse and rolling directions (strain calculation is based on crosshead displacement)

8.1.3.c. 5251 Weld

EBSD mapping was performed for the lower half of the WN (WND) of the weld for accurate determination of the grain size, to compare to the grain size values obtained using optical microscopy, as well as to quantify the fraction of LABs and subgrains that did not fully recrystallise during dynamic recrystallisation (DRX). As shown in Fig. 8.9, the basemetal microstructure has evolved into a DRXed microstructure, with fine equiaxed grains within the size range of 2-18 μm (D_{Eq}). The majority of resolved boundaries (~78%) were found to be HAGBs (misorientation angles >15˚), which indicates the existence of a substructure associated with the remaining 22% of the resolved boundaries. The extent of this substructure is significantly lower than that observed in the H34-BM. However, the existence of a small substructure has been previously observed in 5xxx series welds [27, 28]. Jin *et al.* [27] also found that 80% of the resolved boundaries in AA5182 weld were HAGBs, with a bimodality in misorientation angle distribution.

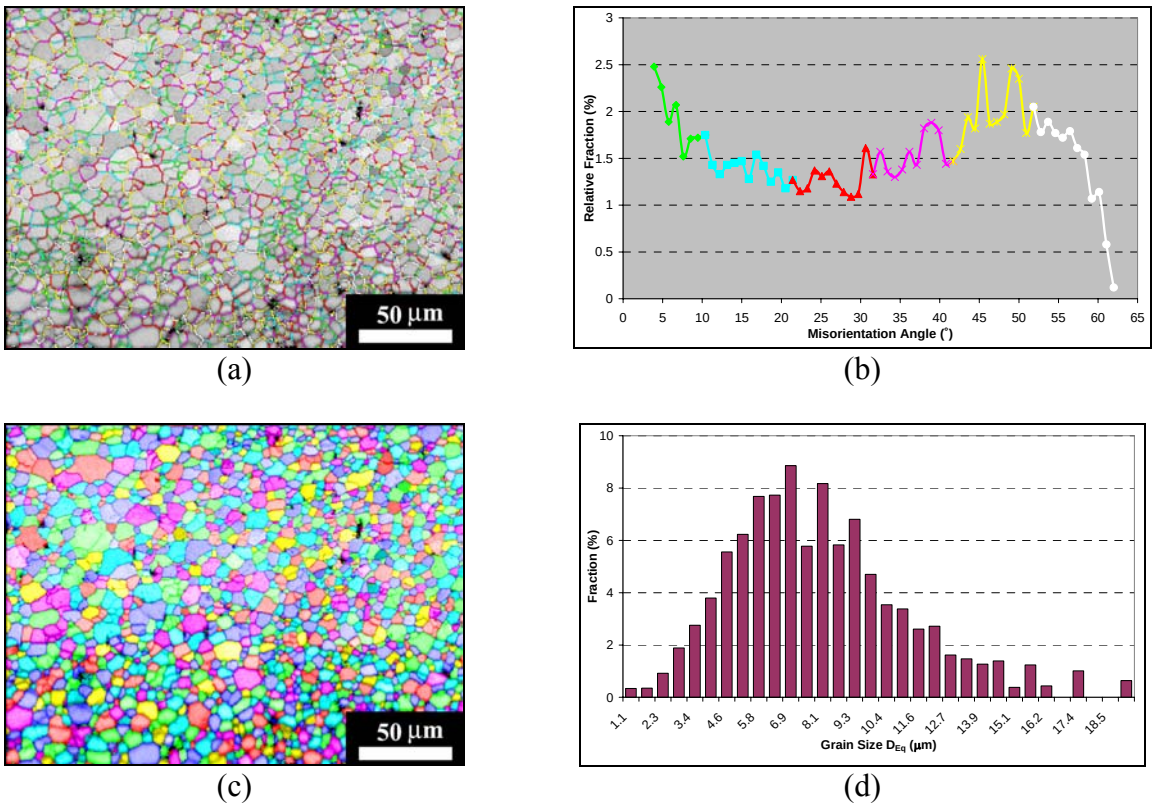

(a) (b) (c) (d)

Fig. 8.9. EBSD map for the 5251 H34-WND, showing (a) boundaries with misorientation range 2 to 61 ˚ superimposed on the quality map, and (b) the distribution of boundary misorientation angles with the same colour code as in (a), (c) generated grain map with grains defined as having misorientation angles >15 ˚, (d) grain size distribution.

The average grain size was found to be ~5.25 μm using EBSD, which is roughly similar to the value obtained by optical microscopy. The existence of LABs is insufficient, given their wide scattering (~50 μm spacing), to provide a significant strengthening contribution to correct the ~7 H_V discrepancy in the Hall-Petch relation for the WND. Therefore, it is necessary to quantify the other strengthening factors that contribute to the weld hardness, such as the stored energy, and particle strengthening.

8.1.4. Stored Energy

8.1.4.a. DSC Measurements and Stored Energy Distribution in the Weld

Using the approach outlined in the experimental section, measurements of the stored energy within the TMAZ of the weld were performed using the DSC. Figure 8.10 shows the DSC traces for the H34-BM, the WND position, and an adjacent specimen from the TMAZ (TMAZD) towards the AS of the weld, as previously shown in Fig. 8.1.

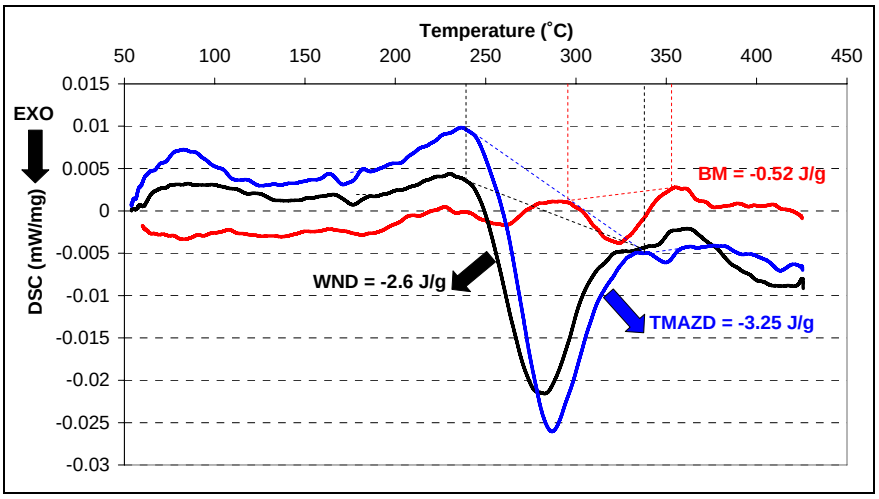

Fig. 8.10. DSC traces for the H34-base metal, compared to selected locations from the H34-weld according to the notation in Fig. 8.1 and the amount of energy release and temperature range

It is obvious that the TMAZ/WN DSC traces differ from the H34-BM with respect to the energy release temperature range, as well as the amount of energy released. In the TMAZ/WN DSC traces, energy release peaks of between ~ -2.5 and -3.7 J/g, which were identified as recrystallisation, occurred between 240 ˚C and 330 ˚C (compared to 320 ˚C and 385 ˚C in the

H34-BM, with -0.52 J/g release). The association of this exothermic peak with recrystallisation in the weld was determined using full weld specimens thermally cycled in the Gleeble to the energy release start and end temperatures, along with microhardness measurements and metallography, in an approach similar to the one used in the H34-BM (section 5.1.4.b). The occurrence of recrystallisation at a lower temperature in the TMAZ specimens, compared to the H34-BM specimen, is expected since recrystallisation is influenced by the extent of driving force for recrystallisation, which is related to the amount of pre-deformation and grain size [29, 30]. The high deformation experienced during FSW and the fine grain size within the TMAZ/WN samples enhances the tendency for recrystallisation at a lower temperature, as well as releasing higher energy, compared to the H34-BM.

In addition to recrystallisation, minor exothermic peaks (energy release <0.1 J/g) were frequently observed in the TMAZ/WN specimens between ~160 ˚C and ~190 ˚C, or between ~340 ˚C and ~360 ˚C which correspond to recovery and grain growth respectively. Similar peaks were observed in the H34-BM (section 5.1.4.b), but they were divided in the recovery range into more peaks, which generated a higher energy release in total compared to the TMAZ/WN. It is expected that the high temperature and high strain deformation during FSW facilitate recovery, which results in a lower energy release in the recovery range during DSC [30].

In the O-weld, exothermic peaks were observed within the same temperature range and energy release levels in the TMAZ (AS and WND) of the weld, Fig. 8.11. Thus, it is evident that the amount of energy stored during the process is independent of the starting condition. The HAZ shows a very small energy release, about two orders of magnitude less than the energy release in the TMAZ, which could have resulted from the annihilation of most dislocations created by the forging pressure of the rotating tool during welding. As the approach used to determine the position of the peaks was based on comparing the single and double-run traces, it was possible to identify even minor peaks with reasonable confidence.

The spatial distribution of the stored energy release within specimens extracted from the weld (covering the tool shoulder width) is shown in Fig. 8.12. It was found that the maximum stored energy at the AS was similar regardless of the starting condition (-3.65 J/g and – 3.72 J/g for the O and H34 conditions respectively). The energy levels in the WNU and WND

specimens for both the O-weld and H34-weld conditions were ~-2.5 J/g. This confirms that the material in the WN (up to ±5 mm from the weld centreline) experienced a similar amount of thermo-mechanical exposure, regardless of the initial condition, resulting in the creation of dynamically recrystallised grains and dislocations. Beyond the WN, the extent of energy released decreased in both conditions until reaching the basemetal energy (-0.5 J/g in the H34 and roughly zero in the O-condition, as clearly seen on the 'down' traces).

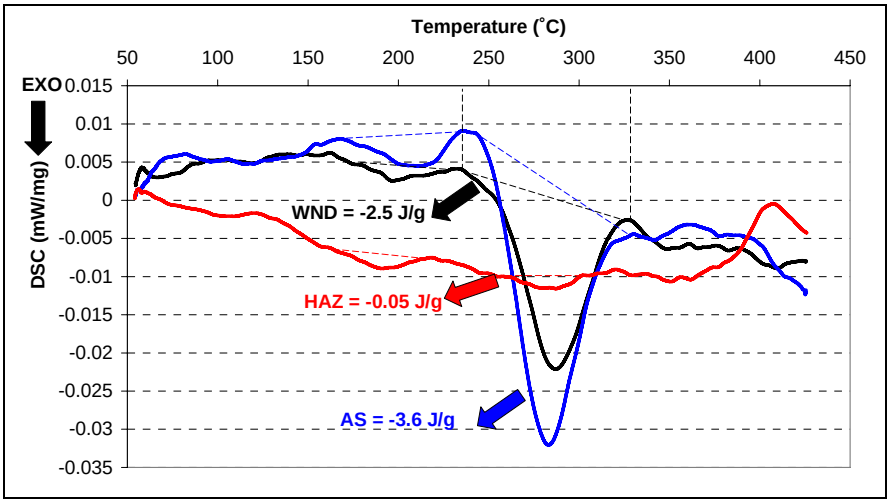

Fig. 8.11. DSC traces for specific locations in the O-weld according to the notation in Fig. 8.1 and the amount of energy release and temperature range

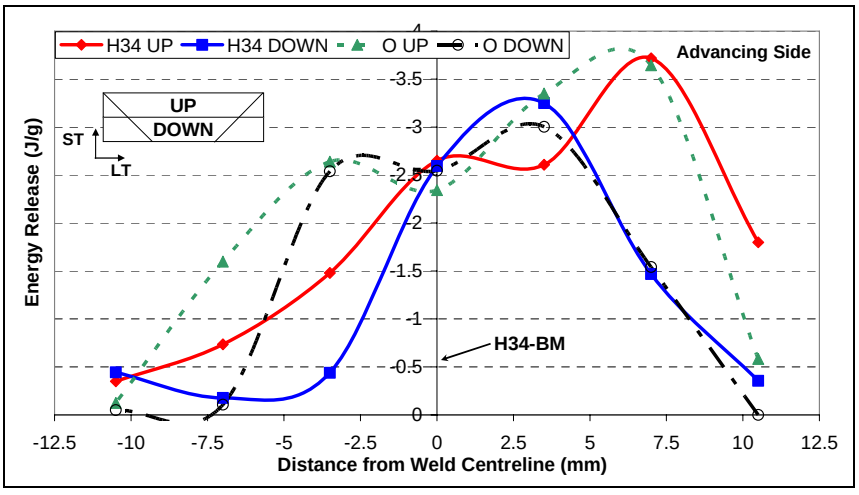

Fig. 8.12. The spatial distribution in energy release within the H34 and O-welds

It was shown in section 8.1.2 that the grain size strengthening contribution was sufficient to justify the hardness of the WNU and RS, but was insufficient to predict the hardness of the AS and WND sites. However, by looking into the results of the DSC measurements, it was found that the stored energy in the WNU and WND specimens were almost the same (≈ -2.5 J/g), whereas the RS was lower (-1.6 J/g in the O-weld, and -0.7 in the H34-weld), and the AS was the highest (-3.7 J/g). The similar stored energy levels in the WNU and WND sites, despite the differences in the Hall-Petch fit, suggest that the energy stored does not correlate directly to the weld strength. An estimate of the dislocation density in the weld, based on the stored energy, is thus required to determine the dislocation strengthening contribution.

8.1.4.b. Dislocation Density Strengthening Contribution

To estimate the dislocation density in the WN based on the DSC measurement of stored energy in the WN, equation (2.22-b) is used with α = 0.5, which is typically used in the literature [30]. It was calculated that a dislocation density of ~6.2×10^{15} m^{-2} corresponds to an energy release of ~-2.5 J/g, which was the average amount in the WN. Using the same approach, it was estimated that a dislocation density of ~1.3 x 10^{15} m^{-2} existed in the H34-BM, which corresponds to -0.5 J/g energy release, which is comparable to the estimates of the dislocation density in cold-rolled Al-Mg-Cu-Mn by Wang *et al.* obtained by both TEM and EBSD [15]. It also falls within the range of $\rho_{Dislocations}$ in plastically deformed particle-containing metals [16, 30].

According to Ashby's model [31], this estimated value of dislocation density, measured through the DSC, is the sum of two types of dislocations: the *statistically stored dislocations* (ρ_S), which are created within the grains due to plastic straining (work-hardening) and independently of any crystalline constraints (e.g. grain boundaries or non-deformable particles), and *geometrically necessary dislocations* (ρ_G), which are created due to the interaction of plastic strain with the abovementioned crystalline constraints. As the strengthening contributions of the dislocation-grain boundary and dislocation-particle interactions are already accounted for in the Hall-Petch and Orowan strengthening contributions, it is important to separate the dislocation-dislocation strengthening contribution through estimating the relative amounts of ρ_G and ρ_S.

According to Ashby's model, the grain boundaries cause a strain incompatibility, resulting in the formation of ρ_G under a shear strain of γ, which can be estimated using [31]:

$$\rho_{G1} = 4\gamma / bd \tag{8.3a}$$

Similarly, the non-deformable intermetallic particles (e.g. the constituent Al(Fe,Mn)Si and the Al_6(Fe,Mn) dispersoids) form ρ_G, which is a function of the area fraction F_v and particle size r, such that [30]:

$$\rho_{G2} = 3F_V \gamma / rb \tag{8.3b}$$

where the total ρ_G is the sum of the contributions from equations (8.3a) and (8.3b).

For ρ_S, Ashby's model estimates its amount, as a function of plastic strain ε and the slip distance λ_S, by:

$$\rho_S = \varepsilon / b\lambda_S \tag{8.4}$$

The microstructural characteristics of the WN are used, with an average grain size of 6 μm, and with particle characteristics of F_v = 0.02, r = 0.5 μm. For the plastic strain, Xu and Deng estimated, using FE thermomechanical modelling of a 6061-T6 weld, that the equivalent plastic strain (ε) in the WN varies between 10 and 20 [32]. Using the lower limit for the strain to calculate the shear strain ($\gamma = \varepsilon / \sqrt{3}$), a total ρ_G value of 1.6 × 10^{16} m^{-2} results. The estimate of ρ_G does not consider the possible decrease in dislocation density associated with recovery due to high strain deformation [30, 31], which explains why it is larger than the estimate calculated based on the DSC measurement of stored energy (using equation 2.22-b with α=0.5). It is known that alloys of similar composition lose about 15% of their strength due to recovery at room temperature following deformation [33], which is equivalent to about ~28% decrease in the dislocation density (using equation 2.16). Assuming a similar drop in dislocation density, the measured dislocation density becomes dominated by the ρ_G contributions. For ρ_S, obtaining an estimate using equation (8.4) would be inaccurate since FSW involves DRX, which defies the concept of Ashby's model (stored dislocations due to cold working). Thus, ρ_S can be only estimated as the remainder of the total dislocation density after subtracting the contribution due to ρ_G.

When using the previous relations, it is important to highlight again that they have been studied for low strain deformation [30, 31]. As previously discussed in section 2.5.1.b, there is evidence that the existence of non-deformable particles increases the dislocation density for deformation in the range of $\varepsilon = 0.1$-3. However, for large strains, it is expected that dynamic recovery, notably in Al-Mg alloys, may reduce the dislocation density from that calculated from Ashby's relations. In weld, the large strains combined with the high temperatures cause DRX in the TMAZ, which is expected to reduce ρ_S compared to ρ_G, which might actually increase due to grain refinement and particle break-up (F_V/r increases).

As the analysis of the DSC results shows, for the plastic strains retained in the WN after dynamic recovery, the sum of the ρ_G contributions dominates the measured stored energy. Thus, despite the high dislocation stored energy in the weld, this does not appear to explain the variances in the TMAZ/WN strength as it does not contribute significantly to the weld strength. Accordingly, it is important to consider the other strengthening contributions due to solid solution and particle (Orowan) strengthening.

8.1.5. Other Strengthening Contributions

8.1.5.a. Solid Solution Strengthening

As discussed in sections 8.1.2 and 8.l.3, solid solution strengthening can provide an additional strengthening contribution through the influence of the Mn and Mg content in solid solution. The influence of the Mn-content was previously considered in justifying the strength of the H34-BM. It was shown that the excess Mn in the H34-BM solid solution undergoes precipitation on thermal exposure during welding or annealing (as in O-BM), forming the fine $Al_6(Fe,Mn)$ dispersoids [10], which ultimately reduces the Mn solid solution strengthening contribution.

Conversely, it was observed that the Mg_xSi particles experience fragmentation-assisted dissolution during welding, decreasing the area fraction to 0.001–0.003 within the TMAZ compared to 0.005 in the base metal. The dissolution of Mg_xSi is expected to increase the Mg-content in the solid solution, which provides a strengthening contribution through solute-dislocation interaction. However, this contribution does not cover the discrepancy between the

WND and AS sites since, assuming that the Mg_xSi particles fully dissolve, only a minor contribution of ~4 H_V would result which corresponds to an increase of ~0.25 wt % Mg.

8.1.5.b. Orowan Strengthening

The precipitation of fine $Al_6(Fe,Mn)$ particles during FSW 5xxx-series alloys has been previously reported to have an influence on the WN hardness [10]. In addition, fragmentation of the constituent particles, due to the stirring action, was also suggested to have a similar influence[34]. Nonetheless, the relative importance of this contribution, with respect to grain size strengthening has not been carefully considered.

As shown in Fig. 8.13, fine $Al_6(Fe,Mn)$ dispersoids were found within the WND with an area fraction of ~ 0.025, and an average size (equivalent circle diameter) of ~195±85 nm. This trend was observed in the AS and WND, along with increased dislocation activity. TEM specimens from the RS did not show a similar extent of precipitation or particle fragmentation, nor a similar level of dislocation activity as discussed in section 7.1.2.c. The existence of fine particles was suggested to provide a strengthening contribution through hindering dislocation movement [16, 30, 35]. Orowan's equation estimates that the shear stress (τ) required to bow a dislocation around a distribution of particles can be calculated using:

$$\tau = Gb/\lambda \tag{8.5}$$

where λ is the average inter-particle spacing. For a random distribution of particles having a volume fraction of F_V and an average equivalent circle radius r, the inter-particle spacing is given by:

$$\lambda = \left(2\pi/3F_V\right)^{1/2} r \tag{8.6}$$

For the range of particles size and fractions observed, the estimated contribution of Orowan strengthening is equivalent to ~ 8.3 H_V in the WND/AS, with a significantly lower contribution in the RS. Sato *et al.* estimated a similar Orowan strengthening contribution in a 5083-O weld, putting it at ~10 H_V. Nonetheless, they did not identify the spatial variability in this parameter in the various locations of the weld. Quantifying this influence is generally difficult as it requires mapping the particle structure distributions in the weld using TEM.

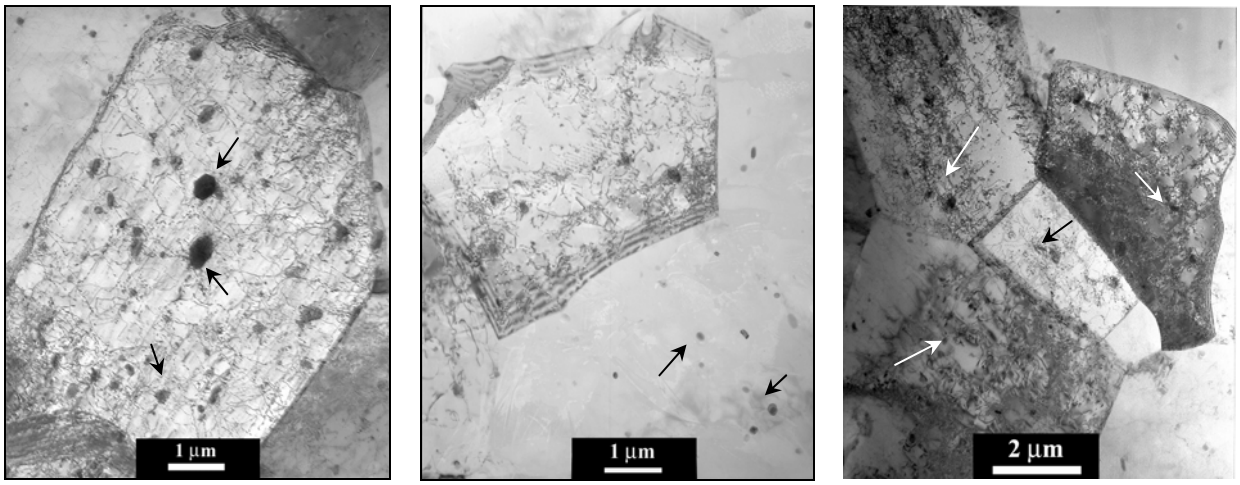

(a) Weld nugget (down) (b) Retreating side (c) Advancing side

Fig. 8.13. TEM micrographs from the weld showing precipitation of the $Al_6(Fe,Mn)$ particles (arrowed) in different regions

8.2. AA5754 Welds

The CC/DC 5754-O welds were used to verify the findings from the 5251 welds. The CC/DC 5754-O BMs contained a lower amount of constituent particles compared to 5251 H34/O BMs, which is expected to influence the particle strengthening contribution and the dislocation stored energy.

8.2.1. Hardness Distribution

The hardness distribution in the 5754-O CC/DC welds was more uniform throughout the TMAZ, compared to the distribution observed in the 5251 welds which showed hardness spikes towards the AS and in the WN. As shown in Fig. 8.14, the hardness traces show a uniform plateau of higher hardness within the WN/TMAZ, which decreases beyond the width of the TMAZ. However, it was generally observed that the hardness of the 'up'-trace is higher than the 'down'-trace in both conditions. In the CC weld, the average TMAZ hardness in the 'up'-trace was ~69±1 H_V, compared to 64.5±1 H_V for the 'down'-trace, then gradually decreasing to the basemetal hardness in both traces. In the DC weld, the average TMAZ hardness was 70.4±0.8 H_V in the 'up'-trace, and 67.7±1.6 H_V in the 'down'-trace.

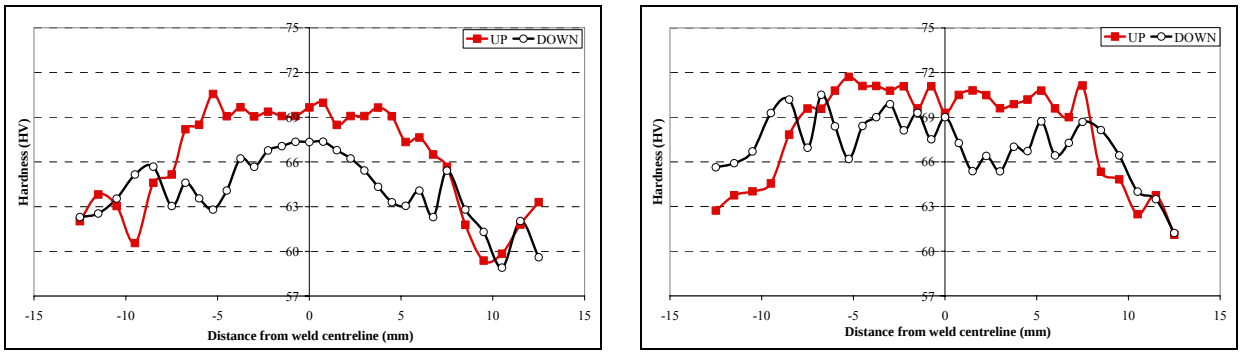

(a) (b)

Fig. 8.14. Hardness traces for the 5754-O (a) CC weld and (b) DC weld taken at 0.75 mm (up, TMAZ width ±6 mm) and 1.55 mm (down, TMAZ width ±4.5 mm) from the surface (the AS of the weld is to the right in each graph)

The analysis of the hardness traces of the 5754-O CC/DC welds shows that, despite the differences in the starting condition processing routes and microstructures (section 5.3), the

hardness distribution in both welds is roughly similar and uniform. No localised increase in the hardness was observed across the TMAZ width, and only a slight variation of ~3-4 H_V was observed across the thickness (decreasing from the weld surface downwards), which could be associated with the finer grain structures observed near to the sheet surface (section 7.2).

8.2.2. Grain Size Strengthening

To establish the grain size strengthening effects, grain size measurements for the DC and CC basemetals were plotted alongside the grain size data for the weld. In the CC-BM, the grain size was found to exhibit a clear variation across the sheet thickness, showing finer grains near to the edge, and coarser grains in the centre region (section 5.3.1). In the welds, grain size measurements were performed in the 'up' and 'down' regions, with the grain size and hardness data averaged across the TMAZ width. As shown in Fig. 8.15, the grain size data of the 5754 welds and the BMs were fitted into a Hall-Petch based relation, given by $H_V = 47+58d^{-1/2}$.

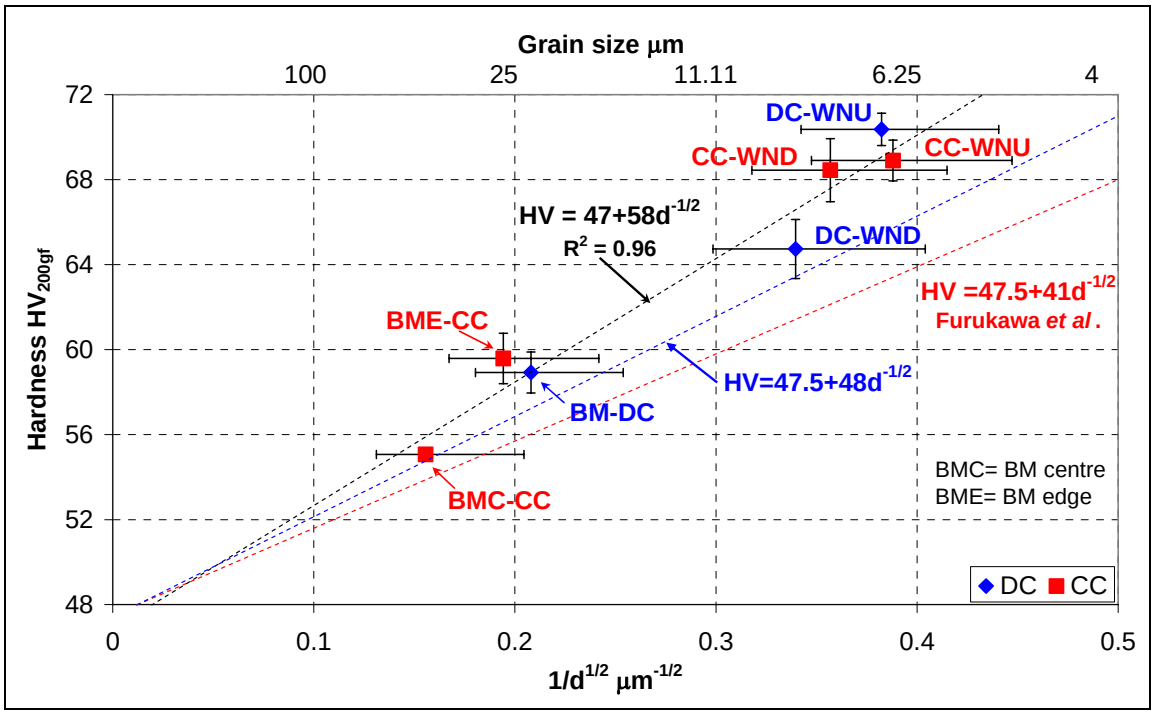

Fig. 8.15. Hall-Petch plot showing the contribution of the grain size to hardness in the 5754-welds and basemetal. Error bars are based on the standard deviation in measured hardness and grain size values.

In the literature, Furkuwa *et al.* [8, 9] estimated the average Hall-Petch relation for an AlMg3 alloy, subjected to severe plastic deformation by ECAP and torsion straining, to be $H_V = 47.5+41d^{-1/2}$. However, it was indicated that the data were scattered over a range with a maximum Hall-Petch of $H_V = 52+52d^{-1/2}$ and a minimum of $H_V = 44.5+32.5d^{-1/2}$. A possible explanation for this is that the data of Furukawa *et al.* covered a wide range of grain sizes with sizes as fine as 90 nm. Therefore, the fitted Hall-Petch relation from this work, compared to the average relation of Furukawa *et al.*, shows a similar Hall-Petch intercept, indicating a similar solid solution strengthening contribution, and possibly the lack of significant amounts of other alloying elements in solution. Although 5754-O CC/DC contain Mg_xSi particles which undergo dissolution during FSW, their area fraction is lower than in 5251 (section 5.3.2), which explains the similarity in the Hall-Petch intercept in the binary AlMg3 alloy and in 5754. However, the Hall-Petch slope (K_H) of the fitted relation is higher compared to Furukawa *et al.*.

Sato *et al.* [10, 11] gathered Hall-Petch data for several Al-Mg alloys, based on which it was suggested that the Mg-content affects K_H such that: $K_H = 38+3.26$ (wt % Mg), which gives K_H of 48 $H_V.\mu m^{-1/2}$ for 5754 (AlMg3), and accordingly a Hall-Petch relation of $H_V = 47.5+48d^{-1/2}$. With this relation, most of the conditions were found to fall within ~ 1-2 H_V of the range of fit, except for the WN specimens which deviated by ~3-4 H_V. The maximum deviation was in the DC-WNU specimen (~4.5 H_V). However, considering the standard deviations in grain size and hardness, this deviation is reasonable.

Thus, based on the above discussion, it can be concluded that grain size strengthening is the main strengthening mechanism in 5754-O welds. The solid solution strengthening contribution is taken into account in the Hall-Petch intercept. Investigating the other strengthening mechanisms is expected to confirm this finding.

8.2.3. Dislocation Stored Energy

8.2.3.a. DSC Measurements and Stored Energy in the Weld

The calorimetric measurements of the stored energy in the CC/DC 5754-O welds revealed somewhat unexpected results, Fig. 8.16. Upon cycling small specimens (3×2×2.3 mm) in the DSC, extracted from the WN (±2.5 mm) and the TMAZ towards the AS, a very low energy release (~ -0.3 J/g) was recorded, compared to the levels observed in the 5251 welds.

However, the energy release took place within a temperature range of ~250-350 ºC, which is similar to the recrystallisation range observed for 5251. The grain sizes in 5754 and 5251 welds are similar, and the deformation levels within the WN are also expected to be similar as both were welded using the same welding parameters, however, the amount of energy release in 5754 is significantly lower.

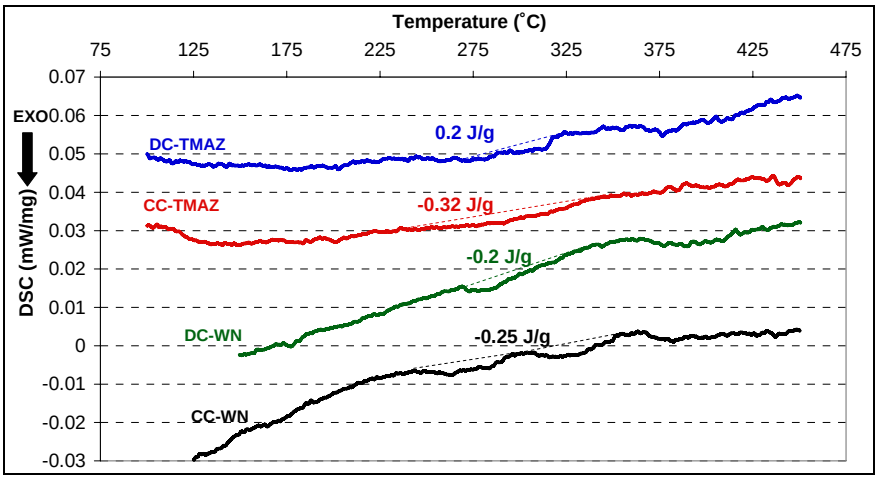

Fig. 8.16. DSC traces for specific locations in the 5754-O CC and DC welds showing the amount of energy release and temperature range

It would be expected that the similar grain size and strains experienced create a similar amount of ρ_G. However, this does not consider the influence of the difference in constituent particles and dispersoids structures between 5754 and 5251. As previously discussed (section 2.5.1.b), it is understood that the presence of incoherent non-deformable particles increases the dislocation density created during deformation, depending on the average size and volume fraction of the particles [30, 36]. As the F_v/r factor in 5754-BM is almost half that in 5251-BM, this is expected to decrease the density of dislocations created during FSW. Moreover, the 5754 welds showed a significantly lower number density of submicron dispersoids compared to 5251 (almost none in some regions, section 7.1.2), which also create ρ_G to accommodate their presence.

8.2.3.b. Quantifying ρ_G due to the Non-Deformable Particles

As both the 5754 and 5251 welds were welded using the same welding parameters (i.e. similar strains), and with a similar grain size, it is expected that the difference between the

stored energy represents the number of geometrically necessary dislocations that were created due to the higher particle content in 5251. This difference can be estimated using [36]:

$$\Delta\rho_G = \frac{E_{5251} - E_{5754}}{\alpha G b^2} \tag{8.7}$$

Using E_{5251} of -2.5 J/g and -0.3 J/g for E_{5754}, the estimated difference in ρ_G was found to be 5.4×10^{15} dislocations/m^2 created due to the higher particle content in 5251. This is ~87% of the total dislocations measured in the WN of 5251. To account for this difference then doubling the particle content must increase ρ_G by a factor of ~6.7.

The influence of the particle content on ρ_G has not been sufficiently investigated in the literature except in the work of Mandal and Baker [36], which compared the variation in ρ_G with strain in 2-phase (particle-containing) and single phase single crystal Cu-Si alloys. It was highlighted that the prediction of the stored energy as a function of strain using Ashby's model results in higher densities as the influence of recovery was not considered, which could explain the significant drop in stored energy in 5754 welds compared to 5251 weld since the recovery rate at room temperature in Al-Mg alloys increases with an increase in Mg-content [33].

8.3. AA5083 weld

The 5083-H116 weld was the last weld used to verify the findings of structure-property modelling. The 5083-BM contained roughly similar amount of constituent particles compared to 5251, yet with different size characteristics.

8.3.1. Hardness Distribution

The hardness in the 5083 weld WN (±3 mm from weld centreline) was fairly uniform compared to the hardness plateau observed in the WN or the peak towards the AS in the 5251 weld. The average WN hardness was 80.2±2.1 H_V, which is lower than the H116 hardness. Due to the low heat input in this weld (lower rotation and feed speeds compared to the 5251 and 5754 welds, and smaller tool compared to 5251), the localised thermal field during welding resulted in a limited HAZ, Fig. 8.17. The HAZ is characterised by a steep increase in the hardness from ~75 H_V at ±7 mm to ~95 H_V at ±11 mm from the weld centreline, Fig. 8.18.

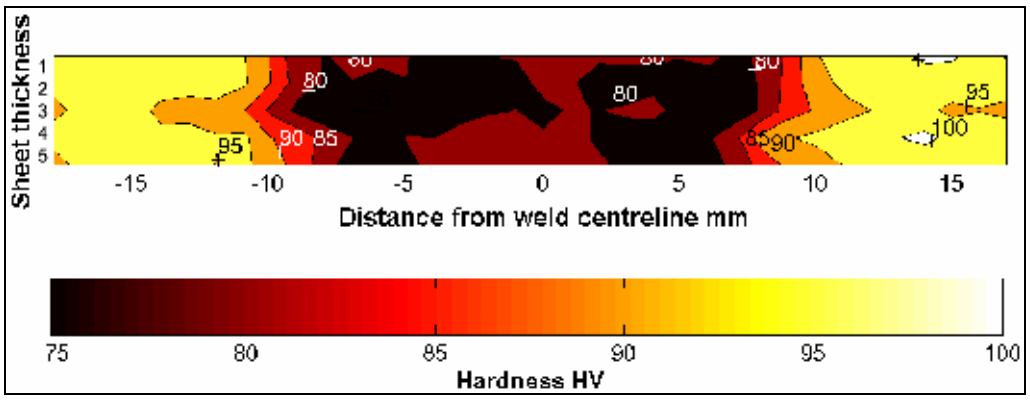

Fig. 8.17. Microhardness contour for the 5083-H116 weld (AS to the right)

Hardness traces taken at depths of 1.5 mm and 3.5 mm from the weld surface clarify the uniformity of the hardness distribution in this weld. As shown in Fig. 8.18, both traces show a roughly similar trend, with the hardness of the WN/TMAZ varying between 76 and 83 H_V, followed by a steep increase in hardness. In contrast with the previous welds, the WN/TMAZ hardness was lower than the basemetal strength, with the lowest hardness detected in the WN. This trend is similar to what is normally observed in the welds of work-hardened alloys (e.g. [1, 4, 11]).

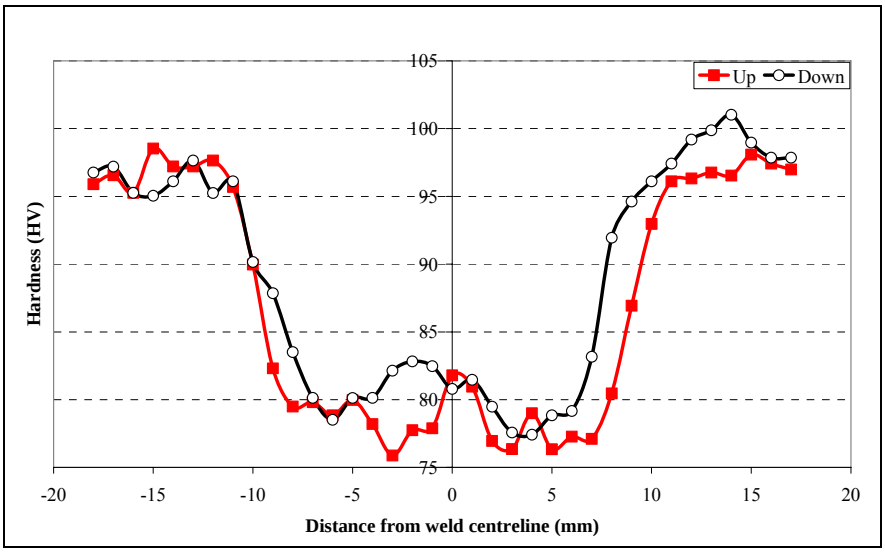

Fig. 8.18. Hardness traces for 5083-H116 taken at 1.5 mm (up, TMAZ width ±7.2 mm) and 3.5 mm (down, TMAZ width ±4.8 mm) from the surface (the AS of the weld is to the right in each graph).

8.3.2. Grain Size Strengthening

To establish a Hall-Petch relation for 5083-H116, basemetal specimens were heat treated to temperatures of 375, 425 and 475 ˚C, followed by performing grain size measurements. It was found that the hardness initially decreased from 375 ˚C to 425 ˚C, then increased at temperatures beyond 425˚C which was related to the dissolution of Mg_xSi. Nonetheless, the grain size did not show a significant variation which was attributed to the influence of the high number density of $Al_6(Fe,Mn)$ submicron particles in 5083-BM on grain size control (section 5.2.3). In the weld, the grain size and hardness distribution in the entire TMAZ was roughly uniform with an average grain size of 15.1±4.5 μm, and hardness of 79.7±2 H_V. Accordingly, only three data points were available from the weld and the annealed basemetal, which are insufficient to provide a Hall-Petch fit.

In the literature, several reports studied the Hall-Petch relations for 5083-O welds [10, 11, 37] and Mg-rich Al-alloys [14]. Sato *et al.* initially suggested a K_H of 33.8 H_V. $m^{1/2}$ in 5083-O weld, with an additional strengthening contribution by Orowan strengthening [10]. However, by covering a larger range of grain sizes, from 230 nm to ~10 μm, it was then indicated by Sato *et al.* that, depending on the grain size, two ranges for K_H existed in 5083-O welds, with the K_H increased in submicron-sized grains to 53 $H_V.\mu m^{-1/2}$ compared to 14 $H_V.\mu m^{-1/2}$ in

above micron grains [11]. Recently, Hirata *et al.* used the data from the previous studies and their own welds to plot a Hall-Petch relation of ~ $H_V = 70+30\ d^{-1/2}$, which represents a more average trend. The main concern with the previous fits is that they did not consider the additional strengthening contribution by Orowan strengthening except in [10].

Using the findings of the previous studies on 5251 and 5754, and assuming a linear relationship between the Mg-content and both H_{VO} and K_H, the Hall-Petch slope for 5083 can be estimated at $H_V = 61.3 + 52.2d^{-1/2}$, with the generalised Hall-Petch relation for Al-Mg alloys given as: $H_V = (19+ 9.5\times Mg\ wt\ \%) + (39 + 3\times Mg\ wt\ \%)d^{-1/2}$, with a possible variation in H_{VO} due to other alloying elements. As shown in Fig. 8.19, this relation shows a consistent fit with the heat-treated basemetal specimens, but it is out of fit with the WN by about 4-7 H_V. Accordingly, the investigation of other strengthening parameters becomes necessary.

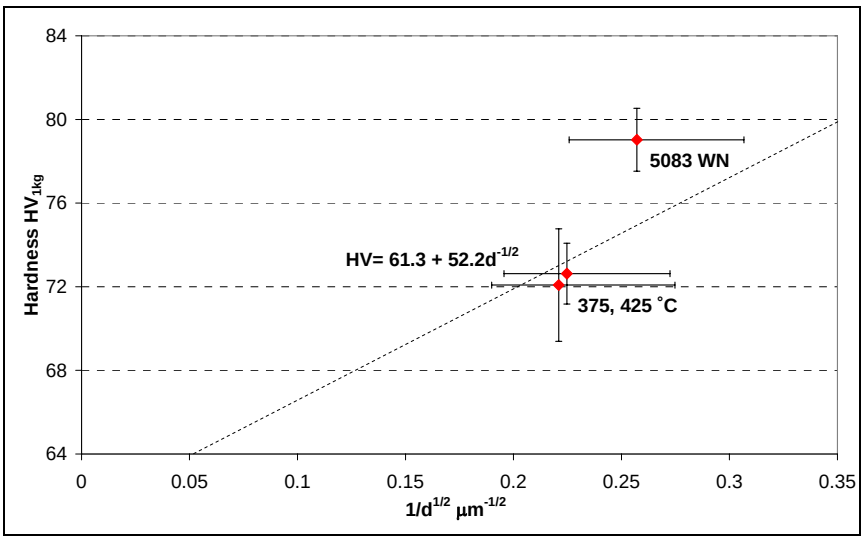

Fig. 8.19. Hall-Petch plot showing the contribution of the grain size to hardness in the 5083-welds and basemetal. Error bars are based on the standard deviation in measured hardness and grain size values.

8.3.3. Orowan Strengthening

TEM micrographs for the TMAZ showed that the weld contained submicron $Al_6(Fe,Mn)$ particles, Fig. 8.20. Stereological analysis of the TEM micrographs estimated their volume fraction to be ~0.04, with an average diameter of ~160 nm. Accordingly, this estimates the Orowan strengthening contribution at ~9-13 H_V, which slightly exceeds the discrepancy in the

Hall-Petch fit. However, it is clear that the variations in this contribution between the different locations of the weld is not as significant as in 5251 as the weld showed roughly similar particle number densities in different locations as shown in Fig. 8.20.

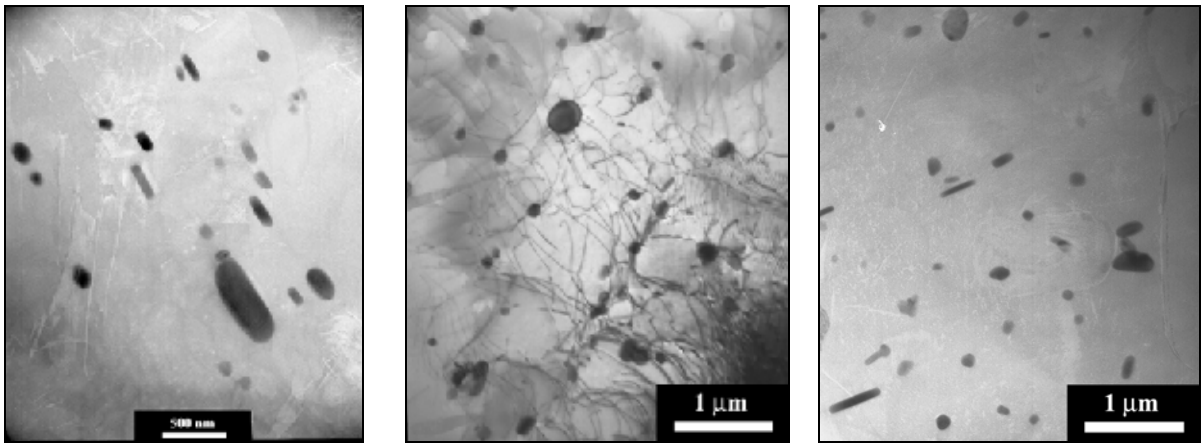

(a) AS (b) WN (c) RS

Fig. 8.20. TEM micrographs for different locations in the 5083-H116 weld

8.3.4. Dislocation Stored Energy

Upon cycling 5083-H116-BM and WND specimens in the DSC, energy release was observed by an amount similar to that measured in the 5251 BM and weld, and higher than that observed in the 5754 welds, Fig. 8.21. In the H116-BM, a single peak occurred between 310 and 370 ˚C, which was identified as recrystallisation, with energy release of -0.6 J/g. In the WND specimen, recrystallisation occurred at a relatively lower temperature, between 235 and 330 ˚C, releasing -2 J/g. Similar to 5251, recrystallisation in the 5083 WN specimens occurred at a temperature lower than the 5083-BM due to the higher driving force for recrystallisation resulting from the higher pre-deformation experienced in the weld.

An important correlation that can be deduced from the DSC results is the influence of the (Fe,Mn)-rich intermetallic particles content on the dislocation stored energy. In 5251-BM, the area fraction of the (Fe,Mn)-rich particles was 0.024±0.004, while the energy release within the WN was ~-2.5 J/g. In 5754 welds, which generated an energy release of ~-0.3 J/g, the area fraction of particles was lower at 0.011±0.005 in the CC-BM and 0.012±0.002 in the DC-BM. Finally, in 5083, which contained an area fraction of 0.02±0.002, the energy release was -2

J/g. Thus, it is obvious that the particle content present in the basemetal influences the energy stored in the weld during deformation, which has been previously suggested in the literature [30, 36].

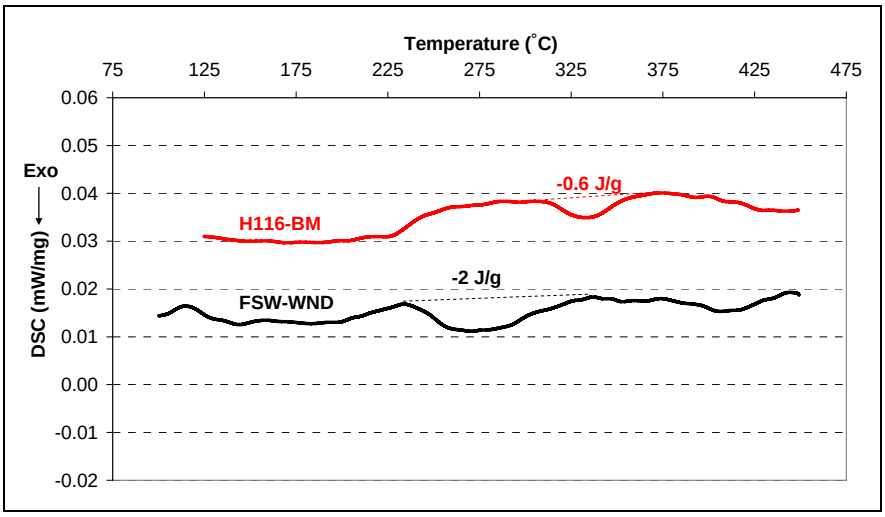

Fig. 8.21. DSC traces for different locations in the 5083-H116 weld

It is important to indicate that the high dislocation stored energy in 5251 and 5083 appears to be principally driven by the interaction of the intermetallic particles with deformation and recrystallisation during FSW. This was indicated by the fact that both the 5251 and 5754 welds were produced using the same welding parameters (i.e. similar strains and temperatures), and had roughly similar WN grain size. Yet, the 5754 had a significantly lower stored energy compared to 5251, which can only be related to the lower particle content in 5754. As previously mentioned, Ashby's model focused on the dislocation density development due to the presence of particles or grains during cold work, whereas FSW is a hot working process, which suggests that there is a discrepancy in studying the influence of hot working on the dislocation density development.

8.4. Discussion

8.4.1. Summary of the Findings

It was shown that the local strength in the TMAZ/WN of the 5xxx welds depends on two microstructural strengthening mechanisms, which are (according to the order of significance): grain-size (Hall-Petch) and particle (Orowan) strengthening. A third minor contribution by solid solution strengthening was infrequently encountered, and was attributed to the stirring-assisted dissolution of the Mg_xSi particles, thus enriching the Mg content of the TMAZ/WN. The earlier mechanism was uniform and consistent in distribution in all the welds, whereas the latter mechanisms are dependent on the microstructure of the base alloy (e.g. Fe/Mn-rich constituents, $Al_6(Fe,Mn)$, and Mg_xSi volume fraction). Additional mechanisms (e.g. dislocation stored energy or grain substructure strengthening) did not contribute to the weld strength despite the relatively high levels of stored energy, or the fraction of the LABs observed in the TMAZ/WN. The high levels of dislocation stored energy observed in the TMAZ (5-7 times higher than the H34-BM) were associated mainly with the creation of geometrically-necessary dislocations, which form due to the grain refinement and the presence of intermetallic particles in the weld. Nonetheless, the subgrain structure significantly contributed to the deformed base metal strength, alongside contributions by grain and solid solution strengthening, and similarly for the stored energy (section 5.4.1.b). Table 8.1 summarises the contribution of the strengthening mechanisms in the investigated welds.

Table 8.1. Strengthening contributions of the various mechanisms in AA5xxx welds

Alloy & Location / Mechanism	5251-H34		5754-O			5083-H116
	AS	**WND**	**WNU CC**	**WND CC**	**WNU DC**	**WN**
Hall-Petch (grain size)	Major	Major	Major	Major	Major	Major
Orowan (particle)	Medium	Medium	Main	Medium	Medium	Medium
Mg-solid solution	Minor	Minor	X	X	X	X
Stored Dislocations	X	X	X	X	X	X
Subgrain size strengthening	X	X	X	X	X	X

The findings of the present study provided an explanation for the conflicting reports on the influence of the microstructural strengthening mechanisms on the weld strength [1, 3, 10, 11, 38], especially the influence of the particle and dislocation strengthening, by identifying or eliminating the individual strengthening contributions. Moreover, this study also highlighted the spatially heterogeneous microstructure-property development associated with FSW, notably for the $Al_6(Fe,Mn)$ particle distribution, which resulted in regions with higher contributions from particle strengthening, as in the WND and AS sites in the 5251 weld, compared to regions with lower contributions, as in the RS. Conversely, a uniform distribution of the $Al_6(Fe,Mn)$ particles was observed in the 5083 welds, where all the TMAZ/WN showed a roughly uniform particle densities and volume fraction, and accordingly particle strengthening contribution. This correlation clarified the influence of the processing route of the base metal, whereby the welds of homogenised DC alloys (e.g. 5083) would have a uniform hardness distribution in the WN, while non-homogenised CC alloys (e.g. 5251 and 5754-CC) would be expected to develop non-uniform spatial distribution in hardness and microstructure. This would also depend on the intermetallic particle characteristics (e.g. banding, size, and area fraction). The influence of the base metal microstructure on the strengthening contributions in the welds, with the microstructural evidences observed in this study, are summarised in Table 8.2.

Table 8.2. The base metal microstructural factors and the evidence for their effect on the strengthening contributions in AA5xxx welds

Mechanism	BM Effect	Evidence
Hall-Petch (grain size)	None	• 5251 O and H34 conditions showed similar TMAZ hardness trends. • Similar welding parameters resulted in similar grain sizes (5251 and 5754 welds)
Orowan (particle)	Evident	• DC alloys (e.g. 5083) resulted in a uniform spatial distribution of $Al_6(Fe,Mn)$ particles due to homogenisation. • CC alloys (e.g. 5251 and CC 5754) resulted in particle segregation in certain regions, and accordingly high hardness regions (AS, WND). • Fe/Mn-rich particle fraction affected this strengthening contribution.
Mg-solid solution	Evident	• Mg_xSi volume fraction affected this strengthening contribution.
Stored Dislocations	None	• The presence of dislocations was linked to the particles and grains. • The TMAZ/WN hardness development was independent of the starting condition (e.g. 5251 O and H34)
Grain substructure	None	• Only a small fraction of the boundaries were LABs.

8.4.2. Interpretation for the Microstructure-Property Relations

From a design perspective, the hardness distribution, alongside the detailed microstructural characterisation, provide useful information on the fracture toughness of the welded joint. Compared to other welding techniques, FSW does not normally result in the formation of features that could deteriorate the fracture toughness of the weld (e.g. oxide films, volumetric defects, liquation, etc… as in fusion welding). Nonetheless, microstructural features, such as: grain size, constituent particles distribution, and texture, could also influence the fracture toughness.

Previous studies (e.g. Reynolds and co-workers [39-41] and Mahoney *et al.*[42]) on the influence of particle segregation on the fracture showed that the localised segregation of coarse intermetallic particles, as in the onion rings, created a crack growth path. It was observed that the fracture toughness of the weld regions are generally better than the base alloy in heat-treatable and work hardenable alloys, with the WN showing the highest cross-weld regions toughness properties [43]. However, as the microstructure-property investigations in this field are actually limited, the microstructural influences that could lead to this have not been assessed. It is generally known that certain parameters (e.g. fine grain structure and particles) enhance the fracture toughness, while other parameters (e.g. high fraction of HAGBs and high hardness) deteriorate the toughness [43]. Based on this, it is possible to predict the fracture toughness response of the weld regions in the investigated welds based on the microstructure-property development.

In the 5xxx welds, the fracture toughness is expected to be dependent on both the starting microstructure and the welding parameters. The presence of banded constituent particles of high area fraction, as in the 5251 weld, was found to result in hardness fluctuations across the TMAZ/WN, as well as the noted segregation of coarse particles within the ORZ bands, which would ultimately create fracture crack paths in these regions, resulting in poor toughness. Conversely, randomly oriented particles (as in 5083 and DC 5754) resulted in a uniform hardness distribution within the TMAZ, which would result in improved weld toughness. Moreover, welding of annealed conditions, with un-banded particle structures, resulted in a roughly uniform hardness distribution across all the weld regions, and less sharp transition between the HAZ and BM regions (e.g. comparing 5754-O, Fig. 8.14, and 5083-H116, Fig.

8.18). Other parameters (e.g. texture and grain size) are also expected to influence the toughness, but their influence is roughly similar for the same welding parameters.

Although this has not been investigated in great detail, the welding parameters should also influence the fracture toughness of the 5xxx welds; either through the thermal influence at the HAZ/BM interface, or by the microstructural development within the TMAZ. Expressing the welding parameters in terms of the APR, it is expected that low APRs (~0.1-0.3 mm/rev) would result in better particle distribution by breaking up of the bands. High APRs (>1 mm/rev) would conversely result in more particle segregation in banded materials. Although the work of Reynolds and co-workers did not find any trends for the influence of the APR on particle distribution in 2xxx [41], this can be attributed to the nature of particles in 2xxx alloys.

8.5. Conclusions

This chapter investigated the structure-property relations in AA5xxx welds. It was found that grain size (Hall-Petch) strengthening is the major strengthening mechanism, with additional contributions by particle (Orowan) strengthening, and minor contribution by solid solution strengthening. The main characteristics of the secondary contributions are their localised variations within the various weld regions, and their dependence on the starting condition. Orowan strengthening by the submicron $Al_6(Fe,Mn)$ particles or the fragmented constituent particles was found to vary across the weld regions, showing its highest levels in the WND and the AS of the 5251. However, in 5083 and DC 5754, the Orowan contribution was roughly uniform across the TMAZ. Similarly for solid solution strengthening, the dissolution of the Mg_xSi particles present in the base metal enriched the WN with Mg-atoms in 5251, while in 5083, with originally low Mg_xSi fraction in the base metal, this contribution was not present.

Despite the existence of high dislocation stored energy in the 5251 and 5083 welds, it is apparent that this is not associated with any work-hardening effects (statistically-stored dislocations), but rather with the production of geometrically-necessary dislocations due to the intermetallic particles and fine grains produced during welding. It was also found that the dislocation stored energy is directly influenced by the content of (Fe,Mn)-rich constituent particles.

This chapter also attempted to cover and highlight the gaps present in the FSW microstructure-property literature, notably the influence of the base metal starting microstructure and the possible influence of the microstructure-property development from a design perspective on the weld mechanical properties (e.g. fracture toughness).

8.6. References

[1] Y. S. Sato, Y. Sugiura, and H. Kokawa, "Hardness Distribution and Microstructure in Friction Stir Weld of Aluminum Alloy 5052," presented at 4th International Symposium on Friction Stir Welding, Park City, Utah, USA, 2003.

[2] I. Shigematsu, Y. J. Kwon, K. Suzuki, T. Imai, and N. Saito, "Joining of 5083 and 6061 aluminum alloys by friction stir welding," *Journal of Materials Science Letters*, vol. 22, pp. 353-356, 2003.

[3] L.-E. Svensson, L. Karlsson, H. Larsson, B. Karlsson, M. Fazzini, and J. Karlsson, "Microstructure and Mechanical Properties of Friction Stir Welded Aluminium Alloys with Special Reference to AA 5083 and AA 6082 aluminium," *Science and Technology of Welding and Joining*, vol. 5, pp. 285-296, 2000.

[4] P. Threadgill, "Friction Stir Welds in Aluminium Alloys: Preliminary Microstructural Assessment," *TWI Bulletin*, vol. 38, pp. 30-33, 1997.

[5] H. G. Salem, "Friction stir weld evolution of dynamically recrystallized AA 2095 weldments," *Scripta Materialia*, vol. 49, pp. 1103-1110, 2003.

[6] Y. J. Kwon, I. Shigematsu, and N. Saito, "Mechanical properties of fine-grained aluminum alloy produced by friction stir process," *Scripta Materialia*, vol. 49, pp. 785-789, 2003.

[7] S. P. Chen, M. S. Vossenberg, F. J. Vermolen, J. van de Langkruis, and S. van der Zwaag, "Dissolution of [beta] particles in an Al-Mg-Si alloy during DSC runs," *Materials Science and Engineering A*, vol. 272, pp. 250-256, 1999.

[8] M. Furukawa, Z. Horita, M. Nemoto, R. Z. Valiev, and T. G. Langdon, "Microhardness measurements and the Hall-Petch relationship in an Al-Mg alloy with submicrometer grain size," *Acta Materialia*, vol. 44, pp. 4619-4629, 1996.

[9] M. Furukawa, Y. Iwahashi, Z. Horita, M. Nemoto, N. K. Tsenev, R. Z. Valiev, and T. G. Langdon, "Structural evolution and the Hall-Petch relationship in an Al-Mg-Li-Zr alloy with ultra-fine grain size," *Acta Materialia*, vol. 45, pp. 4751-4757, 1997.

[10] Y. S. Sato, S. H. C. Park, and H. Kokawa, "Microstructural factors governing hardness in friction-stir welds of solid-solution-hardened Al alloys," *Metallurgical and Materials Transactions A: Physical Metallurgy and Materials Science*, vol. 32, pp. 3033-3042, 2001.

[11] Y. S. Sato, M. Urata, H. Kokawa, and K. Ikeda, "Hall-Petch relationship in friction stir welds of equal channel angular-pressed aluminium alloys," *Materials Science and Engineering A*, vol. 354, pp. 298-305, 2003.

[12] G. B. Burger, A. K. Gupta, P. W. Jeffrey, and D. J. Lloyd, "Microstructural control of aluminum sheet used in automotive applications," *Materials Characterization*, vol. 35, pp. 23-39, 1995.

[13] K. L. Kendig and D. B. Miracle, "Strengthening mechanisms of an Al-Mg-Sc-Zr alloy," *Acta Materialia*, vol. 50, pp. 4165-4175, 2002.

[14] D. J. Lloyd and S. A. Court, "Influence of grain size on tensile properties of Al-Mg alloys," *Materials Science and Technology*, vol. 19, pp. 1349-1354, 2003.

[15] S. C. Wang, Z. Zhu, and M. J. Starink, "Estimation of dislocation densities in cold rolled Al-Mg-Cu-Mn alloys by combination of yield strength data, EBSD and strength models," *Journal of Microscopy*, vol. 217, pp. 174-178, 2005.

[16] R. W. Hertzberg, *Deformation and Fracture Mechanics of Engineering Materials*, 4 ed. USA: John Wiley & Sons Inc., 1996.

[17] S. A. Court, K. M. Gatenby, and D. J. Lloyd, "Factors affecting the strength Al-3 and formability of alloys based on wt.% Mg," *Materials Science & Engineering A:*

Structural Materials: Properties, Microstructure and Processing, vol. A319-321, pp. 443-447, 2001.

[18] G. J. Mahon and G. J. Marshall, "Microstructure-property relationships in O-temper foil alloys," *JOM*, vol. 48, pp. 39-42, 1996.

[19] J. R. Bowen, P. B. Prangnell, D. J. Jensen, and N. Hansen, "Microstructural parameters and flow stress in Al-0.13% Mg deformed by ECAE processing," *Materials Science and Engineering A*, vol. 387-389, pp. 235-239, 2004.

[20] N. Hansen, "Effect of Grain Size and Strain on the Tensile Flow Stress of Aluminium at Room Temperature," *Acta Metallurgica*, vol. 25, pp. 863-869, 1977.

[21] N. Hansen, "Hall-petch relation and boundary strengthening," *Scripta Materialia*, vol. 51, pp. 801-806, 2004.

[22] N. Hansen, "Boundary strengthening in undeformed and deformed polycrystals," *Materials Science and Engineering A*, vol. 409, pp. 39-45, 2005.

[23] N. Hansen, X. Huang, R. Ueji, and N. Tsuji, "Structure and strength after large strain deformation," *Materials Science and Engineering A*, vol. 387-389, pp. 191-194, 2004.

[24] D. A. Hughes and N. Hansen, "High angle boundaries formed by grain subdivision mechanisms," *Acta Materialia*, vol. 45, pp. 3871-3886, 1997.

[25] F. J. Humphreys, "Grain and subgrain characterisation by electron backscatter diffraction," *Journal of Materials Science*, vol. 36, pp. 3833-3854, 2001.

[26] O. R. Myhr and O. Grong, "Process modelling applied to 6082-T6 aluminium weldments--II. Applications of model," *Acta Metallurgica et Materialia*, vol. 39, pp. 2703-2708, 1991.

[27] H. Jin, S. Saimoto, M. Ball, and P. L. Threadgill, "Characterisation of microstructure and texture in friction stir welded joints of 5754 and 5182 aluminium alloy sheets," *Materials Science and Technology*, vol. 17, pp. 1605-1614, 2001.

[28] M. Peel, A. Steuwer, M. Preuss, and P. J. Withers, "Microstructure, mechanical properties and residual stresses as a function of welding speed in aluminium AA5083 friction stir welds," *Acta Materialia*, vol. 51, pp. 4791-4801, 2003.

[29] I. Baker, L. Liu, and D. Mandal, "The effect of grain size on the stored energy of cold work as a function of strain for polycrystalline nickel," *Scripta Metallurgica et Materialia*, vol. 32, pp. 167-171, 1995.

[30] F. J. Humphreys and M. Hatherly, *Recrystallization and Related Annealing Phenomena*. Great Britain: Pergamon, 1995.

[31] M. F. Ashby, "The Deformation of Plastically Non-Homogeneous Alloys," in *Strengthening Methods in Crystals*, A. Kelly and R. B. Nicholson, Eds. Amsterdam: Elsevier Publishing Company Ltd., 1971.

[32] S. Xu and X. Deng, "A Three-Dimensional Model for the Friction-Stir Welding Process," presented at 21st Southeastern Conference on Theoretical and Applied Mechanics (SECTAM XXI), Orlando, Florida, 2002.

[33] E. Nes, "Recovery revisited," *Acta Metallurgica et Materialia*, vol. 43, pp. 2189-2207, 1995.

[34] W. Baeslack, K. Jata, and T. Lienert, "Structure, properties and fracture of friction stir welds in a high-temperature Al-8.5Fe-1.3V1.7Si alloy (AA-8009)," *Journal of Materials Science*, vol. 41, pp. 2939-2951, 2006.

[35] A. Kelly and R. B. Nicholson, "Strengthening Methods in Crystals." Amsterdam: Elsevier Publishing Company Ltd., 1971.

[36] D. Mandal and I. Baker, "On the effect of fine second-phase particles on primary recrystallization as a function of strain," *Acta Materialia*, vol. 45, pp. 453-461, 1997.

[37] T. Hirata, T. Oguri, H. Hagino, T. Tanaka, S. W. Chung, Y. Takigawa, and K. Higashi, "Influence of friction stir welding parameters on grain size and formability in

5083 aluminum alloy," *Materials Science and Engineering: A*, vol. In Press, Corrected Proof, 2007.

[38] Y. S. Sato, Y. Sugiura, Y. Shoji, S. H. C. Park, H. Kokawa, and K. Ikeda, "Post-weld formability of friction stir welded Al alloy 5052," *Materials Science and Engineering A*, vol. 369, pp. 138-143, 2004.

[39] M. A. Sutton, B. Yang, A. P. Reynolds, and R. Taylor, "Microstructural studies of friction stir welds in 2024-T3 aluminum," *Materials Science and Engineering A*, vol. 323, pp. 160-166, 2002.

[40] M. A. Sutton, B. Yang, A. P. Reynolds, and J. Yan, "Banded microstructure in 2024-T351 and 2524-T351 aluminum friction stir welds. Part II. Mechanical characterization," *Materials Science and Engineering A*, vol. 364, pp. 66-74, 2004.

[41] B. Yang, J. Yan, M. A. Sutton, and A. P. Reynolds, "Banded microstructure in AA2024-T351 and AA2524-T351 aluminum friction stir welds. Part I. Metallurgical studies," *Materials Science and Engineering A*, vol. 364, pp. 55-65, 2004.

[42] M. W. Mahoney, C. G. Rhodes, J. G. Flintoff, R. A. Spurling, and W. H. Bingel, "Properties of friction-stir-welded 7075 T651 aluminum," *Metallurgical and Materials Transactions A: Physical Metallurgy and Materials Science*, vol. 29A, pp. 1955-1964, 1998.

[43] R. S. Mishra and Z. Y. Ma, "Friction stir welding and processing," *Materials Science and Engineering: R: Reports*, vol. 50, pp. 1-78, 2005.

Chapter 9
CONCLUSIONS & FUTURE WORK

9.1. Summary and Conclusions

9.1.1. Thermal Modelling and HAZ Development in FSW

The presented work has demonstrated a 3-D MATLAB® model for predicting the thermal fields during FSW, based on the process parameters and the thermo-mechanical and thermo-physical properties of the material. The model utilises the ADI finite difference scheme to solve the heat transfer equation during FSW. Mixed friction-deformation heat generation was used, employing an annular heat flux under the tool shoulder and a volumetric heat source for the pin. Experimental verification was performed through *in-situ* thermocouple measurements and Gleeble thermal simulations of the thermal cycle. The predicted thermal fields were used to interpret the HAZ microstructure and hardness development.

Based on the results presented, the following conclusions can be drawn:

- The model is capable of providing reasonable predictions for the transient thermal cycle, within the experimental error of thermocouple measurements (±30 ˚C), and with similar accuracy to other models. The use of ADI boosted the computational speed, compared to FE modelling, although the speed can be further enhanced by using adaptive grid.
- The model relies on two main assumptions to simplify the estimation of the heat generation, which are a constant friction coefficient and a fitted function for the thermomechanical properties based on the ASM data. Beyond this, fitting becomes limited only to the contact conductance between the machine anvil and workpiece.

- The simplest approach for modelling the contact conductance, in vacuum or mechanically-clamped welds, is to divide the weld into regions of low conductivity (behind the tool), and high conductivity (under and in front of the moving tool), depending on the sheet thickness.
- The model thermal predictions were consistent with the observed microstructure and hardness distributions. Gleeble simulations for the predicted HAZ thermal cycles in 5251 weld were also consistent with the microstructural development.
- It was found that the recrystallisation start temperature is dependent on the thermal history of the heating rates. A critical heating rate is necessary to avoid recovery during heating to full recrystallisation.

9.1.2. Microstructural Development

The presented work has attempted to provide a fundamental understanding for the microstructural development in Al-based alloys welds, focusing on the parameters controlling the formation of the onion rings structure.

For the alloys and the range of welding parameters investigated, the following conclusions can be drawn:

9.1.2.a. Onion Rings Formation

- The onion rings structure has been identified as a region of microstructural heterogeneity in the grain and particle/precipitate structure.
- The microstructural heterogeneities associated with the ORZ were identified as the existence of coarse and fine grains bands, with grain boundary precipitation coinciding with the fine grain bands, and segregation of coarse-particles within the coarse grain bands. These features are manifested in the form of a selective etching response, which creates the unique bands of alternating contrast.
- The shape of the bands seems to be influenced by the tool type, where the MX-Triflute created randomly oriented bands, compared to concentric ellipses using a threaded tool.
- On the weld face, it was difficult to find a correlation between the welding parameters, basemetal inter-particle bands spacing, and the ORZ bands spacing (thickness). However, on the longitudinal section at the weld centreline, along the WD, the microstructural

heterogeneities are observed at a rate of occurrence equivalent to the tool advance per rotation.

- The formation of the ORZ is linked to the intermetallic particles distribution in the basemetal, where the presence of banded intermetallic particles along the RD (e.g. 5251, 5754-CC and 2024) led to the formation of an ORZ. No ORZ was observed in the welds where the particles are randomly distributed in the basemetal (e.g. 5083 and 5754-DC).
- The type of the banded particles (i.e. constituent Al(Fe,Mn)Si or Al_6(Fe,Mn) in 5xxx or equilibrium phases Al_2Cu and Al_2CuMg in 2xxx) does not affect the ORZ formation.
- For the same welding parameters, the banded particles area fraction influences the ORZ etching intensity, where high area fraction led to a more pronounced ORZ.

9.1.2.b. Qualitative & Quantitative Microstructural Development

- FSW leads to grain refinement, with the grain size increasing from the AS to the RS, and from the top to the bottom of the weld before decreasing again towards the ORZ. Typical grain sizes observed are within a range of 3-15 μm, depending on the welding parameters and the location in the weld.
- For given welding parameters, the basemetal condition (work-hardened or annealed) does not influence the TMAZ grain size, or the particle distribution.
- The intermetallic particles undergo a stirring-assisted development depending on their types. In 5xxx welds, Fe-containing constituent particles are thermally stable, thus they only experience breaking-up of the continuous bands to fine particles, while the Mg_xSi particles almost completely dissolve within the WN/TMAZ. In 2024, the Cu-rich equilibrium particles partially dissolved, decreasing their A_f.
- Grain boundary precipitates form due to the existence of solutes atoms, either prior to welding as in the case of Mn-solutes in AA5xxx alloys which form the Al_6(Fe,Mn) precipitates during welding, or due to dissolution and re-precipitation as in the case of Cu-rich phases in AA2xxx welds.
- The formation of the dislocation structure in AA5xxx depends on the starting condition microstructure, and can be linked to the presence of intermetallic particles and dispersoids. In alloys with high particle content (e.g. 5251 abd 5083), dislocations were observed within the DRXed grains, tangled with particles. In alloys with low particle content (e.g. 5754), low dislocation density was observed.

- The distribution of the $Al_6(Fe,Mn)$ dispersoids was uniform in the 5083 weld, compared to a heterogeneous distribution in 5251 weld with higher densities in the WN and the AS of the TMAZ and lower densities in the RS.

9.1.3. Structure-Property Relations in AA5xxx welds

The influence of the microstructural factors governing the strength in AA5xxx welds were studied using a combination of several experiment techniques, such as: DSC, EBSD, OM, SEM and TEM, to provide a quantitative representation for the local mechanical property (microhardness) development in the weld. The following conclusions can be drawn:

- In the 5251 weld, which showed a strong ORZ, FSW resulted in a non-uniform TMAZ hardness distribution, with high hardness spots towards the AS and in the ORZ. In 5083 and 5754, hardness distribution was roughly uniform within the TMAZ. Beyond the TMAZ, the hardness increased gradually returning to the BM hardness depending on the initial condition (work-hardened or annealed).
- Grain size (Hall-Petch) strengthening nearly accounts for the 5251 weld hardness in most of the weld locations, except in the AS and WN. Additional strengthening contributions were found in these regions due to particle (Orowan) strengthening by the $Al_6(Fe,Mn)$ dispersoids and the constituent particles, and solid solution strengthening due to the dissolution of Mg_xSi.
- The hardness of the 5251 H34-basemetal was attributed to the strengthening contribution of the low angle boundaries of the subgrains, which form the majority of the boundaries in the deformed structure. Within the weld and in the annealed basemetal, the majority of the boundaries were high angle boundaries, which are considered in the Hall-Petch effect.
- The Orowan strengthening contribution was localised in the WND region and towards the AS, as evident in the higher particle area fraction and number density, while the RS showed an almost negligible contribution. However, in the 5083 weld, the particle distribution was roughly uniform across the TMAZ. These differences were suggested to be due to the differences in the starting condition.
- A minor contribution of solid solutions strengthening, due to dissolution of the Mg_xSi particles during welding, was found in the 5251 weld. However, this contribution is dependent on the thermal fields experienced during welding and the basemetal content of

the Mg_xSi particles. Accordingly, this contribution was found insignificant in 5083 and 5754 welds.

- The high dislocation stored energy in the 5251 and 5083 welds was attributed to the presence of the geometrically-necessary (non-strengthening) dislocations, which are created due to the presence of the intermetallic particles and the fine grains.

9.2. Future Work

The present work has provided a fundamental understanding for the microstructure-property development in Al-based alloys welds, which covered thermal modelling, HAZ and TMAZ microstructural development, as well as the structure-property relations in AA5xxx welds, while considering the influence of the basemetal microstructure. Future work is still required to quantify the influence of the basemetal microstructural factors on the weld microstructure, as well as to produce simple and quick numerical models for FSW. This would concentrate on the following aspects:

- To establish models for the recrystallisation by PSN under the influence of transient thermal cycles, and to further assess the influence of the heating rate on recrystallisation and the microstructural parameters influencing this.

- To study the influence of the Mn-solutes present in the basemetal in AA5xxx on the distribution of the dispersoids in the weld, and determine the parameters that leads to heterogeneous (as in 5251 weld) or homogeneous dispersoid distribution (in 5083). For this, experimental techniques such as thermo-electric power (TEP) and SAXS could be useful to quantify the solute content and dispersoid size and number density.

- To investigate the influence of the basemetal particle band spacing and area fraction on the formation of the ORZ, weld stored energy, and heterogeneity of the local mechanical properties. For this, cast alloys can be used to de-couple the influence of the particle characteristics (size, area fraction, band spacing, etc…).

- To study the dynamic recrystallisation mechanisms in 5xxx welds, and the texture within the ORZ bands.

- To study the influence of the starting condition processing route on the weld mechanical and corrosion properties.

- To increase the robustness of the simplified model by using adaptive grids, and to predict the hardness development in heat-treatable and work-hardenable alloys.

Noting the difficulty in decoupling the influence of the process parameters and the basemetal microstructural factors on the microstructure-property development, it will be beneficial to re-design the experiments to investigate all the factors. Since it was found that the intermetallic particles actually play an important role in the microstructure-property development (e.g. the onion rings structure and the particle strengthening contribution), one possible way to investigate their influence is through the utilisation of cast Al-alloys (e.g. Al-Si alloys) of different Si composition, which will result in different intermetallic particles content. This can be a part of a fractional-factorial experiment (3^{3-1}), investigating the influence of the constituent particles area fraction, advance per revolution, and rotation speed (heat input) on the microstructure-property development. One disadvantage is that this will require about 9 welds, which is larger than the number of welds investigated (4), but will ultimately provide stronger indications on the significance of certain parameters.